Document Version
Final published version

Citation (APA)
Stolte, E. W. (2026). *Faster control or longer lifetimes: Expanding the toolbox for electron and nuclear spin dynamics in on-surface atoms.* [Dissertation (TU Delft), Delft University of Technology]. https://doi.org/10.4233/uuid:3d54cda8-fcfd-494c-a2d6-501fd2f70f9d

Faster control or longer lifetimes

Expanding the toolbox for electron and nuclear spin dynamics in on-surface atoms

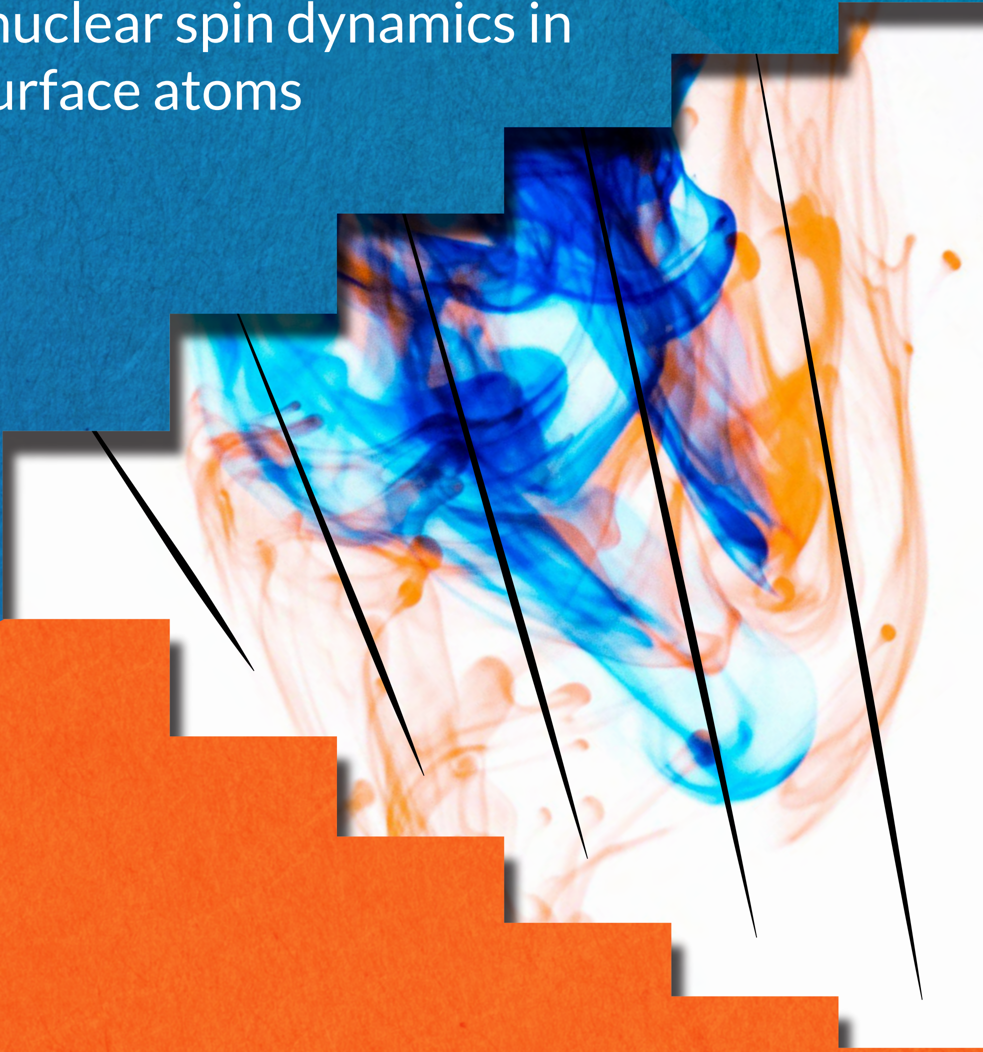

Evert Stolte

Faster control or longer lifetimes

Expanding the toolbox for electron and nuclear spin dynamics in on-surface atoms

Dissertation

for the purpose of obtaining the degree of doctor
at Delft University of Technology
by the authority of the Rector Magnificus, prof. dr. ir. H. Bijl,
chair of the Board for Doctorates
to be defended publicly on
Friday, 24 April 2026 at 12:30

by

Evert Willem STOLTE

This dissertation has been approved by the promotors.

Composition of the doctoral committee:

Rector Magnificus,	chairperson
Prof. dr. A.F. Otte,	Delft University of Technology, *promotor*
Prof. dr. ir H.S.J. van der Zant,	Delft University of Technology, *promotor*
Independent members:	
Prof. dr. M. Blaauboer,	Delft University of Technology
Prof. dr. G.A. Steele,	Delft University of Technology
Dr. T. Esat,	Forschungszentrum Jülich, Germany
Dr. Y. Bae,	Swiss Federal Laboratories for Materials Science and Technology (Empa), Switzerland
Prof. dr. S. Gröblacher,	Delft University of Technology, *reserve member*

Keywords: Scanning tunneling microscopy, ESR-STM,
arbitrary waveform generator, AWG, nuclear spin, quantum control

Printed by: Ridderprint

Cover by: Evert Stolte

ISBN 978-94-6384-922-7

An electronic copy of this dissertation is available at
https://repository.tudelft.nl/.

If you want to have an alliance to truth, you have to trade away the comfort of constant certainty.

Hank Green

Contents

Summary

Magnetism at the atomic scale is governed by the laws of quantum mechanics, with individual atoms possessing magnetic moments, called 'spin', quantized in discrete levels. Even small quantum spin systems, consisting of only a few coupled atoms, can display complex time dynamics. Uncovering this behavior and learning how to control the spins in these model systems might lead to insights about larger, even more complex systems that are yet poorly understood.

It is an experimental challenge to both measure and control atomic spins in their solid state environments. We achieve these feats in this thesis with a scanning tunneling microscope (STM). This is, in essence, an atomically sharp needle that ends in a singular atom. This needle tip scans over a surface to measure a topographic image that identifies individual atoms on the surface.

Over the last decade, the capabilities of atomic-resolution scanning probes, such as STM, to read out and control single atomic spins on a surface in time, have extended tremendously by the introduction of pump-probe schemes and electron spin resonance (ESR) to this field of research. However, the potential of both sensing and quantum control capabilities in this platform have been limited by the short coherence times compared to the control time scales. This means the spins lose their quantum properties before these can be exploited.

In this thesis, we explore two directions to improve the degree and complexity of coherent control of individual spins in on-surface atoms using an STM equipped with electron spin resonance capabilities. Firstly, we integrate an arbitrary waveform generator (AWG) into our STM setup for faster and more complex voltage signal generation for readout and spin control. Secondly, we investigate the time dynamics of individual nuclear spins in on-surface atoms, which potentially have longer coherence times. We realize a time-resolved readout of the nuclear spin state with the STM via the hyperfine-coupled electron spin.

In chapters 3 and 4 we show that a 65 GSa/s AWG interfaced with an STM can be used, as a singular signal generator, to accomplish previously reported techniques for coherent single-atom electron spin control that have required multiple instruments in the past, including Rabi oscillations and initialization of coherent flip-flop dynamics with electron scattering. Furthermore, with the AWG we combine these separate techniques in one experiment by generating nanosecond DC and RF pulses together, and in general go beyond previous experimental capabilities in terms of the complexity in experiment design.

Parts of chapter 4 are dedicated to initial experiments to probe the time-evolution of on-surface nuclear spins. We observe coherent nuclear spin dynamics with the STM for the first time, with the initialization and readout mediated by hybridization with the accompanying electron spin in the same atom in a small magnetic field. We also

performed an initial attempt to measure the nuclear spin lifetime T_1 in the high-field regime that results in a tentative lower bound in the microseconds range.

For chapter 5 we use the AWG to measure both the amplitude and phase voltage transfer functions of the RF cabling in the STM. This allows us to compensate for the distortions to pulse shapes caused by the phase transfer function when generating the pulses with the AWG. By applying this compensation, we are able to achieve shorter DC pulses in the STM junction, reaching sub-nanosecond widths. This enables spin readout at higher time resolution and potentially faster spin control.

In chapter 6, we extend the search for the nuclear spin lifetime in Ti adatoms to longer time scales and find a T_1 in the order of seconds, which is orders of magnitude longer than any other on-surface spin that has been shown to be controllable by ESR-STM. Furthermore, this lifetime is long enough to measure the spin before it changes, and thus perform single-shot readout of the nuclear spin state, which allows us to investigate various relaxation mechanisms of the nuclear spin experimentally.

In chapter 7 we investigate the nuclear spin relaxation theoretically. From the combination of experimental and theoretical results, we conclude that the incoherent flip-flop rate between the electron and nuclear spin in the same adatom is the limiting factor for the lifetime.

Samenvatting

Op de atomaire lengteschaal gedraagt magnetisme zich volgens de regels van de kwantummechanica, waar de magnetische momenten van individuele atomen, genaamd 'spin', in discrete richtingen wijzen, in plaats van een continuüm. Zelfs kleine kwantumspin systemen, bestaande uit slechts enkele atomen, kunnen complexe dynamica volgen. Het begrijpen en aansturen van deze bewegingen in de tijd in modelsystemen kunnen inzichten opleveren over grotere, nog complexere systemen die nog slecht worden begrepen.

Het is een experimentele uitdaging om die atomaire spins daadwerkelijk te meten en aan te sturen. In dit proefschrift maken we gebruik van een scannende tunnelmicroscoop (STM). Dit is, in essentie, een uitermate scherpe naald die eindigt in een enkel atoom. Die naaldtip wordt vervolgens over een oppervlakte gescand om een topografische afbeelding met atomaire resolutie vast te leggen en individuele atomen te identificeren.

In het afgelopen decennium zijn de mogelijkheden van STMs voor het dynamisch uitlezen en aansturen van individuele atomaire spins op oppervlaktes enorm toegenomen door de introductie van gepulseerde excitatie-uitlees tijdspectroscopie ('pump-probe') en elektronspinresonantie (ESR) methodes in het STM-vakgebied. Potentiële toepassingen van dit STM-platform, bijvoorbeeld voor precisiemetingen in kwantummagnetisme experimenten, worden echter gelimiteerd door de relatief korte coherentietijd van de spins in vergelijking met de tijd die nodig is om de spins aan te sturen. Dit betekent dat de spins hun kwantumeigenschappen kwijt zijn voordat die eigenschappen kunnen worden gebruikt.

Dit proefschrift verkent twee verschillende richtingen om de kwaliteit en complexiteit van het kwantumcoherent aansturen van spins te verhogen voor individuele atomen op een oppervlakte bij het gebruik van een STM opstelling met ESR capaciteiten. Ten eerste integreren we een *arbitrary waveform generator* (AWG) in de opstelling. De AWG kan willekeurige voltagesignalen genereren in de tijd, wat helpt bij snellere en complexere experimenten met spins. Ten tweede onderzoeken we de dynamica van individuele nucleaire spins in de atomen. Die zijn potentieel langer kwantumcoherent dan de elektronspins die de STM direct kan meten. In deze experimenten gebruiken we de hyperfijninteractie tussen de elektronspin en de nucleaire spin in hetzelfde atoom om de richtingsveranderingen van de nucleaire spin indirect uit te lezen in de tijd.

In hoofdstuk 3 en hoofdstuk 4 demonstreren we dat een 65 GSa/s AWG, in combinatie met een STM, alle eerder gepubliceerde kwantumcoherente aanstuurtechnieken voor spins op oppervlakten kan uitvoeren, inclusief Rabi oscillaties en initialisatie van flip-flop dynamica met elektronspin excitaties. Hier waren in voorgaande experimenten verschillende instrumenten voor nodig, maar deze technieken kunnen nu dus worden uitgevoerd met een enkel apparaat. Daarnaast laten we zien dat de AWG meerdere technieken tegelijkertijd in één experiment integreren door DC en RF pulsen van enkele nanoseconden samen te genereren, en dat de AWG met meer complexe series van pulsen nieuwe experimenten mogelijk maakt.

Delen van hoofdstuk 4 zijn gewijd aan een set experimenten om de tijdsevolutie van een individuele nucleaire spin op een oppervlakte te meten. We observeren, voor de eerste keer, coherente flip-flop dynamica tussen de nucleaire spin en de elektronspin in een enkel atoom in een laag extern magnetisch veld met behulp van initialisatie met elektronspin excitaties. Vervolgens doen we een eerste poging om de relaxatietijd T_1 te meten van de nucleaire spin in een hoog magnetisch veld. Dit leidt tot een voorlopige ondergrens van tientallen microseconden.

In hoofdstuk 5 gebruiken we de AWG om beide de amplitude en de fase transferfuncties te meten van het voltage door de RF-bekabeling van de STM-opstelling. Hiermee kunnen we vervolgens compenseren voor de vervormingen van de door-de-AWG-gegenereerde pulsen veroorzaakt door de fase transferfunctie. Met die compensatie lukt het om kortere DC pulsen bij de sample onder te tip te krijgen, met een pulsewijdte van minder dan een nanoseconde. Deze kortere pulsen kunnen worden gebruikt voor een betere tijdsresolutie voor het uitlezen van spins en potentieel ook voor het sneller aansturen van spins.

In hoofdstuk 6 breiden we de zoektocht naar de nucleaire spinrelaxatietijd uit naar langere tijdschalen. We vinden een T_1 in de orde van seconden, wat meerdere ordes van grootte langer is dan elke andere bekende atomaire spin op een oppervlakte met ESR-STM aanstuurcapaciteit. Deze relaxatietijd is lang genoeg om de spin uit te lezen voordat deze verandert (‘single-shot readout’), wat het mogelijk maakt om verschillende relaxatie mechanismes experimenteel te onderzoeken.

In hoofdstuk 7 benaderen we de relaxatie van de nucleaire spin vanuit de theorie. Uit een combinatie van experimentele en theoretische resultaten kunnen we concluderen dat de snelheid van de incoherente flip-flop met de elektronspin in hetzelfde atoom de limiterende factor is voor de relaxatietijd.

Prologue

It was twilight again. The He3 lab lay in silence, and it was a silence in three parts. The most obvious part was a hollow, echoing quite, made by the things that were lacking. If there had been a window that could have opened, there would have been a wind that sighed through the curtains, bringing in sounds from the parking lot above the ground. If there had been a crowd, even a handful of PhD students inside the lab, they would have filled the silence with conversations and discussion, the clatter and clamour one expects from a late Friday afternoon. If there had been a pulse tube... but no, of course there was no pulse tube. In fact, there were none of these things, and so the silence remained.

Inside the He3 lab, a single PhD student sat huddled in front of the measurement computer. He worked with quiet determination, avoiding distractions from the troubling outside world. In doing this he added a small, sullen silence to the larger, hollow one. It made an hybridization of sorts, a counterpoint.

The third silence was not an easy thing to notice. If you listened for an hour, you might start to feel it in the desk filled with frantic post-it notes and in the countless tangled cables running to the machine in the centre of the room. It was in the fluorescent tube lighting, half of them broken. It was in the slow back and forth movements of the computer mouse. And it was in the hands of the man who sat there, clicking abstract buttons on a digital interface that, at first and even second glance, didn't seem to affect anything inside the lab.

The man had dark blond hair. His eyes were focussed, and he moved his hand with the subtle certainty that comes from knowing many things about a very specific subject.

The He3 lab was his, for the moment, just as the third silence was his. This was appropriate, as it was the greatest silence of the three, wrapping the others inside itself. It was deep and still as a cryogenic vacuum. It was heavy like a large-volume scroll pump. It was the patient, anticipating sound of a researcher who is waiting for an important result.

(Adapted from 'The Name of the Wind')

1

Introduction

I made a huge pot of tea and sat down on the couch,
Ready to find out what becomes of you when you refuse to surrender to chaos.

Lulu Miller (Why Fish Don't Exist)

1.1. SCANNING PROBE MICROSCOPY FOR QUANTUM MAGNETISM

Developments in microscopy have been at the forefront of scientific progress. Being able to measure at a smaller scale, or even a new type of object, often teaches us something new about the world we live in. At the same time, such developments open up technological frontiers: measuring something is the first step to manipulating it to our benefit. Extending the domains of our microscopy methods is thus a well-worth effort.

For condensed matter physics, the study of substances consisting of atoms in their solid state, the ultimate spatial resolution is the atomic length scale. There are multiple microscopy methods that can achieve (sub-)atomic resolution, but the most versatile class are the surface scanning probes. Scanning probe microscopy at the nanoscale was conceived in the early 1980s with the invention of the scanning tunneling microscope (STM) [1], and other types of scanning probes were introduced soon after [2]. The fundamental idea is to bring a sharp tip in close proximity to the surface. This tip scans over the surface to image the sample properties locally, with the spatial resolution set by the size of the tip apex. In many cases, an atomically sharp tip can be used to resolve the individual atoms on the surface of the material, with various scanning probe variants relying on different detection mechanisms. The imaged quantity can simply be the position of the atoms on the surface (the surface topography), but other local material properties could also be probed, like the electronic conductance or the magnetic structure.

In this thesis, the scanning probe of choice will be the STM, which can be sensitive to all of the above-mentioned properties. Conceptually, the STM measures the electrical tunneling current between the tip and the sample through a vacuum. Quantum mechanics allows tunneling through the high potential energy barrier of the vacuum because a quantum-mechanical wavefunction must have a finite spatial distribution for finite potentials. As such, the wavefunctions of the electrons in the material under study have a slight spatial extension beyond of the borders of the material, as defined by the positions of the positively charged atomic nuclei and the finite minima of the potential energy they represent. Generally, the tunneling current depends exponentially on the tip-sample distance and is thus very sensitive to the sample's topography.

One of the driving goals in the development of STM was actually to perform tunneling spectroscopy with a varying bias voltage between tip and sample to extract the local conductance, although it was soon realized that adding a scanning motion would offer topographic imaging as well [3]. Topographic imaging was achieved first [1, 4] and spectroscopy soon followed [5, 6].

Sensitivity to the magnetic sample properties was accomplished by the use of a tip apex made from magnetic material [7]. The current tunneling to the sample from such a tip consists of spin-polarized electrons, the majority of which have their magnetic moments pointing in the same direction. Due to magnetoresistance, the tunneling current magnitude then depends on the local magnetic polarization in the atom under the tip on the sample surface. Hence, magnetic ordering of the sample (ferromagnetic, anti-ferromagnetic, etc) could now be imaged at the atomic scale.

At this short length scale, magnetism is governed by the rules of quantum mechanics.

This often leads to non-trivial phenomena, making quantum magnetism an interesting subject matter for STM research. Every electron, proton or neutron carries an intrinsic quantized magnetic moment inside, called spin. A single spin is a pretty simple object to understand. However, in quantum mechanics, the complexity grows exponentially as more spins interact with each other and with the substrate. The complexity found in nature can sometimes be disentangled by resolving the individual atomic spins that contribute to the whole [8, 9]. Other times, non-trivial spin systems can be found that are surprisingly elementary, which then serve as model systems and test beds for our understanding of quantum mechanics [10–12].

Not just spatial distribution of sample properties can be probed, but also the dynamics in the time domain. Initially, the time resolution of STM recordings was limited to milliseconds by the effective low-pass filter in the current amplifiers required to measure the small tunneling signal. The time-scale of dynamics in spin systems is often set by spin-to-spin and spin-to-bath couplings, which range from MHz to THz frequencies, so most spin dynamics remained out of reach for STM. The current amplifier limit was overcome in 2010 by the application of pump-probe schemes, where the dynamics are read out stroboscopically with short readout pulses [13]. Now, instead, the possible time resolution is limited by the achieved widths of readout pulses in the tunneling junction, which can be as short as picoseconds in specialized cases with the use of THz lasers [14].

1.2. CONTROLLING ATOMIC SPINS FOR QUANTUM SIMULATION

The progress in scanning probe microscopy was accompanied by developments in the control over single atoms. It was discovered that the STM tip could be used to move and position individual atoms adsorbed on the crystalline surface [15]. Furthermore, it turns out that localized spin-polarized currents can also be employed to control the direction of the electronic spin under the tip, on top of just reading out the spin state, by applying a sufficiently high voltage bias (enough energy) for inelastic electron scattering [16, 17]. These developments opened up possibilities to investigate magnetism in engineered structures that do not exist in nature, or to build up the complexity step-by-step towards natural structures to aid fundamental comprehension in poorly understood systems [18]. In other words: one of the goals is analog quantum simulation using spins on surfaces.

ESR-STM

A boost to the field of single-atom magnetism arrived in 2015 with the addition of electron spin resonance (ESR) to the STM toolbox [19, 20]. In an ESR-STM experiment, one sends a radio-frequency (RF) voltage to a spin-polarized STM tip. This voltage in the tunneling junction is converted to an effective oscillating magnetic field at the same frequency, which can drive Rabi oscillations [21] in the spin of the atom under tip if, and only if, the frequency matches the energy difference between different spin states. The spin's energy can thus be found as a resonance peak in an ESR frequency sweep.

The energy resolution of this method of detection is, unlike previous spin-polarized

STM methods reliant on electron scattering, not limited by the temperature. This results in an increase in spin energy sensitivity of (at least) three orders of magnitude. The developments in atomic-scale spin control have therefore come full circle to contribute back to microscopy.

COHERENT CONTROL

Rabi oscillations can not only be used to flip spins, but can also bring a spin into a quantum-mechanical state with a controlled wavefunction phase, like a superposition. A spin in a superposition is pointing in multiple directions at the same time. The phase is a property related to the relative time-delays between the separate dynamics of those directions. Random interactions with the environment can influence the time delays, such that the phase becomes unknowable during an experiment. This process is called decoherence.

A state that holds on to its coherence by maintaining a well-defined phase, retains its 'quantumness'. Since ESR-STM can bring the spin into states with a well-defined phase by applying an RF pulse of a certain time length [22], we call it a type of coherent control. Recently, it was shown that electron scattering with short DC voltage pulses from an STM tip can also flip spins coherently in specific (but not rare) circumstances [23].

Coherent control is crucial for realizing analog quantum simulation, especially for accessing dynamics and initializing into excited states. Already, analog simulation is sometimes required to accurately figure out a ground state [24], the lowest energy configuration of a quantum-mechanical system without any dynamics of the system involved. Often, the behavior of excited states prepared with coherent operations can be even more complex. All states in a superposition evolve over time with different dynamics that can interfere with each other. Moreover, the excited state must decohere after some time, or even relax to the ground state, via interactions with the environment. For many existing qubit platforms[1] used for quantum simulation, or the more general quantum computing that relies on superpositions in their algorithms, short decoherence time scales limit their application.

SUITABLE QUANTUM SIMULATION PROBLEMS FOR STM

STM can serve a unique role in the field of quantum simulations by accessing and helping to understand quantum systems that currently cannot be studied or engineered in any other way at the required length scales in existing small universal quantum processors, or specialized cold-atom or ion traps. This includes atomically precise structures assembled on specific substrates, like majorana chains [25], and structures with aperiodic spacing [26], like quasi-periodic Fibonacci chains [27–29]. Beyond determining the ground state, the interest in these systems extents to the excited states and quantum dynamics.

Using the established time domain control, STM can also be a platform to investigate fundamental decoherence processes. These are often poorly understood in existing qubit systems [30], either because the microscopic origins of those processes cannot be

---

[1] A quantum bit, or 'qubit' is the name of an abstract unit of quantum computation or memory with two states, like a bit in classical/normal computing that is either 0 or 1.

probed with the qubit devices themselves or due to the inability to systematically alter the chemical environment around a qubit device at an atom-by-atom basis to investigate nano-scale origins. Naturally, an STM-controlled qubit platform offers both a probe for the microscopic environment and the ability to modify that environment.

1.3. TOWARDS A USEFUL SIMULATION PLATFORM

Before we can use the STM for a fruitful investigation of non-trivial spin decoherence processes, excited-state dynamics in quantum spin systems, or any other super interesting problem, more work needs to be done. While the progress on the control of remote spins (i.e. not under the tip) is an important step forward [31], an atomically assembled (spin) qubit platform controlled locally with an STM that can effectively tackle these goals beyond classical computation is still under development. At the time of writing, the realized maximum number of coupled qubits with universal control is just three [31], using the electron spins of Ti atoms adsorbed (‘adatoms’) on two atomic layers of MgO on bulk Ag, although local spectroscopy with coherent methods has been performed on more extended engineered Ti adatom structures in other experiment without simultaneous universal control of all spins [32–34].

More importantly yet, the achieved coherence times are rather unimpressive in relation to the time it takes to do coherent operations on the spins: in the above-cited three-qubit system, only ~10 Rabi spin flips could be performed within the coherence time. That operation speed has not improved significantly over the years since the first ESR-STM Rabi oscillation results in 2019 [22]. Interestingly, the coherence time is limited by the energy relaxation of the spin to the sample bath, rather than some pure dephasing source that could be compensated with dynamic decoupling.

The same limit has applied to other adatom systems explored with ESR-STM [19, 35–43]. The spin relaxation times, and thus decoherence times, are dominated by processes that are, fundamentally, electronic in nature: electron scattering from the bulk metallic sample and the metallic tip, or, in some cases [38], exchange coupling to other adatoms required for spin readout. This also means the coherence time is in this case limited by the chosen substrate in combination with the adatom species.

Making improvements to the coherence times and the degree of coherent control in ESR-STM experiments is an active field of research. The task is clear: either we assert much faster and more complex control over the spins that we do have, or we find systems with longer spin coherence times. In this thesis, we take steps to tackle both of these issues.

1.4. CONTENTS OF THIS THESIS

1.4.1. USING AN AWG FASTER AND MORE COMPLEX SPIN CONTROL

After a thorough discussion of the theoretical and experimental background of ESR-STM in chapter 2, we start with the former issue in chapter 3. There, we introduce an arbitrary waveform generator (AWG) as a versatile signal generator up to 25 GHz for our ESR-STM setup. An AWG outputs a voltage waveform in time that consists of consecutive samples where the voltage of each sample can be programmed independently, thus forming an arbitrary waveform. For our purposes, the AWG allows us to generate multiple RF voltage pulses of different frequencies with (sub-)nanosecond timings and full phase control. Furthermore, we can combine the coherent control of RF pulses with the timed electron scattering of DC voltage pulses within one experiment.

Chapter 3 is an in-depth overview of the many considerations when using an AWG in an STM setup. It includes, for example, various RF circuit configurations to interface the AWG with the STM. Experiment design with an AWG on the software side is also discussed, in particular for lock-in contrast schemes that are common in (ESR-)STM experiments.

We demonstrate the experimental capabilities of our AWG in chapter 4. Here, we reproduce a selection of recent experiments on atomic spins on surfaces with the AWG that were originally performed with more specialized electronic instruments: DC pump-probe time-delay spectroscopy [13], Rabi oscillations in a single spin [22], and combining DC and RF pulses with nanosecond timing [22]. Along the way, these methods are also applied to investigate the nuclear spin present in the same atom as the electronic spin (more on nuclear spins in the next section).

We find experimentally that the minimum widths of voltage pulses arriving at the tunneling junction limited to approximately 2 ns. The rise times of the AWG are faster, but the achievable pulse widths are hampered by the voltage transfer function of the RF cabling to the junction in the GHz regime that distorts the pulse shape. We can use the AWG to compensate for the transfer function, but that requires an *in-situ* measurement of the RF transfer function. In chapter 5 we apply existing methods [44, 45], with small modifications, to measure the amplitude and phase components of the transfer function based on rectification currents in the tunneling junction. Then we apply the pulse correction and show that we can reach sub-nanosecond pulse widths. This result opens up possibilities for faster spin operations in the future.

1.4.2. PROBING NUCLEAR SPINS IN THE TIME DOMAIN

Observing that the dominant decoherence processes in electron spins in individual atoms explored with ESR-STM have been, fundamentally, electronic in nature, in this thesis we explore the use of nuclear spins instead. Parts of chapter 4, and chapters 6 and 7 are dedicated to this effort.

Much like the electrons around an atom, the protons and neutrons in the nucleus of an atom can configure themselves to carry a net spin, depending on the isotope. These nuclear spins are expected to have longer lifetimes than on-surface electron spins in the same system, because they can only coupling magnetically to their environment. Moreover, the magnetic g-factor of nuclear spins is generally three order of magnitude smaller, so they are also much less susceptible to magnetic sources of decoherence.

It was shown in 2018 that nuclear spins can be probed in certain adatom isotopes of Ti and Fe using ESR-STM via the electron spin that is coupled to the nuclear spin with the hyperfine coupling [46]. This interaction splits the ESR peak into multiple resonances representing the different nuclear spin states. Soon after, it was even shown that, through yet unknown mechanisms, NMR-type transitions can be driven in these nuclear spins using the same RF voltages in the tunneling junction that can drive ESR [36, 47], although no coherent Rabi oscillations have been shown yet. Therefore, nuclear spins on surfaces could be the STM-controlled qubit candidates with potentially much longer coherence times that we are looking for.

All past results with ESR-STM on nuclear spins, in the limited literature on the topic, involved only time-averaged measurements (except for a short report stating no sign of any dynamics had been resolved in time in Ref. [46]). Much work is yet to be done to understand the available nuclear spin systems, find new ones, and show that nuclear spins can indeed be used to execute more coherent operations before they decohere, which requires a time-resolved readout. In this thesis, therefore, we set out to investigate the Ti nuclear spin in the time domain.

In section 4.3 we observe coherent nuclear spin dynamics with the STM for the first time. This experiment uses DC pulses to initialize a singlet-triple electron and nuclear spin system into a non-eigenstate by projecting on a spin product state, and we readout the ensuing coherent flip-flop oscillations via magnetoresistance of the electron spin state using another DC pulse. Here, we operated in the low-field regime with large hybridization between the nuclear spin and electron spin. Later in the same chapter, in section 4.7, we perform an initial experiment to measure the nuclear spin lifetime in the high-field regime that results in a tentative lower bound of 50 μs.

In chapter 6 we extend the search for the nuclear spin lifetime in Ti adatoms to longer time scales and find a T_1 in the order of seconds in the high-field regime. This is long enough to perform single-shot readout of the nuclear spin state, which allows us to investigate various relaxation mechanisms of the nuclear spin experimentally. Chapter 7 is dedicated to a theoretical investigation of the nuclear spin lifetime.

REFERENCES

[1] G. Binnig, H. Rohrer, C. Gerber and E. Weibel. ‘Tunneling through a controllable vacuum gap’. In: *Applied Physics Letters* 40.2 (1982), pp. 178–180. ISSN: 0003-6951. DOI: 10.1063/1.92999.

[2] G. Binnig, C. F. Quate and C. Gerber. ‘Atomic Force Microscope’. In: *Physical Review Letters* 56.9 (1986), pp. 930–933. ISSN: 0031-9007. DOI: 10.1103/PhysRevLett.56.930.

[3] G. Binnig and H. Rohrer. ‘Scanning Tunneling Microscopy—from Birth to Adolescence (Nobel Lecture)’. In: *Angewandte Chemie International Edition in English* 26.7 (1987), pp. 606–614. ISSN: 15213773. DOI: 10.1002/anie.198706061.

[4] G. Binnig, H. Rohrer, C. Gerber and E. Weibel. ‘7 × 7 Reconstruction on Si(111) Resolved in Real Space’. In: *Physical Review Letters* 50.2 (1983), pp. 120–123. ISSN: 0031-9007. DOI: 10.1103/PhysRevLett.50.120.

[5] A. L. de Lozanne, S. A. Elrod and C. F. Quate. ‘Spatial Variations in the Superconductivity of Nb3Sn Measured by Low-Temperature Tunneling Microscopy’. In: *Physical Review Letters* 54.22 (1985), pp. 2433–2436. ISSN: 0031-9007. DOI: 10.1103/PhysRevLett.54.2433.

[6] A. Baratoff, G. Binnig, H. Fuchs, F. Salvan and E. Stoll. 'Tunneling microscopy and spectroscopy of semiconductor surfaces and interfaces'. In: *Surface Science* 168.1-3 (1986), pp. 734–743. ISSN: 00396028. DOI: 10.1016/0039-6028(86)90905-2.

[7] R. Wiesendanger. 'Spin mapping at the nanoscale and atomic scale'. In: *Reviews of Modern Physics* 81.4 (2009), pp. 1495–1550. ISSN: 15390756. DOI: 10.1103/RevModPhys.81.1495.

[8] S. Heinze, K. Von Bergmann, M. Menzel, J. Brede, A. Kubetzka, R. Wiesendanger, G. Bihlmayer and S. Blügel. 'Spontaneous atomic-scale magnetic skyrmion lattice in two dimensions'. In: *Nature Physics* 7.9 (2011), pp. 713–718. ISSN: 17452481. DOI: 10.1038/nphys2045.

[9] U. Kamber, A. Bergman, A. Eich, D. Iusan, M. Steinbrecher, N. Hauptmann, L. Nordström, M. I. Katsnelson, D. Wegner, O. Eriksson, O. Eriksson and A. A. Khajetoorians. 'Self-induced spin glass state in elemental and crystalline neodymium'. In: *Science* 368.6494 (2020). ISSN: 10959203. DOI: 10.1126/science.aay6757.

[10] A. Yazdani, B. A. Jones, C. P. Lutz, M. F. Crommie and D. M. Eigler. 'Probing the local effects of magnetic impurities on superconductivity'. In: *Science* 275.5307 (1997), pp. 1767–1770. ISSN: 00368075. DOI: 10.1126/science.275.5307.1767.

[11] V. Madhavan, W. Chen, T. Jamneala, M. F. Crommie and N. S. Wingreen. 'Tunneling into a single magnetic atom: Spectroscopic evidence of the Kondo resonance'. In: *Science* 280.5363 (1998), pp. 567–569. ISSN: 00368075. DOI: 10.1126/science.280.5363.567.

[12] F. Friedrich, A. Odobesko, J. Bouaziz, S. Lounis and M. Bode. 'Evidence for spinarons in Co adatoms'. In: *Nature Physics* 20.January (2023), pp. 28–34. ISSN: 17452481. DOI: 10.1038/s41567-023-02262-6.

[13] S. Loth, M. Etzkorn, C. P. Lutz, D. M. Eigler and A. J. Heinrich. 'Measurement of Fast Electron Spin Relaxation Times with Atomic Resolution'. In: *Science* 329.5999 (2010), pp. 1628–1630. ISSN: 0036-8075. DOI: 10.1126/science.1191688.

[14] T. L. Cocker, V. Jelic, M. Gupta, S. J. Molesky, J. A. Burgess, G. D. L. Reyes, L. V. Titova, Y. Y. Tsui, M. R. Freeman and F. A. Hegmann. 'An ultrafast terahertz scanning tunnelling microscope'. In: *Nature Photonics* 7.8 (2013), pp. 620–625. ISSN: 17494885. DOI: 10.1038/nphoton.2013.151.

[15] Eigler D. M. and Schweizer E. K. 'Positioning single atoms with a scanning tunnelling microscope'. In: *Nature* 344.April (1990), pp. 524–526.

[16] A. J. Heinrich, J. A. Gupta, C. P. Lutz and D. M. Eigler. 'Single-Atom Spin-Flip Spectroscopy'. In: *Science* 306.5695 (2004), pp. 466–469. ISSN: 0036-8075. DOI: 10.1126/science.1101077.

[17] S. Loth, K. Von Bergmann, M. Ternes, A. F. Otte, C. P. Lutz and A. J. Heinrich. 'Controlling the state of quantum spins with electric currents'. In: *Nature Physics* 6.5 (2010), pp. 340–344. ISSN: 17452481. DOI: 10.1038/nphys1616.

[18] R. Toskovic, R. Van Den Berg, A. Spinelli, I. S. Eliens, B. Van Den Toorn, B. Bryant, J. S. Caux and A. F. Otte. ‘Atomic spin-chain realization of a model for quantum criticality’. In: *Nature Physics* 12.7 (2016), pp. 656–660. ISSN: 17452481. DOI: `10.1038/nphys3722`.

[19] S. Baumann, W. Paul, T. Choi, C. P. Lutz, A. Ardavan and A. J. Heinrich. ‘Electron paramagnetic resonance of individual atoms on a surface’. In: *Science* 350.6259 (2015), pp. 417–420. ISSN: 10959203. DOI: `10.1126/science.aac8703`.

[20] Y. Chen, Y. Bae and A. J. Heinrich. ‘Harnessing the Quantum Behavior of Spins on Surfaces’. In: *Advanced Materials* 35.27 (2023). ISSN: 0935-9648. DOI: `10.1002/adma.202107534`.

[21] J. J. Sakurai and J. Napolitano. *Modern Quantum Mechanics*. Cambridge University Press, 2017. ISBN: 9781108499996. DOI: `10.1017/9781108499996`.

[22] K. Yang, W. Paul, S.-H. Phark, P. Willke, Y. Bae, T. Choi, T. Esat, A. Ardavan, A. J. Heinrich and C. P. Lutz. ‘Coherent spin manipulation of individual atoms on a surface’. In: *Science* 366.6464 (2019), pp. 509–512. ISSN: 0036-8075. DOI: `10.1126/science.aay6779`.

[23] L. M. Veldman, L. Farinacci, R. Rejali, R. Broekhoven, J. Gobeil, D. Coffey, M. Ternes and A. F. Otte. ‘Free coherent evolution of a coupled atomic spin system initialized by electron scattering’. In: *Science* 372.6545 (2021), pp. 964–968. ISSN: 0036-8075. DOI: `10.1126/science.abg8223`.

[24] I. Rončević, F. Paschke, Y. Gao, L.-A. Lieske, L. A. Gödde, S. Barison, S. Piccinelli, A. Baiardi, I. Tavernelli, J. Repp, F. Albrecht, H. L. Anderson and L. Gross. ‘A molecule with half-Möbius topology’. In: *Science* First Release.0 (Mar. 2026). DOI: `10.1126/science.aea3321`.

[25] S. Nadj-Perge, I. K. Drozdov, J. Li, H. Chen, S. Jeon, J. Seo, A. H. MacDonald, B. A. Bernevig and A. Yazdani. ‘Observation of Majorana fermions in ferromagnetic atomic chains on a superconductor’. In: *Science* 346.6209 (2014), pp. 602–607. ISSN: 10959203. DOI: `10.1126/science.1259327`.

[26] P. W. Anderson. ‘Absence of Diffusion in Certain Random Lattices’. In: *Physical Review* 109.5 (1958), pp. 1492–1505. ISSN: 0031-899X. DOI: `10.1103/PhysRev.109.1492`.

[27] H. Tsunetsugu and K. Ueda. ‘Ising spin system on the Fibonacci chain’. In: *Physical Review B* 36.10 (1987), pp. 5493–5499. ISSN: 01631829. DOI: `10.1103/PhysRevB.36.5493`.

[28] K. Singh, K. Saha, S. A. Parameswaran and D. M. Weld. ‘Fibonacci optical lattices for tunable quantum quasicrystals’. In: *Physical Review A - Atomic, Molecular, and Optical Physics* 92.6 (2015), pp. 1–8. ISSN: 10941622. DOI: `10.1103/PhysRevA.92.063426`.

[29] C. Chiaracane, F. Pietracaprina, A. Purkayastha and J. Goold. ‘Quantum dynamics in the interacting Fibonacci chain’. In: *Physical Review B* 103.18 (2021), pp. 1–11. ISSN: 24699969. DOI: `10.1103/PhysRevB.103.184205`.

[30] C. Müller, J. H. Cole and J. Lisenfeld. 'Towards understanding two-level-systems in amorphous solids: Insights from quantum circuits'. In: *Reports on Progress in Physics* 82.12 (2019). ISSN: 13616633. DOI: 10.1088/1361-6633/ab3a7e.

[31] Y. Wang, Y. Chen, H. T. Bui, C. Wolf, M. Haze, C. Mier, J. Kim, D.-J. Choi, C. P. Lutz, Y. Bae, S.-h. Phark and A. J. Heinrich. 'An atomic-scale multi-qubit platform'. In: *Science* 382.6666 (2023), pp. 87–92. ISSN: 0036-8075. DOI: 10.1126/science.ade5050.

[32] K. Yang, S. H. Phark, Y. Bae, T. Esat, P. Willke, A. Ardavan, A. J. Heinrich and C. P. Lutz. 'Probing resonating valence bond states in artificial quantum magnets - SuppMat'. In: *Nature Communications* 12.1 (2021), pp. 1–18. ISSN: 20411723. DOI: 10.1038/s41467-021-21274-5.

[33] H. Wang, P. Fan, J. Chen, L. Jiang, H. J. Gao, J. L. Lado and K. Yang. 'Construction of topological quantum magnets from atomic spins on surfaces'. In: *Nature Nanotechnology* 19.12 (2024), pp. 1782–1788. ISSN: 17483395. DOI: 10.1038/s41565-024-01775-2.

[34] L. M. Veldman. 'Coherent dynamics of atomic spins on a surface Veldman'. PhD thesis. Delft University of Technology, 2024. DOI: 10.4233/uuid:c3e888a9-cfaa-4d67-8ff2-74deebb6ee46.

[35] K. Yang, Y. Bae, W. Paul, F. D. Natterer, P. Willke, J. L. Lado, A. Ferrón, T. Choi, J. Fernández-Rossier, A. J. Heinrich and C. P. Lutz. 'Engineering the Eigenstates of Coupled Spin-1/2 Atoms on a Surface'. In: *Physical Review Letters* 119.22 (2017), p. 227206. ISSN: 0031-9007. DOI: 10.1103/PhysRevLett.119.227206.

[36] K. Yang, P. Willke, Y. Bae, A. Ferrón, J. L. Lado, A. Ardavan, J. Fernández-Rossier, A. J. Heinrich and C. P. Lutz. 'Electrically controlled nuclear polarization of individual atoms'. In: *Nature Nanotechnology* 13.12 (2018), pp. 1120–1125. ISSN: 17483395. DOI: 10.1038/s41565-018-0296-7.

[37] S. Kovarik, R. Robles, R. Schlitz, T. S. Seifert, N. Lorente, P. Gambardella and S. Stepanow. 'Electron Paramagnetic Resonance of Alkali Metal Atoms and Dimers on Ultrathin MgO'. In: *Nano Letters* 22.10 (2022), pp. 4176–4181. ISSN: 1530-6984. DOI: 10.1021/acs.nanolett.2c00980.

[38] S. Reale, J. Hwang, J. Oh, H. Brune, A. J. Heinrich, F. Donati and Y. Bae. 'Electrically driven spin resonance of 4f electrons in a single atom on a surface'. In: *Nature Communications* 15.1 (2024), p. 5289. ISSN: 2041-1723. DOI: 10.1038/s41467-024-49447-y.

[39] G. Czap, K. Noh, J. Velasco, R. M. Macfarlane, H. Brune and C. P. Lutz. 'Direct Electrical Access to the Spin Manifolds of Individual Lanthanide Atoms'. In: *ACS Nano* 19.3 (2025), pp. 3705–3713. ISSN: 1936-0851. DOI: 10.1021/acsnano.4c14327.

[40] P. Willke, T. Bilgeri, X. Zhang, Y. Wang, C. Wolf, H. Aubin, A. Heinrich and T. Choi. 'Coherent Spin Control of Single Molecules on a Surface'. In: *ACS Nano* 15.11 (2021), pp. 17959–17965. ISSN: 1936-0851. DOI: 10.1021/acsnano.1c06394.

[41] T. Esat, D. Borodin, J. Oh, A. J. Heinrich, F. S. Tautz, Y. Bae and R. Temirov. ‘A quantum sensor for atomic-scale electric and magnetic fields’. In: *Nature Nanotechnology* 19.10 (2024), pp. 1466–1471. ISSN: 1748-3387. DOI: 10.1038/s41565-024-01724-z.

[42] S. Kovarik, R. Schlitz, A. Vishwakarma, D. Ruckert, P. Gambardella and S. Stepanow. ‘Spin torque–driven electron paramagnetic resonance of a single spin in a pentacene molecule’. In: *Science* 384.6702 (2024), pp. 1368–1373. ISSN: 0036-8075. DOI: 10.1126/science.adh4753.

[43] G. Czap, C. Wolf, J. Reina-Gálvez, M. H. Sherwood and C. P. Lutz. ‘Magnetic Resonance Imaging of Single Organic Radicals with Sub-Molecular Resolution’. In: (2025). arXiv: 2504.18043.

[44] W. Paul, S. Baumann, C. P. Lutz and A. J. Heinrich. ‘Generation of constant-amplitude radio-frequency sweeps at a tunnel junction for spin resonance STM’. In: *Review of Scientific Instruments* 87.7 (2016). ISSN: 10897623. DOI: 10.1063/1.4955446.

[45] S. Baumann, G. McMurtrie, M. Hänze, N. Betz, L. Arnhold, L. Malavolti and S. Loth. ‘An Atomic-Scale Vector Network Analyzer’. In: *Small Methods* 8.9 (2024), pp. 1–9. ISSN: 2366-9608. DOI: 10.1002/smtd.202301526.

[46] P. Willke, Y. Bae, K. Yang, J. L. Lado, A. Ferrón, T. Choi, A. Ardavan, J. Fernández-Rossier, A. J. Heinrich and C. P. Lutz. ‘Hyperfine interaction of individual atoms on a surface’. In: *Science* 362.6412 (2018), pp. 336–339. ISSN: 0036-8075. DOI: 10.1126/science.aat7047.

[47] L. M. Veldman, E. W. Stolte, M. P. Canavan, R. Broekhoven, P. Willke, L. Farinacci and S. Otte. ‘Coherent spin dynamics between electron and nucleus within a single atom’. In: *Nature Communications* 15.1 (2024), p. 7951. ISSN: 2041-1723. DOI: 10.1038/s41467-024-52270-0.

2

Theoretical and experimental background

> *Reminder to myself: if one goes in search of nature in its wildest forms,*
> *you shouldn't expect it will be pleased to see you.*
>
> Cal Flyn (Islands of Abandonment)

The instrument at the heart of all experiments presented in this thesis is the scanning tunneling microscope (STM). This chapter introduces the STM's principles of operation, and additional STM methods and techniques that will be relevant throughout this thesis. In particular, we will discuss STM with spin-polarized tips and the combination of STM with electron spin resonance (ESR). This chapter also introduces the quantum systems we will investigate with our STM: individual magnetic atoms on a surface, with and without nuclear spins. We will build up a theoretical description of the spin system in an effective Hamiltonian by discussing the various relevant spin interactions. Furthermore, we will discuss how a STM can be used to not only readout the spin state of the atoms, but also control their electronic spin. Lastly, this chapter closes with an overview of previous STM work done on on-surface nuclear spins.

We are interested in looking at individual atoms. These cannot be imaged with a conventional optical microscope that measures light reflecting off or transmitting through a sample. The wavelength of visible light is orders of magnitude larger than an atom, so the diffraction limit prevents resolving them.

A different approach to microscopy is to use a scanning probe. You can imagine picking up a needle and dragging it over a surface with your eyes closed. Even if you cannot see the surface structure, you can feel the height differences. By scanning the needle in regular lines you can make an image of the surface. A sharper needle will naturally result in a higher achievable image resolution. Taking this to the limit, a needle with an atomically sharp tip can be used, in principle, to resolve single atoms on a sample surface.

How to detect height differences at the position of the probe tip, and what properties of the surface should the probe be sensitive to? Different answers to these questions have resulted in various types of scanning probe microscopes. The type we will employ in this thesis is the scanning tunneling microscope.

2.1. PRINCIPLES OF SCANNING TUNNELING MICROSCOPY

A scanning tunneling microscope (STM) measures the electrical current between a metallic sample surface and a metal probe tip that is hovering just above the surface with a vacuum in between. Classically, no current should be expected to flow without the tip and sample touching. However, in quantum mechanics the available electron states are delocalized throughout the metals, meaning there is a probability distribution in space where an electron can be found. These states even extent a little outside the material surfaces, as defined by the positions of the atomic nuclei. As such, there is a finite chance that an electron originating from the tip is measured in a state in the sample on the other side of the vacuum and stays there. We say the electrons can 'tunnel' through the vacuum.

By applying a voltage between the tip and the sample, the tunneling process is biased towards one direction, resulting in a finite time-averaged tunneling current. It can be shown that this tunneling current I depends exponentially on the tip-sample distance (or tip height) z [1]:

$$I \sim e^{-z/z_0} \tag{2.1}$$

The tunneling decay length scale z_0 depends on many things, including the tip and sample materials, but generally an increase in z of 1 Angstrom (0.1 nm) reduces the current by one or two orders of magnitude. This means the tunneling current is sufficiently sensitive to changes in z, that sub-atomic distances are measurable.

STMs can control the tip height with sub-atomic displacements using actuators based on piezoelectric crystals. The same holds for the lateral tip positions x and y, which enables imaging of the height differences on the surface. Since the tunneling rate decreases so quickly with distance, the current from the tip is localized laterally on the sample under the tip to the degree that positions of atoms can be resolved in the surface height texture. For the same reason, the STM tip does not have to be a perfectly shaped needle with a single apex. As long as one protrusion sticks out a few more atoms than

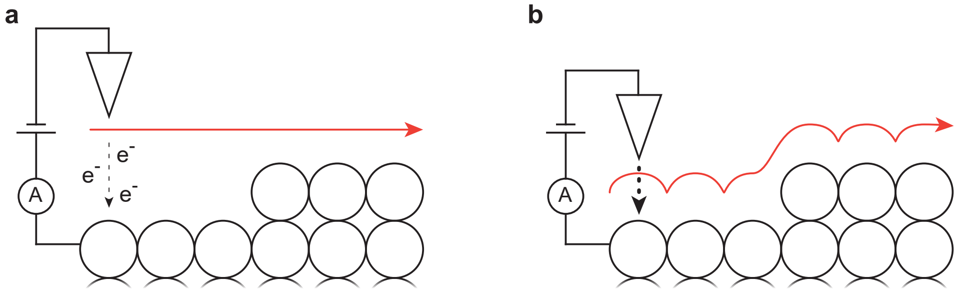

Fig. 2.1 | STM scanning operation modes. Depicted are schematics of STM circuits containing a tunneling junction between a tip and a crystalline sample, a DC voltage source, and a current detector. **a** Illustration of the constant height scanning mode over an atomic lattice. Here, the tip height is kept constant, so the distance between the tip and sample changes while scanning sideways (red line). When operating with a constant voltage bias, this results in a changing tunneling current. **b** Illustration of the constant current scanning mode. Here, a PID feedback loop alters the tip height continuously to hold a target current, which corresponds to a constant tip-sample distance.

any other and ends in a single atom, virtually all the current will originate from the tunneling junction at this ultimate tip termination.

THE THREE CONTROLLABLE PARAMETERS

It is illustrative to discuss typical parameter values used during an STM measurement. In this thesis we often operate the STM somewhere around 10 pA with a 60 mV bias. The corresponding tip height is less than a nanometer. In any given experiment, the values of two of these three parameters - current, bias, and tip height - can be selected, and the third will then be fixed.

The STM can be operated by selecting a voltage and a tip height, and then measuring the current which contains information about the sample. This mode of operation is often called ‘constant height’ or sometimes ‘feedback off’. Another approach is to choose a target current value and apply a (digital) negative feedback loop that adjusts the tip height continuously to reach this setpoint current. This ‘constant current’ mode, or ‘feedback on’, is advantageous while scanning because it keeps the current, which is always the only measured parameter, within the limited operating range of a trans-impedance amplifier that is required to record the small tunneling currents. The two modes of operation are illustrated in fig. 2.1.

In this thesis, tip heights are almost exclusively referred to by a combination of setpoint current and bias voltage, rather than an absolute height, because the piezoelectric actuators often experience unintended drift that makes it inconsistent to relate a setpoint tip height at the piezoelectric actuator to an actual tip-sample distance on a minute-to-minute basis. By moving the tip to a certain current setpoint at a chosen voltage bias and subsequently turning off the feedback, you can perform a constant height experiment at a repeatable tip height. This allows for a different voltage signal to be sent after the feedback is turned off.

2.2. MAGNETIC ATOMS ON MGO/AG

The objects that we will investigate with STM are single atoms adsorbed on a substrate surface, also called adatoms. These can have a well-defined quantized magnetic moment. It is these quantized states that we are interested in.

More specifically, we will study individual magnetic adatoms on MgO thin-films of two atomic layers on top of a bulk Ag(100) crystal. This insulating film serves to (partly) isolate the spin from the metal substrate, which enhances spin lifetimes (see section 2.8).

MgO has a cubic crystal structure with a unit cell of alternating Mg and O, which is illustrated in fig. 2.2a. The MgO films appear as individual rectangular-shaped islands with sizes on the order of 50 x 50 nm^2, often nucleated along a step edge of the Ag surface, A STM topographic image of such an island is shown in fig. 2.2b.

The adatoms species used in this thesis are exclusively iron (Fe) and titanium (Ti). Both have been studied on the MgO/Ag surface before, due to their historically useful properties for ESR-STM [2–5] (see also section 2.11). These adatoms are visible in the fig. 2.2b topography as light-colored dots.

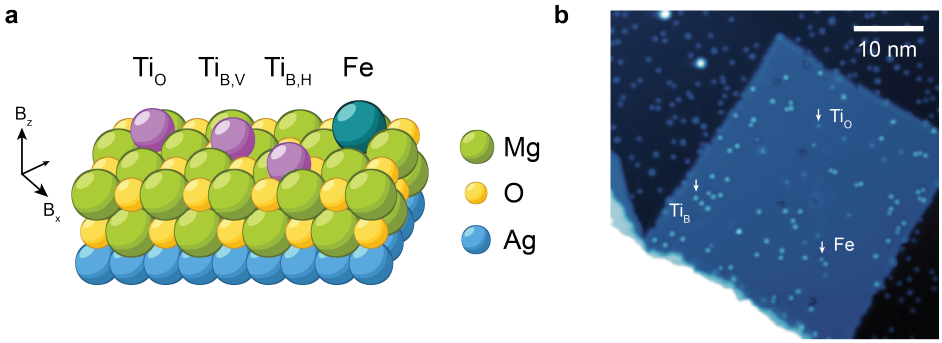

Fig. 2.2 | The MgO/Ag sample. a Schematic of the atomic lattice of a two-layer MgO thin-film on bulk Ag. The stable binding sites of Ti and Fe adatoms are shown on the lattice. The orientation of the external magnetic field components B_x and B_z are shown on the side. **b** STM topography image of an MgO island (rectangular section) on the Ag substrate surface. Constant current mode with 10 pA at 60 mV. The dots are individual adatoms. The colormap is thresholded to a range spanning 570 pm for color contrast, which cuts out the features in the bottom-left corner that covers multiple Ag step edges

SAMPLE PREPARATION

The single MgO/Ag sample used throughout in this thesis was prepared in-situ in a vacuum chamber with a residual pressure of 10^{-10} mbar. The surface of the Ag(100) crystal was cleaned by two cycles of Ar^{+} sputtering and annealing to 650°C. Subsequently, two-layer MgO islands were grown epitaxially by evaporating Mg in an oxygen environment of 10^{-6} mbar while the sample was annealed to ~500°C. We deposited Fe and Ti atoms on the surface by electron beam evaporation [6].

TI ADATOMS

The majority of experiments in this thesis were performed on Ti adatoms on bilayer MgO/Ag [3]. As experimentally verified by ESR-STM measurements, Ti acts as a prototypical spin-1/2 system on this surface, due to a charge redistribution of a nature that is still debated [3, 7, 8]. Furthermore, lateral atom manipulation of Ti adatoms with the STM tip has proven reliable, such that electron spin-spin couplings between neighbouring Ti adatoms can be engineered by changing their relative distance with atomic precision [3, 9–11]. These properties have made Ti on MgO/Ag a model system for the spins-on-surfaces research community.

Ti has three stable chemical binding sites on the MgO thin film surface, which are illustrated in fig. 2.2a. A Ti atom can be positioned right on top of an oxygen atom with a four-fold C_{4v} symmetry, or it can bind on a two-fold C_{2v} symmetric bridge position between two Mg atoms in either a vertical or horizontal alignment. The two Ti bridge sites are electronically equivalent, except for their orientation relative to an in-plane external magnetic field (see also section 2.3).

Ti on the oxygen binding site has an orbital momentum excitation around 100 mV [5, 12, 13]. This is a sharp transition for electrons traveling from sample to tip, but appears smeared out over an energy range for electrons traveling the other direction. Although much is still debated on specifics of this orbital excitation, we will nonetheless make use of its tunneling current properties multiple times in chapters 4 and 5.

There are also multiple stable isotopes of Ti. Only two of those have a non-zero total nuclear spin I. ^{47}Ti has $I = 5/2$ and a natural abundance of 7.4%. ^{49}Ti has $I = 7/2$ and a natural abundance of 5.4%.

FE ADATOMS

Fe adatoms have an electronic total spin of $S = 2$ on the MgO/Ag surface and bind on the oxygen site [14]. For this thesis, the main role of Fe is in the fabrication of spin-polarized tips (see section 2.5) by picking up Fe adatoms sequentially with the apex of the STM tip. Fe adatoms are a common choice because a cluster of them on the tip becomes a stable magnet already for a small number of atoms due to their strong ferromagnetic coupling.

2.3. STM OPERATING CONDITIONS

The STM experiments performed in this thesis require a set of extreme operating conditions, which will be discussed in this section. These conditions can all be met by the commercial STM we used throughout this thesis: the Unisoku USM 1300. Our setup is pictured in fig. 2.3, together with a schematic of its operating elements described below.

VIBRATION ISOLATION

Imaging with atomic resolution is, naturally, hindered by mechanical vibrations of the STM tip with amplitudes on the order of atomic distances. Random vibrations vary the tip-sample distance and thus show up in the tunneling current as noise. Operating the STM does not cause significant vibrations, but external vibration sources are ubiquitous at a large range of frequencies and can often not be mitigated at the source (non-exhaustive list: sounds in the air, pumps running outside the lab, building resonances). Utmost vibration isolation of the STM head, which holds the sample and tip stages, from external vibration sources is therefore paramount.

This is primarily achieved in the Unisoku USM 1300 design with a mass-spring damping system build into the STM head. Furthermore, the entire setup is positioned on a table floating on pressurized nitrogen gas. The large combined mass of the table and setup decouples the setup from lower frequency vibrations than the mass-spring system in the STM head can handle. Electronic instruments are not mounted on this anti-vibration table, because vibrations caused by their cooling fans are often significant sources of noise. Electronic cables running to the STM setup are connected with slack

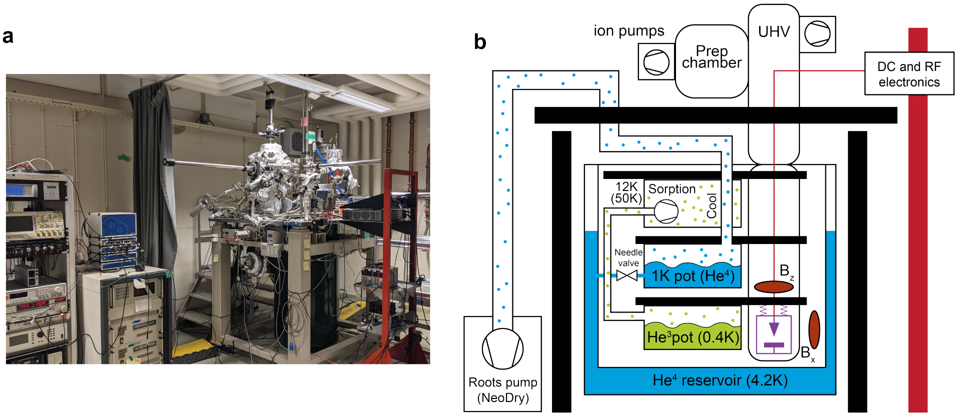

Fig. 2.3 | The STM setup. a Photograph of the ‘He3 Lab’ STM setup with a Unisoku USM 1300 from the Otte Lab research group. All experimental STM results in this thesis were measured using this setup. **b** Schematic of the operations of the Unisoku USM 1300, depicting the STM head (purple), vibration isolation table (black bars), cooling stages, UHV chambers, magnetic coils (brown), and RF electronics. (Not exhaustive and not to scale).

to prevent rigid mechanical connections that undermine the anti-vibration table.

CRYOGENIC TEMPERATURES

The sample needs to be at cryogenic temperatures in our experiments for multiple reasons. Firstly, we are interested in adatoms on the sample surface, but the thermal energy must be lower than the surface energy associated with adsorption to hold the atoms of our choice on the surface. In our case, cryogenic temperatures are required.

Secondly, we want to study quantized magnetic electron state of the adatoms with small energy differences. In general, electrons follow a Fermi-Dirac distribution over states of different energies, where a higher temperature spreads out the thermal occupation over multiple states. A low temperature is thus required to distinguish these states, but also to meaningfully thermally initialize atom electrons into specific states.

The STM head is positioned on the last, coldest stage of the cryostat of the of the Unisoku USM 1300. The first stage is a liquid ^{4}He dewar with a maximum hold time of approximately 7 days, which keeps this stage at 4.2 K by evaporative cooling. The second stage consists of a separate smaller liquid ^{4}He pot connected to the main reservoir by a narrow opening. The flow from the larger dewar to the pot can be controlled with a needle valve, such that only a small amount of ^{4}He is present in the pot at the same time. The evaporated helium in this smaller pot is continuously pumped away by an external (room-temperature) scroll pump, causing a reduced vapor pressure that minimizes the boiling temperature of the ^{4}He in the pot. This evaporative cooling with active pumping keeps the pot and the STM at a temperature of 1.6 K continuously as long as the helium reservoir in large dewar does not run empty.

The third and last cooling stage of the Unisoku USM 1300 consists of a pot filled with liquid ^{3}He. This stage also runs on evaporative cooling combined with a mechanism to pump away the vapor, but the minimum boiling temperature of ^{3}He is lower than ^{4}He. In our setup, we can reach a base temperature of 0.4 K. Furthermore, the pumping is performed by a passive sorption pump to reduce vibrations and keep the ^{3}He in a closed cycle. Over time, the ^{3}He pot empties and the pumping power decreases as more ^{3}He is adsorbed on the porous pump material, so the hold time at the base temperature is limited to approximately 24 hours. After this time, the cycle has to be reset by heating the sorption pump, which desorbs ^{3}He gas that can be reliquified back into the ^{3}He pot by the 1 K pot at the second stage.

ULTRA-HIGH VACUUM

The sample surface needs to be clean and stable for STM scans. Atmospheric pressure conditions would introduce a host of impurities that continuously adsorb and desorb on the surface. One atomic layer coverage would already entirely obscure the sample atoms that we are interested in. Therefore, we operate our STM in ultra high vacuum (UHV). We prepare our samples in a separate UHV chamber, which is connected to the STM chamber by a gate valve such that these samples are not exposed to a contaminated environment during transfer.

After pumping down the vacuum with turbomolecular pumps, we reach and maintain UHV with ion pumps, which do not add additional vibrations. During the experiments presented in this thesis, we achieved a pressure of 2 × 10^{-10} mbar in the room-temperature section of the STM vacuum chamber, where our pressure gauge and ion pump are connected. The pressure in the cryogenic section where the STM head is located likely has an even lower pressure due to cryopumping, where the cold surfaces of the vacuum chamber walls adsorb more particles and thus reduces the pressure.

Magnetic fields

To study magnetism, it is useful to have a magnet of variable strength to controllably modify magnetic states in the sample. The Unisoku USM 1300 has a two-axis vector electromagnet covering the vertical out-of-plane (z) and one of the in-plane directions, with respect to the sample surface. The electromagnet is constructed from two superconducting coils directed along the respective two axes, with persistent current switches to achieve stable fields over time. The superconducting magnets are cooled by the liquid ^{4}He reservoir of the cryostat at 4.2 K.

The maximum magnetic field that can be produced by the in-plane coil is 2 T. The out-of-plane coil can produce a field up to 9 T, but the total magnetic field magnitude (in any direction) is limited to 2 T whenever the in-plane coil holds a finite supercurrent. For our experiments, the direction of the in-plane field will be at an angle of 14° relative to the MgO crystal lattice. This orientation can only be controlled when placing the Ag bulk crystal on the STM sample holder.

RF cabling

An important feature of our STM setup is an RF-compatible bias line from room-temperature to the STM tip. Our standard USM 1300 model is equipped with cabling to send RF voltages up to 18 GHz to the tunneling junction. This makes it possible to perform ESR-STM measurements [5], a technique that will be discussed in section 2.11, and pump-probe experiments at the nanosecond scale [15].

Without specialized RF cabling, high frequency signals experience severe dielectric losses that prevent RF signal from reaching the junction with any significant amplitudes, when using conventional RF generators and without causing extreme dissipative heating. Non-magnetic materials were used for the RF cable to operate in the strong magnetic fields of the superconducting coils. Furthermore, standard RF cables with low loss are rigid, but a rigid cable would negate the mass-spring vibration-isolation system build into the STM head. Therefore, flexible RF cables are used for the final section to reach the tip.

These compromises result in a voltage transfer function that is far from ideal, with a non-trivial frequency dependence. In chapter 5, we discuss how the transfer function can be measured, both for the amplitude and the phase, and we show that we can compensate for this transfer function in experiments.

2.4. Tunneling conductance and density of states

The tunneling current in our STM is a function of the bias voltage applied between the tip and sample. This relation need not be linear and thus does not necessarily follow

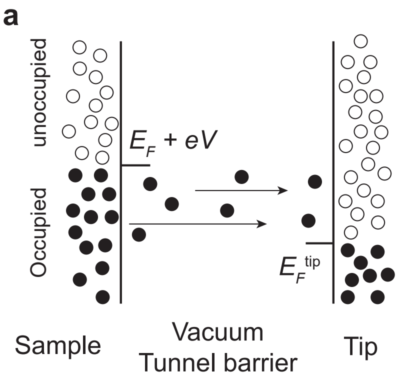

Fig. 2.4 | Relation between tunneling conductance and DoS. a Schematic of the tunneling process between two metal leads (tip and sample). Both have electron states (circles) filled up to a Fermi level. Electrons tunneling only in one direction where states are available at a similar energy, resulting in a net current. **b** A larger voltage bias shifts the Fermi energy on one side and results in more current. The extra current per unit voltage (the conductance) is proportional to the number of extra filled states per unit of voltage (the DoS).

Ohm's law. In general, the proportionality factor between current I and voltage V, known as the tunneling conductance $\sigma(V) = dI/dV$, can itself depend on voltage. It can be shown that $\sigma(V)$ scales with the local densities of states in the sample and the tip at a given bias [1]. Here, we aim to provide a non-rigorous explanation to build intuition.

The density of state (DoS) corresponds to the number of quantized energy eigenstates for electrons that exist in a material within an (infinitesimal) energy interval. The DoS is generally a function of the electron state energy, for instance with the band structure of a metal. The fermionic electrons fill up the states in the sample to the Fermi energy level E_F, where a specific DoS is available with unoccupied states for new electrons entering the sample material. The tip has its own Fermi energy E_F^{tip}.

The voltage applied between the tip and sample can be considered as an additional energy given to the electron states in the sample, which effectively shifts the sample's Fermi level to higher or lower energies, depending on the polarity. As illustrated in fig. 2.4a, the electrons occupying the side with the highest of the two Fermi energies, tip or sample, naturally want to move to the other side to fill the lower energy states available at the lower Fermi level. Quantum tunneling through the vacuum provides a pathway to do so. The Fermi energy levels never equalize through this transport, however, because the electrons originate from the bulk and are ultimately replenished by the voltage bias source. And so a constant tunneling current keeps running.

The current is determined by the number of states available for energy-equalizing tunneling. The higher the voltage, the larger the difference between Fermi levels, and the more electron states participate in the tunneling to find a lower energy. Hence, the current increases with increasing voltage. As illustrated in fig. 2.4b, the amount of extra tunneling current per unit of voltage is proportional to the number of states in the sample that become available with an additional voltage at the bias-shifted Fermi level. In other words, the conductance $\sigma(V)$ is proportional to the DoS(V) at the applied bias voltage.

We can get the DoS for a range of energies around the Fermi level by measuring $\sigma(V)$ in a bias spectroscopy experiment, where we sweep the voltage bias at constant tip height. Note that only electron states that can be tunneled into contribute to the DoS measured with the conductance. Tunneling is restricted to a localized region directly under the scanning tip, so the conductance probes a local density of states (LDoS) and the spectroscopy method is named scanning tunneling spectroscopy (STS).

2.5. SPIN-POLARIZED STM

A sample with (local) magnetic properties has a ground state with a higher DoS at the Fermi level for one electron spin direction over the other. Tunneling from the tip into the sample happens as normal for tip electrons with a spin projection parallel to the sample's spin-polarized states, since these states are available without restrictions. However, tunneling with the other spin direction is suppressed due to the comparatively lower LDoS for this opposite spin state. Therefore, the overall tunneling current is spin-polarized, as portrayed in fig. 2.5a.

Nonetheless, a change in the sample's spin state, for example due to a spatial spin texture during scanning, is not reflected in the overall STM tunneling current when using a standard metal tip. Since all electron spin polarization directions are equally populated in a normal metal tip, an equal number of electrons with every polarization is available for tunneling to any sample spin direction. As such, the measured tunneling current remains independent of the sample's spin state.

Sensitivity of the tunneling current to the atomic-scale magnetic states in the sample can be achieved with a magnetized tip, where there is a prefered spin polarization for the electrons in the tip [16]. Using a spin-polarized tip, the tunneling rate will be reduced if the spin projections in tip and sample are anti-parallel, because there would not be any electrons available in the tip with a spin state corresponding to the sample's. This blocked current is illustrated in fig. 2.5b. Now there is a measurable current contrast depending on the sample's spin state under the tip.

Still, as portrayed in fig. 2.5c-e, there is only a current contrast if a spin-polarized tip's magnetic moment has the same axis as the sample's spin axis of quantization. Otherwise, with the tip polarization at a perpendicular angle, there are again equal populations available for tunneling for both spin projections. The tunneling junction is essentially a spin valve, a type of magnetoresistance. An expression for the spin-state-dependent conductance through a spin-1/2 adatom at any tip polarization angle is given by

$$\sigma = \sigma_0 + \sigma_{SD}\left(\frac{1}{2} + \frac{\xi}{2S}\begin{pmatrix}\langle S_x\rangle\\ \langle S_y\rangle\\ \langle S_z\rangle\end{pmatrix}\cdot\hat{\vec{P}}\right) \tag{2.2}$$

Here, σ_{SD} and σ_0 corresponds conductances of tunneling channels that are and are not spin-dependent, respectively. $\langle S_x\rangle$, $\langle S_y\rangle$, and $\langle S_z\rangle$ are the expectation values of the sample's spin projection operators for the three axes, $\hat{\vec{P}}$ is a unit vector representing the polarization direction of the tip magnetic moment, and S the sample's total spin quantum number that normalizes the vector dot product.

Note that, unlike the visualization in fig. 2.5, the spin-polarization is typically not 100%. Any imbalance in LDoS between two spin directions is sufficient for some degree of spin-polarization in the current. In eq. (2.2), ξ is a fraction between 0 and 1 that represents this degree of spin-polarization of the electron states in the tip, with $\xi = 1$ corresponding to a total polarization without any electrons with opposite spin direction present in the tip. This results in zero contribution of the σ_{SP} to the total conductance if the sample spin is anti-parallel with the tip polarization. In practice, the tip polarization is never absolute, so at least some current runs through the spin-dependent channel for any polarization.

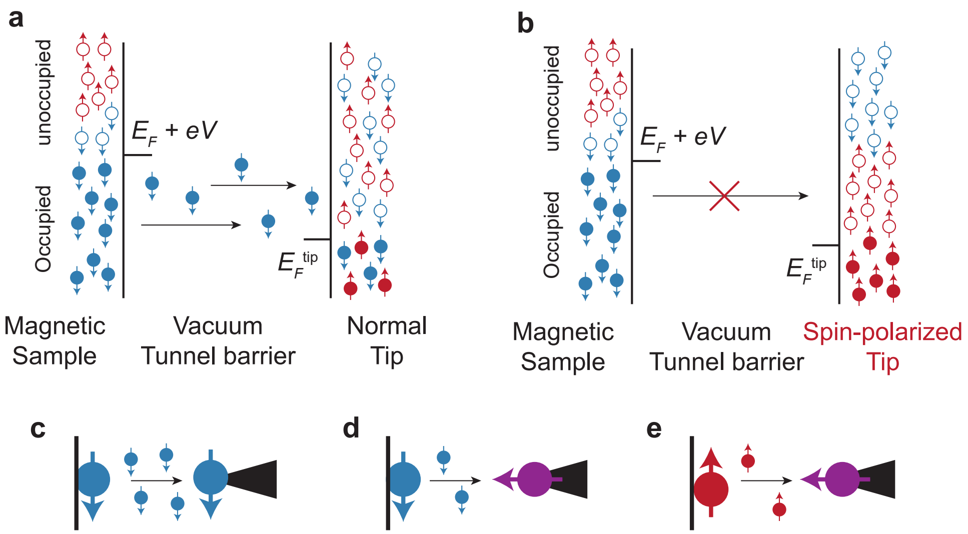

Fig. 2.5 | Schematic for tunneling with a spin-polarized tip. **a** In the case of a magnetic sample, where one spin direction (red arrows) has states only at higher energies, the current flows similarly as in fig. 2.4, but the current is spin-polarized (blue arrows). **b** A spin-polarized tip has no states available for tunneling electrons with spin opposite to the polarization, and so the current cannot flow. This spin-dependent transport corresponds to a measurable magnetoresistance. **c-e** The tunneling junction with a spin-polarized tip functions as a spin valve. A large current can flow if the magnetization of the sample and tip are aligned (**c**), but the number of available states is halved when the tip-polarization is perpendicular (purple) and the current is reduced (**d**). In that case, electrons with the other spin polarization can flow at the same rate (**e**).

MAKING A SPIN-POLARIZED TIP

In our experiments, we make spin-polarized tips by picking up individual Fe atoms from the surface with a silver-coated tungsten tip. The starting point is a thin tungsten wire, which is chemically etched into a tip shape outside of the STM setup. The rough tip is transferred into the vacuum, sputtered with argon, and inserted into the cryogenic STM head. Note that the same etched tip has been used throughout this thesis, because the tungsten tip is generally stable at this rough length scale.

To form a tip apex for atomic resolution imaging, we crash the tip into a bulk silver surface with a depth on the other of 1 nm, Quickly we pull the tip out with a 0.5 V bias applied. The resulting current generates heat that reconfigures the microscopic tip surface (or 'microtip'), now coated with silver, such that a break junction-like apex is formed.

We start picking up Fe atoms from the MgO islands by approaching them with the tip and applying a voltage pulse to pull them from the surface such that they will attach to the tip apex instead. Between 10 and 40 Fe atoms, picked up sequentially, were required for the various microtips used for the experiments performed in this thesis. The degree of spin-polarization can be verified with inelastic electron tunneling spectroscopy (IETS) on Fe and Ti atoms (see sections 2.6 and 2.11).

THE TIP MAGNETIC FIELD

The Fe atoms at the tip apex form a ferromagnetic cluster with a stable collective magnetic moment. The direction of a constructed tip's magnetic moment is typically correlated with the external magnetic field, but not necessarily aligned. Some microtips were stable for months at high external magnetic fields, if they were not used for atom manipulation or large range topography scans. For others, the tip magnetization changed after days, or sometimes just hours. Some micro tips build this way are bistable, but these were not used in this thesis.

The Fe spin at the tip apex exerts an effective magnetic field on the sample on top of the external field. This field can be as strong as 10 T [17]. At typical tip heights, the tip magnetic field is on the order of 100 mT and is primarily an exchange field for electronic spins, with a smaller dipole field component. Therefore, the tip field has an exponential tip-height dependence and is localized almost entirely to the spin under the tip.

2.6. INELASTIC ELECTRON TUNNELING SPECTROSCOPY (IETS)

Adatoms, molecules, or other atomic impurities on the surface that are sufficiently electronically isolated from the bulk, for example with an insulating thin film, can introduce distinguishable quantized states with finite energies into the LDOS. These states are associated with changes in the electron state configurations on the impurity, rather than the presence of addition electrons. Examples of such state changes are different spin projections, higher-energy vibrational modes, or orbital excitations. The energies required of these excitations can be probed with STS via inelastic electron tunneling [18].

For inelastic electron tunneling spectroscopy (IETS), the adatom system can be understood as containing an Anderson impurity [19] in between two tunneling leads. To a second order, transport from lead to lead partly happens in a sequential tunneling process (i.e. hop off, hop on, hop off ...) through the highest-energy occupied impurity state. This single state lies below (or at) the sample's Fermi level and can be considered an effective ground state of the system. Electrons from the tip at a higher Fermi level can tunnel into the impurity state, but the conductance remains constant as a function of bias, because only this one tunneling channel is available regardless of electron energy.

That is, until the bias reaches the energy of the first unoccupied, excited state of the adatom. Suddenly a second channel can be accessed by the tunneling electron carrying sufficient energy. This channel remains accessible at higher bias, so it shows up as a discrete step in $\sigma(V)$ to a higher plateau. The step is present for both a positive and negative bias polarity, because the energy can be provided by electrons transporting in both directions. This energy is used up by the adatom excitation, so it is an inelastic

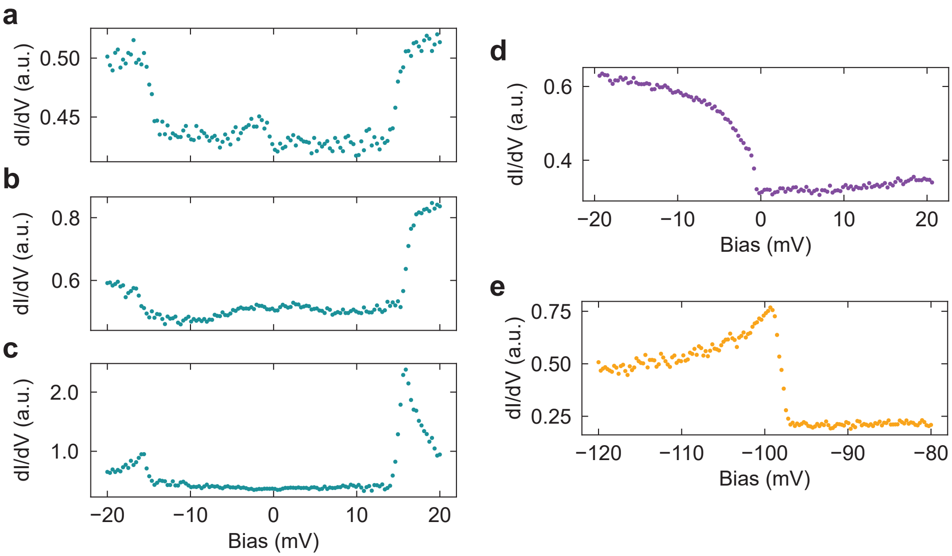

Fig. 2.6 | IETS on adatoms. Bias spectroscopies of the conductance (dI/dV) on various adatoms on two-layer MgO/Ag. **a-c** Spin IETS steps of Fe, with different degrees of spin-polarization of the tip. Tip height setpoint: 300 pA, -20 mV. (**a**) Using a silver-coated tip without any spin-polarization (B_x = 0 mT, B_z = 50 mT). (**b**) Using a slightly spin-polarized tip after picking up a few Fe adatoms with the tip apex (B_x = 450 mT, B_z = 0 mT). (**c**) Using a tip with large spin-polarization (B_x = 0 mT, B_z = 50 mT). **d** Spin IETS step of Ti on a bridge binding site, with a spin-polarized ESR-active tip. Tip height setpoint: 300 pA, -20 mV (B_x = 450 mT, B_z = 0 mT). **e** An IETS step of Ti on the oxygen binding site, likely related to an orbital excitation [5]. Tip height setpoint: 80 pA, -120 mV. Measurements for all spectra were performed using with a lock-in amplifier bias modulation of 1 mV. Temperature: 1.5 K.

process.

Various examples of IETS measurements are shown in fig. 2.6. Spin excitations in Fe adatoms on MgO/Ag are visible in fig. 2.6a-c. These are the $m_S = \pm 1 \rightarrow m_S = \pm 2$ transitions, which have energies in the mV range due to crystal field anistropy [14].

Fig. 2.6d shows a spin excitation for the $S = 1/2$ Ti on the bridge binding site. Since only the relatively small Zeeman energy contributes to the spin splitting, which cannot be resolved with bias spectroscopy at 1.5 K, this IETS appears as a single step at zero bias that is only visible with a spin-polarized tip (see also section 2.9).

Lastly, fig. 2.6e is an IETS measurement on Ti on the oxygen binding site, which contains a orbital momentum excitation around ±100 mV[5, 12, 13]. This sharp conductance feature as a function of voltage, at a finite bias and unrelated to spins, will be used multiple times throughout this thesis. As discussed in chapter 5, non-linearities in the conductance can be a tool to measure properties of dynamic voltage signals in the tunneling junction when you cannot resolve the time-evolution directly.

2.7. GENERALIZED SPIN SCATTERING

The tunneling transport between tip and sample during an IETS measurement of a spin excitation can be categorized as part of a more general class of spin scattering phenomena on magnetic adatoms. Bulk electrons can, for instance, also tunnel from the sample and back into the sample, or from the tip back into the tip. Furthermore, on top of second-order tunneling events, higher orders can also contribute to observed IETS features [20].

Spin scattering in Ti adatoms on MgO/Ag thin-films has been described successfully using two different interaction pictures that are typically considered as operating in distinct non-compatible regimes: cotunneling in the strong Kondo regime [20, 21] and sequential tunneling in the regime of low Coulomb charging energy on the adatom [22]. Here we first adopt the sequential tunneling perspective in our explanation and comment afterwards on the cotunneling perspective.

For sequential tunneling, an electron hops on or off an Anderson impurity state at every step. The second-order transport process during an IETS measurement is illustrated in fig. 2.7: an electron entering from one lead occupies the excited spin state, while the spin ground state also remains occupied simultaneously. This double occupation is short-lived, in our case, because the charging energy associated with the coulomb repulsion between the negatively charged electrons is larger than the typical energy provided by the voltage. Next, either the excited or the ground state empties into the other lead, leaving the remaining spin state occupied. Hence, the adatom often ends up in the excited spin state after a scattering event, but sequential tunneling also contributes to elastic transport.

The sequential tunneling picture requires a relatively small charging energy to produce double occupations with thermal fluctuations at rate compatible with measurable currents as seen in experiments. In contrast, cotunneling happens in the (Kondo) regime of very large charging energies compared to the bias voltage and the temperature. The magnitude of the charging energy does not significantly influence the cotunneling rate, although it does contribute to the spin flip chance. The charged state does not otherwise

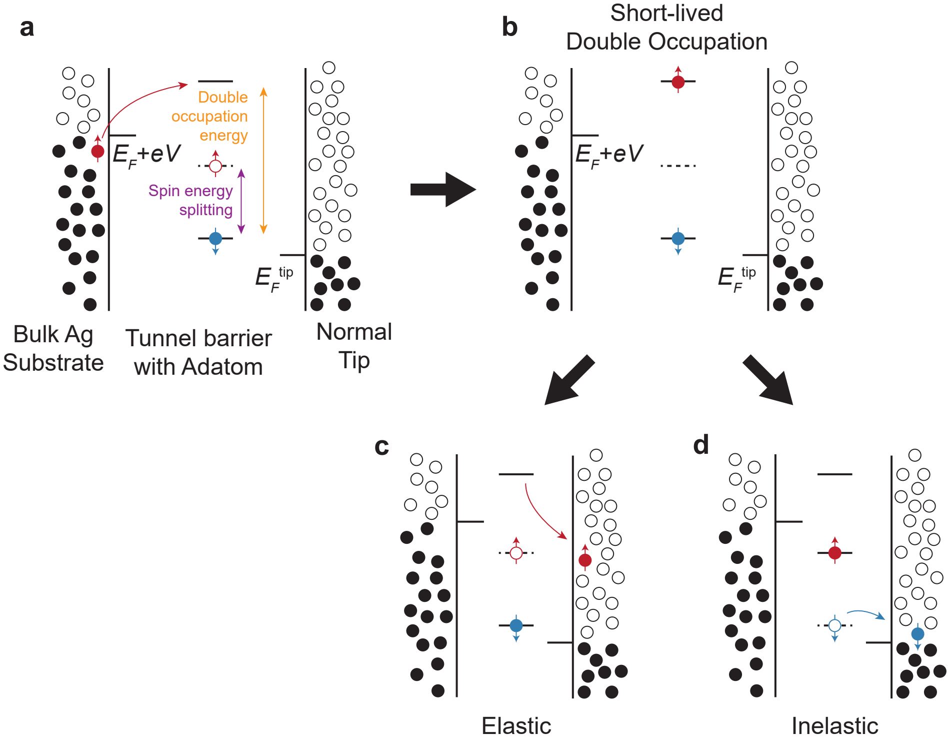

Fig. 2.7 | Sequential tunneling through an Anderson impurity during (in)elastic electron spin scattering. a A schematic depicting two spin states with an energy splitting (purple) on the adatom between two tunneling leads. As the initial state for a sequential tunneling event, the lower (down, blue) and upper (up, red) spin states are occupied (filled circle) and unoccupied (open) respectively. A third, upper state represents the charging energy required for double occupation (orange) during transport. **b** The thermally excited double occupation is short-lived, since the charging energy is higher than the available Fermi level. From there, either **c**: the excited spin states empties into the tip lead, bring the system back to the initial state in (**a**). Or **d**: the blue lower energy spin moves on, leaving the adatom in an excited spin state and effectively flipping the spin compared to the initial state.

play a part in the effective low-energy Anderson Hamiltonian after a Schrieffer–Wolff transformation [23]. In the cotunneling picture, the two electrons tunnel simultaneously. Therefore, the double occupation should be considered a virtual state, in the sense that a simple spin-flip is a first-order process, rather than second-order.

With both approaches seemingly able to model experiments on the MgO/Ag system, adatoms on atomically thin insulating films appear to be somewhere in between the two pictures. Regardless, the spin scattering processes described above are often generally referred to as Kondo scattering, named after Jun Kondo who first described scattering on localized magnetic impurities in bulk metals in the cotunneling regime [24].

2.8. THERMAL RELAXATION DUE TO SPIN SCATTERING

Kondo scattering can causes inelastic spin flips in the adatom electron spin. The net energy required for the flip originates from the tunneling electron. For IETS this is provided by the voltage, but thermal bulk electrons following a Fermi-Dirac energy distribution around the Fermi level can also Kondo scatter inelastically when $k_B T$ is comparable to the adatom spin energy splitting. Therefore, spin scattering is generally the limiting factor for the electron spin relaxation time for adatoms on conductive surfaces,

Furthermore, the transport of an electron during a spin scattering event can be interpreted as forcing a projection of the electron spin state of the adatom on the spin product state basis [10, 25]. This means quantum phase coherence (defined in more detail in section 2.11.2) can be lost, even if no energy relaxation takes place with elastic scattering events.

To achieve a long relaxation and decoherence time, then, Kondo scattering should be suppressed all together. One straight-forward approach is to physically distance the adatom from the bulk electrons in the metal substrate underneath. This is the main function of the insulating MgO thin-film in our experiments.

A thicker layer enhances spin lifetimes [4]. As a trade off, this requires the metal tip placed closer to the surface for measurable tunneling currents. At some point the Kondo coupling with the tip electrons starts dominating, which then limits the achievable spin lifetime and decoherence. On two atomic layers, Ti on the oxygen binding site can reach a spin lifetime of up to 190 ns [3].

2.9. SPIN CONTROL THROUGH SCATTERING

Since total angular momentum is conserved, the spin of the adatom can only be flipped by a incoming electron with a spin polarization opposite to the adatom's current polarization. When using a spin-polarized tip, electrons only tunnel with one polarization, so flipping the adatom spin happens exclusively in one direction.

The flip direction depends on the bias voltage polarity. With the tunneling electron originating from the tip, the spin arriving at the adatom will always be polarized equal to the tip. This only allows for adatom spin flips towards an adatom spin projection equal to the tip polarization.

On the other hand, if the tunneling electron originates from the non-magnetic bulk sample, it can initially have either spin polarization. After arriving at the adatom, however, only the spin equal to the tip polarization can enter the tip to complete the tunneling event. Therefore, the spin with polarization opposite the tip's will always remain on the adatom.

This spin pumping can be observed in IETS measurements. The IETS spectrum in fig. 2.6b was measured on Fe using a spin-polarized tip. We observe that the IETS steps are at different heights for negative and positive bias. We can infer that spin scatting events in one direction happen at a higher rate than the other, contributing more to the tunneling conductance channel. This is in contrast to fig. 2.6a, where a normal metal tip apex was used and the step heights are equal for both polarities.

Some tips even produce IETS peaks of different height at the spin excitation energies, rather than uneven steps. An example is shown in fig. 2.6c. This is commonly observed when many Fe atoms are picked up by the tip apex while fabricating a spin-polarized tip. This IETS feature for Fe on MgO/Ag does show up in the literature, for instance in Ref. [5]. However, to our knowledge, it has not been commented on. The phenomena might be related to higher order cotunneling processes [20], which can generate (what are essentially) Kondo resonances at finite bias.

The spin pumping mechanism can be used for intentional single atom spin control, with the desired spin direction selected by the bias polarity [26]. Spin pumping can even be selective in time by applying a DC voltage pulse, instead of a continuous bias, to generate a precisely timed spin-polarized current, with potentially a single spin scattering event per pulse. Such pulses were used to measure an adatom's spin lifetime on the typical sub-microsecond timescale in pump-probe experiments [15] and opened up possibilities to investigate spin dynamics out of thermal equilibrium.

2.10. SPIN HAMILTONIAN

To theoretically understand the magnetic states of an individual on-surface adatom, and Ti on MgO/Ag in particular, we can capture all magnetic interactions of the adatom with a spin Hamiltonian that describes its energy within the adatom's spin degrees of freedom. Its Hilbert space then covers tensor products of both the electron spin of the adatom as well as the nuclear spin, but not the degrees of freedom of the bulk system coupled to the adatom.

In the case of MgO/Ag, we will not need the orbital angular momentum as degree of freedom because it is mostly quenched, partly due to the symmetry-breaking of the sample's surface. By approximation, we can instead capture the effect of the crystal field as emerging anisotropy in various spin interactions depending on the spatial axis. The effective spin Hamiltonian $\hat{H}_{\text{eff}}$ is then the sum of contributions from separate spin Hamiltonians that will be discussed in this section:

$$\hat{H}_{\text{eff}} = \hat{H}_{\text{Zeeman}} + \hat{H}_{\text{hyper}} + \hat{H}_{\text{quad}} \ . \tag{2.3}$$

ZEEMAN SPLITTING

An individual magnetic moment has the lowest energy when aligned with the magnetic field $\vec{B} = (B)$ at the position of the magnetic moment. For a single electron quantum spin S of an adatom, which has states with quantized magnetic moment, this interaction between an external magnetic field and the spin is the Zeeman coupling. The corresponding spin Hamiltonian can be written as

$$\hat{H}_{\text{Zeeman}} = \sum_{i=x,y,z} \mu_B g_i B_i \hat{S}_i \ . \tag{2.4}$$

Here, $\mu_B = 1.3996 \times 10^{10}$ Hz/T is the Bohr magneton. It's value is determined by physical constants, including the electron mass. $\hat{S}_i$ is the spin projection operators for all three spatial axes.

g_i is the magnetic g-factor, a dimensionless quantity that characterizes the ratio between the spin angular momentum and the magnetic moment. For a free electron $g_i \approx 2$ and isotropic. However, for an adatom, the electron spin g-factor is in general anisotropic with the external magnetic field direction, due to a combination of spin-orbit coupling and the crystal field from the chemical environment affecting the electronic orbitals of the adatom. We can write the g-factor here as a 3-component vector g_i rather than the more general 3x3 tensor due to the symmetry of the adatom binding sites imparted by the crystal lattice.

For Ti on the oxygen binding site of MgO/Ag, the g-factor anisotropy is given by $\vec{g} = (g_x\ , g_y\ , g_z) = (1.67, 1.67, 0.61)$ [7]. The in-plane components are the same because the x and y external field directions are indistinguishable in the C_{4v} symmetry of the binding site. This does not hold for the bridge sites of Ti because of the two-fold C_{2v} symmetry. The Ti bridge g-factors with respect to the lattice are: $\vec{g} = (1.70, 1.89, 2.01)$ [27]. For our setup's in-plane external field direction field oriented a 14° angle relative to the MgO crystal lattice, the g-factors are 1.71 and 1.89 for the vertical and horizontal site, respectively.

Note that the total magnetic field on an adatom in all experiments in this thesis is the sum of the external field generated by superconducting coils $\vec{B}^{\text{ext}}$ and a field emanating from the spin-polarized STM tip $\vec{B}^{\text{tip}}$. The tip field can be controlled by the tip height. This can be used to tune the energies of the spin under the tip.

For $S = 1/2$, there are two eigenstates that can be labeled with the corresponding magnetic quantum number $m_S = \pm 1/2$, the expectation value of the spin projection operator along the magnetic field direction. The ground state has $m_S = \text{-}1/2$ and in this thesis we refer to this state as $|\downarrow\rangle$. The excitated state $m_S = +1/2$ is referred to as $|\uparrow\rangle$.

Note that the negative spin projection in the ground state aligns the electron's magnetic moment with the field. The spin and magnetic moment are defined anti-parallel for an electron because of its negative charge. There is a Zeeman energy splitting $\Delta E = g\mu_B|\vec{B}|$ between the ground and excited state.

A nuclear spin also experiences a Zeeman splitting. Here, the Zeeman interaction strength, or gyromagnetic ratio γ, is given by $\mu_N g_i^N$, instead of $\mu_B g_i^e$, with a nuclear magneton μ_N based on the proton's mass and a separate anistopic g_i^N. The gyromagnetic ratio of a nuclear spin is generally three order of magnitude smaller than for electron spins because of the larger proton mass.

General spin-spin couplings

Pairs of individual spins can interact in different ways. Firstly, a spin's magnetic dipole moment tends to align with the magnetic field emanating from another spin's dipole moment. A general Hamiltonian $\hat{H}_{\text{dipole}}$ of this dipole-dipole interaction can be written as

$$\hat{H}_{\text{dipole}} = \frac{\mu_0 \gamma_1 \gamma_2 \hbar^2}{2\pi|\vec{r}_{12}|^3}\left(3\left(\vec{S}_1 \cdot \vec{r}_{12}\right)\left(\vec{S}_2 \cdot \vec{r}_{12}\right) - \vec{S}_1 \cdot \vec{S}_2\right). \tag{2.5}$$

Here, μ_0 is the vacuum permeability, γ_1 and γ_2 are the gyromagnetic ratios of the interacting spins 1 and 2, and $\vec{r}_{12}$ is the relative distance vector between the two spins.

$\vec{S}_1$ and $\vec{S}_2$ are spin operator vectors $(\hat{S}_x, \hat{S}_y, \hat{S}_z)$ for both spins, respectively.

Pairs of spins of electrons can also couple via the exchange interaction, which arises from an interplay between orbital bonding energy, Coulomb repulsion, and the Pauli exclusion principle. In general, a bonding orbital — a linear combination of orbital wavefunctions added with a symmetric phase (the sum), with the electron located at the center between orbital positions before combining — has a lower energy due to constructive interference of the wavefunction. This is opposed to the higher kinetic energy of antisymmetric anti-bonding wavefunctions (the difference), with steeper slopes in the spatial wavefunction and electrons located at either ends away from the center.

To access this lower bonding energy for both electrons, the two electrons trying to occupy this one phase-symmetric wavefunction need to have opposite spin to maintain an overall antisymmetric wavefunction required for indistinguishable fermions according to the Pauli exclusion principle, which can be stated, roughly, as: the electrons should be ‘exchangable’ without changing the observables. In this sense, an antiferromagnetic spin configuration is energetically favored, indirectly, due to this exchange principle. The exchange interaction can be captured in a Heisenberg spin Hamiltonian $\hat{H}_{\text{exch}}$ with an effective positive spin-spin exchange coupling parameter J that sets the interaction strength:

$$\hat{H}_{\text{exch}} = \sum_{i=x,y,z} J_i \, \hat{S}_{1,i} \hat{S}_{2,i} \,. \tag{2.6}$$

Two electrons in close proximity in the same bonding orbital also contribute a high capacitive energy due to the Coulomb repulsion between the negative charges. In some cases, depending on the environment, this charging energy is larger than the kinetic energy gained in the bonding orbital. Therefore, the anti-bonding orbital, accompanied by a ferromagnetic coupling with aligned spins, may be favored. This can be expressed with a negative J.

The exchange interaction as described above is, in principle, isotropic ($J_x = J_y = J_z$) and the interaction strength decays exponentionally with the relative distance between the spins. More complex charge environments and second-order tight-binding interactions may alter this simplified picture.

HYPERFINE INTERACTION

Many adatoms have isotopes that carry non-zero nuclear spin. This means the nucleus of the atom, containing protons and neutrons, has its own quantized magnetic moment. The nuclear and electron magnetic moments can interact with each other. This so-called hyperfine interaction can often be captured in a spin Hamiltonian $\hat{H}_{\text{hyper}}$ by a 3x3 tensor hyperfine coupling that is, in general, anisotropic. For an on-surface atom, this can be reduced to an anistropic effective hyperfine vector (argumentation provided below). This can be written as:

$$\hat{H}_{\text{hyper}} = \sum_{i=x,y,z} A_i \hat{S}_i \hat{I}_i \,. \tag{2.7}$$

Here, $\hat{S}_i$ and $\hat{I}_i$ are the spin projection operators for the electron and nuclear spin, respectively. A_i is the effective hyperfine coupling for the different axes and is here given as an energy quantity in units frequency.

According to literature values, the hyperfine coupling vector for Ti on the oxygen binding site is given by $(A_x, A_y, A_z) = (10, 10, 130)$ MHz [6]. Note that, as with the electron spin g-factor, the in-plane components are the same due to the C_{4v} binding site symmetry.

The hyperfine coupling is build up from different contributions originating from various electron orbitals. In principle, the magnetic moments of a nuclear and an electron interact exclusively through their dipolar coupling. Inner shell s-electrons contribute indirectly via the isotropic Fermi contact interaction that depends on the electron spin density at the position of the nucleus [28, 29].

Outer shell d-orbitals contribute a more direct dipole-dipole coupling, which, as illustrated by eq. (2.5), is anisotropic in general. Still, the generality of the anisotropy is constrained because the symmetry of the orbitals are dictated by the substrate crystal lattice and the surface plane. Therefore, the effective relative distance vector between the electron and nuclear magnetic moments coincides with the crystalline out-of-plane z-axis. Since we write our Hamiltonian in this crystalline basis, the dipole interaction contributing to the hyperfine tensor does not contain any off-diagonal terms (e.g. $A_{xz}\hat{S}_x\hat{I}_z$) and we can write the hyperfine coupling as a vector instead.

QUADRUPOLE INTERACTION

For nuclei with a larger total spin than $I = 1/2$, multiple protons and neutrons contribute to the spin density distribution in space. As such, the spin density is linked to a non-spherical charge distribution, leading to an electrical field quadrupole moment Q. The surrounding electron cloud of the adatom with an electric field gradient q can exert a torque eq on this collective quadrupole moment of the protons contributing to the nuclear spin. This rotation thus interacts with the nuclear spin, giving rise to the following effective spin Hamiltonian

$$\hat{H}_{\text{quad}} = \sum_{i=x,y,z} Q_i \hat{I}_i^2 \tag{2.8}$$

Here, Q_i are the components of a vector $\vec{Q}$ representing the more general 3x3 quadrupole tensor that is not required in our binding site symmetry. These components, which represent a quadrupole spin energy, take the form:

$$\vec{Q} = \frac{e^2 qQ}{4I(2I-1)} \begin{pmatrix} -(1-\eta) \\ -(1+\eta) \\ 2 \end{pmatrix} . \tag{2.9}$$

with $0 \le \eta \le 1$ the anisotropy of the in-plane electric field gradient. For Ti on the oxygen binding site, $\vec{Q} = (1.5, 1.5, -3)$ MHz [6].

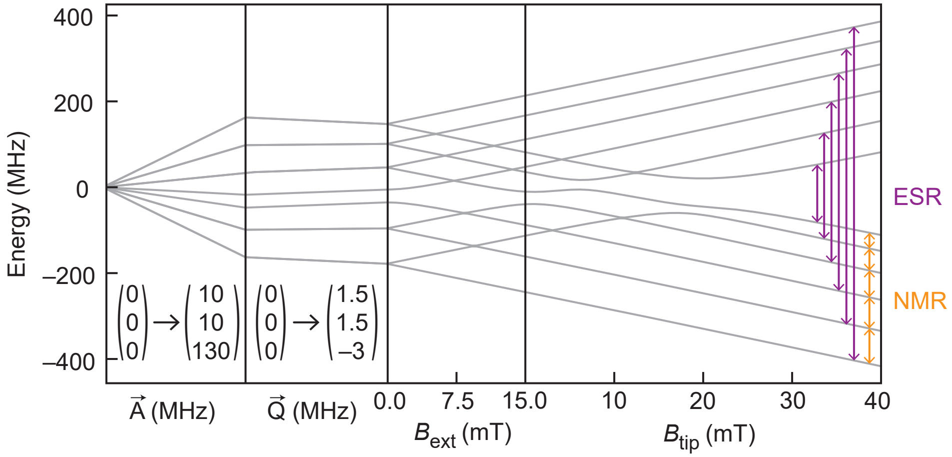

Fig. 2.8 | Energy diagram of the spin eigenstates of Ti on the oxygen binding site. Calculated using the Hamiltonian in eq. (2.10) as a function of hyperfine coupling, quadrupole moment, an out-of-plane (z) external magnetic field, and a tip-induced magnetic field with angle of 8° relative to the z-axis. Vertical arrows indicate ESR-type (purple) and NMR-type (orange) transitions between eigenstates in the large field, spin product state regime. This figure is reproduced from Ref. [6].

COMPLETE HAMILTONIAN

By filling in eq. (2.3), we can combine all the contributions from the discussed spin interactions into a single effective spin Hamiltonian that models the adatom spin system, including the nuclear spin:

$$\hat{H}_{\mathrm{eff}} = \sum_{i=x,y,z} \mu_B g_i^e (B_i^{\mathrm{ext}} + B_i^{\mathrm{tip}})\hat{S}_i + \mu_N g_i^N (B_i^{\mathrm{ext}} + B_i^{\mathrm{tip}})\hat{I}_i + A_i \hat{S}_i \hat{I}_i + Q_i \hat{I}_i^2 \, . \tag{2.10}$$

The calculated the eigenstates energies of this Hamiltonian for a ^{47}Ti (I=5/2) on the oxygen binding site are plotted in fig. 2.8 for a range of magnetic fields. For larger magnetic fields, we can see that the Zeeman energy dominates and the eigenstates are approximately the spin product states, with eigenenergies separated by the hyperfine coupling. Therefore, ESR and NMR-type transitions are well-defined. Most experiments in this thesis are performed in this regime, with field up to 1.6 T.

At small to intermediate magnetic fields, the Zeeman splitting is comparable to the hyperfine coupling. Here, we see avoided level crossings between the spin states. At an avoided crossing, the eigenstates are spin singlets or triplets. Although in this case, multiple avoided crossings overlap and the eigenstate compositions are a combination of more than two spin projections.

2.11. ESR-STM

An important technique used in this thesis is ESR-STM: the combination of STM with electron spin resonance (ESR). This method was developed relatively recently [2]. ESR-STM can be used to measure the spin state energies of individual atoms or molecules on a surface with a significantly higher resolution than any other existing STM method. Furthermore, ESR-STM provides options for comprehensive coherent control of the electron spins [30].

2.11.1. MAGNETIC RESONANCE

ESR-STM belongs to a subset of the more general magnetic resonance class of experiments, which are typically performed on bulk samples. To explain magnetic resonance, we start with an abstract individual spin with an energy splitting, for example due to Zeeman splitting from the external magnetic field. We can write the energy splitting Hamiltonian along the spin quantization axis that we here define as the z direction:

$$\hat{H}_{\mathrm{ES}} = \hbar\omega_0\,\hat{S}_z. \tag{2.11}$$

Over time, the spin eigenstates with energy differences $\hbar\omega_0$ will accumulate a relative phase difference with a rate ω_0. This is often called precession.

In magnetic resonance experiments, an oscillating magnetic field B_x is applied perpendicular to a spin's quantization axis. This can be written as a time-dependent Hamiltonian term $\hat{H}_{\mathrm{MR}}$, with ω the angular frequency of the oscillating magnetic field:

$$\hat{H}_{\mathrm{MR}} = B_x \cos(\omega t)\,\hat{S}_x. \tag{2.12}$$

This term can drive a spin transition between energy eigenstates with a difference in spin projection $\Delta m_z = \pm 1$, but only if the magnetic torque direction of the driving field is synchronized with the precession frequency, $\omega = \omega_0$, which is called the resonance condition. If this condition is met, the expectation value $\langle \hat{S}_z \rangle$ oscillates as a sine between the two spin levels, with a rate that scales linearly with the driving field B_x. These periodic spin flips are called Rabi oscillations.

By sweeping the frequency of the driving field and simultaneously reading out any changes to the magnetization direction of target spin, the resonance frequency ω_0 can be determined. This is a direct measure of the spin transition energy. ESR is thus a powerful spectroscopy tool for electron spins. Moreover, since the resonance frequency of the target electron spin can be very sensitive to Zeeman splitting from magnetic fields in the environment, an individual spin can be used as an atomic magnetic field sensor.

2.11.2. SPIN DECOHERENCE

The resonance frequency is, in practice, never one singular value during an experiment. For instance, background magnetic fields in the environment fluctuate perpetually and, therefore, so does the Zeeman energy that contributes to the resonance frequency. Hence, there is always a finite frequency width in a time-averaged ESR-resonance peak.

In a continuously driven experiment, the resonance peak width is set by the amplitude of the background fluctuations.

Trying to drive the randomly fluctuating resonance point with a fixed frequency leads to inefficient Rabi oscillations over time. At any moment in time, the fixed frequency driving applies a magnetic torque in a partly random direction, because the torque desyncs with the spin precession set by the fluctuating resonance. The larger the resonance fluctuates, the faster the spin dynamics trajectory will deviate from clear Rabi oscillations.

This could be prevented by continuously changing the driving frequency to match the fluctuating resonance, but the randomness of the environment prevents this. You lose track of the exact amount of accumulated phase in the spin precession and at some point it is entirely unknowable when to start driving to flip the spin towards an intended direction. This process is called spin decoherence, or dephasing and is observed as increasingly incomplete spin flips with longer driving time. The corresponding time scale is the decoherence time T_2*, which is defined as an exponential decay of the Rabi oscillation amplitude. This translates to a resonance peak width (or line width) by taking the inverse $1/T_2$ to get a frequency.

An energy relaxation event that flips the spin at a random moment, such as Kondo scattering, is not a purely dephasing process because it does not fluctuate the transition energies. Still, a projective event like spin relaxation can be interpreted as a decoherence event, since the phase information is entirely reset. In the presence of both dephasing and relaxation channels, the relaxation timescale (or spin lifetime) T_1 acts as a maximum achievable decoherence time: $T_2^{\text{max}} = 2T_1$ [31]. The factor two relates to the way the phase and energy decay rates are conventionally defined.

2.11.3. ENERGY RESOLUTION & TEMPERATURE

Since the frequency resolution to readout the resonance point is limited by the decoherence time, the ESR resolution for the spin state energies is ultimately determined by spin decoherence. This is in contrast to many other STM spectroscopy methods, such as IETS, which rely on electron transport. Those are fundamentally limited in their energy resolution by temperature, due to the Fermi-Dirac distribution smearing out bulk state occupations over a range of energies.

In the case of ESR, however, the temperature only limits the signal strength, not the resolution, because the spin states are initialized using their thermal populations. At a high temperature relative to the spin state energy differences, all states are equally populated. Driving transitions between equally populated spin states does not change the total magnetization, and thus no contrast can be observed at the resonance frequency. Sufficiently low temperatures are required for a measurable magnetization change, with the maximum temperature for ESR experiments set by the achievable signal-to-noise ratio.

At our setup's minimum operating temperature of 0.4 K, the thermal energy k_BT corresponds to 8.3 GHz ($E = hf$). Therefore we need a spin energy splitting on the same order of magnitude, preferably higher, for a significant thermal population difference to measure a spin contrast. For the g-factors of Ti adatoms, we need magnetic fields on the order of 1 T to achieve a Zeeman splitting in this required range, which is possible in our STM setup.

However, generating an oscillating magnetic field at these radio frequencies in our STM setup to match the energy splitting is more involved, as will be discussed in the sections below. The methods to achieve ESR driving at these frequencies using RF voltages in the tunneling junction, were the breakthrough that made ESR-STM possible [2].

2.11.4. ESR UNDER THE STM TIP

Aside from the sufficient energy splitting from an external magnetic field, performing ESR experiments in our STM setup requires a magnetic driving field at RF frequencies and a method to readout the spin state in the sample. We can realize both inside our STM tunneling junction for a magnetic adatom under our tip. The relevant elements are illustrated in fig. 2.9a.

For standard ESR experiments with bulk samples, magnetic contrast readout requires an ensemble average over a volume containing many spins to reach a measurable signal-to-noise ratio. Using STM, we can instead read out the spin state of a single atom via magneoresistance by using a spin-polarized tip. An undriven spin stays in the thermal ground state, which corresponds a certain time-averaged current set by the magnetoresistance. Continuous wave (CW) ESR driving equalizes the time-averaged population distribution over the two spin states involved in the ESR transition, resulting in a different current. The difference between these mean currents is the ESR-STM signal.

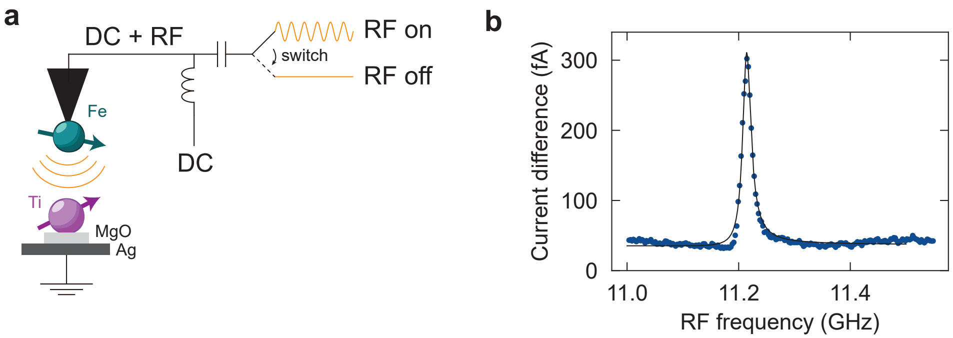

Fig. 2.9 | ESR-STM spectroscopy. a Schematic of an ESR-STM circuit. RF and DC voltages are combined to reach the tunneling junction using a bias tee. The adatom spin under study (Ti) is irradiated by an RF electric field (orange), which drives the ESR. The time-averaged DC magnetoresistance is measured using a spin-polarized tip with Fe at the apex. The ESR signal is the current difference between RF on and RF off. **b** Blue markers: ESR-STM frequency spectroscopy on a Ti adatom on the horizontal bridge binding site of two-layer MgO/Ag. Black line: fit of the observed resonance peak with a Fano line shape. Measured in constant current mode. Tip height setpoint: 5 pA, 30 mV. B_x = 450 mT, B_z = 0 mT. Temperature: 0.4 K

For the ESR driving, we apply an RF voltage to the tunneling junction via the tip. This is, evidently, not a magnetic field. However, the oscillating voltage will be converted into an effective oscillating Hamiltonian term that turns out to be capable of driving the spin under the tip according to magnetic resonance principles. The proposed ESR-STM driving mechanisms will be discussed in more detail in the next subsection.

Fig. 2.9b showcases a typical ESR-STM spectroscopy frequency sweep. We compare the currents with and without a CW RF voltage applied. The ESR resonance peak can be observed as an increase in the current difference between the two situations at a specific RF voltage frequency.

Note that there is a finite current difference even with off-resonant driving. This is a rectification current caused by applying a RF voltage on the slightly non-linear conductance of the Ti adatom. The rectification current is discussed in more detail in chapter 5.

2.11.5. DRIVING MECHANISMS

Multiple ESR-STM mechanisms have been proposed to explain the conversion of the oscillating electric field from applied RF voltage into an effective oscillating magnetic field that drives the ESR transitions [32]. At the time of writing, three candidates are still deemed plausible for explain experimental observations. However, it is considered likely that multiple mechanisms can contribute to the ESR driving at the same time, with different ratios depending on the spin system under study. The existence of multiple mechanisms also makes ESR-STM more broadly applicable, rather than only working for specific substrates.

As a first conversion mechanism, the oscillating electric field should induce an oscillating electromagnetic wave while propagating from the tip to the sample, according to the Maxwell equations. This far-field solution is suppressed, however, because the tip-sample distance is much smaller than the free-propagating wavelength at radio frequencies. Still, it has been proposed that the near-field conversion to magnetic fields could be sufficient to explain the observed ESR-STM driving amplitudes regardless due to MgO surface effects [33].

The most frequency described driving mechanism is the piezoelectric model [32, 34, 35]. In the model, the oscillating electric field moves the adatom under the tip up and down due to a piezoelectric interaction in the substrate. Since the tip magnetic field has a strong gradient in the tip-sample direction (exchange field dominated), the adatom's spin experiences an oscillating magnetic field during the periodic movement. Alternatively, without significantly moving the adatom, the piezoelectric interaction periodically alters the crystal field anisotropy, which oscillates the g-factor and drives the spin in any external magnetic field.

The strongest proponent in favor of the piezoelectric model on MgO/Ag is the possibility to drive Ti adatoms away from the tunneling junction under the tip if, and only if they are positioned next to the gradient magnetic field of a single atom magnet [36]. This is possible because the RF electric field emanating from the tip extents beyond the exponentially decaying tunneling region and can thus also induce the piezoelectric displacement remotely.

A driving model based on cotunneling, as a broad mechanism, has also been proposed [21, 22]. This theory suggests that an oscillating virtual tunneling barrier, in a very general sense, from a spin-polarized lead (the tip, or another exchange-coupled magnetic adatom on the surface) to an Anderson impurity can be enough to drive ESR efficiently in the impurity, even if no oscillating current ends up running through the impurity. The tunneling barrier can be varied by an RF voltage, or more indirectly via an above-described piezoelectric mechanism. This perspective is supported by recent experimental observation of spin-torque driven ESR-STM [37] in molecules [38, 39], which also falls under the more generalized cotunneling model in the limit where an oscillating current does flow [40].

2.11.6. ESR-ACTIVE TIPS

One thing has at least become (painfully) clear in the ESR-STM community: the exact tip apex configuration matters for observing ESR. A strongly spin-polarized STM tip is not sufficient to drive ESR. The exact qualifiers are unclear and the best method to fabricate an ESR-active tip remains trial and error.

One important property is likely the tip magnetization angle relative to the external field. ESR driving requires an oscillating magnetic field perpendicular to the spin quantization axis. Similarly, a small perpendicular tip magnetization component seems required to drive ESR-STM. The Fe cluster at the tip apex tend to generally align with the external field, but never perfectly, so there is a natural variability during tip fabrication regardless.

Our approach is to start with an atomically sharp tip that images adatoms as mostly circular shapes (as opposed to elongated), prepared by dipping in the Ag substrate. We start preparing a spin-polarized tip with Fe adatoms and, between sequential pickups, monitor the spin IETS step of Ti on the bridge-site around zero bias. We look for a specific curve shape, showcased in fig. 2.6d, with a square-root-like profile for the downwards IETS step at negative bias and a flat conductance for positive bias. Furthermore, ESR-active tips with large IETS step height tend to produce strong ESR currents.

Other IETS shapes can also correspond to ESR-active tips with good signal strength, but we find that the above-described shape has a more consistent success rate and this saves time. We only check the ESR signal with a time-consuming ESR frequency sweep for tips with these features. Otherwise we pick up more Fe adatoms or, if the topography image indicates a very distorted tip apex, we reset the tip by dipping in Ag again.

2.11.7. DC AND HOMODYNE DETECTION

As discussed in eq. (2.2), the tunneling magnetoresistance through a Ti adatom with a spin-polarized tip depends on the expectation values of spin projections $\langle S_i \rangle$ in all three axes $i = x, y, z$. Since all $\langle S_i \rangle(t)$ change dynamically as a function of time due to the combination of ESR driving and spin precession, the magnetoresistance also changes at that fast GHz timescale. However, we need millisecond averaging times to measure the small ESR current signal above the current noise.

There are two relevant detection mechanisms that convert the fast dynamics into finite time-averaged contributions to the DC current: 'DC magnetoresistive' and 'homodyne' detection [41]. For either contribution, the time-averaged current with a resonant RF voltage ESR driving the spin is different compared to the current when no RF voltage is applied and the spin stays in its ground state. This ESR current I_{ESR} difference makes the the ESR driving detectable.

DC MAGNETORESISTIVE

For the DC magnetoresistive contribution we consider the magnetic polarization in the direction of the adatom's spin-1/2 quantization axis z. At zero temperature, the spin ground state has $\langle S_z \rangle_{GS}$ = -1/2 at all moments in time, although the actual ground state polarization is reduced towards 0 with higher temperature T according to the Boltzmann distribution. Meanwhile, ESR driving oscillates $\langle S_z \rangle(t)$ between -1/2 and +1/2, so the driven time-averaged $\langle S_z \rangle = 0$ when the driving is efficient (Rabi oscillation period is faster than T_2).

Using eq. (2.2), if the direction of the tip magnetic polarization $\hat{\vec{P}}$ has a finite component P_z in the z-direction, the time-averaged DC magnetoresistive contribution I_{DCmr} to the measured ESR current difference will be

$$I_{\text{DCmr}} = V_{DC}\sigma_{SD}\langle S_z \rangle_{GS} P_z\,, \tag{2.13}$$

where V_{DC} is the applied DC bias, σ_{SD} the base-line conductance of the spin-dependent tunneling channel.

HOMODYNE

For the homodyne contribution we consider the time evolution of the spin's polarization in the x, y-plane. In contrast to the z component, the in-plane polarization time-averages to zero with and without Rabi oscillations, so there is no current difference with a DC bias applied. The ground state is an S_z eigenstate, and thus has $\langle S_x \rangle_{GS} = \langle S_y \rangle_{GS} = 0$ at all times. During Rabi oscillations, with the spin in a superposition between eigenstates, the spin state precesses laterally around the Bloch sphere with the Larmor frequency ω_0. As such, $\langle S_x \rangle(t)$ and $\langle S_y \rangle(t)$ oscillate as $\sim \cos(\omega_0 t)$, so the time-averaged in-plane polarization is also zero.

These oscillations at the Larmor frequency ω_0, however, are at the exact same frequency as the RF voltage V_{RF} driving the ESR resonance. That oscillating voltage with an amplitude $|V_{\text{RF}}|$ can contribute to a DC spin-polarized curent, opposed to the DC bias, since a squared sinusoidal does produce a finite time-averaged component. This the principle behind homodyne detection.

Still, the situation is more complicated because, as illustrated in fig. 2.10a, the amplitude of the Larmor precession also oscillates in time with the Rabi rate ω_{Rabi} with the maximum amplitude $|S_x|$ on the equator of the Bloch sphere. The Rabi rotation is typically significantly slower than the Larmor precession. We can now write out an expression for the time-dependent homodyne current during Rabi oscillations. Defining the perpendicular tip polarization component P_x in the x-direction and also making the choice that the global phase of the spin precession is in the x-direction at $t = 0$ (cosine):

$$I_{\text{hom}}(t) = \sigma_{SD}|V_{RF}|\sin(\omega_0 t + \alpha)|S_x|\cos(\omega_0 t)\sin(\omega_{\text{Rabi}} t)P_x\,. \tag{2.14}$$

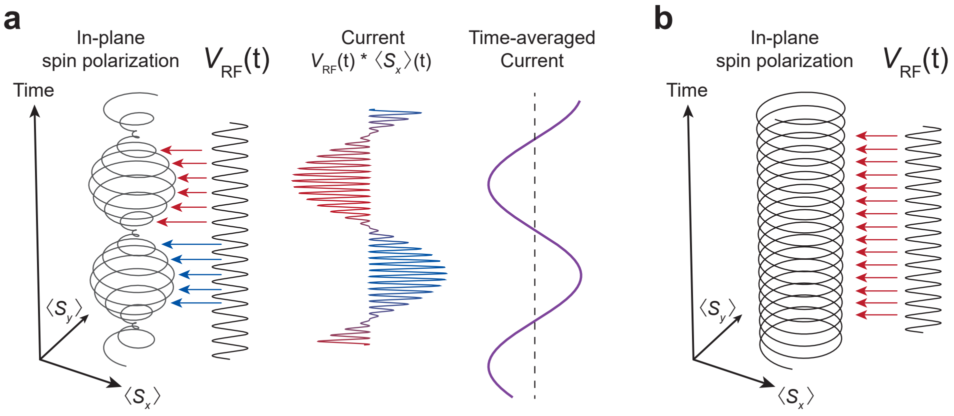

Fig. 2.10 | Illustration of homodyne detection. a Schematic of the Larmor precession of the in-plane magnetizations $\langle S_x \rangle(t)$ and $\langle S_y \rangle(t)$ of the adatom spin during coherent Rabi oscillations, simultanious with the oscillating RF voltage $V_{\mathrm{RF}}(t)$. Their product results in an oscillating current when time-averaged over the precession period (purple line) because the phase difference between precession and V_{RF} changes sign (red and blue) during one Rabi period. **b** Schematic of Larmor precession during an ESR-driven decoherent steady state, where the phase difference with V_{RF} remains fixed. In contrast to (**a**), this situation result in a finite homedyne current averaged over time-scales longer than the Rabi period, with the magnitude depending on the fixed phase between the precession and $V_{\mathrm{RF}}(t)$.

Here, α is the relative phase difference between the driving voltage and the precession. The product between the sinusoidals results in the finite time-averaged component $\sin(\alpha)$ in the current. However, the Rabi oscillation on top results in a zero time-averaged current regardless.

This changes when the spin decoheres and the time-evolution follows a steady-state solution, portrayed in fig. 2.10b, with a fixed $\langle S_z \rangle$ and thus a finite $\langle S_x \rangle$ amplitude at all times. Experiments have shown that α is generally equal to 0, meaning the RF voltage and the Larmor precession component along the tip polarization direction are in-phase during ESR-STM driving [41]. Therefore, the time-averaged current at resonance is still zero.

By generating a slightly detuned RF voltage ω, the homodyne contribution does nonetheless result in a finite time-averaged current. The frequency difference $\omega_0 - \omega$ can be considered an effective non-zero α at any point in time. For RF voltage frequencies too far detuned from the resonance, the Rabi oscillations are not driven at all anymore, the spin stays in the groundstate without precession and no ESR current difference is produced. Hence, a homodyne peak is formed only around the resonance. The opposite sign of $\sin(\alpha)$ on either side of the resonance frequency produces a markedly asymmetric peak shape in CW-ESR spectroscopies.

IMPACT OF TIP MAGNETIZATION

The DC magnetoresistance contributes to the ESR current with a component of the tip polarization aligned with the spin axis of quantization, while homodyne only contributes with a perpendicular tip polarization component. Both can contribute at the same with a polarization angle somewhere in between. This is generally the case. since the tip magnetization direction is not controlled perfectly during fabrication. The combination of the symmetric DC magnetoresistive and the asymmetric homodyne contributions to the ESR resonance peak shape is often fitted phenomenologically with a Fano resonance.

2.12. COHERENT SPIN CONTROL WITH STM

Coherent control over a spin means to bring it to any (superposition) state with a well-defined phase at a selected moment in time. This is opposed to spin dynamics controlled in a time-averaged way, such as the spin scattering from a continuous spin-polarized current or the CW ESR experiments described above. The mechanisms of those types of continuous spin actuations can still be used for coherent control by limiting the actuation to a pulse that is shorter than the coherence time, while the spin retains its well-defined phase.

A resonant RF voltage pulse only drives the ESR Rabi oscillations for a certain time-interval. After applying the Rabi pulse, the spin will end up in a controlled superposition between spin up and down, depending on the pulse width τ_{Rabi} that sets the endpoint of the oscillations. The sinusoidal Rabi oscillations can be measured in ESR-STM by varying τ_{Rabi}, which can be used to extract the Rabi rate and the driven coherence time T_2^* directly. This has been shown for the first time by Yang *et al.* [30].

A DC voltage pulse can be used to project a spin state to a selected spin product state with precise timing via spin-polarized electron scattering (see section 2.9). This can also be used as a form of coherent control, especially in the case where the eigenstate are not spin product state, as was shown by Veldman *et al.* [10]. A projection to a non-eigenstate leaves the state with a well-defined phase and induces free coherent dynamics.

2.13. PREVIOUS STM WORK ON NUCLEAR SPINS

One focus in this thesis is the exploration of dynamics of individual on-surface nuclear spins using STM. The main results reported in limited literature on the topic of nuclear spins probed with STM are summarized in this section. Notably, all past experiments involved only time-averaged measurements, except for a short statement that no sign of any dynamics had been resolved in time in Ref. [42].

RESOLVING THE HYPERFINE SPLITTING

The hyperfine coupling between the nuclear spin of an adatom and an accompanying electron spin splits a single ESR transition of the electron spin into multiple resonances representing the different nuclear spin states. It was shown in 2018 that ESR-STM can be used to resolve that splitting and identify the nuclear spin states of adatom isotopes of Ti and Fe on MgO/Ag [42].

Following this discovery, hyperfine splitting has also been observed for Cu adatoms [43], alkaline dimers (unresolved) [44], and the lanthanites Eu and Sm [45] (all on 2-layer MgO/Ag). Additionally, there has been the observation of anisotropy in the hyperfine coupling for Ti [27, 46], with a splitting depending on the external magnetic field direction. The strongest hyperfine anisotropy has been observed for Ti on the oxygen binding site [6].

NUCLEAR SPIN CONTROL

It has been demonstrated that, through yet unknown mechanisms, NMR-type transitions can be driven continuously in Cu and Ti nuclear spins using the same RF voltages in the tunneling junction that can drive ESR [6, 43], although no coherent Rabi oscillations have been shown yet. Furthermore, these experiments operated in a low magnetic field regime with large hybridization between the nuclear and electron spin, so the demonstrated transitions are between eigenstates that contain both electron and nuclear spin components. It is still unclear whether the NMR driving mechanism allows for transitions between nuclear spin product states without hybridization.

In the cases of Cu and Ti on the oxygen binding site, it has also proved possible to control the nuclear spin using a spin-polarized DC current [6, 43]. According to the Boltzmann distribution at typical STM operating temperatures of 1.5 K, all nuclear spin states are essentially equally populated because of their small energy differences in the MHz range. With the current applied, the nuclear spin populations initialize to either the maximum or minimum spin projection state, depending on the direction of the current.

These changes to the time-averaged nuclear spin populations are reflected in CW-ESR spectra as different hyperfine peak heights: the electron spin is driven for a larger fraction of the averaging time if the nuclear spin state corresponding to the

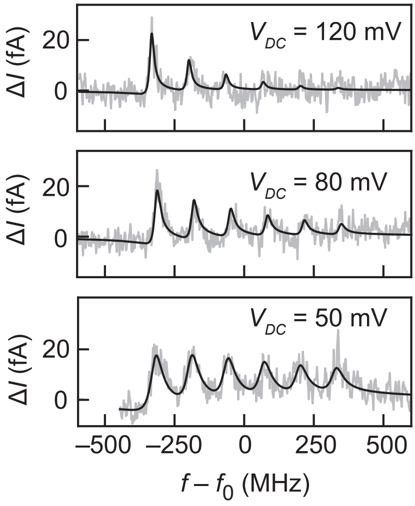

Fig. 2.11 | Resolved hyperfine splitting and nuclear spin pumping. ESR-STM spectra on a ^{47}Ti adatom isotope on the oxygen binding site of two-layer MgO/Ag at different DC bias voltages, measured in constant current mode. The spectra are plotted relative to the center frequency f_0, which shifts due to a changing tip field. ΔI is the ESR current difference. (Tip height setpoint: 2.5 pA. B_x = 0 T, B_z = 1.5 T. Temperature: 1.5 K. Zero-to-peak V_{RF} = 25 mV.) This figure is reproduced from a dataset published in Ref. [6].

probed hyperfine resonance is populated more often. Fig. 2.11 shows an example of a polarized hyperfine ESR-STM spectrum on Ti on the oxygen site. This adatom species happens to have a strong nuclear spin polarization that was also shown to depend on non-trivially the applied DC bias, rather than just the amount of current [6], the details of which is still poorly understood.

In general, the mechanism behind electrically controlled nuclear spin polarization is a type of hyperpolarization [47] that relies on a finite hybridization between the nuclear and electron spin caused by the hyperfine coupling. The process is discussed in detail in chapter 7. In essence, the nuclear spin can flip-flop with the electron spin with a rate depending on the degree of hybridization, which exchanges angular momentum ±1, so the state moves back and forth to adjacent nuclear spin projections m_I. However, the electron spin is polarized due to inelastic electron spin scattering from the spin-polarized current, so it can only receive angular momentum from the nuclear spin in flip-flops towards one m_I direction. After subsequent directional flip-flops, the nuclear spin state eventually lands at an extremal spin projection $m_I = \pm I$ where it cannot flip-flop in either direction anymore.

REFERENCES

[1] C. Julian Chen. *Introduction to Scanning Tunneling Microscopy*. 3rd edition. Oxford University Press, 2021, p. 492. ISBN: 9780198856559.

[2] S. Baumann, W. Paul, T. Choi, C. P. Lutz, A. Ardavan and A. J. Heinrich. ‘Electron paramagnetic resonance of individual atoms on a surface’. In: *Science* 350.6259 (2015), pp. 417–420. ISSN: 10959203. DOI: `10.1126/science.aac8703`.

[3] K. Yang, Y. Bae, W. Paul, F. D. Natterer, P. Willke, J. L. Lado, A. Ferrón, T. Choi, J. Fernández-Rossier, A. J. Heinrich and C. P. Lutz. ‘Engineering the Eigenstates of Coupled Spin-1/2 Atoms on a Surface’. In: *Physical Review Letters* 119.22 (2017), p. 227206. ISSN: 0031-9007. DOI: `10.1103/PhysRevLett.119.227206`.

[4] W. Paul, K. Yang, S. Baumann, N. Romming, T. Choi, C. P. Lutz and A. J. Heinrich. ‘Control of the millisecond spin lifetime of an electrically probed atom’. In: *Nature Physics* 13.4 (2017), pp. 403–407. ISSN: 17452481. DOI: `10.1038/nphys3965`.

[5] Y. Chen, Y. Bae and A. J. Heinrich. ‘Harnessing the Quantum Behavior of Spins on Surfaces’. In: *Advanced Materials* 35.27 (2023). ISSN: 0935-9648. DOI: `10.1002/adma.202107534`.

[6] L. M. Veldman, E. W. Stolte, M. P. Canavan, R. Broekhoven, P. Willke, L. Farinacci and S. Otte. ‘Coherent spin dynamics between electron and nucleus within a single atom’. In: *Nature Communications* 15.1 (2024), p. 7951. ISSN: 2041-1723. DOI: `10.1038/s41467-024-52270-0`.

[7] M. Steinbrecher, W. M. J. van Weerdenburg, E. F. Walraven, N. P. E. van Mullekom, J. W. Gerritsen, F. D. Natterer, D. I. Badrtdinov, A. N. Rudenko, V. V. Mazurenko, M. I. Katsnelson, A. van der Avoird, G. C. Groenenboom and A. A. Khajetoorians. ‘Quantifying the interplay between fine structure and geometry of an individual molecule on a surface’. In: *Physical Review B* 103.15 (2021), p. 155405. ISSN: 2469-9950. DOI: `10.1103/PhysRevB.103.155405`.

[8] S.-H. Phark, H. T. Bui, W.-H. Seo, Y. Liu, V. Sheina, C. Lee, C. Wolf, A. J. Heinrich, R. Robles and N. Lorente. 'Spin-State Engineering of Single Titanium Adsorbates on Ultrathin Magnesium Oxide'. In: (2025). arXiv: `2507.23299v1`.

[9] K. Yang, S. H. Phark, Y. Bae, T. Esat, P. Willke, A. Ardavan, A. J. Heinrich and C. P. Lutz. 'Probing resonating valence bond states in artificial quantum magnets - SuppMat'. In: *Nature Communications* 12.1 (2021), pp. 1–18. ISSN: 20411723. DOI: `10.1038/s41467-021-21274-5`.

[10] L. M. Veldman, L. Farinacci, R. Rejali, R. Broekhoven, J. Gobeil, D. Coffey, M. Ternes and A. F. Otte. 'Free coherent evolution of a coupled atomic spin system initialized by electron scattering'. In: *Science* 372.6545 (2021), pp. 964–968. ISSN: 0036-8075. DOI: `10.1126/science.abg8223`.

[11] H. Wang, P. Fan, J. Chen, L. Jiang, H. J. Gao, J. L. Lado and K. Yang. 'Construction of topological quantum magnets from atomic spins on surfaces'. In: *Nature Nanotechnology* 19.12 (2024), pp. 1782–1788. ISSN: 17483395. DOI: `10.1038/s41565-024-01775-2`.

[12] L. Arnhold. 'Surface-governed dynamics of atomic-scale magnetic moments'. PhD thesis. University of Stuttgart, 2024. DOI: `10.18419/opus-15626`.

[13] D. Sostina, L. Arnhold, L. M. Veldman, N. Betz, W. Wernsdorfer, S. Baumann, F. Delgado, P. Willke and S. Loth. 'Tuning the orbital state of a single spin on a surface'. In: *Forthcoming* ().

[14] S. Baumann, F. Donati, S. Stepanow, S. Rusponi, W. Paul, S. Gangopadhyay, I. G. Rau, G. E. Pacchioni, L. Gragnaniello, M. Pivetta, J. Dreiser, C. Piamonteze, C. P. Lutz, R. M. Macfarlane, B. A. Jones, P. Gambardella, A. J. Heinrich and H. Brune. 'Origin of Perpendicular Magnetic Anisotropy and Large Orbital Moment in Fe Atoms on MgO'. In: *Physical Review Letters* 115.23 (2015), pp. 1–6. ISSN: 10797114. DOI: `10.1103/PhysRevLett.115.237202`.

[15] S. Loth, M. Etzkorn, C. P. Lutz, D. M. Eigler and A. J. Heinrich. 'Measurement of Fast Electron Spin Relaxation Times with Atomic Resolution'. In: *Science* 329.5999 (2010), pp. 1628–1630. ISSN: 0036-8075. DOI: `10.1126/science.1191688`.

[16] R. Wiesendanger. 'Spin mapping at the nanoscale and atomic scale'. In: *Reviews of Modern Physics* 81.4 (2009), pp. 1495–1550. ISSN: 15390756. DOI: `10.1103/RevModPhys.81.1495`.

[17] K. Yang, W. Paul, F. D. Natterer, J. L. Lado, Y. Bae, P. Willke, T. Choi, A. Ferrón, J. Fernández-Rossier, A. J. Heinrich and C. P. Lutz. 'Tuning the Exchange Bias on a Single Atom from 1 mT to 10 T'. In: *Physical Review Letters* 122.22 (2019), p. 227203. ISSN: 10797114. DOI: `10.1103/PhysRevLett.122.227203`.

[18] A. J. Heinrich, J. A. Gupta, C. P. Lutz and D. M. Eigler. 'Single-Atom Spin-Flip Spectroscopy'. In: *Science* 306.5695 (2004), pp. 466–469. ISSN: 0036-8075. DOI: `10.1126/science.1101077`.

[19] P. W. Anderson. 'Theory of localized magnetic states in metals'. In: *Journal of Applied Physics* 37.3 (1966), p. 1194. ISSN: 00218979. DOI: `10.1063/1.1708389`.

[20] M. Ternes. ‘Spin excitations and correlations in scanning tunneling spectroscopy’. In: *New Journal of Physics* 17.6 (2015). ISSN: 13672630. DOI: `10.1088/1367-2630/17/6/063016`.

[21] J. Reina-Gálvez, C. Wolf, F. Delgado and N. Lorente. ‘Cotunneling mechanism for all-electrical electron spin resonance of single adsorbed atoms’. In: *Physical Review B* 100.3 (2019), pp. 7–12. ISSN: 24699969. DOI: `10.1103/PhysRevB.100.035411`.

[22] J. Reina-Gálvez, C. Wolf and N. Lorente. ‘Many-body nonequilibrium effects in all-electric electron spin resonance’. In: *Physical Review B* 107.23 (2023). ISSN: 24699969. DOI: `10.1103/PhysRevB.107.235404`.

[23] J. R. Schrieffer and P. A. Wolff. ‘Relation between the Anderson and Kondo Hamiltonians’. In: *Physical Review* 149.2 (1966), pp. 491–492. ISSN: 0031-899X. DOI: `10.1103/PhysRev.149.491`.

[24] J. Kondo. ‘Resistance Minimum in Dilute Magnetic Alloys’. In: *Progress of Theoretical Physics* 32.1 (1964), pp. 37–49. ISSN: 0033-068X. DOI: `10.1143/ptp.32.37`.

[25] F. Delgado and J. Fernández-Rossier. ‘Spin decoherence of magnetic atoms on surfaces’. In: *Progress in Surface Science* 92.1 (2017), pp. 40–82. ISSN: 00796816. DOI: `10.1016/j.progsurf.2016.12.001`.

[26] S. Loth, K. Von Bergmann, M. Ternes, A. F. Otte, C. P. Lutz and A. J. Heinrich. ‘Controlling the state of quantum spins with electric currents’. In: *Nature Physics* 6.5 (2010), pp. 340–344. ISSN: 17452481. DOI: `10.1038/nphys1616`.

[27] L. Farinacci, L. M. Veldman, P. Willke and S. Otte. ‘Experimental Determination of a Single Atom Ground State Orbital through Hyperfine Anisotropy’. In: *Nano Letters* 22.21 (2022), pp. 8470–8474. ISSN: 1530-6984. DOI: `10.1021/acs.nanolett.2c02783`.

[28] E. Fermi. ‘Über die magnetischen Momente der Atomkerne’. In: *Zeitschrift für Physik* 60.5-6 (1930), pp. 320–333. ISSN: 1434-6001. DOI: `10.1007/BF01339933`.

[29] M. Bucher. ‘The electron inside the nucleus: An almost classical derivation of the isotropic hyperfine interaction’. In: *European Journal of Physics* 21.1 (2000), pp. 19–22. ISSN: 01430807. DOI: `10.1088/0143-0807/21/1/303`.

[30] K. Yang, W. Paul, S.-H. Phark, P. Willke, Y. Bae, T. Choi, T. Esat, A. Ardavan, A. J. Heinrich and C. P. Lutz. ‘Coherent spin manipulation of individual atoms on a surface’. In: *Science* 366.6464 (2019), pp. 509–512. ISSN: 0036-8075. DOI: `10.1126/science.aay6779`.

[31] A. Abragam and B. Bleaney. *Electron Paramagnetic Resonance of Transition Ions*. Oxford University Press, 1970, p. 726. ISBN: 9780199651528.

[32] T. S. Seifert, S. Kovarik, D. M. Juraschek, N. A. Spaldin, P. Gambardella and S. Stepanow. ‘Longitudinal and transverse electron paramagnetic resonance in a scanning tunneling microscope’. In: *Science Advances* 6.40 (2020), pp. 1–12. ISSN: 2375-2548. DOI: `10.1126/sciadv.abc5511`.

[33] C. R. Ast, P. Kot, M. Ismail, S. De-La-Peña, A. I. Fernández-Domínguez and J. C. Cuevas. 'Theory of electron spin resonance in scanning tunneling microscopy'. In: *Physical Review Research* 6.2 (2024), pp. 23–27. ISSN: 26431564. DOI: `10.1103/PhysRevResearch.6.023126`.

[34] J. L. Lado, A. Ferrón and J. Fernández-Rossier. 'Exchange mechanism for electron paramagnetic resonance of individual adatoms'. In: *Physical Review B* 96.20 (2017), pp. 1–6. ISSN: 24699969. DOI: `10.1103/PhysRevB.96.205420`.

[35] A. Ferrón, S. A. Rodríguez, S. S. Gómez, J. L. Lado and J. Fernández-Rossier. 'Single spin resonance driven by electric modulation of the g -factor anisotropy'. In: *Physical Review Research* 1.3 (2019), pp. 1–13. ISSN: 26431564. DOI: `10.1103/PhysRevResearch.1.033185`.

[36] Y. Wang, Y. Chen, H. T. Bui, C. Wolf, M. Haze, C. Mier, J. Kim, D.-J. Choi, C. P. Lutz, Y. Bae, S.-h. Phark and A. J. Heinrich. 'An atomic-scale multi-qubit platform'. In: *Science* 382.6666 (2023), pp. 87–92. ISSN: 0036-8075. DOI: `10.1126/science.ade5050`.

[37] A. M. Shakirov, A. N. Rubtsov and P. Ribeiro. 'Spin transfer torque induced paramagnetic resonance'. In: *Physical Review B* 99.5 (2019), pp. 1–7. ISSN: 24699969. DOI: `10.1103/PhysRevB.99.054434`.

[38] S. Kovarik, R. Schlitz, A. Vishwakarma, D. Ruckert, P. Gambardella and S. Stepanow. 'Spin torque–driven electron paramagnetic resonance of a single spin in a pentacene molecule'. In: *Science* 384.6702 (2024), pp. 1368–1373. ISSN: 0036-8075. DOI: `10.1126/science.adh4753`.

[39] P. Greule, W. Huang, M. Stark, K. H. Au-Yeung, J. Schwenk, J. Reina-Gálvez, C. Sürgers, W. Wernsdorfer, C. Wolf and P. Willke. 'Spin-Electric Control of Individual Molecules on Surfaces'. In: (2025). arXiv: `2507.13699`.

[40] J. Reina-Gálvez, M. Nachtigall, N. Lorente, J. Martinek and C. Wolf. 'Contrasting exchange-field and spin-transfer torque driving mechanisms in all-electric electron spin resonance'. In: (2025). arXiv: `2503.24046`.

[41] Y. Bae, K. Yang, P. Willke, T. Choi, A. J. Heinrich and C. P. Lutz. 'Enhanced quantum coherence in exchange coupled spins via singlet-triplet transitions - SuppMat'. In: *Science Advances* 4.11 (2018). ISSN: 23752548. DOI: `10.1126/sciadv.aau4159`.

[42] P. Willke, Y. Bae, K. Yang, J. L. Lado, A. Ferrón, T. Choi, A. Ardavan, J. Fernández-Rossier, A. J. Heinrich and C. P. Lutz. 'Hyperfine interaction of individual atoms on a surface'. In: *Science* 362.6412 (2018), pp. 336–339. ISSN: 0036-8075. DOI: `10.1126/science.aat7047`.

[43] K. Yang, P. Willke, Y. Bae, A. Ferrón, J. L. Lado, A. Ardavan, J. Fernández-Rossier, A. J. Heinrich and C. P. Lutz. 'Electrically controlled nuclear polarization of individual atoms'. In: *Nature Nanotechnology* 13.12 (2018), pp. 1120–1125. ISSN: 17483395. DOI: `10.1038/s41565-018-0296-7`.

[44] S. Kovarik, R. Robles, R. Schlitz, T. S. Seifert, N. Lorente, P. Gambardella and S. Stepanow. ‘Electron Paramagnetic Resonance of Alkali Metal Atoms and Dimers on Ultrathin MgO’. In: *Nano Letters* 22.10 (2022), pp. 4176–4181. ISSN: 1530-6984. DOI: 10.1021/acs.nanolett.2c00980.

[45] G. Czap, K. Noh, J. Velasco, R. M. Macfarlane, H. Brune and C. P. Lutz. ‘Direct Electrical Access to the Spin Manifolds of Individual Lanthanide Atoms’. In: *ACS Nano* 19.3 (2025), pp. 3705–3713. ISSN: 1936-0851. DOI: 10.1021/acsnano.4c14327.

[46] J. Kim, K. Noh, Y. Chen, F. Donati, A. J. Heinrich, C. Wolf and Y. Bae. ‘Anisotropic Hyperfine Interaction of Surface-Adsorbed Single Atoms’. In: *Nano Letters* 22.23 (2022), pp. 9766–9772. ISSN: 1530-6984. DOI: 10.1021/acs.nanolett.2c02782.

[47] J. Eills, D. Budker, S. Cavagnero, E. Y. Chekmenev, S. J. Elliott, S. Jannin, A. Lesage, J. Matysik, T. Meersmann, T. Prisner, J. A. Reimer, H. Yang and I. V. Koptyug. ‘Spin Hyperpolarization in Modern Magnetic Resonance’. In: *Chemical Reviews* 123.4 (2023), pp. 1417–1551. DOI: 10.1021/acs.chemrev.2c00534.

3

Interfacing an Arbitrary Waveform Generator with an STM

On a page torn from this book, I drew a waveform with my blood.

Pinegrove ('Waveform')

The advent of pump-probe lock-in contrast schemes in scanning tunneling microscopy (STM) has made it possible to probe sub-microsecond dynamics on surfaces at the atomic scale[1]. Together with the development of ESR-STM that uses RF voltages in the tunneling junction for coherent spin control, this has put a larger emphasis on voltage signal generation in the gigahertz frequency range in STM setups. As such, integrating an arbitrary waveform generator (AWG) to STM setups will inevitably be required for the ever more complex control and readout schemes used for experiments on atomic quantum systems. This chapter introduces multiple hardware configurations and considerations for interfacing the Keysight M8195A, an AWG model with a maximum sampling rate of 65 gigasamples per second, with an STM that has RF cabling to the tunneling junction. Furthermore, various experiment designs that use the AWG are discussed, together with complications due to the limitations of the AWG.

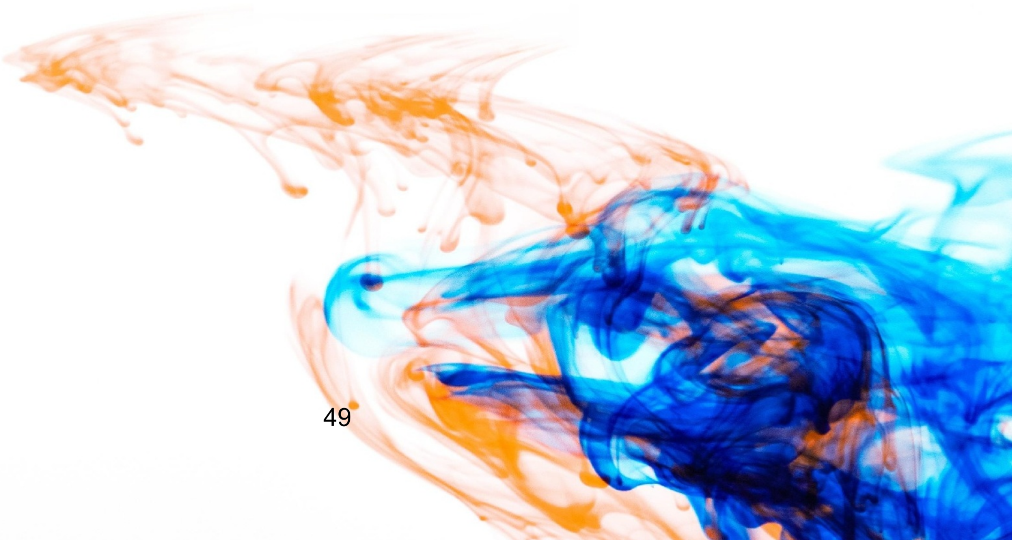

3.1. INTRODUCTION

Scanning tunnelling microscopy (STM) is generally perceived as a slow method. For instance, the piezoelectric motors are limited in movement speed, constraining the scanning speed for imaging. Ultimately, the tunnelling current is weak and requires amplification with a transimpedance amplifier, effectively a low pass filter in the kHz range, which limits the readout speed considerably. However, maybe surprisingly, this does not necessarily need to limit the timescale at which we can observe dynamics in the system under study. With so-called 'pump-probe' schemes, we can encode time-resolved signals into time-averaged measurements.

The fundamental idea is to initiate dynamics out of equilibrium at a short time scale (the 'pump') and probe only for a narrow window of time after a short interval. Neither pump nor probe pulses might be resolvable in time by the recorder in the experiment, but the time-averaged signal from the probe is different than the equilibrium signal. The trick is now to vary the time interval between the pump and the probe. The measured time-averaged signal as a function of the interval will contain information on the dynamics of the system between the pump and the probe. Interestingly, the pump-probe scheme moves the limits on time resolution from the readout to the signal generation of the pump and probe. There is a better time resolution if the probe covers only a short time interval and the time between pump and probe is controlled in smaller steps. Furthermore, the pump pulse needs to act on the system faster than the dynamics that you are trying to probe.

For our ESR-STM setup and the spin systems under study, both the controlling pumps and readout probes consist of voltage pulses to the tip. In our experiments, the readout signal is a current due to a voltage in the tunnelling junction. When using a spin-polarized tip, this current depends on the spin state of an atom under the tip (see chapter 2). Spin control can be achieved with spin scattering by applying DC pulses, or with electron spin resonance (ESR) by applying with radio frequency (RF) pulses. The time scales of spin dynamics under study are generally in the GHz range, while ESR requires RF voltages up to 14 GHz for our purposes. These time scales are set by Zeeman splitting from the external magnetic field and typical couplings between spins in the system.

While there are many (combinations of) instruments that can fulfil some of the roles outlined above, the most flexible option is an Arbitrary Waveform Generator (AWG) in the Super High Frequency (SHF, 3-30 GHz) range. AWGs can generate any voltage waveform shape within their sampling rate. As such, they can easily combine DC and RF pulses in the same experiment. In particular for RF pulses, an AWG also offers relatively straightforward control of multiple frequencies and their relative phases in experiments with multiple pulses, in comparison to other methods like gating of a RF source or (IQ) mixing the signal from continuous wave (CW) RF generators with a lower frequency AWG. These alternatives also generally have a limited bandwidth within one experiment and complicate the combination with DC pulses.

Following the demand from the high-speed data communication field and quantum computing applications, several AWGs with sampling rates in the tens of gigasamples per second (GSa/s) have become available on the commercial market over the last decade [2, 3]. Still, options remain limited to two manufactures for ESR-STM frequency ranges, where RF signals are required to exceed 10 GHz and at the same time, ideally, the available frequency range should go down to DC to generate DC pulses without causing offsets (see section 3.3.1 for a discussion on that offset). Most suppliers that focus on the quantum computing scale-up industry (Qblox, Quantum Machines, Zurich Instruments, Liquid Instruments) do not offer suitable solutions, because their products have too limited bandwidth without involving multiple channels (typically 0-400 MHz, potentially upconverted within a 2-18 GHz range). Only the Tektronix AWG7000 series and the Keysight AWG M8100 series offer the full flexibility of a sampling rate (50 GSa/s and 65 GSa/s, respectively) that is sufficiently high to generate all required voltage signals directly.

We decided on purchasing the Keysight AWG M8195A, which will be the AWG used throughout the rest of this thesis. The choice for the M8195A over the Tektronix model was based on the superior signal frequency range of 25 GHz with a single channel and the ability to switch to a 2-channel operation mode between experiments with each outputting 12.5 GHz maximum frequency. 12.5 GHz still mostly covers our preferred ESR operating range of 11.0-13.7 GHz for our ESR-STM setup. For Tektronix, the 2-channel option is a hardware choice that cannot be changed ‘on-the-fly’ via software.

This chapter will explore some of the technical nuances of using the Keysight M8195A AWG in the context of ESR-STM. First, we will discuss interfacing the AWG with other instruments, starting with a broader perspective on the lab setup and then focussing on RF electronics on the interface between the AWG and the STM cabling specifically. Following this, we will discuss typical experiment designs using the AWG sequencer and corresponding considerations for generating AWG waveform files in software. The discussed experiment design elements include lock-in contrast schemes, millisecond ESR probe pulses, and long-timescale periodic signals.

3.2. Interfacing the M8195A

The AWG signal output channels need to interface with the cabling to the STM tip at the tunnelling junction. At the same time, the AWG needs to interface with other instruments (lock-in amplifier, STM controller) and the measurement PC in the lab that coordinates all instruments, including the AWG. Since the AWG is a very flexible signal generator, there are multiple options depending on the goals of the experiment. On the other hand, the flexibility also results in added complexity and more stringent requirements on some of the interfaces.

3.2.1. Interfacing with the PC

One notable challenge is, in fact, the communication between the AWG and the measurement PC because of the large amount of waveform data that needs to be transferred. The AWG does not contain an on-board general purpose PC that can generate signal waveforms for experiments, so waveforms based on the experiment parameters need to be generated on the side of the measurement PC and then uploaded to the AWG. Considering that, firstly, the voltage needs to be specified for each sample in the waveform, secondly, the M8195A has a maximum sampling rate of 65 GSa/s, and, finally, some experiments require waveforms in the millisecond range per datapoint, the amount of digital waveform data that needs to be transferred in an experiment can easily reach tens of gigabytes (GB).

Setting aside some inputs in the chassis of the AWG (M9502A) that only control the fans, the AWG M8195A has two digital ports for communication with a PC: a USB-b mini input and a Gen 3 PCIe port in a Keysight-mandated connector format (Molex iPass PCIe x8). The former is straightforward and useful for quick setup and debugging purposes, but has an uploading speed that is too slow for the experiment conditions outlined above and, moreover, introduces significant noise in the AWG output channels when uploading. Therefore, the PCIe port is the more appropriate choice.

Keysight offers a PCIe cable (Y1202A) of the right connector format and data bandwidth (8 GB/s and a PCIe riser card (M9048B) as a host adapter that is compatible with the cable and can be inserted into the measurement PC motherboard. Unfortunately, this PCIe cable is only two meters long. This is a general limit for voltage-signal-based Gen 3 PCIe cables due to losses in the metallic wiring. This is a problem, because measurement PCs are typically positioned further than 2m away from a STM setup to avoid acoustic noise. Some setups, as will ours in the near future, are even enclosed in soundproof rooms with the experimenters sitting in a separate room.

PCIe communication over optical fibre cables does not suffer from significant loss on a length scale of meters and would thus be a suitable option. Keysight themselves recommends using an ‘active optical’ cable from the Samtec PCIEO-8G3 series, which offers distances up to 100m and has the conversion between electrical and optical signal built into the connectors. Unfortunately, this cable has long been out of production and only versions of 2m or shorter are available on the second-hand market.

Fortunately, PCIe over optical fibre is a standard solution for high-bandwidth servers, for example to connect graphics processing units (GPUs) separated in distance from a host PC, so other options are available. We opted for a solution from Adnacom (S31): a PCIe server circuit board from Adnacom (R34) connected to a riser card (H18) in the host PC via fibres with two parallel active-optical QFSP+ connectors. The Adnacom server is essentially an extension of the host PC motherboard where more PCIe riser cards can be inserted remotely. Here, we connect the original Keysight PCIe riser card that is compatible with 2m electrical PCIe cable and complete the connection to the AWG. The PCIe server is powered by an off-the-shelves fanless computer power supply. See fig. 3.1 for a schematic of the PC-AWG interface.

3.2.2. INTERFACING WITH THE LOCK-IN AMPLIFIER FOR CONTRAST MEASUREMENTS

The AWG also often needs to interface with readout instruments. For instance, a lock-in amplifier is used in many experiments to extract a signal from the tunnelling current at a better signal-to-noise ratio (SNR). On top of ESR-STM measurements outlined in chapter 2, pump-probe experiments also rely on measuring a time-averaged signal that differs from the equilibrium situation. Both thus lends themselves well to contrast

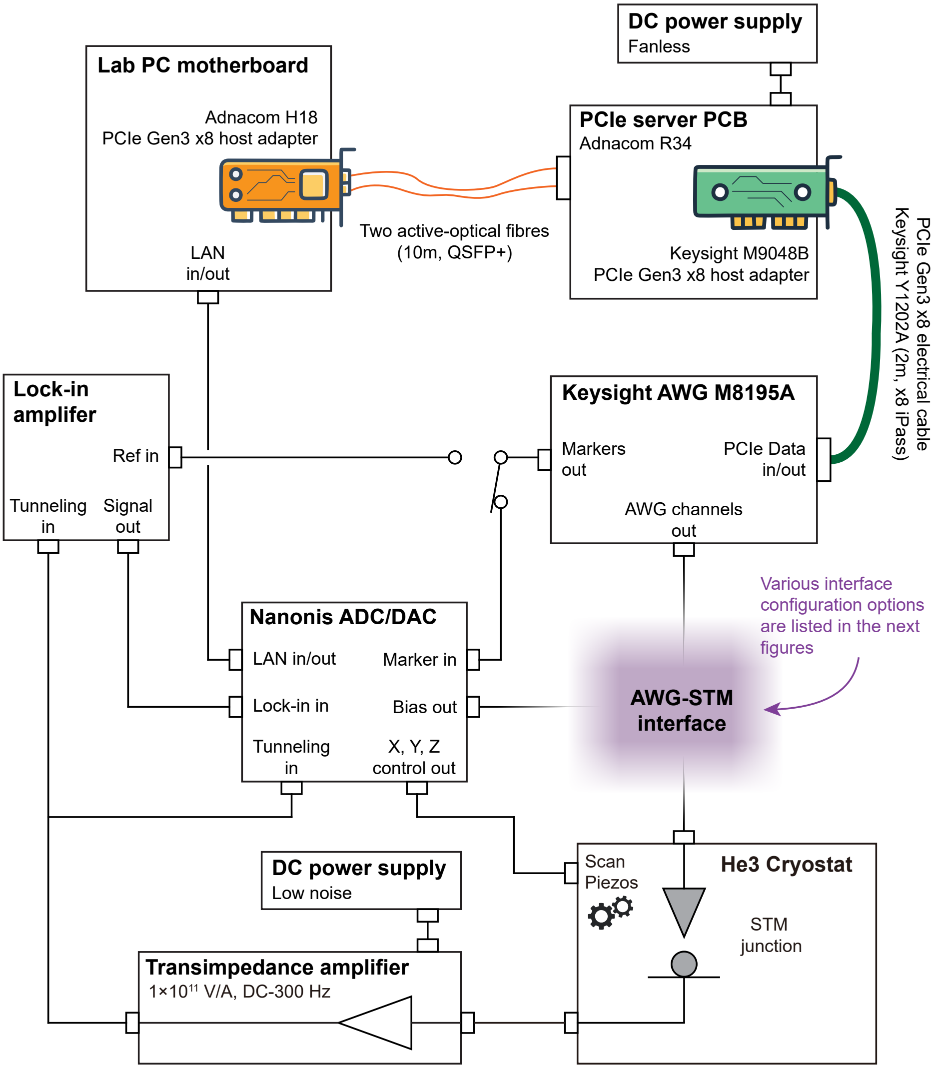

Fig. 3.1 | Overview of all AWG interfaces. Solid black lines are electrical connections. The transimpedance amplifier model is the NF corp. SA608F2, with its internal analog 300 Hz low-pass filter active and the NF corp. LP5393 as a low noise DC power supply. The lock-in amplifier used throughout this thesis is the Stanford Instruments SR830.

measurements that record the difference between two signals. A lock-in amplifier can be used to record a contrast signal by alternating between two generated signals (i.e. the pump-probe signal and the equilibrium) at the lock-in reference frequency, which results in an alternating measured current signal at the lock-in amplifier input. The lock-in amplifier only records the generated periodic signal at this reference frequency. All other frequencies, which contain unwanted noise, are rejected. This large reduction of the effective noise bandwidth results in a nominal improvement of the SNR in the lock-in contrast scheme compared to averaging the current signal directly from a time trace.

In a typical continuous-wave (CW) ESR-STM contrast measurement, the initial generated signal of the two is a DC bias, resulting in constant background current. The contrasting signal is the same DC bias, but now with an additional CW RF voltage. As explained in chapter 2, this adds an ESR current on top of the current background, which is what we want to measure via the contrast between the two generated signals. In a more general lock-in contrast measurement, the two generated voltage signals can be more complex to observe specific contrasts.

It will be the AWG that generates these two signals that define the contrast measurement. As such, the AWG needs to match the switching between its signal waveforms to the internally-defined lock-in frequency. This is typically set to a value on the order of 1 kHz because it needs to pass the transimpedance amplifier of the tunnelling current (we use 270 Hz). Alternatively, it is possible to set the frequency in the lock-in amplifier based on an external reference. Therefore, we also have the option to match the lock-in amplifier to the frequency that the AWG sets in its output.

In all of our lock-in experiments we opted for the latter, where the AWG controls the lock-in frequency and the lock-in amplifier (Stanford Instruments SR830) listens to the AWG for a reference to match this frequency. This is beneficial because, for various reasons (waveform granularity, easier waveform design; see section 3.4.3), the lock-in frequencies that the AWG can operate at are typically discrete on the 0.1 Hz scale, leading to some precise lock-in frequencies being hard to match from the AWG side.

The AWG uses one of its two marker channels to communicate the reference frequency to the lock-in amplifier. These marker channels have the same output sampling rate as the waveform outputs with samples synchronized across the board, but each marker sample can only either be positive or negative at one voltage amplitude (e.g. +0.5 V or -0.5 V), though this amplitude can be controlled per experiment. In the case of lock-in experiments, the marker signal is a square wave at the lock-in frequency: high during the first waveform signal and low in the second.

One of the AWG marker channels is sometimes also used in other experiments without a lock-in amplifier. In these cases, the AWG marker is recorded directly together with the tunnelling current signal by the Analog-to-Digital converter (ADC) from the Nanonis STM controller, to mark moments in a longer time trace. As the ADC sampling time is in the millisecond range, these schemes are only used to probe signal developments at longer time scales (see section 3.4.5).

3.3. THE INTERFACE BETWEEN THE AWG AND STM

The most important interface is between the AWG signal output channels and the electrical cabling to the STM tip. This involves combining either one or two AWG channels with the DC bias that is needed for tunnelling. The considerations here are not always trivial, since RF voltage signals require specialized components. Furthermore, the STM setup demands low electrical noise and also low vibrational coupling at this interface. Different configurations of the electronic circuit with the AWG have been used for the various experiments in this thesis. These configurations are outlined in figs. 3.2 to 3.4.

One of the main limitations of the AWG compared to other RF signal sources is the low maximum voltage output amplitude of only 1 V (single ended, zero-to-peak). Combined with the ~20 dB losses at 12 GHz in the STM setup cabling (see chapter 5), there is a maximum of only about 10 mV RF amplitude in the junction. This can technically be enough for ESR-STM, but more amplitude would be required for more complicated experiments. It is therefore key to minimize RF losses at the interface, for example in the cables. This is at odds with the requirement of low mechanical coupling to the anti-vibration table, since rigid RF cables have the lowest transmission losses. Therefore, we opt for semi-rigid cables that add ~1 dB loss total, which additionally add flexibility to the circuit design. Furthermore, the AWG is positioned close to the STM table, so less than a meter of room-temperature RF cabling is needed. This helps minimizing the loss, but also adds to the vibrational noise via sound due to the closer proximity of the cooling fans of the AWG to the setup.

3.3.1. BASIC SINGLE-CHANNEL CIRCUITS

The core element of the AWG-STM electronic interface is the bias tee, which combines the DC voltage from the Nanonis STM controller with the high frequency AWG signal. The RF cabling requires 50 Ohm impedance matching throughout the system to avoid losses in reflections and standing waves, while the DC source is not impedance matched to GHz frequencies. The bias tee provides the impedance matching for the DC side and also prevents a DC load on the AWG channel output. The latter should not be a problem regardless for the biases that we use in experiment (below 0.2 V) [cite/footnote: private communication, Keysight Technologies, Inc.]. The AWG-STM interface configuration with the bias tee is shown in fig. 3.2a.

Because the AC input of the bias tee is effectively a high-pass filter, connecting the AWG channel output to this bias tee input does block transmission of signals from the AWG at 10 kHz or slower. This prevents DC probe pulses at the timescale of the Nanonis ADC samples. Furthermore, it causes a DC offset from the intended bias if there is a non-zero time-averaged voltage. This is commonly the case when using DC pulses in pump-probe experiments with lock-in contrast schemes and happens even if the pulses themselves are at the nanosecond timescale. This offset can be hard to compensate for in practice and varies between or even during experiments as the pulses in the waveforms change to contain different time-averaged voltages. So, while the bias tee works great for combining DC bias with AC signals (which have no DC component) in ESR-STM experiments, another option needs to be found for DC pump-probe.

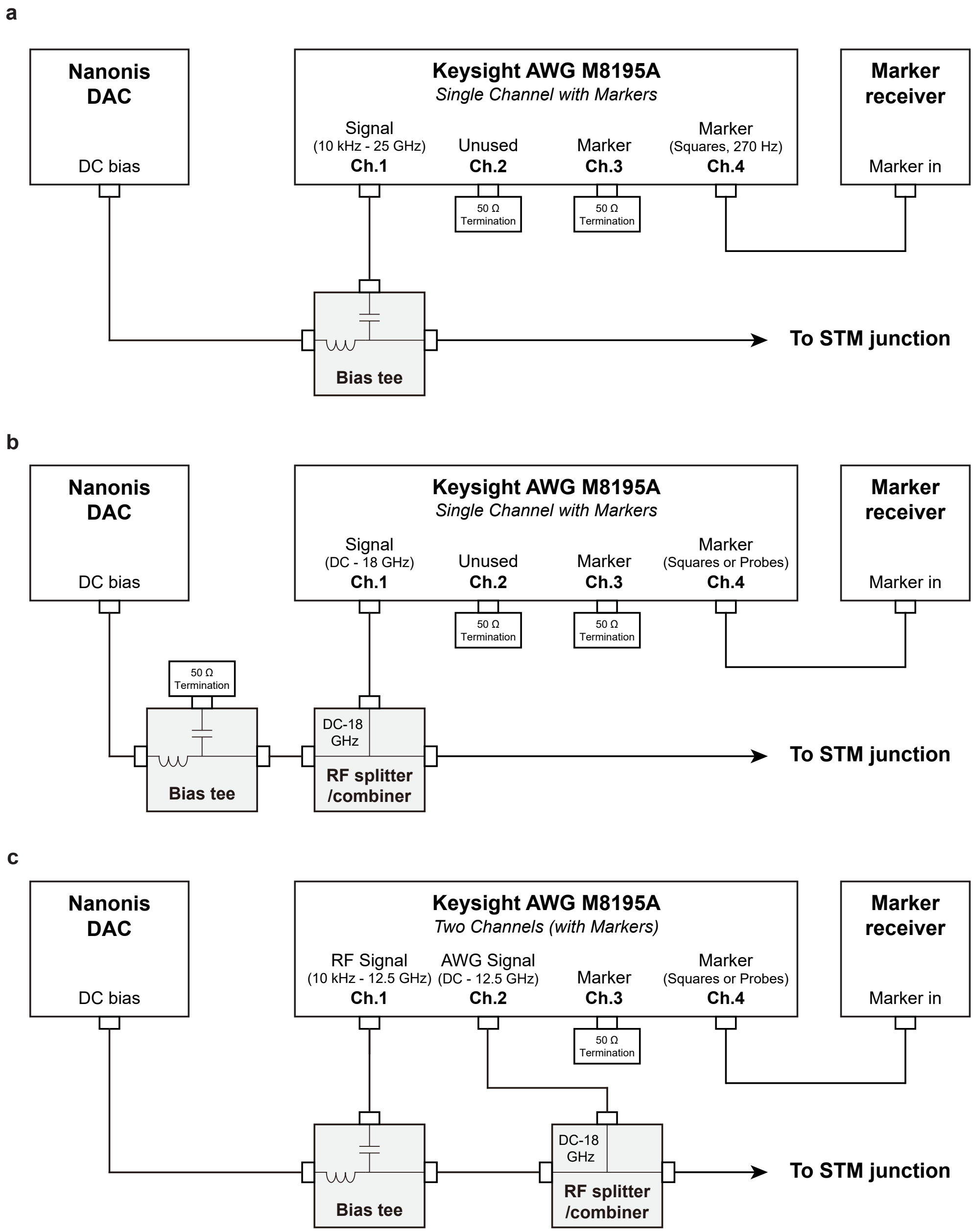

Fig. 3.2 | AWG-STM electronic interface configurations for basic circuits. **a** Single channel configuration through the bias tee (Tektronix PSPL5542) for RF signals. **b** Single channel configuration with a RF combiner/splitter (Minicircuit ZFRSC-183-S+) to include DC components from the AWG signal. **c** Dual channel configuration with AWG signals entering through both a bias tee and a RF combiner/splitter.

The simple solution applied here, shown in fig. 3.2b, is to use a passive non-isolated RF combiner/splitter. These offer transmission from DC up to limited GHz ranges (18 GHz for our model, which is especially high). A voltage input signal at any of the three ports is shared equally over the other two. There is no directionality among all three ports, hence the dual name for splitting and combining. (Note, however, that one port is calibrated to be the combined side with optimalization for equal signal division to the others with higher precision). This non-directionality is also a downside when combining signals, because the inputs are not 'isolated'. Half of the signal does not go to the combined port, but instead towards the other input side that you want to combine with. In other words, half of the input signal amplitude does not go to the STM tip and is lost. This includes the DC bias, which is halved and must be compensated for. Furthermore, the other signal input side in the circuit must deal with the load caused by the leaking signal. Since all AWG channel outputs are 50 Ohm matched within certain limitations, we don't expect RF reflections. As mentioned above, our experiments should operate within a voltage range where this holds and we don't have to worry about that here.

We also need to make sure we avoid reflections in the RF combiner branch with the DC bias line from Nanonis. Here, we use a bias tee as a choke with an inductor to block RF signal from entering the DC bias line, of which the coaxial cable is not 50-Ohm-matched up to the required RF frequencies. This bias line would otherwise act as an unmatched side branch of the main RF circuit and this results in (additional) standing waves in the voltage amplitude transfer function to the STM junction. The RF input of the bias tee is terminated with 50 Ohm to prevent standing waves in the short wire branch from the choke to the RF combiner that remains.

Another practical issue needs to be accounted for when using the RF combiner: we have observed that the AWG channels unfortunately apply a DC offset themselves (single-ended). This offset is in the range of a few millivolts, depending on the channel. The AWG DC bias would be blocked when connected through an AC-coupled element like the bias tee, but through the RF combiner it reaches the STM junction. Fortunately, this bias can easily be compensated for, at least compared to forgoing the RF combiner, by for example using the Nanonis bias output, because the offset is independent from the waveform playing. Though, the AWG offset voltage value is different between when the AWG channel is 'disabled', 'enabled and not running', or 'enabled and running'. Furthermore, for unknown reasons, the first sequence in the AWG sequencing table (see section 3.4.2) also has a different offset. Anecdotally, the AWG bias offsets drifts on the order of a millivolt for the first minutes of running the AWG after a few hours of not running. This might be related to the temperature of the internal AWG electronics.

Yet another practical note: enabling or disabling one of the AWG channels generates a milliseconds-long voltage pulse from the target channel with an amplitude on the order of a few volts. Again, this reaches the STM junction when the channel is connected through the RF combiner. A voltage pulse of this magnitude can move adatoms when the STM tip is positioned above it in tunnelling range, so care must be taken, but the pulse is inconsequential when the tip is withdrawn.

3.3.2. BASIC TWO-CHANNEL CIRCUIT

The RF combiner also comes into play for circuit configurations using two AWG output channels at the same time. This can be advantageous for increasing the RF amplitude when combining DC and RF, as they would not have to share the limited voltage range of a single channel, while still maintaining a strict timing between samples. However, it comes at the cost of halving the AWG sampling rate per channel, because the total internal sampling rate that was dedicated to one channel is now divided over two, thus the maximum signal frequency is 12.5 GHz.

At the AWG-STM interface, we need to combine both of the two channels and the Nanonis DC. As long as one of the two AWG channels will exclusively generate RF signals, this channel can be connected through the AC input of the bias tee. The Nanonis bias output enters again through the bias tee and the bias tee is then connected to one inputs of the RF combiner. The other AWG channel connects to the other input of the RF combiner, which is thus available to send both DC bias, DC pulses, and RF signals. This configuration is shown in fig. 3.2c.

3.3.3. ACTIVE RF AMPLIFICATION

Another approach to increase the amplitude of RF signals is active amplification. When choosing a commercial RF amplifier, there are trade-offs between amplification gain, input power range, frequency bandwidth, and electronic noise. The amplification should in principle be maximized within the range of acceptable values for the other parameters. The input power range is fixed and set by the AWG itself. The bandwidth should cover as much as possible of the AWG signal output range. However, there are limited options for a broad band of 25 GHz, in particular when including the lower frequencies. Fortunately, the lowest frequencies <2 GHz typically don't need amplification, as the losses in the STM cabling are small in this range (see chapter 5).

The limits for the electronic noise from the AWG for our STM system was one of the open questions. While the total integrated noise from the amplification on the tunnelling current would most likely be neglectable, the effects of RF noise on spin coherence in ESR-STM, for example, are unclear. The so-called 'noise figure', the fraction of degradation in SNR after the electronic element, is typically a strong trade-off with amplification power. In the end, we kept on the safe side and aimed for low noise with medium amplification. We settled on the RF Lambda's R01G24GSM, with a gain between 13.5 and 15 dB and a noise figure between 2.5 and 5.5 dB, both depending on the input frequency in a bandwidth of 1 to 24 GHz.

Since the RF amplifier is an active element, it needs a DC power supply. Furthermore, the RF amplifier needs to dissipate significant heat. Considering this, the RF amplifier is mounted on a passive heat sink. This provided enough heat dissipation, since a cooling fans so close to the STM would not be an option. The heat sink itself is mounted on the STM anti-vibration table together with integrated connector inputs for DC power. The RF amplifier can be inserted into any of the above circuit configurations. In particular, it is useful on the AWG channel through the bias tee when doing experiments with only RF pulses, either in a single channel configuration or with the second channel providing DC pulses and < 1 GHz RF signals via the RF combiner. These configurations are

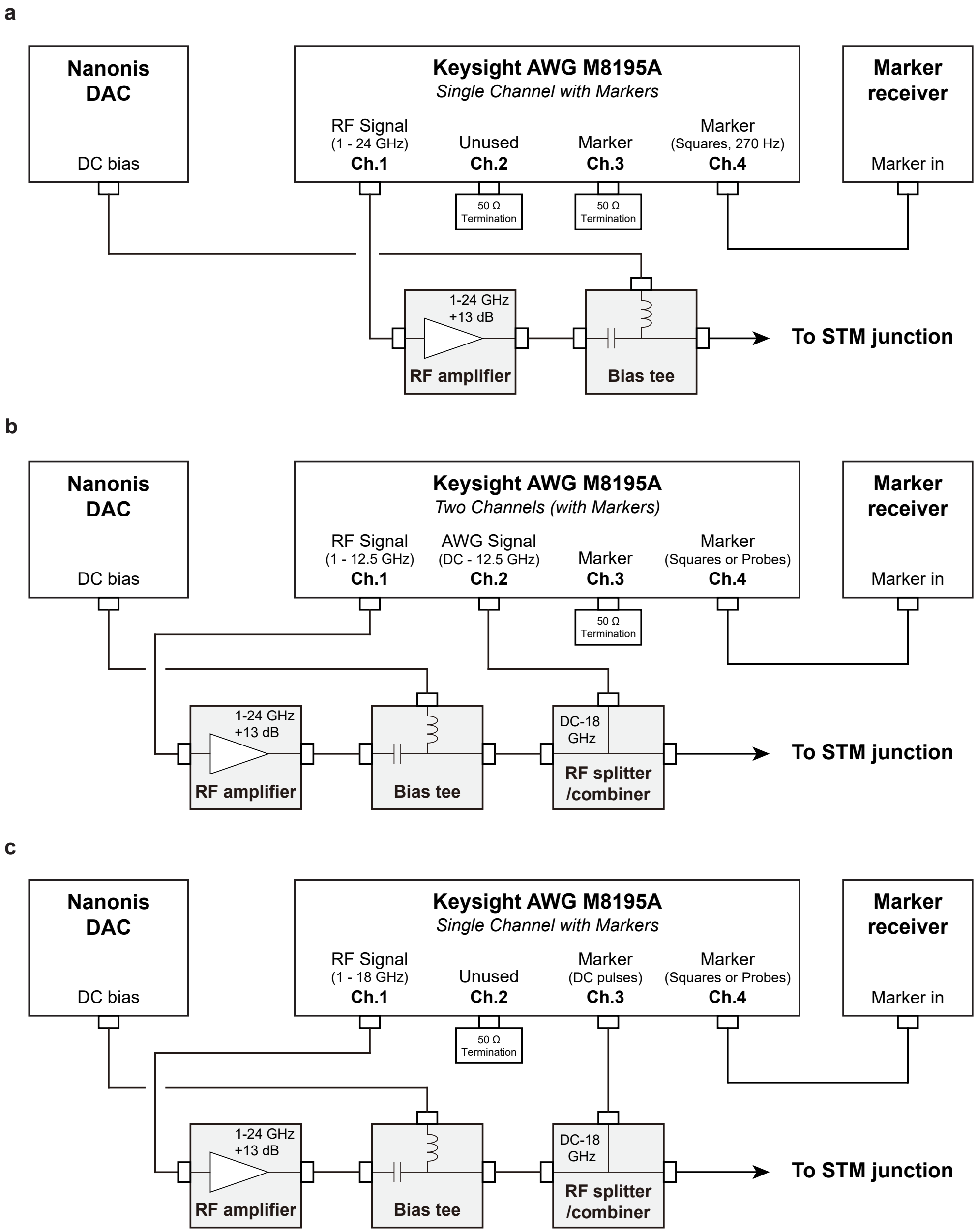

Fig. 3.3 | AWG-STM electronic interface configurations with a RF amplifier. a Single channel configuration through the RF amplifier (RF-Lambda R01G24GSM) and a bias tee. **b** Dual channel configuration with DC pulses entering through a RF combiner/splitter and amplified RF signals through the bias tee. **c** Single channel + marker configuration, analogous to (**b**), where instead the marker channel generates DC pulses. This allows for a higher available AWG sampling rate compared to (**b**).

showcased in fig. 3.3a, b.

One more configuration with the RF amplifier has been used in this thesis (fig. 6.8 in particular), which is shown in fig. 3.3c. This circuit uses two separate channels for DC pulses and RF, while still employing the maximal AWG sampling rate to reach 25 GHz in those signals: instead of using the two AWG output channels, which halves the sampling rate, we can operate in single channel mode with markers at the full sampling rate and use one of the two marker channels for DC pulses. These marker channels can send only a single set of high or low voltage levels in an experiment, but do so at the same full sampling rate as the single AWG channel. Furthermore, the marker voltage amplitude and offset bias are controllable, meaning the high and low marker levels can be set for one experiment. This is enough for square DC pulses, as long as the experiment only needs one DC pulse height. The single AWG output channel can then be operated for RF up to 25 GHz, potentially through the RF amplifier.

3.3.4. UNUSED CIRCUITS: DOUBLE BIAS TEES, AND IQ MIXING

There are two more AWG-STM interface configurations worth discussing, even if these haven't found practical applications for this thesis. One of these is a straightforward idea avoid a DC load on the AWG output channel from the Nanonis bias. As previously mentioned in section 3.3.1, these loads are negligible for most experiments. However, a circuit using two bias tees can be used to mitigate the load for experiments with a bias in the range of volts, which could affect or even damage the AWG output channel. Fig. 3.4a shows an example of this for a single channel circuit analogous in function to fig. 3.2a.

Since the bias tee is a passive device, like the non-isolated RF combiner/splitter discussed before, it can also be used with the roles of input and output reversed. An AWG output signal containing RF and DC components can be separated into these components by inputting the AWG signal to the RF+DC port of a bias tee. The DC component can then go through a one-directional diode before being combined with the Nanonis bias. The total DC signal can then be combined again with the RF component of the AWG signal with a second bias tee that functions as in circuits discussed before.[1]

The second unused interface configuration involves an RF mixer, which is shown in fig. 3.4b. Mixers can be used to 'multiply' voltage signals. This, in turn, can be used to upconvert a low-frequency signal to higher RF by multiplying the signal with a simple constant sine wave around these much higher radio frequencies. The low frequency signal is typically referred to as the 'intermediate frequency' (IF) and this constant sine wave is known as the local oscillator. In the context of our AWG, this means we could use a mixer to move the complicated AWG waveform signal below 25 GHz to any RF range where we have enough transmission in the STM cable.

Simple mixers create a so-called 'image' in the RF sideband when upconverting that appear at the difference between the AWG signal frequency and the local oscillator frequency, apart from the desired sideband at the sum of frequencies. Since we generally only want to drive the ESR at a single frequency, we need to filter out this image sideband. This can be achieved without a band filter circuit, which would both be inflexible in choice of frequency and physically heavy on the anti-vibration table,

---

[1] Special thanks to Nicolaj Bets for our discussion about this circuit design

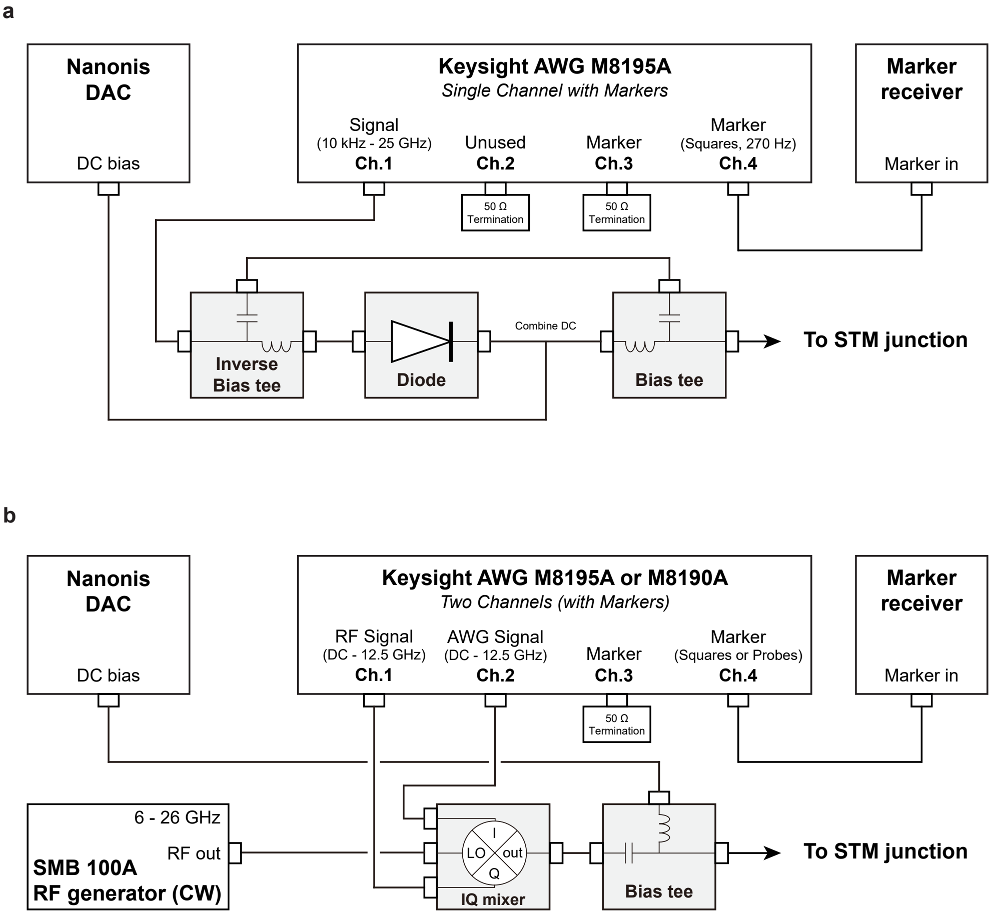

Fig. 3.4 | AWG-STM electronic interface configurations two unused circuits. a Configuration with two bias tees and a diode that prevents a voltage load on the AWG ouput channel generated by the Nanonis DAC. **b** Configuration with an IQ mixer to modulate the RF signal from a continuous-wave (CW) RF generator, which could potentially upscale the signal frequency outside of the range of the AWG.

by using a single sideband (SSB) mixer. An SSB mixer employs a second mixer to simultaneously upconvert a 90 deg-shifted duplicate of the IF signal with a 90 deg-shifted duplicate of the local oscillator. Combining this with the original upconverted signal cancels out the image sidebands created from both because of a 180 deg phase difference, while the intended sidebands adds constructively.

An SSB mixer thus consists of two mixers and two hybrid couplers, which is a piece of hardware to divide an input voltage signal into 90 deg-shifted duplicates. However, for a practical implementation of an SSB mixer, the hybrid coupler for the signal is typically not present, leaving the inputs of the two mixers as two free inputs: the one in-phase with the local oscillator (I) and the one in quadrature (Q). This configuration is called the IQ mixer.

An IQ mixer functions as a SSB mixer if the I and Q inputs are 90-deg-shifted duplicates of the intended IF signal from the beginning. This is of course an option if both IF signals are generated with the two channels of our AWG. Using an IQ mixer instead of a hardwired SSB mixer can result in even better sideband rejection because of the option to calibrate the shift around the intended 90 deg to correct for hardware imperfections in the balance [4].

The resulting interface configuration with an IQ mixer is shown in fig. 3.4b. An RF generator up to 40 GHz, Rhode & Schwarz's SMB 100A, is already present in our lab to act as the local oscillator. IQ mixers at this range do exist (MMIQ-1040), so this could extend our AWG range. Options above 40 GHz, however, come with other limitations.

An important parameter for IQ mixers is the frequency range of the I and the Q ports. This IF input range sets the available bandwidth in an experiment around the local oscillator frequency. This range must be large enough to cover the physics system under study. In our case, we must consider how far apart resonances are in frequency that we want to drive in the same experiment. These typically consists of exchange-coupled electron spins, or are different hyperfine resonances. These transitions are separated by 100's of MHz, or in some cases a few GHz[5]. As such, the IF range around 5 GHz is ideal.

The IQ mixer interface configuration becomes especially useful when considering the applications in combination with AWG models that operate at lower sampling rates. For example, the Keysight M8190A (present in our lab) has a 12 GSa/s sampling rate, resulting in a max frequency output of 4.8 GHz. This can be extended to the same practical frequency range as the M8195A in combination with the Marki Microwave MMIQ-0626HS IQ mixer (also present in our lab), though with slower pulse risetimes.

3.4. WAVEFORM FILE GENERATION AND SEQUENCING

The AWG output sampling rate is too fast for live calculations of what sample voltage to send, so waveforms need to be uploaded to the AWG before running an experiment. We generate our waveforms on the lab PC and upload them to the AWG instrument via a LabVIEW API of the Keysight 'soft front' interface that communicates with the AWG. For simple waveforms, the waveform can be generated in LabVIEW internally. However, often, we generate a set of waveforms in Python and save those as a collection of waveform files in a directory that corresponds to a complete experiment. Our home-build

Python library for AWG waveform generation can be more modular than LabVIEW code and integrates much better in our GitLab development environment. LabVIEW, on the other hand, excels in providing a live user interface that aids in the process of experimentation. Furthermore, LabVIEW interfaces well with SPECS' Nanonis, which is written in LabVIEW, too.

3.4.1. KEYSIGHT M8195A WAVEFORM PROPERTIES

An AWG waveform is, in essence, an array of voltage values. For the M8195A, each sample value in the array is actually defined as a fraction (-1 to +1) of the AWG channel output voltage amplitude. This channel amplitude can be varied between 75 mV and 1 V in steps of 0.01 mV. As an example: a sample value of -0.5 ('in-file amplitude') with a channel amplitude of 800 mV would result in a single-ended voltage output of -400 mV for that sample. Note that the channel amplitude cannot be controlled quickly enough to change it during one datapoint.

Waveform arrays for the M8195A have to conform to a set of requirements or limits. For instance, the AWG voltage output is 8-bit, which limits the voltage resolution. The -1 to +1 fractions are mapped to the signed integer range -127 to +127 (the +128 value stays unused to keep the waveform resolution symmetric under a sign-change). This corresponds to a voltage resolution of ~7.87 mV when using the maximum AWG channel amplitude of 1 V. A complicated interpolation scheme could be devised to optimize the generated output for the intended ideal waveform, but for most applications a rounding down suffices and this is what we have done for all waveforms used for this thesis.

In a waveform file, this signal byte is combined with another 8-bit byte containing the marker information. Together, with little-endian byte ordering, they form one sample as a 16-bit word[6]. Sequential samples are then appended to the array in a normal order. This binary format is the native file format (.bin) for the M8195A in single channel mode. The native binary file format for the dual channel mode (.iqbin) appends two 16-bit words, one word per channel, with the two marker bytes in the two separate words each dedicated individually to a single marker channel. At the cost of significantly slower generation and uploading times, a human-readable .csv format can also be uploaded, both for one and two channels. This .csv format will then be converted internally.

Another limitation on the waveform arrays is a required granularity in the waveform sample length. The total amount of samples in one waveform file must be a multiple of 256 samples when using a single channel. In the dual channel mode, the granularity is 128 samples. At the maximum sampling rate of 65 GSa/s, 256 samples correspond to ~3.94 ns. On top of the waveform granularity, there is also a minimum waveform length of 1280 samples (20 ns at 64 GSa/s). There is a maximum waveform length, too. The total AWG memory for all loaded waveforms is limited to 2 GSa, for the standard M8195A version, so an individual waveform cannot exceed that length either. An extended 16 GSa memory purchase option is available, too, which we also had access to.

3.4.2. THE AWG SEQUENCING TABLE

A typical experiment in STM setups require signal generation for seconds, because the recorded STM current signal is recorded through a kHz transimpedance amplifier and often a lock-in amplifier with a seconds settling time. However, the 2 GSa AWG memory limit corresponds to a play time of only approximately 30 ms. To overcome limitations of this kind, the M8195A has the option to play a programmed sequence of waveforms. There are often repeating segments in an experiment, so memory can be conserved.

The M8195A sequencing table is a list of waveform segments, each corresponding to a waveform file that is played when the AWG reaches their table index. An example of an AWG sequencing table is shown in fig. 3.5. Multiple sequencing table indices can play the same waveform file for their segment, using the segment number as a ‘pointer’ into AWG memory. Each index is repeated a controlled number of times, then the AWG moves to the next index.

The way the AWG advances after all segment repeats are completed can be programmed according to a few options. The simplest option is an automatic advancement to the index next in the table. The other option is to jump back to an earlier index in the table, from where it will continue down the indices as normal. This results in a loop. All indices contained within one loop are collectively called a ‘sequence’ in the terminology of Keysight. A sequence cannot be nested within another sequence. Sequences also have an advancement mode. They can be repeated a number of times before moving on automatically, or they can repeat indefinitely until a trigger. In our setup, this conditional advancement is triggered by a software ping from the Lab PC, but this can also be a hardware trigger (the ‘event trigger’ input). Note that the entire sequence will finish before moving on after a trigger in the middle of the sequence.

Multiple of such programmed sequencing tables can be present in the AWG memory simultaneously. In the Keysight terminology, these are each called a ‘scenario’. In the context of this thesis, each loaded experiment corresponds to one scenario. However, conditional hardware triggers are available to jump between scenarios while running.

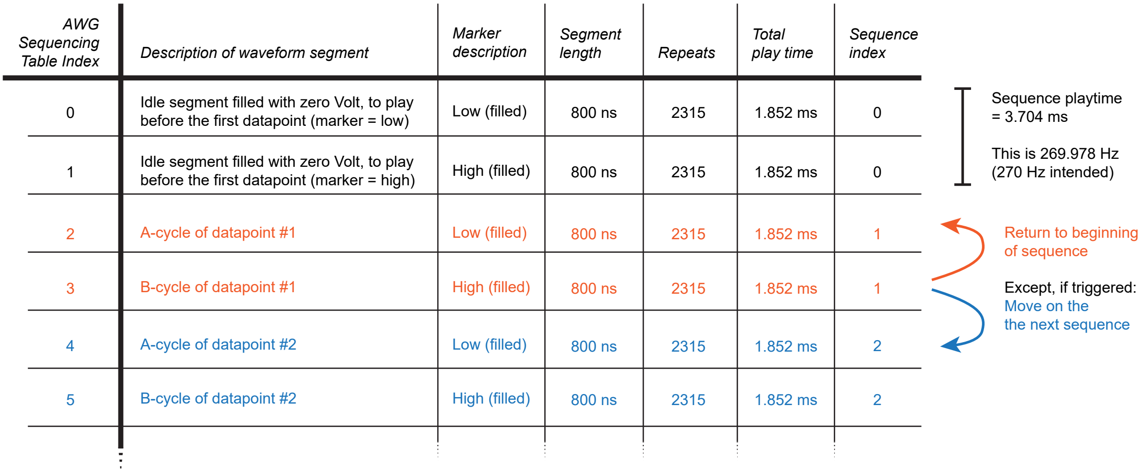

AWG Sequencing Table Index	*Description of waveform segment*	*Marker description*	*Segment length*	*Repeats*	*Total play time*	*Sequence index*
0	Idle segment filled with zero Volt, to play before the first datapoint (marker = low)	Low (filled)	800 ns	2315	1.852 ms	0
1	Idle segment filled with zero Volt, to play before the first datapoint (marker = high)	High (filled)	800 ns	2315	1.852 ms	0
2	A-cycle of datapoint #1	Low (filled)	800 ns	2315	1.852 ms	1
3	B-cycle of datapoint #1	High (filled)	800 ns	2315	1.852 ms	1
4	A-cycle of datapoint #2	Low (filled)	800 ns	2315	1.852 ms	2
5	B-cycle of datapoint #2	High (filled)	800 ns	2315	1.852 ms	2

Sequence playtime = 3.704 ms

This is 269.978 Hz (270 Hz intended)

Return to beginning of sequence

Except, if triggered: Move on the the next sequence

Fig. 3.5 | Example of an AWG sequencing table. In particular, this is an example scenario of a lock-in contrast scheme.

3.4.3. EXPERIMENT DESIGN WITH SEQUENCING: LOCK-IN SCHEMES

In some experiments, one datapoint consists of one waveform repeated many times. Electron spin dynamics under study are often contained within short waveforms of microsecond length, resulting in a large repetition rate within the required averaging times of seconds. In the sequencing table, each datapoint is then a simple sequence of only a single table index with its waveform segment that keeps repeating, advancing only to the next sequence with a software trigger after the averaging time has passed.

The lock-in contrast scheme is a common experiment with the AWG. In this scheme, there are two short waveforms per datapoint, A and B, both intended to result in a different time-averaged tunnelling current based on the physics under the STM tip. First, waveform A is repeated to cover half of a lock-in period. For a lock-in frequency of 270 Hz, half a period corresponds to 1.852 ms. After that, B is repeated until the second half of the period is covered, then back to repeating A in a cycle. The resulting low-passed current is a square wave at 270 Hz with the two levels corresponding to the time-averaged currents of A and B. The recorded lock-in signal is proportional to the difference between the A and B current levels. The A and B segments of a datapoint are loaded into the AWG table as one sequence with a conditional advancement mode. When triggered, the AWG moves on to the next sequence with a new set of alternating A and B segments to record the next datapoint.

The aforementioned sample granularity creates challenges when combining shorter waveform together in the sequencing table, like in the lock-in contrast scheme. For example, it is not trivial to build a perfectly continuous sine wave by repeating a short waveform containing a sine. The waveform length needs to be commensurate with both the period of the sine frequency and the 256 samples. With sine frequencies in the GHz range and MHz precision, this is often only possible for fairly long waveform lengths that are larger than the AWG waveform memory. Another option is to change the sampling rate, but that only works for one frequency, and there the sampling rate of the M8195A can only be controlled in steps of 25 MSa/s. More details on perfect periodic waveforms will be discussed in section 3.4.7.

The graduality is also an issue when trying to match a specific waveform play time, like a recording sampling rate. The ~3.9 nanoseconds mismatch per millisecond of repeated waveform length adds up over minutes in longer measurements, up to ~2 milliseconds per 10 minutes. While this mismatch is unavoidable, the more common practical issue of this type comes from the experiment design requiring a certain waveform length that is not commensurate with the intended playtime.

As a realistic example: in pump-probe contrast experiments we often choose a specific waveform length, say 800 ns exact, based on physics in the experiment or to set the repetition rate. But this waveform repeated many times must match an optimal lock-in frequency of 270 Hz. However, 4629 repeats yields 270.037 Hz, while 4630 repeats yields 269.978 Hz. Neither match 270 Hz exactly. It is important to adjust the actual frequency of the lock-in to avoid a drifting phase of the signal over seconds. The main reason we chose to set the lock-in frequency with the AWG marker channel as an external reference input (see fig. 3.1) is to fix this automatically.

A notable side-effect of using the AWG marker as a reference is a changing lock-in frequency in contrast experiments with varying waveform length. The chosen intended lock-in frequency is generally fixed because it is the optimal available low-noise point in the tunnelling current spectrum. The current noise in STMs does not meaningfully change with a shift of 37 mHz between the intended and actual lock-in frequency in the above example, but a waveform length change of 810 ns results in a lock-in frequency shift of 3 Hz with the same amount of waveform repeats.

Of course the lock-in frequency mismatch described above can be minimized in theory, at least to the fundamental 256 granularity. A dedicated empty waveform segment could be added in the datapoint sequence for both the A and the B cycle to complete . However, this leads to some overhead in the implementation. For example, this would mean any generated waveform directory can only be used for a dedicated lock-in frequency. Also, sometimes a very short waveform array would be needed below the 1280 sample minimum waveform limit, leading to AWG errors. This should be save-guarded against if this correction would be implemented in the future.

3.4.4. CONSIDERATIONS FOR LARGE WAVEFORM FILES

In rare cases, an experiment cannot be done with a repeating waveform segment. One signal waveform that covers the millisecond range individually might be needed per data point. This requirement is often related to continuously changing phase relations between sines over a full lock-in cycle (see, for example, chapter 5). These millisecond waveforms take up a digital size in the gigabytes range, which results in a number of issues.

Firstly, enough random excess memory (RAM) must be available on the PC that runs the script to generate the waveform array. Though this is typically not a fundamental limitation in modern PCs, the order of magnitude of the required RAM still has the potential to throttle PCs in a lab setting that run many processes and instruments in parallel. You have to keep it in mind before you start generating such large waveform segments.

Secondly, running the waveform generation script might take a significant amount of time: up to minutes per data point in Python code utilizing the ‘numpy’ module. This often adds up to a generation time much longer than the actual measurement time. A significant speed up can be achieved by optimizing Python, which is a scripting programming language, with modules like ‘numba’ that offer tools to compile functions before running. Still, compiled Python code generally does not result in a speed up for saving the waveform to a binary file, which might contribute to the bulk of the runtime. It simply takes time to move the gigabytes waveform data from the RAM to the hard drive. Furthermore, this waveform file then needs to be loaded into the RAM again later when uploading to the AWG using LabVIEW. Time could be saved by forgoing the saving to file and upload to the AWG directly while the waveform is still loaded in RAM. This is possible in our framework when we calculate the waveform in LabVIEW instead, though it comes at the cost of less modular code. As with Python, the LabVIEW code should be optimized by using compiled functions for waveform sample calculations. For LabVIEW, the best option is to load functions from .dll library files compiled from C++ code.

3.4.5. PROBING MILLISECOND DYNAMICS WITH ESR

ESR-STM can be utilized to sense changes in magnetization over time at the sub-nanometer scale by using an individual atomic electron spin that can be ESR-driven as a probe in close proximity to the magnetic object under study [7–11]. If the coupling between probe and magnetic object is stronger than the ESR linewidth, a change in magnetization causes an observable shift in the resonance frequency of the probe spin. Lock-in pump-probe contrast schemes have generally been used to observe the dynamics in the magnetization with ESR because the frequencies of spin dynamics are often faster than the limited bandwidth of the STM's transimpedance amplifier[7, 9].

An advantage of using a lock-in contrast scheme, in general, is the improved signal-to-noise ratio (SNR). However, the main limitation of this type of scheme is that it cannot probe time scales longer than the used lock-in period. Our lock-in amplifier (Stanford Instruments SR830) can go as low as 1 mHz. Nonetheless, the current noise in STM setups is generally larger around 1 Hz or lower compared to the previously-used 270 Hz, because of the larger vibration amplitude and electronic 1/f noise. Therefore, other methods than pump-probe contrast schemes should be explored for systems with timescales longer than milliseconds. An example of such a need arises from section 4.7, where a lock-in pump-probe contrast scheme is used to measure the lifetime of a nuclear spin via its hyperfine coupling to a Ti electron spin. Since no signal decay is observed within the time-scale limits of this method, the conclusion is drawn that the nuclear spin lifetime might indeed be longer than milliseconds

To probe longer time scales that fall within the amplifier bandwidth, the obvious option is to sample the current directly. One could simply continuously drive an ESR transition at a single frequency and monitor the tunnelling current directly to observe the ESR current contribution. The fastest available sampling rate of the ADC in the Nanonis V5e STM controller is 200 Hz, or 5 ms/sample, which is on par with the 300 Hz bandwidth of our transimpedance amplifier with the lowest noise. A sampling time of 20 ms, or multiples thereof, is a particularly optimal choice for SNR in direct current sampling, because this averages out the often-significant 50 Hz noise that originates from the national AC electricity grid (or 16.667 ms multiples for 60 Hz grids).

On the other hand, the changes we want to observe in the ESR current can be as small as femtoampere, so the SNR in the tunnelling current might not be good enough in some case. For a second option, then, the lock-in amplifier can be brought back in to probe the ESR current similarly as done for CW-ESR frequency sweeps, with a RF on/off contrast scheme at the high 270 Hz frequency. Then, opposed to a direct contrast schemes with a low lock-in frequency, this faster lock-in signal is monitored in time to observe the change on longer timescales [8, 10, 11].

This comes at the cost of time resolution compared to monitoring the current directly, because the lock-in requires a settling time to reject the noise. This settling time needs to be at least a few multiples of the used lock-in periods. Using the maximum lock-in frequency within the transimpedance amplifier of 300 Hz that corresponds to a lock-in period of 3.33 ms, we can use a maximum filter bandwidth equal to the lock-in frequency for the fastest possible settling time. For our lock-in instrument it takes five filter response times (inverse of the filter bandwidth) to settle at the final lock-in signal value[12]. This means the minimum settling time is five lock-in periods, totalling to 16.66

ms. The lock-in value must then also be recorded by the Nanonis ADC at a minimum sample time of 5 ms. The resulting fastest sampling rate of this lock-in monitoring method is therefore around 21.66 ms.

In practice, a more narrow lock-in filter bandwidth needs to be chosen to meaningfully outperform the SNR of direct current sampling, which always contains the integrated noise over the full bandwidth of the transimpedance amplifier. This requires longer settling times than 16.66 ms. Furthermore, the ESR current signal strength is halved with lock-in monitoring compared to direct current sampling because half of the RF signal generation time is spend with RF off. Overall, this means direct sampling of the current is the better option starting from 5 milliseconds up to some SNR breakeven point at a few tens of milliseconds. For time scales longer than that, lock-in monitoring will be the better choice.

The RF signal needed for direct sampling of continuous ESR driving could be generated with the AWG, but this can also be achieved with less complexity using continuous-wave RF generators. However, working within the bandwidth of the transimpedance amplifier also opens up a lot of other experimental options that are well-served by using the AWG. For example, one could sequentially probe different ESR transitions quickly, such as monitoring multiple nuclear spin projections using different hyperfine resonance frequencies. It is convenient to use one internally-timed instrument to perform those RF pulses at different frequencies.

3.4.6. ESR PROBE-PERTURB-PROBE EXPERIMENTS

Another large class of hypothetical experiments in the millisecond range would be of the type ’probe-perturb-probe’. At this time scale, the ‘perturb’ action could consist of, for instance, voltage pulses and variable waiting times, or even movements with the tip. Applying a DC bias or ESR driving could affect the system unintentionally in the perturbing section, which needs to be avoided, so the probe must be an actual pulse of RF and DC that should be timed with the sampling rate. The measurement protocol is illustrated in fig. 3.6a, with an example of an experimentally recorded time trace in fig. 3.6b.

In these types of experiments especially, it is useful to use the marker channel to record the timing of probe pulses. DC marker pulses can be send to an extra input channel of the Nanonis ADC and sampled simultaneously with the tunnelling current. This simplifies the data analysis of recorded time traces immensely. One important challenge with millisecond AWG probe pulses in Nanonis-recorded time traces comes from matching the AWG waveform playtime to the Nanonis ADC sampling rate. The issue is rooted in the limited waveform memory of the AWG. In order to reach the 20 ms ADC sampling rate, a shorter waveform segment needs to be repeated. However, it might not be possible to choose a waveform length that is perfectly commensurate with the Nanonis sampling rate. Even if this is just one AWG sample difference (~20 ps) per 1 µs waveform segment, this adds up to ~1 ms/minute of drift between the pulse timings and the Nanonis sampling. The misalignment in time between the probe signal and the sampling interval is illustrated by the schematic in fig. 3.6c. The drift over time of this desynch is shown experimentally in fig. 3.6d.

Desynching can lead to erroneous recorded pulses. In particular, certain oversampling

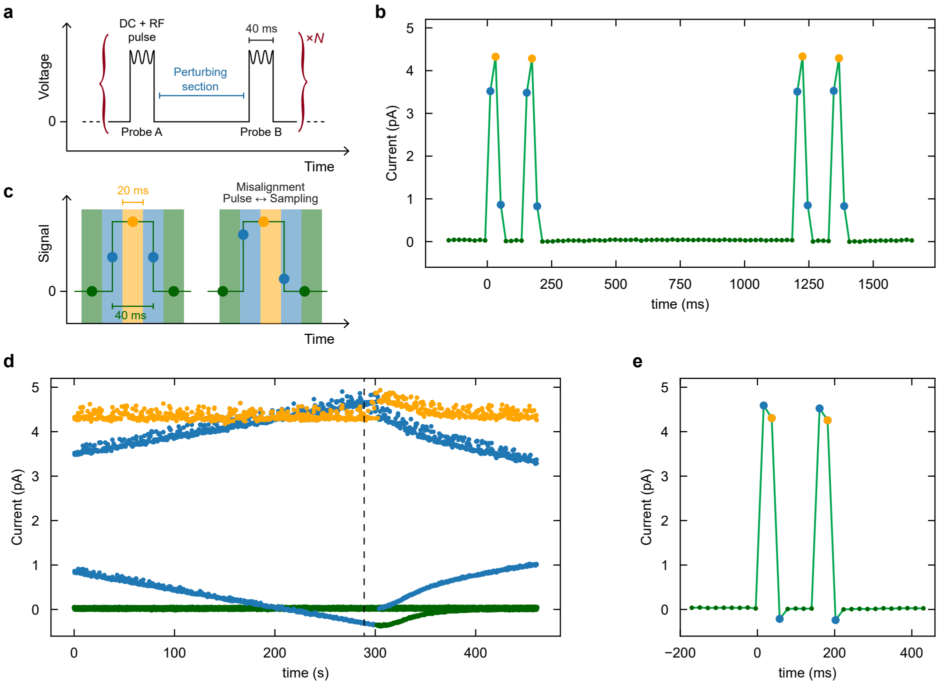

Fig. 3.6 | ESR Probe-Perturb-Probe measurements. a Schematic of the AWG voltage output for a probe-perturb-probe protocol with ESR probe pulses. **b** Experimentally recorded current time trace of two probe-perturb-probe events. The sample recorded at the centre of each probe are yellow, edge samples are blue, and background samples are green. **c** Schematic of the relative timing of the signal caused by a 40 ms AWG-generated probe pulse (green line), and the Nanonis ADC 20 ms sampling interval (vertical bars). The left shows a perfect alignment with the probe centre (yellow circle) at a sample centre, while right has a relative time shift between these that results in an asymmetry between edge samples. **d** A longer current time trace containing many probe events, such that the current levels of centre, edge, and background samples are visualized as bands in different colours. The sampling alignment shifts over time, resulting in a drift of the edge sample current levels. The current signal levels of all bands jump vertically at the 300 second mark, right where the probe pulse edges aligns with a sample interval edges. **e** Zoom-in on the probe event at the black dashed line in (**d**) showcasing the edge sample overshoot present in this recording.

data processing methods of ADCs result in non-linear overshooting of the sample value if there are large signal changes within a sample close to the edge of a sample period bin, like at the start and end of a probe pulse (see fig. 3.6e). Furthermore, components in the electronic circuit, like the STM's transimpedance amplifier and other effective lowpass filters, can introduce settling times on the order of the sampling interval, causing undershoots at pulse edges. This over/undershoot is also very dependent on jitter noise in the pulse timings, preventing post-data-processing solutions. The best solution is to choose a probe pulse width of at least one more sample than the Nanonis sampling rate (e.g. a 40 ms probe width at a 20 ms sampling rate). In this way, there is always a full sample in the middle of the probe pulse that is therefore unaffected by jitter. The pulse edges can then be discarded.

Unfortunately, this is not always enough to prevent edge-related effects on the probe centre sample signal, which can be observed in the time trace example shown in fig. 3.6d. When the sample interval edge approaches the probe centre, the edge sample overshoots the centre sample. Here, the centre sample level still stays unaffected. However, as this point is passed, both the centre samples and some of the background (only the samples adjacent to the edge after a pulse) jump to offset current levels. Note that the (originally higher current) left edge sample starts again at the low background current. The right edge jumps to a high level equal to the current level of the probe centre.

The left edge sample has essentially shifted to the right to become the new centre sample without containing any section of the edge anymore. However, the edge now seemingly does change this new centre sample current level as if the pulse current level is not quite settled yet. As such, this current level does not solely reflect the ESR current and thus this section of the time trace is unusable. Only after the sampling desynch drifts more and the centre sample is far enough removed from the pulse edge, does the centre sample current (and the current of the right pulse-adjacent background samples) return to the expected level. This leaves the remainder of the time trace usable again for analysis.

3.4.7. PERFECTLY PERIODIC AWG WAVEFORMS

As we have seen, many pulse schemes for experiments with the AWG require repetitions of short waveform segments, either for practical reasons (generation and uploading of waveforms would take longer than the experiment itself) or fundamental limits (limited total waveform memory). Often, we do not need to use waveforms of very specific lengths. For example, the CW sine waveform segment for ESR experiments only needs to be longer than the electron spin coherence time on the order of hundreds of nanoseconds. However, some experiments do require precise and specific waveform segments. One example would be coherent control of nuclear spins, which potentially could have millisecond coherence times. In this case, we need a waveform length that is exactly commensurate with the period of the NMR driving frequency, such that we can repeat the segment to reach milliseconds without causing decoherence with sudden phase jumps in the driving. These we define as ‘perfectly periodic’ waveforms.

The playtime of a perfectly periodic waveform must thus be a multiple of the periodicity of the intended signal. This playtime is set by the waveform length in samples and the AWG sampling rate. Both of these can be selected for an individual experiment, but need to conform to certain conditions. The waveform length needs to be a multiple of 256 samples with a minimum of 1280 samples, and the possible AWG sampling rates range from 53.775 GSa/s to 65 GSa/s in steps of 0.025 GSa/s.

The algorithmic approach to generating a perfectly periodic waveform is then to find the lowest common integer multiple between a 256 sample block and the number of (fractional) samples of one signal period for a given set of available sampling rates. We can select the sampling rate corresponding to the lowest resulting waveform sample length for the optimal use of AWG memory. A 1280 sample minimum can be enforced by repeating perfectly periodic sections smaller than 1280.

A lowest common multiple can be efficiently found numerically, for example using a build-in numpy function, with the caveat that such algoritms rely on integer inputs, while the number of samples in one signal period is in general a fraction. For the the purpose of common multiples, floats with finite decimals can be converted into integers by scaling up both the period and the 256 sample block by a few orders of magnitude. For a large number of decimals, corresponding to the amount of significant figures in the intended signal frequency, this approach runs into the limited integer byte size of a programming language. A standard numpy int64 has a maximum on the order of 10^{19}. In practice, while using this standard python infrastructure, this comes down to a frequency with 8 significant figures for our timescales.

The final limitation in periodicity is, in the end, the maximum waveform length in AWG memory of 2 GSa (16 GSa for the extended memory option). This corresponds to a maximum segment playtime of 30 ms (250 ms). Longer playtimes are needed to reach a commensurate length for more precisely defined signal period. A play time of 30 ms is not long enough to, for example, define a perfectly period waveform for a signal frequency of (13 GHz + 7 mHz): there is not enough time available for a mHz component to complete a full period where it can be commensurate with the GHz component. This can be overcome with a sampling rate that happens to be particularly commensurate with the signal frequency. However, our AWG cannot tune its sampling rate this finely.

For a sine wave in the MHz range, which is relevant for NMR, the maximum AWG memory ultimately sets our practical limit in how precise we can choose our frequency, such that perfectly periodicity is available at one of our possible AWG sampling rates for a 2 GSa memory, to steps on the order of 1 Hz (0.1 Hz for 16 GSa).

REFERENCES

[1] S. Loth, M. Etzkorn, C. P. Lutz, D. M. Eigler and A. J. Heinrich. ‘Measurement of Fast Electron Spin Relaxation Times with Atomic Resolution’. In: *Science* 329.5999 (2010), pp. 1628–1630. ISSN: 0036-8075. DOI: `10.1126/science.1191688`.

[2] Keysight Technologies inc. *M8100 series Arbitrary Waveform Generators*. URL: `https://www.keysight.com/nl/en/products/arbitrary-waveform-generators/m8100-series-arbitrary-waveform-generators.html` (visited on 26/10/2025).

[3] Tektronix Technology Systems LLC. *Tektronix AWG70000B Arbitrary Waveform Generators*. URL: `https://www.tek.com/en/products/arbitrary-waveform-generators/awg70000` (visited on 26/10/2025).

[4] D. Jorgesen and Marki Microwave. *IQ/IR/SSB Mixer Primer*. 2020. URL: `https://markimicrowave.com/technical-resources/white-papers/iq-ir-ssb-mixer-primer/` (visited on 26/10/2025).

[5] Y. Bae, K. Yang, P. Willke, T. Choi, A. J. Heinrich and C. P. Lutz. 'Enhanced quantum coherence in exchange coupled spins via singlet-triplet transitions - SuppMat'. In: *Science Advances* 4.11 (2018). ISSN: 23752548. DOI: `10.1126/sciadv.aau4159`.

[6] Keysight Technologies inc. *User's Guide Keysight M8195A Arbitrary Waveform Generator (Revision 2)*. 2019.

[7] Y. Wang, Y. Chen, H. T. Bui, C. Wolf, M. Haze, C. Mier, J. Kim, D.-J. Choi, C. P. Lutz, Y. Bae, S.-h. Phark and A. J. Heinrich. 'An atomic-scale multi-qubit platform'. In: *Science* 382.6666 (2023), pp. 87–92. ISSN: 0036-8075. DOI: `10.1126/science.ade5050`.

[8] W. Huang, K. H. Au-Yeung, P. Greule, M. Stark, C. Sürgers, W. Wernsdorfer, R. Robles, N. Lorente and P. Willke. 'An electrically controlled single-molecule spin switch'. In: *Nature Communications* 16.1 (2025), p. 8242. ISSN: 2041-1723. DOI: `10.1038/s41467-025-63574-0`.

[9] S. Reale, J. Hwang, J. Oh, H. Brune, A. J. Heinrich, F. Donati and Y. Bae. 'Electrically driven spin resonance of 4f electrons in a single atom on a surface'. In: *Nature Communications* 15.1 (2024), p. 5289. ISSN: 2041-1723. DOI: `10.1038/s41467-024-49447-y`.

[10] F. D. Natterer, K. Yang, W. Paul, P. Willke, T. Choi, T. Greber, A. J. Heinrich and C. P. Lutz. 'Reading and writing single-atom magnets'. In: *Nature* 543.7644 (2017), pp. 226–228. ISSN: 0028-0836. DOI: `10.1038/nature21371`.

[11] A. Singha, P. Willke, T. Bilgeri, X. Zhang, H. Brune, F. Donati, A. J. Heinrich and T. Choi. 'Engineering atomic-scale magnetic fields by dysprosium single atom magnets'. In: *Nature Communications* 12.1 (2021), p. 4179. ISSN: 2041-1723. DOI: `10.1038/s41467-021-24465-2`.

[12] Stanford Research Systems. *Model SR830 DSP Lock-in (Revision 2.5)*. 2011.

4

Time-resolved readout of spins in a STM with an AWG for signal generation

> *Think a new thought, they sometimes tell themselves. Think a new one, a completely fresh unthought one. But there are no new thoughts. There are just old thoughts born into new moments*
>
> Samantha Harvey ('Orbital')

The previous chapter has outlined some of the technical details in hardware and software for using the Keysight M8195A arbitrary waveform generator (AWG) in our STM setup. This chapter continues with its application in a variety of experiments on spin dynamics in adatoms on a surface. First, we test the capabilities of the AWG for DC pump probe experiments, and showcase a novel experiment to probe the dynamics of an individual nuclear spin with this STM technique. Next, we verify that the AWG can be used as an RF source for ESR-STM experiments, both in the continuous-wave (CW) limit and for coherent control with pulsed ESR. For the latter, we introduce a new pulse scheme to investigate the origin of slopes in the current signal as a function of pulse width, which is facilitated by the flexibility that the AWG provides. Lastly, we combine DC and RF pulses in a single experiment and use this to examine the lifetime of an individual nuclear spin. This leads to the preliminary conclusion that this lifetime might be longer than the microsecond time scale.

4.1. DC PUMP-PROBE

The Otte Lab has extensive experience with using DC pulses to incite dynamics in atomic spins [1]. Despite this, the DC pulse generator used in past experiments (Agilent 81110A) was somewhat limited. The minimum 10-90% rise time was 1.6 ns. Furthermore, only two types of pulses could be sent within one pulse train with freely chosen width and amplitude. Three or four pulses are also still possible at a cost of limited timing options and the requirement that only two pulse types are used overall. The AWG proved to extend the lab's capability to shorter timescales and to offer more flexibility in pulse train design for pump-probe contrast schemes.

The first test one can do to check whether square pulses arrive at the STM junction is a so-called 'pulse autocorrelation' measurement [2]. The idea, visualized in fig. 4.1a, b, is to do a sweep of the delay time τ_{delay} between two identical pulses, including the sections where the two voltage pulses overlap. With a linear IV-curve in the tunnelling junction, the measured current does not depend on the overlap of the two pulses: double the voltage is double the current, which is the same as just having two pulses without overlap. This changes with a non-linear IV-curve. In this case, double the voltage is not quite double the current, and so the section with overlap now has a different current level compared to separated pulses. The resulting time-averaged current then depends proportionally on the fraction of overlap, with a maximum when the two pulses fully overlap. For perfectly square pulses, the overlap increases linearly with the τ_{delay} to this maximum point. As such, the expected time-averaged current as a function of probe delay time has a triangular shape with a base of twice the pulse width.

In the experiment, the non-linear IV-curve is provided by a Ti adatom on the oxygen binding site, which was introduced in chapter 2. This adatom has large inelastic scattering steps in the density of states around positive and negative 80 mV, possibly of an orbital excitation origin [3]. In this case, we utilize the positive bias side because it is a more gradual step in the dI/dV (see fig. 4.1a). This allows for reaching this non-linear section of the IV curve with a variety of pulse heights in the junction, which could drop significantly for smaller pulse width due to the frequency-dependent losses. Furthermore, with a broad non-linearity, the autocorrelation signal also contains less binary information about the pulse height than with a sharp step in the IV. The latter only conveys whether a pulse did or did not reach the non-linearity threshold.

We connect the AWG via the RF combiner according to circuit fig. 3.2b for a lock-in contrast scheme and measure the autocorrelation signal for pulses with a width of 2 ns, which is shown in fig. 4.1c. Indeed, the result is an isosceles triangle with a base of 4 ns, confirming that the AWG and the STM cabling can achieve this time resolution without problems. Efforts to send shorter DC pulses are discussed in chapter 5.

4.2. ERRATIC CAPACITIVE SIGNAL IN LOCK-IN CONTRAST MEASUREMENTS

While using the AWG for lock-in contrast experiments, like the DC pulse autocorrelation described in the previous section, we observed a persistent erratic signal on top of the intended signal of a yet unknown origin that needs to be accounted for when interpreting experiments. The intended signal is present in the contrast between the A and B cycle, which is recorded by the lock-in amplifier from the component that is in-phase with the reference signal. This is often called the ‘resistive’ component, since the resistive contribution to a voltage transfer function introduces no phase shift. A lock-in amplifier can simultaneously separate the out-of-phase component from the input signal, which is called the ‘capacitive’ component, since a capacitor causes a 90 degree phase shift in a voltage sine signal.

For a lock-in contrast measurement, we expect to see no signal in the out-of-phase component because there should be no time-averaged contrast between the two 90-degrees-shifted cycles in the generated waveforms. The shifted cycle A* consists of the second half the in-phase A cycle and the first half of the in-phase B cycle, while B* consists of the second half of the B cycle and the first half of the A cycle. These shifted cycles A* and B* should result in an equivalent time-averaged current in the measurement protocol.

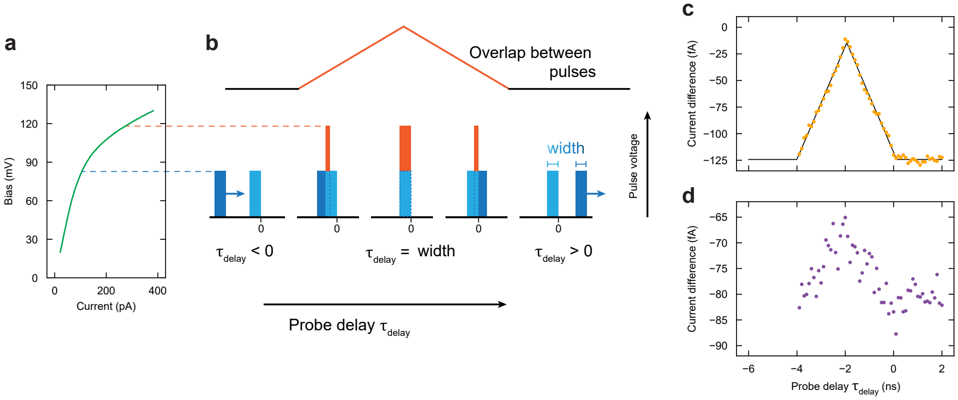

Fig. 4.1 | DC pump probe autocorrelation test. **a** IV curve of Ti on the oxygen binding site with positive bias. Tip height setpoint: 20 pA, 60 mV. **b** Schematic of DC pump-probe contrast measurement for lock-in cycle A. The used B-cycle is the same, but with opposite polarity. The delay time τ_{delay} is swept such that the probe overlaps with the pump. The sections with overlap (orange) have double the pulse voltage amplitude, reaching a non-linear part of the IV curve in (**a**). The upper part illustrates the dependence of the width of overlapped section on τ_{delay}: a triangle with the maximum at the negative of the pulse width. **c** The in-phase (resistive) current contrast between the A and B cycle as a function of τ_{delay}, detected with the lock-in amplifier. Tip height setpoint: 10 pA, 60 mV. The pulses were generated by the AWG with a width of 2 ns and an amplitude of 100 mV (halved to 50 mV by the RF combiner). The solid black line is a fit with an isosceles triangle. Here, the triangle amplitude, centre position, base width, and base offset were free fit parameters with the values [109 ± 1 fA], [-1.937 ± 0.009 ns], [4.13 ± 1 ns], and [124.3 ± 0.7 fA], respectively. **d** The out-of-phase (capacitive) current contrast between A and B cycle as a function of τ_{delay} in the same measurement as (**c**).

However, as is shown in fig. 4.1d, we do see a clear signal in the out-of-phase lock-in component in our DC pulse autocorrelation measurement. There is a triangle as a function of probe delay, similar to the in-phase signal, and also a significant offset. Furthermore, there are some features present from $\tau_{\text{delay}} = 0$ to 2 ns that do not conform to a triangle nor to a flat offset.

The triangle in the out-of-phase signal can be attributed to an imperfect phase calibration of the lock-in in the setup. Since the marker reference and the signal through the STM take a different route from the AWG to the lock-in amplifier, there is always some finite phase difference between the signal and the reference. This phase is fixed in the setup and can therefore be accounted for by changing the definition of the zero point of the phase in the lock-in instrument such that it corresponds to the resistive tunnelling signal. This calibration is always imperfect, however, which leads to some 'leakage' of the resistive signal to the recorded capacitive lock-in component, and vice versa.

Nevertheless, the offset observed in the in-phase signal in fig. 4.1c is not enough to account for the offset observed in the out-of-phase signal in fig. 4.1d, considering the low amplitude of the leaked triangle. This means that there is a source present that contributes specifically to the capacitive signal, even if the pulse scheme was intended to not produce any. Moreover, this capacitive source's signal depends non-trivially on the probe delay and thus, possibly indirectly, on the voltage generated by the AWG. This is problematic, because such a large out-of-phase signal can also leak into the in-phase channel with imperfect phase calibration and overshadow a weak resistive signal. In that case, it might be mistaken for the real resistive signal of the physics one wants to probe.

This capacitive signal contribution has also been observed in other lock-in contrast experiments with our AWG (see, for example, section 5.3), but it's origin has not been ascertained. Programming the contrast experiment with one waveform that covers the full lock-in period, instead of repeating small waveforms, suppresses the capacitive signal. This points to an issue in the AWG sequencer, although the waveforms look identical on an oscilloscope. We can confirm the AWG as the origin, because the out-of-phase offset is only present if the AWG is running. Furthermore, it remains even if the outputting AWG channel is disabled while the sequencer is running. This suggests a relation to the lock-in reference signal from the marker channel. However, adding the AWG output channel via a high-pass filter, such as the RF input of a bias tee in circuit configuration fig. 3.2a, does seem to suppress the offset, which does not support an origin in the marker channel alone. More investigations are needed to understand and ultimately prevent this erratic signal source.

For now, the best approach is to filter out the capacitive component with the lock-in amplifier in contrast experiments and only look at the resistive channel. This is already common practice in pump-probe experiments to eliminate the noise from capacitive sources. Here, the proper lock-in phase calibration is now also crucial to avoid an incorrect interpretation of weak resistive signals.

4.3. NUCLEAR-ELECTRON SPIN FLIP-FLOP DYNAMICS

An exciting opportunity to test the abilities of the AWG presented itself as part of a project to investigate nuclear spin dynamics. This project was led by Lukas Veldman and is published as Veldman *et al.*[4]. Its main results are described below.

As discussed in chapter 2, the ^{47}Ti isotope has finite nuclear spin $I = 5/2$ and a sizable hyperfine coupling in the MHz range. Therefore, the electron spin of the adatom hybridizes with the nuclear spin. In the regime of low external magnetic field, where the electron spin Zeeman splitting equals the energy difference between two nuclear spin projections from the hyperfine coupling, there are avoided level crossings at finite magnetic fields, where specific nuclear spin projections and the electron spin are maximally hybridized. At those points, in a simplified view, one of the excited eigenstate can be interpreted as a singlet-like superposition state.

The idea for the experiment is then to excite the nuclear spin to the appropriate nuclear spin subspace with the singlet-triplet eigenstates and project the electron spin with a voltage pulse. The projected spin-product state of the electron and nuclear spin is not a stationary eigenstate, and so the projection will incite flip-flop dynamics where the electron spin exchanges its angular moment back-and-forth with the nuclear spin. These dynamics can be observed as an oscillating magnetoresistance at the frequency of the coherent flip-flop as the electron spin projection evolves in time, which is measurable with a DC pump-probe contrast scheme. This scheme is similar to earlier experiments in our lab on coupled electron spins from two neighbouring Ti atoms [1].

In reality, the above view is complicated by the presence of the nuclear quadrupole moment, anisotropy of the hyperfine coupling, and a small, but significant amount of magnetic field in-plane while the spin quantization axis is out-of-plane. These introduce more avoided level crossings and results in some overlap between crossings as a function of external field, which are showcased in the energy diagram in fig. 4.2a. The dynamics are therefore not expected to be clean single-frequency oscillations at dedicated magnetic field setpoints.

Then there is the question how to polarize the nuclear spin and excite it to the appropriate subspace to initialize the flip-flop. Interestingly, it was found that a DC current can polarize the nuclear spin of an adatom under the an STM tip due to hybridization with the electron spin, mediated by the in-plane component of the hyperfine coupling. This was first shown for Cu [5], but we found that this polarization is very strong in ^{47}Ti and ^{49}Ti when adsorbed on the oxygen binding site [4] (see also section 2.13 for more information). This provided an ideal mechanism for the pump-probe experiment: we can use DC voltage pulses to pump the nuclear spin to an excited state.

The ground state is $|\downarrow,+5/2\rangle$, though all nuclear spin projections are about equally populated in the thermal equilibrium. We were able to initialize to $|\downarrow,-5/2\rangle$, which is not an eigenstate due to hybridization with $|\uparrow,-5/2\rangle$ from the small in-plane field originating from the STM spin-polarized tip apex, and hybridization with $|\downarrow,-3/2\rangle$ from the in-plane hyperfine coupling. The resulting dynamics for two different tip magnetic field strengths are shown in fig. 4.2. For the tip field strength used in fig. 4.2b, we find a complex free time evolution of the spin system involving three oscillation frequencies. Each frequency can be attributed to the energy splitting for the two avoided level crossings present at this tip field and their frequency sum. Most interestingly, this includes a coherent flip-flop between nuclear and electron spin degrees of freedom. We can also tune the tip field to have an isolated oscillation $|\downarrow,-5/2\rangle \leftrightarrow |\uparrow,-5/2\rangle$ at the edge of this broader avoided level crossing, with the resulting oscillations shown in fig. 4.2c. These are purely electron spin dynamics, but could not exist without the presence of the nuclear spin.

The free evolution oscillations die out quickly due to the short coherence time of the electron spin, which is limited by the short electron spin lifetime and (here mainly) magnetic field fluctuations from vibrations of the spin-polarized tip [3]. The coherence

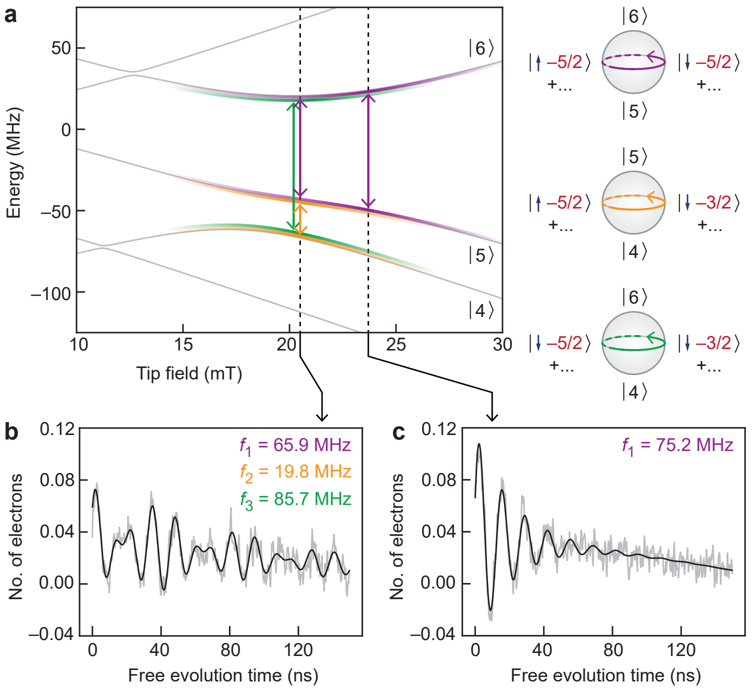

Fig. 4.2 | Coherent flip-flop dynamics between an electron spin and a nuclear spin. **a** Energy diagram of the atomic eigenstates as a function of tip-induced magnetic field (Zoom in of fig. 2.8, based on the Hamiltonian in eq. (2.10)). Two avoided crossings are coloured purple and yellow, with arrows indicating the corresponding energy splittings at the crossing points. Their sum is indicated in green. The Bloch spheres illustrate the dominating dynamics arising from the superpositions of the corresponding states. **b** Pump-probe data showing a beating pattern, measured at the tip-atom distance that corresponds to a tip field around 20 mT. The black line is a fit containing the two frequencies corresponding to the energy splitting in the avoided crossings and their sum frequency, with only the amplitudes as fit parameters (and a linear background). **c** Pump-probe data showing a single-frequency oscillation, measured at the tip-atom distance that corresponds to a tip field around 24 mT.

is extended a little for flip-flops with the nuclear spin, likely because these are clock transitions that are more independent from the magnetic field.

The AWG pulse scheme to achieve the spin initialization is shown in fig. 4.3a. First, a 400 ns positive bias pulse is sent. This causes spin-flip excitations in the atom's electron spin via Kondo scattering from spin-polarized tunnelling electrons. As mentioned, these excitations will also affect the nuclear spin, polarizing it in the same direction to $m_I = -5/2$.

A second pump pulse of 5 ns with negative bias is sent immediately after the longer pump, which was found empirically to improve signal strength (see fig. 4.3b). This second pump likely initializes the electron spin more often to $m_S = \downarrow$ after the longer pump brought it to $\uparrow$, while leaving the nuclear spin mostly unchanged at $m_I = -5/2$ due to the short length.

Lastly, a 5 ns probe pulse instantaneous reads the magnetoresistance after a controlled waiting time. To improve the current contrast in the lock-in scheme, the A-cycle has a positive probe bias, while the B-cycle probe has the opposite polarity. The 5 ns pulse width was found to be a practical optimum between the signal-to-noise increase of longer probe pulses and decrease of the amplitude of the measured oscillation dynamics due to the pulse being a wider sampling averaging window.

The total waveform segment length was 600 ns to allow the electron spin to relax thermally before repeating. Pulses were 5 ns wide and a 5 GHz low-pass filter was applied to the AWG waveform segments during the waveform calculations to avoid artifacts from phase-shifts in higher frequency components (see chapter 5). These kinds of pulse shape control are another advantage of the AWG. Overall, the above described pulse scheme would not have been possible in our lab with signal-generation equipment that was previously present.

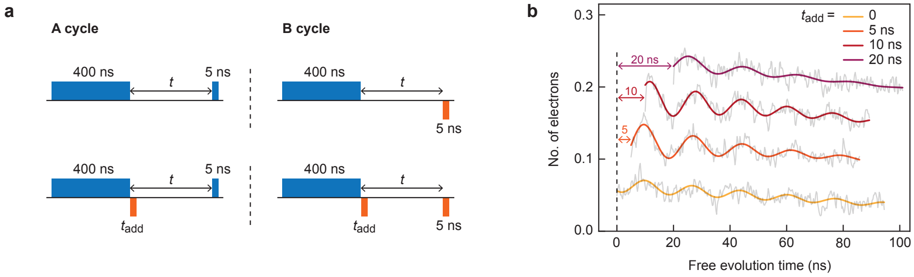

Fig. 4.3 | Pulse scheme for coherent nuclear spin dynamics. **a** Pulse schemes for the lock-in A and B cycles in the DC pump-probe contrast measurement used for fig. 4.2, without (top) and with (bottom) additional pump pulse. **b** Comparison between measurements obtained using different widths t_{add} for the additional pump pulse (tip height setpoint: 4 pA, 130 mV). Curves were shifted vertically for clarity. The free evolution time on the horizontal axis corresponds to the time t indicated in (**a**). The measurements shown in fig. 4.2b and c were performed using t_{add} = 5 ns.

4.4. CONTINUOUS-WAVE ESR FREQUENCY SWEEPS

One of the main applications we had in mind for the AWG, was the coherent control of electron spins through ESR-STM driving mechanisms. Verifying that we can use the AWG as an RF signal generator to drive ESR in the continuous wave (CW) limit is a first step to more complicated coherent control schemes. Therefore, we perform CW RF frequency sweeps on single magnetic atoms to attempt to observe ESR-STM resonances.

We measure the CW-ESR current signal in a lock-in contrast scheme for improved signal-to-noise ratio, with the A cycle filled with a sine wave at a RF frequency and the B cycle without. Nanonis provides a constant DC bias background to read out the magnetoresistance. Since the AWG only generates RF signals in this scheme, we use the fig. 3.2a electronics configuration that just contains the bias tee.

We want to avoid spending the bulk of the measurement time of the frequency sweep on waveform uploading of millisecond-long segments, so it is preferable to use the AWG sequencer with repeated short segments to program the frequency sweep. However, as discussed in section 3.4.7, getting perfectly periodic sine waves with repeated short segments is complicated and can only be done with tradeoffs, especially in a frequency sweep. Fortunately, we do not need perfectly periodic segments for CW-ESR experiments. Instead, we can get away with waveform segments containing sine waves of a finite fixed length for all frequencies, as long as that length is significantly longer than the coherence time of the spin system under study. This will introduce an occational phase jump in the ESR drive at the border between two segment repeats, but this has a negligible effect on the steady-state in the driven equilibrium of the spin.

A constant RF voltage amplitude at the STM junction is important to identify ESR resonances, but the RF losses in the STM cabling depend on frequency [6]. Chapter 5 discusses how the amplitude transfer function is determined with the AWG to correct for losses. For convenience, the different sine amplitudes at the AWG required for a flat power at the junction are implemented in the waveform segment's 8-bit sample values rather than the AWG channel output amplitude. The latter offers a higher voltage resolution and options for larger dynamic range, but would require a more complicated implementation. It is simply not a limitation in most CW-ESR experiments with limited frequency sweep ranges, where little dynamic range is required.

Applying the above methods for the AWG, we performed CW frequency sweeps on Ti adatoms on MgO adsorbed on the bridge binding site. Fig. 4.4a shows the resulting current difference spectra for both the bridge site mostly aligned and the site perpendicular to an in-plane field, which have a different g-factor [1, 7, 8]. Correspondingly, we observe resonance peaks at different frequencies for these sites at the same magnetic field. Therefore, we can conclude that these peaks are ESR resonances, and consequently that we can drive ESR using the AWG in our setup.

It was an open question whether the increased RF noise from the AWG compared to many other RF generators would be large enough to affect spin coherence in some way. This does not seem to be the case. Linewidths recorded with the AWG rival those recorded in CW-ESR sweeps using our Rhode & Schwarz SMB 100A RF signal generator.

As with other systems from ESR-STM literature, the linewidth is limited by spin

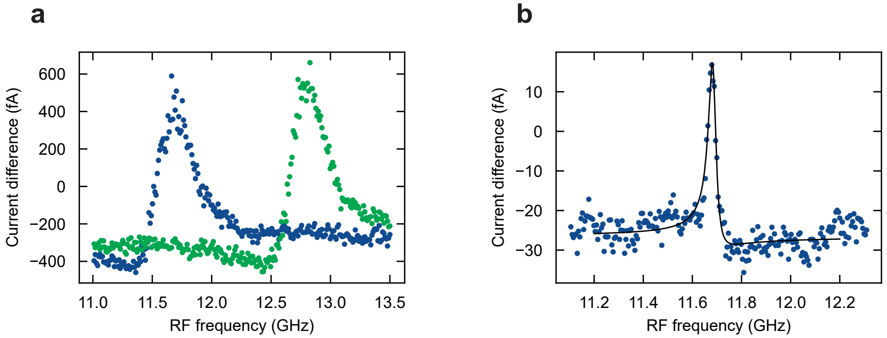

Fig. 4.4 | Continuous-wave ESR frequency sweeps using the AWG. a Measured on a Ti adatom on the vertical (blue) and horizontal (green) bridge binding sites of the MgO/Ag(100) substrate. Tip height setpoint: 50 pA, 60 mV (constant current mode). T = 1.6 K. B_z = 0 mT, B_x = 480 mT. **b** Measured on a Ti adatom on the same substrate on the oxygen binding site. Tip height setpoint: 3 pA, 110 mV (constant current mode). T = 0.4 K. B_z = 1500 mT, B_x = 0 mT. The black line is a phenomenological fit with a Fano resonance function. The extracted full-width at half-maximum is 37 ± 2 MHz.

scattering from the tunnelling current, tip vibrations, and fundamentally the spin relaxation time [3]. For example, we find a full-width at half-maximum (FWHM) linewidth of 37 ± 2 MHz on a Ti at the oxygen binding site at a current setpoint of 3 pA at 110 mV (fig. 4.4b), which is in correspondence with previous measurements in our lab with other RF generators [1]. The additional noise from the AWG can thus be ruled out as a factor on quantum coherence for the coherence times available on ESR-STM spin systems to date.

4.5. TIME-RESOLVED RABI OSCILLATIONS

Being able to drive ESR is just the first step in achieving full coherent control of the spin. For more complicated quantum coherent experiments, with the spin interpreted as a qubit, it is important to implement logical ‘quantum gates’ to bring the spin into any superposition state. For our spins in ESR-STM, the most straightforward gate to implement is a timed Rabi pulse with a controlled width τ_{Rabi}.

From there, more gates can be implemented: two pulses with 90° phase difference can be used to apply any rotation on the Bloch sphere [9], the spin can be decoupled dynamically from some decoherence sources with a spin echo pulse scheme [10], and a series of Rabi rotations on coupled spins using different frequencies can be used to generate entanglement [11]. While specialized RF circuits with often multiple signal generators were needed for these experiments, all of the qubit operations required for the above are straightforward to implement as a pulse scheme in our single AWG as an extension of simple Rabi oscillations. For this reason, we set out to reproduce the original Rabi oscillations observation on Ti adatoms from Yang *et al.* [10] using our AWG.

AWG IMPLEMENTATION

The relevant disadvantage of the AWG in this context is the limited RF amplitude of the output. A larger voltage amplitude in the tunnelling junction results in a higher Rabi rate [10]. With a maximum coherence time T_2 of only 300 ns when lifetime-limited [9], achieving a shorter Rabi time is paramount to observe oscillations before the spin decoheres.

Even worse, for the simple Rabi oscillation experiment on a single atom under the tip that we try here, without a spin echo to counteract inhomogeneous line-broadening due to a slowly changing magnetic field from a vibrating tip, we can expect a T_2 on the order of 80 ns [9, 10]. Therefore, we use the RF wiring scheme shown in fig. 3.3a with an RF amplifier on the AWG output channel to achieve RF voltages in the STM junction comparable to previous Rabi studies in other labs.

An advantage the AWG offers compared to other studies, on the other hand, is the option to try different pulse schemes in the lock-in contrast scheme for the Rabi pulse width sweep. A more straightforward scheme, which was also applied by Yang *et al.* [10], contrasts a single RF pulse on resonant with the ESR transition in the A-cycle with no RF voltage throughout the B-cycle. Each datapoint then has an increasing RF pulse width τ_{Rabi}. As with CW-ESR frequency sweeps, there is a constant DC voltage in the background, used to keep a slow STM feedback running during the measurement for a constant tip-sample height during pulse width-dependent RF heating.

HOMODYNE VS DC MAGNETORESISTIVE DETECTION IN RABI EXPERIMENTS

In their publication, Yang *et al.* postulate that the ESR current resulting from this simple A-cycle scheme is mostly the homodyne contribution [10], at least in this regime where the spin is coherent. With the homodyne case, as discussed in section 2.11.7, the ESR current difference at the lock-in should oscillate around zero as function of τ_{Rabi}. The parts with positive $\langle S_z \rangle$ have the coherent spin Larmor precession in the $\langle S_x \rangle$ and $\langle S_y \rangle$ plane oscillating with 180° phase difference compared to sections with negative $\langle S_z \rangle$, so these current contributions cancel each other in a full Rabi period.

Yet, this oscillation around zero current difference is not what was observed. Instead, they find a linear slope as a background to the oscillations.[1] The cited reason for this slope is the rectification current of the non-linear I-V of the Ti atom, which depends only on time-averaged RF power in the STM junction and should thus, as observed, grow linearly with pulse width τ_{Rabi}.

However, the DC magnetoresistive ESR current contribution is often the main signal in CW-ESR experiments and is also expected to increase with τ_{Rabi} as a linear slope with an imposed oscillation. With every section of time in the excited $\langle S_z \rangle$ projection, the time-averaged difference with the thermal ground state magnetoresistances grows. A significant slope present only at the resonance would indicate that, opposed to suggestions in literature, the DC magnetoresistive ESR current can be the most significant contribution in some Rabi oscillation experiments.

This is important information for future ESR-STM experiments, because the DC and

---

[1] From personal correspondence with the authors: all Rabi oscillation plots in [10] and [12] have a fitted slope subtracted

homodyne current signals require different microtip magnetic structures (see discussion in section 2.11.7). Furthermore, the increasing rectification current changes the tip height during a Rabi pulse width sweep with current feedback turned on, which changes the Zeeman splitting from the tip field and thus detunes the resonance away from the driving frequency. Lastly, from a data analysis standpoint, the signal-to-noise ratio of an oscillating signal is better when recorded on top of a flat background, assuming the same current noise.

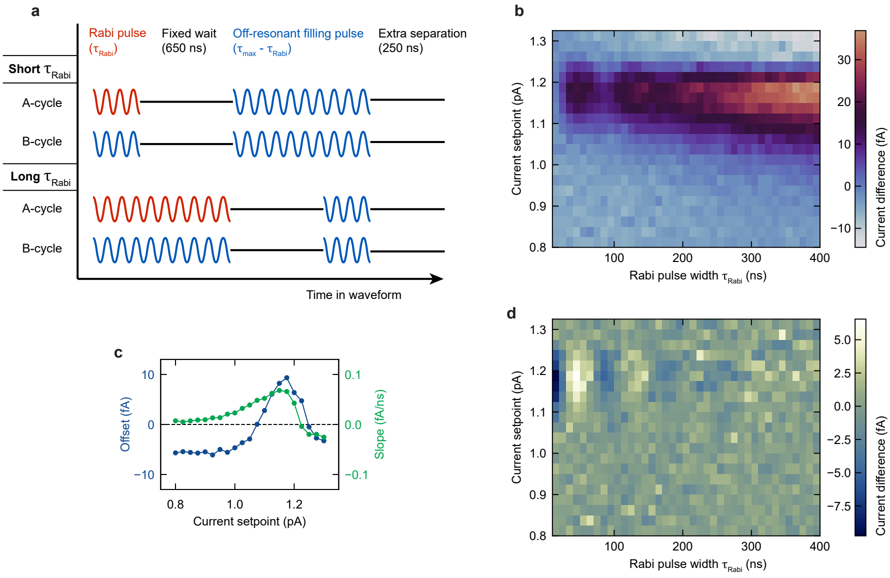

Fig. 4.5 | Rabi oscillations with a retification-compensating pulse scheme. a Pulse scheme for a lock-in contrast measurement of Rabi oscillations where the rectification current is the same between A and B cycles and for all Rabi pulse widths τ_{Rabi}. The red pulse is the on-resonant ESR frequency (11.54 GHz) and the blue filling pulse is off-resonant (8.10 GHz). Both frequencies have similar loss in the RF cabling, and thus cause the same rectification current. **b** 2D colourplot containing sweeps of τ_{Rabi} measured on a Ti adatom on the oxygen binding site, taken at different current setpoints, which effectively varies the tip magnetic field. These were measured in constant current mode, with a DC bias of 60 mV and a feedback time constant of 200 μs. T = 0.4 K. **c** The slope and offset in the constrast current signal as a function of τ_{Rabi} for the measurements at different current setpoint in (**b**). These were extracted by fitting with $[A \cdot \cos(2\pi f_{Rabi}\tau_{\text{Rabi}}) \cdot exp(-T_2/\tau_{\text{Rabi}}) + \text{offset} + \text{slope} \cdot \tau_{\text{Rabi}}]$. The dashed line marks zero. Note that the slope goes negative at 1.25 pA or higher, which is an indication of the asymmetric homodyne detection signal. No oscillations are visible in (**b**) in this current range. This suggests homodyne does not contribute strongly to the Rabi oscillation current signal in this experiment. **d** 2D colourmap with the same data shown in (**b**), but with the slopes and offset from (**c**) subtracted.

LOCK-IN PULSE SCHEME WITH RECTIFICATION COMPENSATION

For these reasons, we implement a more complicated pulse scheme in our waveforms for the sweep of Rabi pulse width τ_{Rabi}, which is shown in fig. 4.5a. The goal of the scheme is to have the same time-averaged total rectification current for all τ_{Rabi} datapoints and also the same rectification current between the A and B cycles. This mitigates both the slope in the lock-in signal and the tip height drift as function of τ_{Rabi}.

We achieve this by using two frequencies and two pulses per cycle waveform segment. One frequency is the ESR driving frequency and the other is an off-resonant 'filler' frequency with a similar amplitude transfer function. As the pulse width of the ESR frequency in the A cycle (τ_{Rabi}) increases, the length of the accompanying off-resonant filling pulse (τ_{fill}) decreases by the same amount. Thus we get $\tau_{\text{fill}} = \tau_{\text{max}} - \tau_{\text{Rabi}}$, with τ_{max} the maximum Rabi pulse width used in the τ_{Rabi} sweep. As such, the rectification contribution stays the same in the A cycle. The B cycle has the same pulse timings, but both are the off-resonant frequency, resulting in the same rectification current for B as in A. Note that a similar schemes with RF pulses in the B cycle have been used by Wang et al. [9], but they had a less general implementation using two frequencies that are both resonant with different ESR transitions.

RABI RESULTS

Experimental results using the above Rabi pulse scheme on a Ti isotope without nuclear spin are shown in fig. 4.5b. To explore detuning of the Rabi driving, we sweep the magnetic tip field strength, and thus the Zeeman splitting, by changing the current setpoint. We observe clear Rabi oscillations at one current setpoint, as expected, accompanied by a positive slope as a function of τ_{Rabi}. This slope is absent at different current setpoints when the Rabi drive is off-resonant, as can be seen in fig. 4.5c. Therefore, the slope must be unrelated to any remnant rectification current due to slightly unequal RF powers for the driving and filling frequencies. Rather, it is likely related to the CW-ESR signal in the limit of long τ_{Rabi}, where the spin decoheres into a driven steady state [3]. As mentioned, this decoherent DC magnetoresistive signal would grow linearly with pulse width.

Furthermore, a negative slope is also observed for setpoint currents just above the resonant setpoint, which would grow into the asymmetric contribution in the ESR-STM resonance line shape in the continuous-wave limit that is characteristic for the homodyne signal contribution. However, unlike the solely-positive DC contribution, no oscillations are overlayed on the negative slope. Conclusively, we can say that, at least in this experiment, the Rabi oscillation signal predominantly originates from the DC magnetoresistive ESR-STM signal, which is different from the original conclusions from Yang *et al.* on this topic [10].

One has to take the slope and offset into account when analysing the oscillations. Fig. 4.5d shows the Rabi oscillations with the fitted slope and offset subtracted. It is clear from this plot that the Rabi oscillations die out quickly due to decoherence because only a few Rabi periods are visible. For more complicated qubit operations in the future, the parameter to optimize is the ratio between the characteristic coherence time T2 and the Rabi period.

Driving power sweep

The period of a Rabi oscillation can be minimized, in general, by increasing the driving power. This has also been shown for ESR-STM [10, 12]. Using the RF amplifier we can, in theory, achieve similar RF powers in the junction as in literature. In practice, the increased heating limits our He3 hold time and there is a risk of moving the atom under the tip, especially with this pulse scheme that contains extra RF sections.

Fig. 4.6a shows Rabi oscillations with varying AWG output amplitude up to half the maximum power for our setup. The corresponding Rabi periods and T_2 are plotted in fig. 4.6b. We reach a minimum Rabi period of 68.5 ± 1.3 ns and the ratio (T_2)/(Rabi period) is approximately 1 around the resonance.

Interestingly, the signal amplitude varies over this power sweep. We attribute this to a changing rectification current at different RF powers, which results in a changing tip height that move the resonant current setpoint with varying power. The notion that the power sweep in fig. 4.6a is also a sweep over the resonance setpoint is supported by

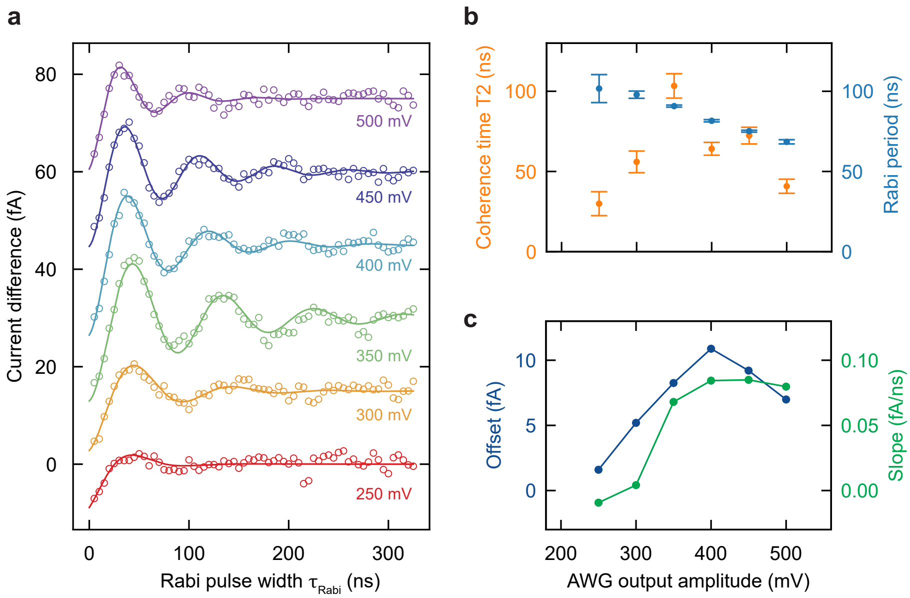

Fig. 4.6 | Rabi driving power dependence. **a** Rabi oscillation measurements at different AWG output voltage amplitudes (zero-to-peak), under the same conditions as in fig. 4.5. Note that the stated amplitudes are before +13 dB amplification from our RF Lambda R01G24GSM amplifier. Slopes are subtracted using the same fitting procedure as in fig. 4.5, and the plots are ffset vertically for clarity. This fitting also the extracts multiple parameters from the Rabi oscillation for each driving power. **b** plots the coherence time T_2 and the Rabi period ($1/f_{\mathrm{Rabi}}$). **c** plots the offset and slope of the background.

the extracted slope and offset (fig. 4.6c). The maximum in the slope and offset coincides with the larger oscillation amplitudes and coherence times.

The shifting resonant setpoint complicates the interpretation a little and introduces additional control parameters for future experiments. It also demonstrates again that the rectification current should be considered as a relevant factor in the design of Rabi oscillation pulse schemes. Though, admittedly, the RF power dependence of the resonant setpoint current is exacerbated by our particular pulse scheme.

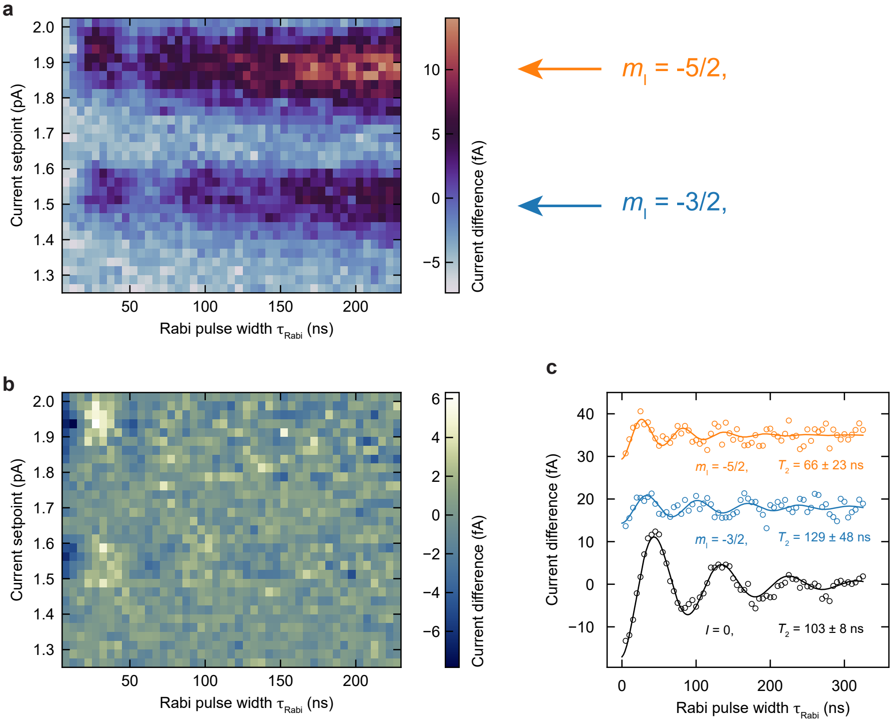

Fig. 4.7 | Rabi oscillations on ^{47}Ti hyperfine resonances. a 2D colourmap of Rabi oscillation measurements at different current setpoint performed on a ^{47}Ti adatom on the oxygen binding site, using the pulse scheme illustrated in fig. 4.5a. Here, the DC bias is 20 mV. The used frequencies are the same. The visible m_I = -5/2 and m_I = -3/2 hyperfine resonances are labelled with arrows. **b** 2D colourmap with the same data shown in (**a**), but with the slopes and offset subtracted after fitting. **c** The Rabi oscillation measurements with the longest T_2 at the m_I = -5/2 resonance (yellow), the m_I = -3/2 resonance (blue), and from the Ti isotope witout nuclear spin (black). Slope-subtracted and offset vertically for clarity. Solid lines are fits.

RABI OSCILLATIONS ON ISOTOPES

We also performed Rabi oscillation experiments on an atom of the isotope ^{47}Ti with nuclear spin I = 5/2, likewise on the oxygen binding site. A current setpoint sweep can be used to find and sweep over the different hyperfine resonance using the magnetic tip field. A 2D colour plot with that covers the hyperfine resonances corresponding to the nuclear spin projections m_I = -5/2 and m_I = -3/2 is shown in fig. 4.7a. A version with the slope subtracted is shown in fig. 4.7b. Rabi oscillations are again clearly visible at the two resonant setpoints. To our knowledge, this is the first time ESR-STM coherent control of a hyperfine resonance has been attempted.

The Rabi oscillations on the ^{47}Ti isotope can be compared with the results on the isotope without nuclear spin. The Rabi pulse width sweeps with maximum coherence time from all three resonances are plotted together in fig. 4.7c. The signal strength is reduced for the hyperfine resonances because the nuclear spin population is thermally distributed over all nuclear spin projections in this time-averaged measurement, meaning most of the time the Rabi driving is off-resonant. The achieved coherence times T_2 are similar, even exceeding coherence times of Ti spins without spin echo reported on 2-layer MgO in literature [9, 10]. Even so, the T_2 for m_I = -5/2 is lower with a statistically significant amount that could be attributed to the higher setpoint current causing more decoherence from tip vibrations [10]. Overall, it can be concluded that the presence of the nuclear spin does not hinder the coherence of the electron spin to a measurable extent in the large magnetic field regime with low hybridization. This is good news for incorporating nuclear spins as a part of a potential on-surface qubit platform [9].

4.6. COMBINING RF AND DC PULSES IN ONE EXPERIMENT

One of the advantages of the AWG in ESR-STM setups is the possibility to combine RF pulses with DC pulses in an experiment with only one instrument. This forgoes the time-intensive task of synchronising different DC and RF pulse source instruments at the nanosecond timescale, which could also drift in time. The relative sub-nanosecond timing between pulses generated by a single AWG channel is self-evident, apart from shifts due to the phase transfer function (see chapter 5). However, this might not be so straightforward when combining two AWG channels. In principle, the M8195A has the different output channels synchronised internally up to the sample, but RF circuit elements inserted before the channels are combined might throw off the timing. In particular, we are interested in checking the relative timing at the STM junction between RF pulses generated by one channel and DC pulses generated by the other channel, all combined via the bias tee and the RF splitter/combiner according to the RF wiring scheme in fig. 3.2c.

The timing of nanosecond RF pulses is not trivial to measure in an ESR-STM setup because the time-averaged current of a sine pulse is zero. As with the DC pulse autocorrelation measurement we can use a non-linearity in the IV curve to our advantage, following a lock-in pump-probe contrast scheme introduced by Yang *et al.* [10] (supplementary material). The general idea is that the RF pulse can generate a finite time-averaged rectification current only if the bias voltage is set at the non-linearity. We can choose a background bias at a linear IV section with a small amount of rectification and set the DC pulse amplitude to reach the non-linearity. As such, there is only a rectification current signal if the DC pulse and the RF pulse overlap. As with the DC autocorrelation, the time-averaged signal increases proportionally with the amount of overlap between the ideally square pulses and we can expect a triangle as function of the controlled delay time. In the pump probe scheme, we have a fixed DC pump pulse within the waveform for both the A and B cycle, and an RF pulse probe only in the A cycle. Then we sweep the probe delay.

Fig. 4.8 shows the experimental result of the above pump-probe scheme for RF and DC pulse widths of 10 ns. We use the 80 mV IETS step of Ti on the oxygen binding site of MgO/Ag as the IV non-linearity. The current difference as a function of delay time does form a triangle, showing that both the RF and DC pulses have the correct rectangular shape in the tunnelling junction. A horizontal shift of the triangle would indicate a timing delay between the channels. Fitting a triangle gives an pulse timing offset of 0.41 ± 0.05 ns. This falls within the 1.5 ns range of the internal software-adjustable delay between AWG channels. Furthermore, this timing offset is negligible at the timescales involved for the experiment that is discussed in the following section.

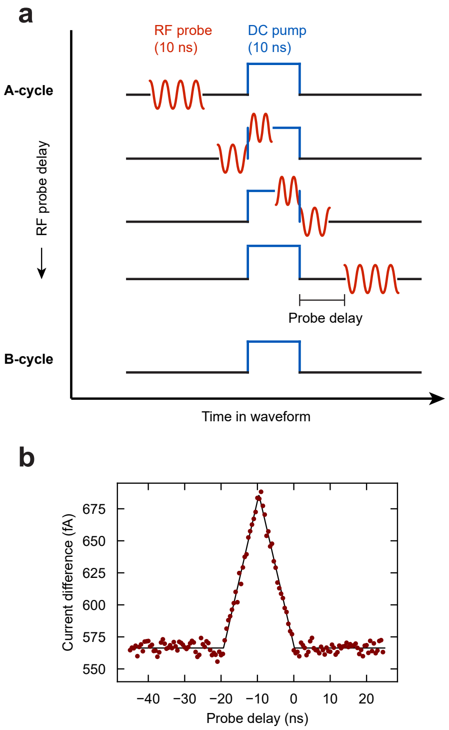

Fig. 4.8 | The timing of combined DC and RF pulses. **a** Pulse scheme of a lock-in constrast measurement for the pulse correlation between a square DC and a square RF pulse. Note that the maximum signal is expected at full overlap at a probe delay equal to negative of the pulse width, because of the way the delay is defined. **b** Experimental results of the above scheme for pulse widths of 10 ns for both DC and RF, using an RF frequency of 11.0 GHz (red). The data is fitted with a triangle (black line). The measured was performed in constant current mode above a Ti adatom on the oxygen binding site. Tip height setpoint: 20 pA, 50 mV.

4.7. INITIAL NUCLEAR SPIN LIFETIME MEASUREMENTS

Being able to probe individual nuclear spins at the atomic scale and image their chemical environment directly, is something that has only recently been made possible by the application of ESR-STM. In fact, the results by Veldman *et al.* [4] from 2024, discussed in section 4.3, are the first ever use of a scanning probe to observe nuclear spin dynamics. There are still many open follow-up questions about the properties of the particular nuclear spin species under study, but also about technical methods to investigate those properties. One such yet-unanswered question is: what is the lifetime of the nuclear spin, and how could we measure it?

It is useful to consider the expected time scales involved when developing a measurement protocol. The results from Veldman *et al.* suggest that the nuclear spin lifetime T_1 is at least longer than the Ti electron spin coherence time, which is on the order of a few hundred nanoseconds, since that was found to be the limiting factor for the observed coherent oscillations. At that time scale, the tools to our disposal are the CW-ESR current, which can be nuclear spin selective by probing one hyperfine transition, and nuclear spin hyperpolarization with a short DC pulse, shown to be capable of pumping the ^{47}Ti nuclear spin to m_I = -5/2 effectively within 400 ns [4]. Combining these tools requires RF and DC pulses together in one experiment, making this a perfect application of the AWG. Consequently, the RF wiring configuration will use is fig. 3.2c.

With a method to pump the nuclear spin out of thermal equilibrium established, we can use a pump-probe lock-in contrast scheme to investigate the nuclear spin T_1 up to, in principle, half of the inverse of the lock-in frequency (1/(2*270) Hz = ~1.85 ms). Methods for longer time scales are discussed in section 3.4.5. The pulse scheme used in this experiment is shown in fig. 4.9a. The lock-in A-cycle starts with a 3 μs DC pulse of 150 mV to pump the ^{47}Ti nuclear spin on the oxygen binding site into the m_I = -5/2 state. After the pump follows a variable delay time before the probe of up to 50 μs. The subsequent probe pulse is a 50 μs RF pulse at a frequency that is intended to be resonant with a hyperfine ESR transition. The B-cycle contains only the DC pump. A constant DC bias is applied throughout the waveform segments, both as a way to detect a change in magnetoresistance for the CW-ESR current in the probe, and to enable the tip height feedback for stability at the ESR-resonant tip height at longer measurement times. A sufficiently low bias background value was chosen, based on Veldman *et al.* [4], to try to avoid causing additional nuclear spin pumping during the probe delay period.

The total segment length adds to 103 μs, which is a significant amount of time compared to the lock-in period, and also a fairly specific value that was chosen intentionally. Care must be taken with contrast schemes containing longer segments to choose a total segment length that is (mostly) commensurate with the intended lock-in period of 270 Hz, because the segment will be repeated an integer amount of times to define the lock-in period in the experiment. At these segment lengths, an incommensurate choice could result in a difference of a few Hz away from the intended lock-in frequency, which might already require a slightly different lock-in phase calibration.

Fig. 4.9b shows experimental results in a 2D colour plot with probe delay sweeps at different current setpoints. This effectively sweeps over two hyperfine resonances

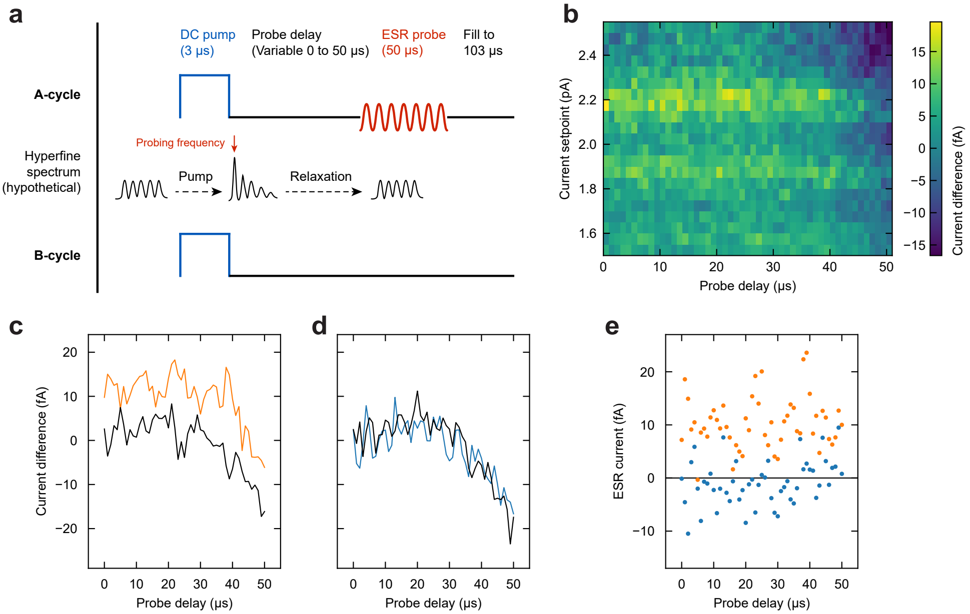

Fig. 4.9 | Initial attempt to determine the nuclear spin lifetime. **a** Pulse scheme for the lock-in contrast measurement. The hypothetical nuclear spin populations at moments during the waveform segment are indicated with a schematic of the ESR hyperfine spectrum, where a higher 'instantaneous' peak amplitude at one nuclear spin projection represents a larger probability to be in that spin projection. Note that a 20 mV DC bias is applied on top of the AWG pulses illustrated here, such that the tip height feedback can run during the measurement. **b** 2D colourmap of sweeping current setpoint and probe delay, measured on a ^{47}Ti adatom on the oxygen binding site. (Orange in **c**) Linecut from (**b**) at 2.2 pA, where the ESR probe is resonant with the hyperfine transition of nuclear spin excited state m_I = -5/2. (Blue in **d**) Linecut at 2.4 pA, where the ESR probe is off-resonant with any hyperfine transition. (Black in **c,d**) Probe delay sweeps on a Ti isotope without nuclear spin at the same current setpoints as the corresponding orange and blue sweeps on ^{47}Ti. So 2.2 pA and 2.4 pA for (**c**) and (**d**), respectivily. **e** Difference between the measured lock-in currents on the ^{47}Ti adatom and the Ti isotope without nuclear spin in (**c**) and (**d**). This should represent the ESR current contribution in the signal. The horizontal black line indicates zero ESR current. The on-resonant (orange) has a finite ESR current that does not show decay, while the off-resonant (blue) has zero ESR current.

that are visible as the horizontal streaks containing a higher current difference at the lock-in. At these resonant setpoints, the signal does seem to reduce as function of the probe delay, as would be expected for a decaying nuclear spin excitation. However, the same decaying trend is also seen at off-resonant current setpoints, which suggests that this decreasing trend is not related to the ESR signal. We performed the same probe delay sweep on a Ti isotope without nuclear spin, where the RF driving would also be off-resonant for ESR, and we observe the exact same background trend as the off-resonant setpoint on the ^{47}Tii isotope with finite nuclear spin. This confirms the background is unrelated to ESR. The relevant probe delay sweeps are plotted together in fig. 4.9c and d to compare them.

Without understanding the details on the origin of this background signal, we can still use the probe delay sweep on the isotope without nuclear spin to subtract the background from the sweeps on the ^{47}Ti isotope. What remains would be solely the ESR current signal. This background-subtracted signal is shown in fig. 4.9e. We can now see that the ESR current does not decrease as a function of probe delay for the entire range explored in this experiment. As such we can, preliminarily, interpret that the nuclear spin state did not change during that time and thus the lifetime has a lower bound of 50 μs. In the way this experiment was set up, however, it cannot be excluded that some spin pumping occurs during the pump or probe, nor that the initial DC pump polarises the nucleus properly. In fact, the DC nuclear spin pumping can be expected to be less efficient in this experiment at high magnetic field (1.5 T) compared to the earlier nuclear spin flip-flop results in section 4.3 at low magnetic field (around 35 mT). A larger magnetic field results in less hybridization between nuclear spin and electron spin states, leading to less spin pumping efficiency (see chapter 7 for an in-depth discussion). Therefore, at this point in time, the experimental results on the nuclear spin lifetime are yet inconclusive.

REFERENCES

[1] L. M. Veldman, L. Farinacci, R. Rejali, R. Broekhoven, J. Gobeil, D. Coffey, M. Ternes and A. F. Otte. ‘Free coherent evolution of a coupled atomic spin system initialized by electron scattering’. In: *Science* 372.6545 (2021), pp. 964–968. ISSN: 0036-8075. DOI: `10.1126/science.abg8223`.

[2] S. Loth, M. Etzkorn, C. P. Lutz, D. M. Eigler and A. J. Heinrich. ‘Measurement of Fast Electron Spin Relaxation Times with Atomic Resolution’. In: *Science* 329.5999 (2010), pp. 1628–1630. ISSN: 0036-8075. DOI: `10.1126/science.1191688`.

[3] Y. Chen, Y. Bae and A. J. Heinrich. ‘Harnessing the Quantum Behavior of Spins on Surfaces’. In: *Advanced Materials* 35.27 (2023). ISSN: 0935-9648. DOI: `10.1002/adma.202107534`.

[4] L. M. Veldman, E. W. Stolte, M. P. Canavan, R. Broekhoven, P. Willke, L. Farinacci and S. Otte. ‘Coherent spin dynamics between electron and nucleus within a single atom’. In: *Nature Communications* 15.1 (2024), p. 7951. ISSN: 2041-1723. DOI: `10.1038/s41467-024-52270-0`.

[5] K. Yang, P. Willke, Y. Bae, A. Ferrón, J. L. Lado, A. Ardavan, J. Fernández-Rossier, A. J. Heinrich and C. P. Lutz. ‘Electrically controlled nuclear polarization of individual atoms’. In: *Nature Nanotechnology* 13.12 (2018), pp. 1120–1125. ISSN: 17483395. DOI: `10.1038/s41565-018-0296-7`.

[6] W. Paul, S. Baumann, C. P. Lutz and A. J. Heinrich. ‘Generation of constant-amplitude radio-frequency sweeps at a tunnel junction for spin resonance STM’. In: *Review of Scientific Instruments* 87.7 (2016). ISSN: 10897623. DOI: `10.1063/1.4955446`.

[7] L. Farinacci, L. M. Veldman, P. Willke and S. Otte. ‘Experimental Determination of a Single Atom Ground State Orbital through Hyperfine Anisotropy’. In: *Nano Letters* 22.21 (2022), pp. 8470–8474. ISSN: 1530-6984. DOI: `10.1021/acs.nanolett.2c02783`.

[8] J. Kim, K. Noh, Y. Chen, F. Donati, A. J. Heinrich, C. Wolf and Y. Bae. ‘Anisotropic Hyperfine Interaction of Surface-Adsorbed Single Atoms’. In: *Nano Letters* 22.23 (2022), pp. 9766–9772. ISSN: 1530-6984. DOI: `10.1021/acs.nanolett.2c02782`.

[9] Y. Wang, Y. Chen, H. T. Bui, C. Wolf, M. Haze, C. Mier, J. Kim, D.-J. Choi, C. P. Lutz, Y. Bae, S.-h. Phark and A. J. Heinrich. ‘An atomic-scale multi-qubit platform’. In: *Science* 382.6666 (2023), pp. 87–92. ISSN: 0036-8075. DOI: `10.1126/science.ade5050`.

[10] K. Yang, W. Paul, S.-H. Phark, P. Willke, Y. Bae, T. Choi, T. Esat, A. Ardavan, A. J. Heinrich and C. P. Lutz. ‘Coherent spin manipulation of individual atoms on a surface’. In: *Science* 366.6464 (2019), pp. 509–512. ISSN: 0036-8075. DOI: `10.1126/science.aay6779`.

[11] R. Broekhoven, C. Lee, S.-h. Phark, S. Otte and C. Wolf. ‘Protocol for certifying entanglement in surface spin systems using a scanning tunneling microscope’. In: *npj Quantum Information* (2024), pp. 1–8. ISSN: 20566387. DOI: `10.1038/s41534-024-00888-9`.

[12] P. Willke, T. Bilgeri, X. Zhang, Y. Wang, C. Wolf, H. Aubin, A. Heinrich and T. Choi. ‘Coherent Spin Control of Single Molecules on a Surface’. In: *ACS Nano* 15.11 (2021), pp. 17959–17965. ISSN: 1936-0851. DOI: `10.1021/acsnano.1c06394`.

5

Compensating for the voltage transfer function of the RF cabling of a STM

> *Ik moet nog een quote vinden voor dit hoofdstuk.*
>
> Evert Stolte

In this chapter, we measure the voltage transfer function of the radio-frequency (RF) cabling from room temperature to the tip of our scanning tunnelling microscope, using an arbitrary waveform generator (AWG) as a RF signal generator. This has to be done in-situ, because the cryogenic environment changes the transfer function. Traditional methods using RF transmission and reflectometry cannot be used for various reasons, so methods based on rectification are used. Amplitude transfer function measurements with continuous-wave (CW) RF sources are common in the field of ESR-STM [1], but only recently has a method been developed to also measure the phase transfer function [2]. Here, we implement a proportional/integrate feedback-based variant on the amplitude transfer function measurement method, introduced by Paul et al., for use with our AWG. Next, we improve on the phase transfer function method introduced by Baumann et al. to speed up the measurement time. This more advanced scheme is made possible by the AWG. Lastly, we apply the new-found full transfer function to correct DC pulse shapes for distortions in order to achieve shorter pulse widths in the STM junction.

5.1. INTRODUCTION

Radio-frequency (RF) cabling to the scanning probe head has become a common attribute of scanning tunnelling microscopes, mostly driven by its requirement for pump-probe [3] and ESR-STM experiments [4]. The RF cabling itself and other circuit elements introduce frequency-dependent loss to the voltage signal. As such, determining the frequency dependence of the voltage amplitude transfer function of this RF cabling from the room-temperature RF generator to the tunnelling junction [1] has become a routine measurement. For example, it is important to check whether enough RF power reaches the tunnelling junction to observe ESR at a given driving frequency, on the order of 10 to 100 mV_{0-p} (-30 to -10 dBm), without significant heating of the sample and cryostat due to the signal losses.

It is paramount for ESR-STM setups to apply the same RF power for all frequencies in an ESR frequency sweep to observe small resonance peaks above the rectification background that depends on RF power in the junction. With a known amplitude transfer function (ATF), the generated output RF power can be adjusted such that the losses are compensated, so the same RF power arrives at the junction for each frequency. As a result, the rectification background is flat and variations as a function of frequency do not show up as apparent resonance peaks or noise.

Determining the transfer function for STM setups needs to be done *in-situ*, mainly because the cryogenically cooled sections of the cable affect the ATF. Furthermore, the ATF has been observed to change in small, but significant amounts over the span of days, so it needs to be re-measured often during a project [1]. In more standard RF circuits without STMs, the *in-situ* method of choice would either be a RF transmission or RF reflectometry experiment, for example with a vector-network analyser (VNA).

However, RF transmission is blocked by the transimpedance amplifier of the tunnelling current that is effectively a low-pass filter up to ~1 kHz. Reflectometry is also not ideal, because the reflection at the macroscopic tip impedance in effect for the far-field RF signal might not represent the RF voltage amplitude reaching the microscopic tunnelling junction and the adatoms at the sample surface. Furthermore, this impedance is very high, so the majority of the generated RF power (on the order of 0 dBm) is reflected. Hence, it is hard to measure the small variances in the transfer function as a function of frequency with the required accuracy in the limited dynamic range of a VNA without a RF circuit specialized for reflectometry (e.g. impendance matching, or carrier cancelation). Therefore, the *in-situ* method for STM setups originally developed by Paul *et al.* [1] instead relies on the rectification current in the junction, which is created due to a non-linearity in the *I*-*V* curve from an adatom localised on the sample surface.

While measuring the amplitude transfer function via the rectification current has become an established method for STM, up until recently no method had been developed to measure the phase transfer function (PTF) that could serve as an alternative for reflectometry. The PTF can be interpreted as manipulating the relative arrival delays between different frequencies. This becomes a relevant aspect to experiments involving short pulses with precise timings and containing multiple frequencies. In particular, the experimentally-achievable widths of DC pulses, which contain many frequency components, have been limited in the tunnelling junction by the non-flat PTF of the RF cabling distorting the pulse shape, rather than a low amplitude of higher frequency components.

Recently, Baumann *et al.* [2] introduced a new method to measure the PTF in an STM setup, which also relies on the rectification current. Furthermore, they showed that they can use the complete transfer function (ATF and PTF) to correct for TF-related distortions in DC pulses. Applying this correction, they were able to send shorter pulse widths to the STM junction than possible without the correction, reaching a minimum width of 333 ps.

In this chapter, we will focus on measuring the full transfer function with our Keysight M8195A Arbitrary Waveform Generator (AWG), introduced in chapter 3, as a RF source. We implement an adaptation of the amplitude transfer function measurement method from Paul *et al.* for use with our AWG. The variant is based on a proportional/integrate feedback control scheme. Next, we improve on the phase transfer function method introduced by Baumann *et al.* to speed up the measurement time. This more advanced scheme, which involves matching the sweep rate of a controlled phase parameter to a lock-in frequency, is made possible by the AWG. Lastly, we apply the new-found full transfer function to correct DC pulse shapes for distortions and show that we achieve shorter pulse widths in the STM junction.

5.2. THE AMPLITUDE TRANSFER FUNCTION FOR A SINGLE RF FREQUENCY

The voltage amplitude transfer function (ATF) is the ratio between the amplitude $\tilde{A}$ of a voltage sinewave generated outside of the STM and the amplitude A that arrives at the tunnelling junction. The ATF can be frequency dependent, but we assume a linear transfer function such that the frequencies themselves in a generated voltage signal do not change. The effect of the full transfer function T on a sinusoidal voltage signal input $\tilde{V}(t)$ therefore results in a junction voltage signal $V(t)$ with the same frequency, which can then be written as:

$$T[\tilde{V}(t)] = T[\tilde{A}\sin(\omega t + \tilde{\varphi})] = A\sin(\omega t + \varphi)\,. \tag{5.1}$$

Note that the phase of the input signal $\tilde{\phi}$ also gets transformed. However, the method described below is not sensitive to this phase. A different method is needed, which is introduced in section 5.5.

5.2.1. RECTIFICATION CURRENT

The generated RF amplitude $\tilde{A}$ is always a known factor, so determining the ATF concerns measuring A in the junction. We will employ the rectification current caused by a non-linearity in the conductance of the junction to measure a signal that depends on this amplitude, as was introduced by Paul *et al.* [1]. The electrical conductance of the tunnelling junction can often be approximated with just a linear term in the current I(V) as a function of voltage, which is the Ohmic conductance. To illustrate the origin of the rectification current, however, we will need to expand the conductance to (at least) second-order in a Taylor series:

$$I(V) = \sigma_0 V_0 + \sigma_1 (V - V_0) + \sigma_2 (V - V_0)^2 \, . \tag{5.2}$$

Here, σ_0, σ_1, and σ_2 are the Taylor series components of the conductance. V_0 is the bias voltage in the junction on top of which $V(t)$ is applied.

In principle, one can fill in $V = V(t) + V_0$ to get an expression for the tunnelling current in time, which could be used to deduce A from experimentally measured time traces. However, in practice the RF voltage signals are too fast for the transimpedance amplifier that is required to observe these small currents. We can only observe the time-averaged current signal. This is equal to the normalised integral over one period T of the sinewave:

$$\langle I \rangle = \frac{1}{T} \int_0^T I(V(t)) \, dt \, . \tag{5.3}$$

The zeroth-order term yields a background current $\sigma_0 V_0$ that does not depend on the RF signal. The first-order term yields a cosine, which averages out to zero. The quadratic sine term does produce a finite contribution, resulting a time-averaged current on top of the $\sigma_0 V_0$ background that is called a rectification current. The total time-averaged current is then

$$\langle I \rangle = \sigma_0 V_0 + \sigma_2 A^2 \frac{1}{T} \int_0^T \sin^2(\omega t + \varphi) dt = \sigma_0 V_0 + \frac{1}{2} \sigma_2 A^2 \, . \tag{5.4}$$

From this expression it is clear that we need at least a second-order non-linearity in the $I(V)$ around the chosen bias to observe the rectification current. However, detecting the rectification current at one bias with a known σ_2 is often not a practically feasible option for extracting A with the expression above. For many systems under study in our STM, the $I(V)$ curve can have non-linearities, but the second-order contribution exists among more complicated features. Higher orders in the conductance also contribute to the rectification current, making the analysis more tricky. These lead to bias dependency of the rectification current and a non-trivial dependence on voltage amplitude beyond eq. (5.4).

5.2.2. MEASUREMENTS WITH A CONDUCTANCE STEP

A class of non-linearity $I(V)$ that is commonly found in STM studies is a step in conductance, i.e. a discontinuity in the slope of the $I(V)$ between two bias regimes that are otherwise linear. These steps are, for example, realised by inelastic tunnelling into excitations of discrete energies (IETS) or superconducting gaps. Fig. 5.1a shows such a conductance step due to an orbital momentum excitation in the $I(V)$ curve of a Ti adatom adsorbed on an oxygen binding site on MgO/Ag [4–6]. We will use this non-linearity for both the ATF and the phase transfer function measurements later on.

Conductance steps have useful properties for rectification experiments. They cause a strong rectification current signal, but only in a small bias range around the step. This range is also indicative of the amplitude of the irradiating RF voltage, as can be understood as follows: if the bias is chosen far away from the step, the $I(V)$ is linear and no rectification current is produced. With the bias exactly at the position of the step, the

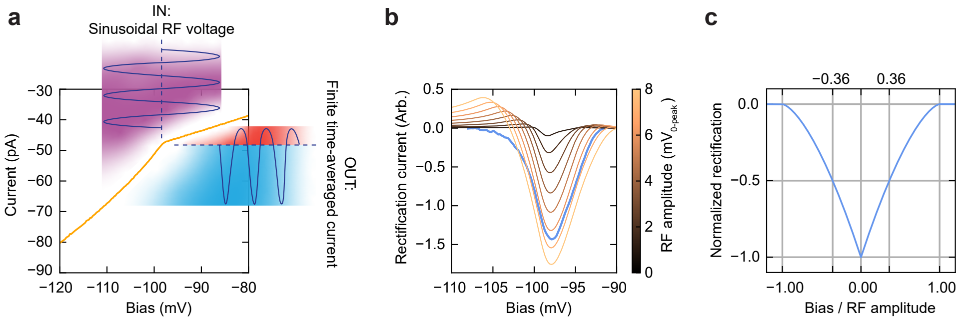

Fig. 5.1 | Bias spectroscopy of the ATF lock-in signal. **a** The $I(V)$ curve over an orbital excitation IETS conductance step in an Ti adatom on the oxygen binding site. The schematic illustrates the rectification process where the balanced sine voltage is converted into an unbalanced current oscillation. Tip height setpoint: 80 pA, -120 mV. Tip height feedback was off. **b** Blue: experimentally-measured rectification current as a function of bias around the IETS step in **a**, detected with a lock-in contrast scheme where the applied voltage is alternating between RF on and RF off. The AWG output frequency is 12.76 GHz with an output amplitude $\tilde{A}$ = 216 mV (zero-to-peak), applied through the RF combiner (the circuit shown in fig. 3.2b). Tip height setpoint: 10 pA, -100 mV. Tip height feedback was on. Black-to-gold: numerical simulations of the rectification current as a function of bias, based on the experimental $I(V)$ curve in (**a**), for different RF amplitudes in the junction. Note that all simulated curves are rescaled by the same constant for a comparison with the experimental data, which was taken at a different tip height. This is justified because the information is in the peak shape, rather than the height. **c** Numerically-simulated rectification current peak for a perfect step in the conductance. The y-axis is normalized by the absolute peak height. The x-axis is the ratio between the bias relative to the conductance step and the zero-to-peak amplitude. The found characteristic peak shape has a FWHM of 0.721.

equal positive and negative sections of the irradiated sine wave experience different conductance slopes. Accordingly, the currents produced at opposite polarity do not cancel out over time, resulting in a rectification current with a strength that depends on the conductance slope difference. The theoretical limit is a perfect diode, where the negative voltage polarity causes no current at all, and the positive polarity is unimpeded. With the bias chosen slightly next to the step, a smaller section of the peak-to-peak sinewave amplitude overlaps with the conductance step, which results in a smaller contribution to the imbalance in the current and thus lower rectification signal. Further detuning reduces the signal until the sinewave and the conductance step do not overlap anymore, producing a peak shape with a base width of the peak-to-peak amplitude $2A$.

We observe this peak shape experimentally in the rectification current in a bias sweep over the Ti orbital excitation, shown in fig. 5.1b. Here, we extracted the rectification current with RF from the background without RF experimentally using a lock-in contrast scheme (see section 3.4.3), where the applied RF voltage is alternating between RF on and RF off. Since the conductance step in this experimental $I(V)$ is not ideal and there are other smaller conductance features present, the base of the rectification peak is ill-defined, and thus half of the base width is not a good measure for A, the zero-to-peak amplitude in the junction. Instead, we can use the full width at half maximum (FWHM) as a proxy.

From a simulation of the rectification on a perfect conductance step, shown in fig. 5.1c, we can extract that the measured FWHM corresponds to $0.72A$, approximately. Applying this to the measurement in fig. 5.1b gives $A = 6.83$ mV. This particular measurement was taken at 12.76 GHz, one of the frequencies with the smallest losses above 10 GHz, at 10.8% of the full AWG output amplitude. Hence, the maximum available power of the AWG in this frequency range is 63.3 mV zero-to-peak, without any additional amplification.

5.2.3. BIAS SWEEP SIMULATION

The FWHM-based value can only be an approximation, because any realistic $I(V)$ curve deviates from a perfect conductance step. As an alternative, we can use the measured $I(V)$ in fig. 5.1a to numerically simulate the expected rectification signal as a function of bias. This approach takes as many details of the rectification contributions into account as possible, hopefully resulting in an exact match with the experimentally observed peak shape.

The simulation takes a sine voltage with a certain amplitude, adds this to a bias to get a total voltage, and samples the current from an $I(V)$ curve for different moments in the sine wave. Taking the mean current over one period of the sine corresponds to the time-averaged current. Then, the background current from the DC bias is subtracted to get the isolated rectification current at that bias. This can be done for different bias to simulate a complete bias sweep. We parameterize the experimental $I(V)$ curve with a smoothened B-spline interpolation to sample the curve continuously. A smooth parameterization is crucial, because the roughness in the curve originating from noise adds undesirably to the simulated rectification, distorting the peak shape.

In fig. 5.1b, we plot the simulated rectification bias sweep for multiple RF amplitudes. These peak shapes more closely resemble the experimental rectification peak compared to the simulation with an ideal conductance step in fig. 5.1c, which was simulated in a similar manner using an artificial $I(V)$ curve. The best match with the experimental peak is achieved between an amplitude of 6 and 7 mV. This corroborates the FWHM approximation.

The simulation does not match the data very well at the lower-bias side of the rectification peak. This might be related to the fact that the experimental data was measured with the tip height feedback turned on. This has the advantage of stability against drift due to RF heating. Additionally, follow-up experiments, such as measurements of the ATF as a function of frequency in the next section, will also be performed in constant current mode. So the rectification signal with feedback on will be a more useful parameter for comparison. Still, the changing tip height during the sweep does effect the $I(V)$ curve. Furthermore, for this Ti system in particular, the bias position of the used orbital excitation (the energy) depends on tip height. Together, these might explain the discrepancy between simulation and experiment for the rectification peak base. Nonetheless, the simulation of the rectification is successful in capturing the features that are important for extracting the RF amplitude in the junction.

5.3. THE ATF FOR A RANGE OF FREQUENCIES: THE FEEDBACK APPROACH

The primary goal of measuring the amplitude transfer function is to calibrate the output RF powers for different frequencies such that all irradiate the sample with the same voltage amplitude at the junction. To achieve this, one could repeatably execute the analysis outlined in the previous section for multiple frequencies by measuring a bias sweep for each. However, this is a time-consuming process. Instead, there are faster methods to measure only the relative ATF, i.e. the ratio of amplitudes reaching the junction among frequencies themselves, rather than the absolute ATF that is relative to the power generated by the instrument outside the STM.

The central idea is that the rectification current is independent of frequency, outside of the fact that the different amplitudes arrive at the junction due to the ATF. Therefore, if the same rectification current is observed for different frequencies, that means the same RF amplitude must be present in the junction for both frequencies, assuming a monotonously increasing (or decreasing) rectification as a function of RF amplitude. This generally holds for conductance steps. As we have seen in the previous section, the exact dependence of rectification current on RF power can be complicated, so the magnitude of the rectification current does not necessarily contain information about the actual value of voltage amplitude in the junction. We can only say that the relative ratio of amplitudes equals one for the two frequencies with equal rectification signal.

The approach to determining the ATF for a range of frequencies thus becomes: adjusting RF output powers iteratively until the same rectification signal is measured for each frequency, then reading off the powers that were generated to achieve this flat rectification signal. This list of used powers is the inverse of the relative ATF. Subsequently, one could determine the absolute ATF for a single frequency with the bias sweep method to get the absolute ATF for all.

The above approach was outlined for the first time in Ref. [1]. The details in the approach used by the Otte lab diverges from this conventional method in how to adjust the RF powers to reach a flat rectification current as a function of frequency. Ref. [1] measures the RF power dependence of the rectification signal for a single frequency and, with a smooth phenomenological polynomial fit, uses this as a mapping between RF power and rectification signal to predict the needed additional RF power for a different frequency after a rectification signal measurement. In our approach we use a proportional/integral (PI) feedback scheme instead to predict the optimal output power for the next iteration. [1]

With proportional feedback control, the adjustment in the power in the next iteration ($i + 1$) depends on the error ε_i between the target rectification signal S_T and the signal S_i measured with the current iteration (i). With the addition of integral feedback, there is also a dependence the accumulated error over all past iterations. For an individual

---

[1] This PI feedback approach was originally conceived by Jérémie Cobeil.

frequency, the next generated voltage amplitude $\tilde{A}_{i+1}$ can be expressed as

$$\tilde{A}_{i+1} = \tilde{A}_i - K_p \cdot \varepsilon_i - K_I \cdot \sum_{n=1}^{i-1} \varepsilon_n \,, \tag{5.5}$$

$$\text{with} \quad \varepsilon_i = S_i - S_T \tag{5.6}$$

Here, K_p and K_I are the proportional and integral feedback parameters, respectively. These need to be calibrated once, and could then ben used to run the feedback loop for any future determinations of the ATF. Note that the error is signed, so the sum of errors for teh integral term does decrease with iterations. Also note that this term only depends on past erros, never including ε_i.

Compared to the PI feedback approach, phenomenological mapping leads, most likely, to a faster convergence on the correct RF power to use to compensate the ATF because the next guess is more well-informed. However, this phenomenological mapping is limited by the accuracy, precision, and range of the mapping. The power sweep is measured separately once, making the entire ATF measurement sensitive to errors in the mapping. Furthermore, since there are a finite amount of points in the power sweep, the mapping relies on interpolation between the points (conventionally a 3rd-order polynomial fit), failing to capture minute details in the mapping. The PI feedback is agnostic about the mapping at every step and thus, with the right choice feedback parameters, can account for additional structure in the power-rectification curve based on the measurement at every iteration. This also makes the feedback optimization robust to possible unexpected dependencies of the rectification signal, like indirect effects of RF frequency-dependent heating.

Of course, the mapping could in principle be measured up to arbitrary precision for consecutive iterations to mitigate concerns about the interpolation, but this is time-consuming for a mapping with a large dynamic range that covers all RF powers and rectification signals that you could expect. Optimalisation up to the noise floor is built into the PI feedback method automatically, and convergence can be reached from any starting point on the power-rectification curve, as long as there is a monotonous mapping. Overall, the PI feedback method is thus an easier approach to achieve a frequency sweep background current with low variance.

The PI feedback method has already been implemented and used by the Otte lab with the continuous-wave RF generator Rhode & Schwarz SMB 100A, contributing to ESR-STM frequency sweeps with some of the smallest background current variances published to date (< 5 fA) [7–10]. In this chapter we now also implement the PI feedback method using our Keysight AWG M8195A as the RF generator. The AWG has a smaller dynamic range of 36.5 dB (75-1000 mV channel output range; minimum 0.2 in-file amplitude for well-defined sinewaves), but the AWG can in principle determine the ATP more accurately than the SMB 100A because of an output amplitude resolution of 10 μV, which is one order of magnitude better.

5.4. MEASURING THE ATF WITH AN AWG: RESULTS

We performed measurements of the relative ATF with the AWG for a wide range of frequencies from 50 MHz to 13.7 GHz, using different sets of feedback parameters K_p and K_I in separate attempts. The resulting ATF after a handful of iterations are shown in fig. 5.2a for two feedback parameter sets, together with an ATF measured two years prior using the proportional feedback method with a CW RF generator. Generally, our AWG results are in agreement with the CW results. The rectification signal recorded with the lock-in amplifier is shown in fig. 5.2b. This rectification signal should have converged to the target value, but it is clear that this was not achieved for all frequencies. For one set of parameters (orange), the frequencies above 5 GHz converge without issue in most sections, while the rectification signal deviates greatly for lower frequencies. In the other feedback parameter regime (blue), the lower frequencies are closer to convergence to the target, but higher frequencies deviate more often. Note that the difference in noise in the high-frequency range can mostly be attributed to a three-times longer averaging time for the blue curve, rather than better feedback.

Overall, we were unable to find a find a set of feedback parameters that resulted in stable feedback for both the low and high RF frequencies at the same time. The underlying reason is the strong non-uniformity in the proportions between the generated RF amplitude and the rectification signal response due to the large transfer function range in the frequency sweep. In the low-frequency regime, with relatively low losses, an absolute amplitude increase of 20 mV routinely doubles the total generated amplitude and thus increases the rectification by a lot. The same absolute increase at higher frequencies changes the rectification signal much less because a larger portion is dissipated. However the feedback needs to be able to capture both regimes with the same linear scaling of the rectification signal error. The solution for future attempts is to apply the feedback in the logarithmic dBm space, as we have done in the past when using the CW RF generator, instead of the linear amplitude space. A proportional change in amplitude thus becomes the same linear shift in dBm anywhere within the dynamic range of the output.

There are also frequency sections in fig. 5.2b that do not converge to the target value for either feedback parameter set. These sections either have such a low-loss ATF that the minimum AWG output amplitude of 15 mV is too much, or the ATF causes so much loss that the maximum AWG output of 1 V is not enough to reach the target rectification signal. Accordingly, they are located in the relative ATF plot in fig. 5.2a at the maximum 0 dB or minimum -36.5 dB respectively.

Another factor influencing the feedback process was the out-of-phase lock-in component of the recorded signal, which was on the same order of magnitude as the in-phase signal, as can be seen in fig. 5.2c. The origin of this unintended erratic signal is discussed in section 4.2. Unfortunately, a careful phase calibration of the lock-in was not executed before this ATF measurement, so some fraction of the erratic out-of-phase signal did leak into the rectification signal in the in-phase component. This signal also contributed to the feedback loop. Because the erratic signal depends non-trivially on the frequency, a converging in-phase signal at different frequencies does, therefore, not entirely constitute the same RF amplitude in the junction.

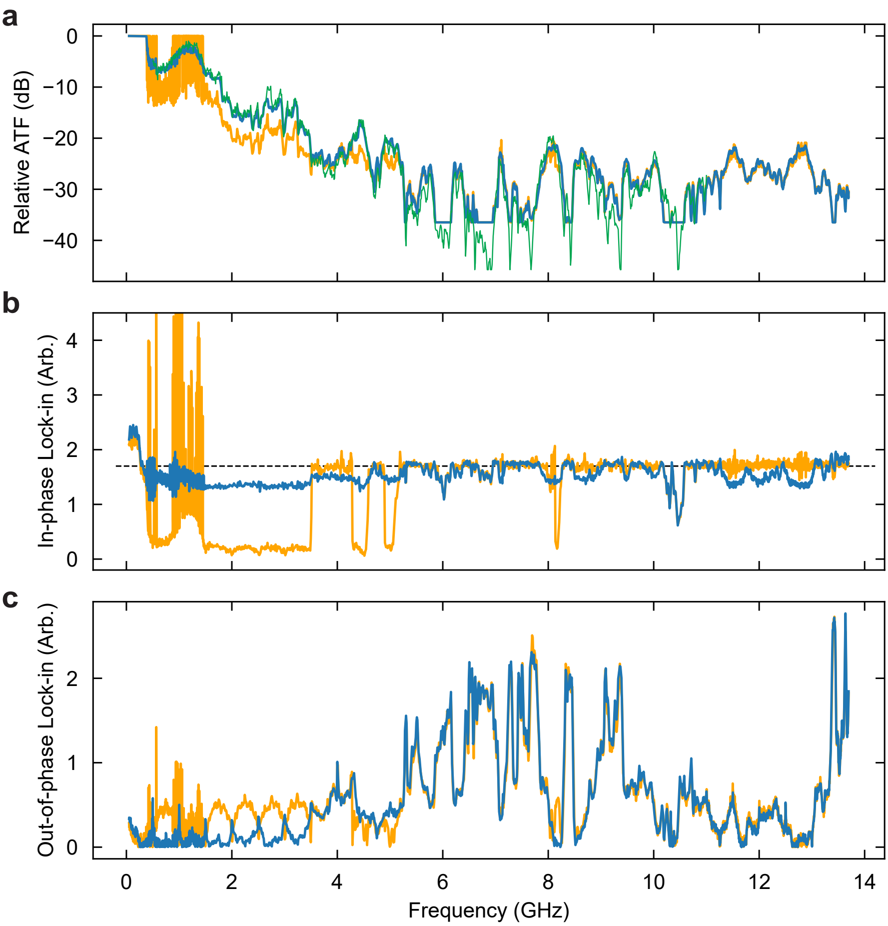

Fig. 5.2 | Amplitude Transfer Function frequency sweep. a The relative ATF as a function of frequency, measured with the AWG using the PI feedback approach with two different sets of feedback parameter values (see eq. (5.6)). Feedback iterations were continued until subsequent iterations did not constitute improvements towards the target value anymore. Orange: K_p=0.15 and K_I=0.15, with 13 iterations. Blue: K_p= 0.01 and K_I= 0.001, with 5 iterations with the orange curve as initial guess. Tip height feedback was on, with setpoint current 10 pA, -97 mV. Green: The ATF measured two years prior using a CW RF generator instead, also with a proportional feedback approach. **b** The in-phase lock-in signal, which was used as the rectification signal in the PI feedback, measured in the last iterations in frequency sweeps in (**a**). The dashed line in the feedback target value, which corresponds to an RF amplitude in the junction of 3 mV (zero-to-peak). **c** The erratic out-of-phase lock-in signal recorded simultaneously. As evidence for a non-ideal phase calibration, look for example at the periodic feature between 1.5 and 3.5 GHz that is also apparent in the in-phase signal.

In conclusion of this section, the results show that the PI feedback approach to measuring the ATF, which has already been very successful with continuous-wave RF generators, can also be effective with an Arbitrary Waveform Generator, despite the above-listed shortcomings in the available data sets. Future improvements to the AWG methodology are to provide feedback on the generated RF in a logarithmic power space instead of amplitude space, and to improve the calibration of the lock-in phase to filter out the erratic out-of-phase signal from the rectification signal. For now, the achieved relative ATF result (the blue curve in particular) is good enough for an application in DC pulse correction, discussed in section 5.10, because it does capture the trends of the ATF over the entire frequency scale.

5.5. THE PHASE TRANSFER FUNCTION BETWEEN TWO FREQUENCIES

The phase transfer function (PTF) can be defined as the phase accumulation over a section of cable of one frequency component compared to another. Following the approach outlined by Baumann *et al.* [2], which will be described below, it turns out that we can encode this phase difference in a DC rectification current signal, like we did for the sinewave amplitude. This makes a measurement of the PTF in RF range accessible to STM systems. Compared to the amplitude measurement, the phase measurement requires an even more specific non-linearity in the I(V) curve, namely a third-order component in the conductance.

$$I(V) = \sigma_0 V_0 + \sigma_1 (V - V_0) + \sigma_2 (V - V_0)^2 + \sigma_3 (V - V_0)^3 \,. \tag{5.7}$$

The generated voltage signal outside of the STM will now consist of two (different) frequencies ω_1 and ω_2 with their own phases φ_1 and φ_2, and an additional controlled phase θ that will be useful later on:

$$\tilde{V}(t) = \tilde{A}_1 \sin(\omega_1 t + \tilde{\varphi}_1) + \tilde{A}_2 \sin(\omega_2 t + \tilde{\varphi}_2) \,. \tag{5.8}$$

Fig. 5.3a shows an example of such a waveform. This signal will be transformed in the cables to the junction by the total transfer function T as follows:

$$T[\tilde{V}(t)] = V(t) = A_1 \sin(\omega_1 t + \varphi_1) + A_2 \sin(\omega_2 t + \varphi_2) \,. \tag{5.9}$$

Substituting this $V(t)$, in addition to a bias V_0, into the $I(V)$ with the third-order conductance term gives us the tunnelling current through the STM junction. This results in a number of (cross) terms:

$$
\begin{aligned}
I(V(t)) = \sigma_0 V_0 &+ \sigma_1 [\, A_1 \sin(\omega_1 t + \varphi_1) + A_2 \sin(\omega_2 t + \varphi_2) \,] \\
&+ \sigma_2 \left[\begin{array}{c} A_1^2 \sin^2(\omega_1 t + \varphi_1) \\ + 2A_1 A_2 \sin(\omega_1 t + \varphi_1) \sin(\omega_2 t + \varphi_2 + \theta) \\ + A_2^2 \sin^2(\omega_2 t + \varphi_2 + \theta) \end{array} \right] \\
&+ \sigma_3 \left[\begin{array}{c} A_1^3 \sin^3(\omega_1 t + \varphi_1) \\ + 3A_1^2 A_2 \sin^2(\omega_1 t + \varphi_1) \sin(\omega_2 t + \varphi_2 + \theta) \\ + 3A_1 A_2^2 \sin(\omega_1 t + \varphi_1) \sin^2(\omega_2 t + \varphi_2 + \theta) \\ + A_2^3 \sin^3(\omega_2 t + \varphi_2 + \theta) \end{array} \right]
\end{aligned}
\tag{5.10}
$$

Since we are again interested in the time-averaged rectification current (see eq. (5.3)), we can eliminate many terms that will trivially average out to zero. These are coloured red. Some terms, coloured blue, will contribute a finite time-averaged current in the same way as described in section 2 in the ATF measurement. Their rectification signal does not depend on the phase in any way. As such, they cannot be used for the purpose of measuring the PTF. Finally, there are the green cross terms originating from the third-order conductance. In contrast to the blue terms, these can produce phase-dependent time-averaged rectification terms. The first green term can be rewritten as

$$
\begin{aligned}
3A_1^2 A_2 \sin^2(\omega_1 t + \varphi_1) \sin(\omega_2 t + \varphi_2 + \theta) = &- \frac{1}{4} \sin\left((2\omega_1 - \omega_2)t + 2\varphi_1 - \varphi_2 - \theta\right) \\
&+ \frac{1}{4} \sin\left((2\omega_1 + \omega_2)t + 2\varphi_1 + \varphi_2 + \theta\right) \\
&+ \frac{1}{2} \sin\left(\omega_2 t + \varphi_2 + \theta\right).
\end{aligned}
\tag{5.11}
$$

If we choose $\omega_2 = 2\omega_1$, the upper term in eq. (5.11) becomes independent of time, so it does not average out. The dependence on the difference of phases remains. For our PTF measurement, we will thus impose this frequency condition $\omega_2 = 2\omega_1$ and use the DC current originating from this upper term to get relative phase information. The other two terms in eq. (5.11) do average out under this condition. The same is true for the other green term in eq. (5.10), which contributes to the rectification only at a different frequency condition $\omega_1 = \pm 2\omega_2$. In general, higher order conductance terms introduce more frequency conditions for phase-dependent DC current contributions that are yet different, so only one term contributes for a single choice of frequency condition. Sticking with the condition $\omega_2 = 2\omega_1$, the total average current in the junction can then be expressed as

$$
\langle I \rangle = \sigma_0 V_0 + \frac{1}{2} \sigma_2 \left(A_1^2 + A_2^2\right) + \frac{3}{4} \sigma_3 A_1^2 A_2 \sin(\Delta\varphi + \theta).
\tag{5.12}
$$

Here we have written $\Delta\varphi = \varphi_2 - 2\varphi_1$, which is what we were looking for: the relative phase information in the junction between two frequencies. Note that $\Delta\varphi$ appears inside a sine term. To extract $\Delta\varphi$ in an experiment, rather than relying on a singular measurement of the current value and calculating with knowledge of the conductance parameters, we can instead vary the controlled phase θ with a linear spacing to measure a sine dependence in the current. As illustrated in fig. 5.3, this sine in the rectification current as a function of θ will have a phase shift relative to the inputted θ range from 0 to 2π, and this shift will be equal to $\Delta\varphi$. Note that this phase shift is independent of the exact shape of the $I(V)$ curve.

5.6. TIME-EFFICIENT PHASE EXTRACTION

In the original experiment from Baumann *et al.*, the experimental procedure was to choose a fixed θ and measure the total rectification current at that one θ with a lock-in contrast scheme with alternating cycles of RF on and off. This is similar to the scheme in the ATF measurement used to isolate the rectification signal from the background current produced by the finite bias. They measured the rectification current for various values of θ to get an experimental result that looks like the schematic in fig. 5.3b. A sinusoidal fit was used in the data analysis afterward to extract $\Delta\varphi$. Many datapoints for θ are needed to get a good-quality fit with low error on the phase fit parameter, making this approach time-inefficient. This becomes relevant once we are interested in the PTF for a range of frequencies.

Here we introduce a more time-efficient method of detecting the phase signal from the same rectification current term: we use the lock-in amplifier to extract the phase from the sinusoidal rectification current directly by sweeping θ live in the experiment. [2] By parameterizing $\theta(t) = \omega_{LI} \cdot t$, with ω_{LI} the (angular) frequency of the lock-in amplifier reference signal, the rectification current signal arriving at the lock-in input I_{LI} will oscillate at this lock-in frequency:

$$I_{LI}(t) = |A_{LI}| \cdot \sin(\omega_{LI} t + \Delta\varphi), \tag{5.13}$$

with

$$|A_{LI}| = |\frac{3}{4}\sigma_3 A_1^2 A_2|. \tag{5.14}$$

When the signal and lock-in reference frequencies match, this rectification signal will be detected by the lock-in amplifier, which is a low-noise measurement due to side band rejection. Neither the background current, nor rectification sources from other conductance orders will match the lock-in frequency and will thus also be rejected. Furthermore, the lock-in will extract the absolute amplitude $|A_{LI}|$ and the phase $\Delta\varphi$ directly from the rectification signal, so only a single datapoint is needed. Although additional averaging time will be needed for this single datapoint compared to individual datapoints with fixed θ, the sideband noise rejection can be expected to contribute to a significantly lower total measurement time for a PTF over a frequency range.

The controlled time-varying phase $\theta(t)$ effectively corresponds to a frequency shift to the frequency of the second sinewave with the lock-in frequency: $\omega_2 = 2\omega_1 + \omega_{LI}$. On its own, this is an easy modification to the RF voltage signal with any RF generator. This

---

[2] This idea was suggested to me (and others) by Prof. Sebastian Loth, one of the authors of Ref. [2], at a seminar in Stuttgart, November 2022.

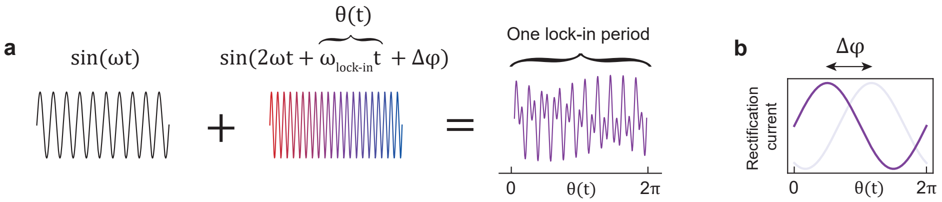

Fig. 5.3 | Phase Transfer Function experiment design. a Illustration of the separate elements in the generated voltage signal according to eq. (5.9): a sine wave added to another sinewave with double the frequency and a relative phase. The phase contains the fixed shift $\Delta\varphi$ due to the PTF ($\Delta\varphi = 0$ in this plot) and a controlled phase $\theta(t)$ shifting linearly at the rate of the lock-in reference. **b** Schematic of the expected sinusoidal rectification current as a function of time during one lock-in period $2\pi/\omega_{LI}$, which corresponds an interval of $\theta(t)$ from 0 to 2π. The phase of the current sinusoidal corresponds to $\Delta\varphi$.

becomes more complicated by the strict phase relation required between the three frequencies in play. The periodic signals of the ω_1, ω_2, and the reference frequency in the lock-in must all have a fixed phase relation for repeated experiments. Furthermore, this relative phase between the lock-in reference and the coinciding starting points of ω_1, ω_2 must also be the same for any ω_1, ω_2. In practice, this can only be achieved with the aid of an arbitrary waveform generator. In our case, we can generate the waveform directly for all frequencies up to $\omega_2 = 25$ GHz. In the PFT experiments below we will use $\omega_{LI} = 821$ Hz, rather than the 270 Hz used elsewhere in this thesis.

5.7. BIAS SPECTROSCOPY OF THE PTF LOCK-IN SIGNAL

5.7.1. EXPERIMENT

To experimentally verify the effectiveness of our measurement scheme, we investigate the rectification current lock-in signal as a function of bias voltage around a conductance step in the $I(V)$ curve at approximately -97.8 mV of a Ti adatom on the oxygen binding site of MgO/Ag. This step is shown in fig. 5.1a and is discussed in more detail in section 5.2. The recorded lock-in amplitude and phase for two pairs of frequencies ω_1, ω_2 at multiple AWG output amplitudes are plotted in fig. 5.4a,b.

The results for $(\omega_1, \omega_2) = (5$ GHz, 10 GHz) are quantitatively different from $(\omega_1, \omega_2) =$ (5 MHz, 10 MHz), but they share common features. In both cases there are two peak features in the lock-in amplitude of different height, with a dip to zero that separates the two peaks, even though the voltage bias point of this dip differs. Coinciding with the peaks, we can observe two plateaus in the lock-in phase signal that are separated by 180°, with a jump between plateaus at the border between peaks.

We can understand these results from the $I(V)$ characteristics. As can be seen from eq. (5.14), the lock-in amplitude scales with the conductance component σ_3 in the Taylor expansion around the bias V_0. Since σ_3 can in general depend on V_0, we can interpret

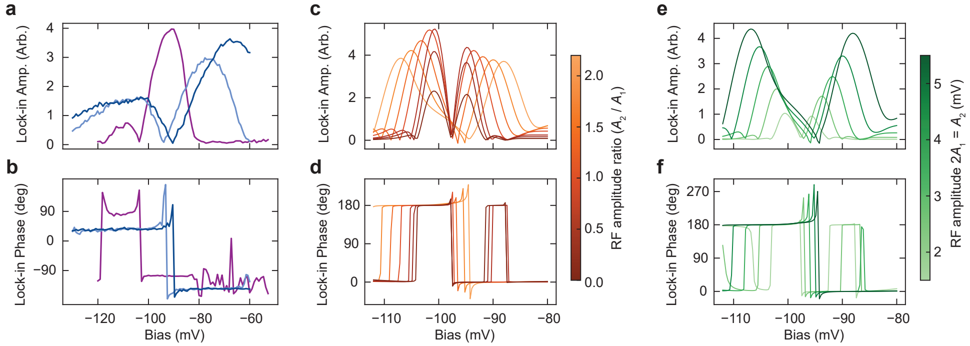

Fig. 5.4 | Bias spectroscopy of the PTF lock-in signal. **a,b** The amplitude and phase, respectively, of the sinusoidal rectification current in a bias spectroscopy over a conductance step, measured experimentally with lock-in detection while sending the voltage signal described in fig. 5.3. Three spectroscopies are plotted. Purple: $\omega_1 = 5$ GHz, $\omega_2 = 10$ GHz, generated RF amplitudes in the AWG $\tilde{A}_1 = \tilde{A}_2 = 50$ mV. Light blue: $\omega_1 = 5$ MHz, $\omega_2 = 10$ MHz, $\tilde{A}_1 = \tilde{A}_2 = 37.5$ mV. Dark blue: $\omega_1 = 5$ MHz, $\omega_2 = 10$ MHz, $\tilde{A}_1 = \tilde{A}_2 = 50$ mV. Tip height feedback was turned on during the bias spectroscopies, with a current setpoint of 20 pA. The total time per data point was 1200 ms, of which 900 ms lock-in settling time and 300 ms averaging time. **c,d** Simulated lock-in amplitude and phase of the rectification current signal, respectively, for different ratios A_2/A_1 of RF amplitudes in the junctions with $A_1 = 5$ mV for all simulations. The simulations are based on the $I(V)$ curve in fig. 5.1a. **g,h** Simulated lock-in amplitude and phase of the rectification current signal, respectively, for different values of $A_2 = 2A_1$ of RF amplitudes in the junction.

the bias-dependence of the lock-in amplitude as an indication of $\sigma_3(V_0)$. The expected shape of $\sigma_3(V_0)$ around a conductance step consists of two extrema on either side of the step with opposite polarity, such that $\sigma_3(V_0)$ must pass through zero (for intuition: see the second derivative of the logistics function). Taking into consideration that the lock-in amplitude is an absolute value, a sudden change in polarity at the conductance step is exactly what we observe with the 180° phase jump. Furthermore, we measured vanishing lock-in amplitude at voltages far removed from the conductance step, at least for $(\omega_1, \omega_2) = (5$ GHz, 10 GHz$)$. In this regime, above -80 mV, the lock-in phase is poorly defined and we observe noise.

With this understanding, we can now attribute the phase value at the plateaus to be equal to $\Delta\varphi$, up to a 180° shift, which is the value we are interested in. As predicted and intended, this measured $\Delta\varphi$ does not depend on the $I(V)$ characteristic at a chosen bias, nor does it depend on the chosen RF amplitude. Only the signal-to-noise ratio is affected, with certain biases resulting in more lock-in amplitude signal. Most importantly, we observe that the measured $\Delta\varphi$ at the plateaus depends on the set of frequencies that we select. This indicates that the PTF does indeed vary with frequency and our method can be used to map this dependency.

Still, there are other observed features in the bias spectroscopies that cannot be explained with only a varying $\sigma_3(V_0)$. For instance, the location of the dip between the peaks varies in the three measurements with different experimental parameters. This horizontal shift of the dip is observed even when the only difference between experimental parameters is the applied RF amplitude. Furthermore, the (ω_1, ω_2) = (5 GHz, 10 GHz) measurement has a second phase jump downwards around -120 mV, which is not seen for (5 MHz, 10 MHz). When looking for an origin of these discrepancies, the most significant difference between these sets of frequencies is the amplitude transfer function (ATF). The same RF amplitudes were used to generate all voltages in the AWG, but not only are the losses in the RF cabling much higher in the GHz range, the ratio between amplitudes reaching the tunnelling junction is also different between 5 and 10 MHz than between 5 and 10 GHz.

5.7.2. SIMULATIONS

To understand the observed RF amplitude dependency of the PTF signal, we perform a simulation of the lock-in rectification signal as a function of bias. The approach is similar to the one described in section 5.2: 1) parameterise the experimentally measured $I(V)$ curve from fig. 5.1a with a spline interpolation; 2) apply the voltage input $V(t)$ from eq. (5.9) and take the mean to get a calculated time-averaged rectification current; 3) repeat for linearly-spaced values of θ and fit with a sine function. This can be done with different V_0 for a simulated bias spectroscopy and with varying RF amplitudes A_1 and A_2.

In a first investigation, with the results in fig. 5.4c,d, we keep A_1 fixed and vary A_2, such that we sweep the ratio between the RF amplitudes. The bias spectroscopy simulation reproduces the two large peak features separated by a dip to zero amplitude, accompanied by a 180° phase jump. The simulation even captures the spike before the jump in the phase signal, which is most likely an artifact of fitting/lock-in onto a low-amplitude sine wave within noise. In the simulation results, we can now see that increasing A_2/A_1 moves the phase jump point to higher bias, at least for our $I(V)$ characteristics. With decreasing A_2/A_1 below 1, the position of the phase jump converges to the location of the conductance step.

In the second investigation, showcased in fig. 5.4e,f, we choose a fixed ratio $2A_1 = A_2$ and increase this RF amplitude. Outside of a generally increasing lock-in amplitude, one of the effects of increased RF amplitude is, again, a shift of the phase jump point towards higher bias. However, this was only the case for simulations with $A_1 \neq A_2$. Therefore, a combination of these two properties of the used RF amplitudes — a different ratio between A_1 and A_2, and a different total amplitude in the junction — is likely responsible for the observed shifting phase jump point between the different measurements.

Both simulations also show the presence of multiple phase jumps. They seem to be a consequence of slight non-linearity outside of the large conductance step, where the $\sigma_3(V_0)$ changes sign again. However, the bias position of these additional jumps moves away from the conductance step with increasing RF amplitudes. The overall lower-loss ATF in the MHz range results in significantly larger RF amplitudes in the junction. Therefore, the one additionally observed phase jump can only be seen in the (5 GHz, 10 GHz) measurement.

Two discrepancies between the simulations and the experiment remain: the exact position of the phase jump and the direction of the asymmetry between the peak heights.

The former could be explained by the fact that the experimental bias sweeps were performed with the tip height feedback turned on, for stability. This was not the case for the measurement of the $I(V)$ curve that was used in the simulation. The bias position of the used conductance step in Ti on the oxygen binding site depends on the tip height [5, 6], which was thus a varying parameter. The tip was most likely further from the sample in the phase measurement compared to the $I(V)$ measurement due to the additional rectification current from the second-order conductance.

As for the asymmetry of the peak heights: in the experiment we observe that the right peak is always higher. However, in the simulation all possible combinations of RF amplitudes predict the left peak to be higher when basing the simulation on the experimental $I(V)$ curve. Furthermore, note that the simulations predict a maximum asymmetry in peak height at $A_1 = A_2$ (see fig. 5.4c), while, based on the ATF (fig. 5.2a), we believe the phase measurement with the largest observed peak height asymmetry, (5 GHz, 10 GHz) actually corresponds to the smallest ratio A_2/A_1. This discrepancy remains unaccounted for.

5.7.3. SPECTROSCOPY CONCLUSIONS

In summary of this section, we have investigated the rectification current signal originating from a third-order conductance as a function of bias. In this, we verified a suitable signal to measure the relative PTF between two frequencies, but only within limited bias regimes that turned out to depend non-trivially on other experimental parameters.

Looking ahead, the role of bias spectroscopy for the main goal of this chapter — the determination of the PTF for a range of frequencies — is small, but critical in so far that a bias value must be chosen to perform a PTF measurement for many sets of frequencies. It can be concluded from our results that it is not guaranteed a bias regime exists where all frequency pairs have a stable phase signal with large signal-to-noise ratio when not accounting for the RF amplitudes in some way. Furthermore, two stable plateau regimes with a 180° phase jump exist directly next to each other, risking an unnoticed cross-over to the other regime during an experiment. As such, taking a bias spectroscopy to map the relevant bias features will be a prerequisite before initiating more complex experiments like frequency sweeps.

Since the origin of the bias-shifting phase plateaus lies in the uneven RF amplitudes in the junction, one solution would be to compensate the RF amplitudes at the AWG with the amplitude transfer function. Similar RF amplitudes in the junction should result in phase plateaus at the same bias. Moreover, we have observed that the rectification current signal is often sufficiently strong that the phase plateaus can cover multiple millivolts, making the PTF measurement forgiving to mistakes in the compensation for the ATF.

5.8. THE LOCK-IN PHASE SIGNAL AS A FUNCTION OF FREQUENCY

5.8.1. CUMULATIVE SUMS AND INTERPOLATION

The experimental method from Baumann *et al.* described in section 5.5 gives the acquired phase difference $\Delta\varphi(\omega_1, \omega_2)$ for a pair of frequencies ω_1 and ω_2 in the specific circumstance that the latter frequency is double the former. Phase relations between frequency pairs that are not related in this way can be determined by cumulatively adding phase differences between successively doubling frequencies $2^n\omega_0$ from a base frequency ω_0 with integer n.

For example, the phase difference $\Delta\varphi(1\omega_0, 4\omega_0)$ cannot be measured directly, but is equal to the sum $\Delta\varphi(1\omega_0, 2\omega_0) + \Delta\varphi(2\omega_0, 4\omega_0)$. As such, we can define the absolute PTF as any phase difference $\Delta\varphi(\omega_0, k\omega_0)$ relative to the phase in the junction of ω_0. However, this simple approach still cannot determine $\Delta\varphi$ for many frequencies. For instance, $\Delta\varphi(\omega_0, 6\omega_0)$ does not work, since $2^n \neq 6$ for any n.

In general, cumulative summing of measured phase differences starting from any ω_0 leaves gaps in the PTF as a function of frequency, and the frequency gap size increases exponentially. On one hand, this can be advantageous because multiple orders of magnitude can be covered without also cumulatively adding up the phase measurement errors many times, which would be a problem for a linear spacing. On the other hand, the frequency spacing quickly become larger than the size of significant transfer function features (< 100 MHz, as can be seen from the ATF results in fig. 5.2a). This makes a simple interpolation scheme for the PTF between points, to cover frequencies that cannot be determined with cumulative sums, inaccurate.

To determined points like $\Delta\varphi(\omega_0, 6\omega_0)$, then, we can start a new series of doubling frequencies starting at a different base frequency. With a base choice of $3\omega_0$, we get a cumulative phase relation series that covers $(6\omega_0, 12\omega_0, 24\omega_0, \ldots)$ which experimentally gives $[\Delta\varphi(3\omega_0, 6\omega_0), \Delta\varphi(6\omega_0, 12\omega_0), \Delta\varphi(12\omega_0, 24\omega_0), \ldots]$. This series is entirely separate from the original $(1\omega_0, 2\omega_0, 4\omega_0, 8\omega_0, \ldots)$ series, without any coincidental point. As illustrated in fig. 5.5a, we can connect these series by inserting $3\omega_0$ between $2\omega_0$ and $4\omega_0$, obtaining $\Delta\varphi(\omega_0, 3\omega_0)$ from an interpolating between the absolute PTF values $\Delta\varphi(\omega_0, 2\omega_0)$ and $\Delta\varphi(\omega_0, 4\omega_0)$. This establishes a phase relation between all frequencies in both series, filling the gaps in the PTF. In contrast to interpolation over exponentially increasing frequency gaps, this interpolation to insert one doubling series into the other is justified for a sufficiently small choice for ω_0 where the PTF can be expected to be smooth, because the insertion gap size is always as small as $2\omega_0$.

Many separate doubling series, inserted between different frequencies spaced $2\omega_0$ apart, are required to arrive at a linear spacing across the entire desired PTF frequency range. Mapping out which frequency pair measurements to take simply comes down to sweeping ω_1 over all integer multiples k of ω_0 up to a maximum range: we measure all $\Delta\varphi(k\omega_0, 2k\omega_0)$. The resulting dataset is enough to derive the PTF, defined as $\varphi(\omega) = \Delta\varphi(\omega_0, \omega)$, relative to ω_0 for all frequency points ω up to the largest used ω_2 with a spacing of $2\omega_0$ (here, we do not count the series base frequency points that were obtained by interpolation).

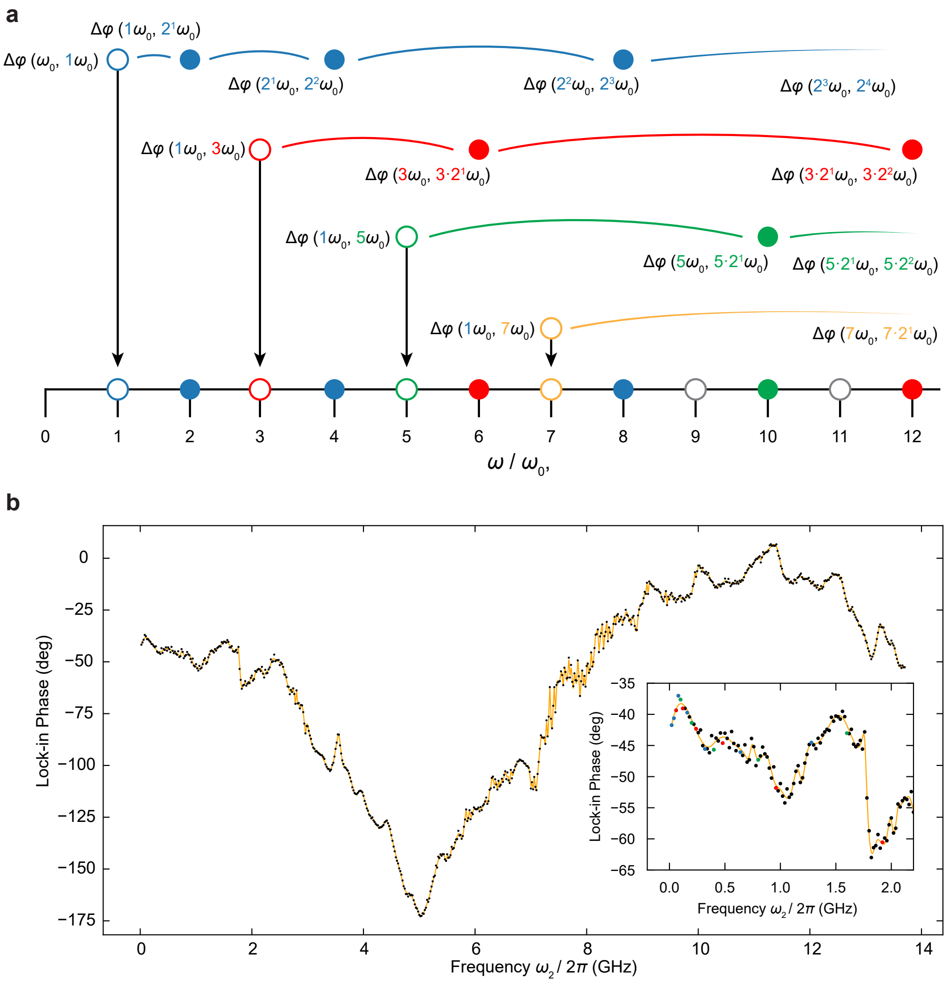

Fig. 5.5 | PTF frequency pair sweep. a Method to combine phase doubling series to obtain the PTF starting from a base frequency ω_0. The horizontal axis represents all ω_2 in the frequency pair sweep of $\Delta\varphi$. Filled points correspond to experimentally measured $\Delta\varphi(\omega_2/2, \omega_2)$ within doubling series, which are represented by different colours. Open points correspond to phase differences $\Delta\varphi(\omega_0, \omega_2)$ relative to ω_0 that are obtained from interpolation in the PTF based on doubling series measured previously to the series corresponding to the point. Open points are thus not measured. The first series (blue) trivially starts with $\Delta\varphi(\omega_0, \omega_0) = 0$. **b** Lock-in phase recorded for different frequency pairs, which is equivalent to $\Delta\varphi(\omega_2/2, \omega_2)$ up to a constant phase offset. The chosen base frequency $(\omega_0/2\pi)$ is 10 MHz. The orange line is a B-spline interpolation with smoothness parameter $N/2$, with N = 685 the number of datapoints. The tip height feedback loop was turned on, with a setpoint current 20 pA at -90 mV. The total times per data point differs per frequency range. Below 3 GHz: 9 s lock-in settling time, 9 s averaging time. Higher than 3 GHz: 45 s lock-in settling time, 6 s averaging time. Inset: a zoom-in on the lower frequencies, with datapoints coloured in accordance with the filled points in (**a**).

5.8.2. EXPERIMENTALLY MEASURED PHASE DIFFERENCES

The lock-in phases recorded in the frequency pair sweep, equivalent to $\Delta\varphi(k\omega_0, 2k\omega_0)$ up to a constant shift due to the phase between the signal and the AWG-generated lock-in reference input, are plotted against ω_2 in fig. 5.5b for a data set with ω_0 = 10 MHz and a maximum ω_2 of 13.7 GHz. We find that the phase differences are never larger than half a period (180°) and the feature size is generally larger than our choice for ω_0. This justifies the interpolation scheme we will use to obtain the PTF. The signal-to-noise ratio could be improved upon for some frequency sections, like 7 to 9 GHz. The lock-in amplitude is significantly lower there than other sections, so this worse performance is related to a reduced rectification current signal strength.

We note that fig. 5.5b is a composite, built from separate measurements with different RF amplitudes and also different averaging times. For ω_2 up to 3 GHz, the amplitudes are determined by our ATF to achieve an equal RF amplitude for all frequencies in the junction. See table 5.1a for the implementation in the AWG. However, we found that this choice caused the atom under the tip to move away at some specific frequency pairs.

Table 5.1 | RF amplitude protocols for a PTF frequency sweep. a Protocol to select the relevant voltage amplitudes in the AWG when generating the sum of a pair of RF frequencies for a PTF measurement (eq. (5.8)), when attempting to get an equal RF amplitude in the junction for all frequencies based on the ATF. The amplitude $\tilde{A}_1$ (or $\tilde{A}_2$) at the worst frequency with most loss is taken as 1 V (the AWG's maximum) and amplitudes at all other frequencies are taken relative to this. The sum of $\tilde{A}_1$ and $\tilde{A}_1$ (left column) then determines the AWG channel output A_{AWG} and the in-file amplitudes (their sum must be between 0 and 1) in the waveform segment files. Different ranges have different protocols to work within the limitations of the AWG, like the min and max A_{AWG}. A minimum in-file amplitude of 0.2 was selected to avoid discretization issues within the 8-bit voltage resolution. **b** Alternative approach of setting the voltage amplitudes in a PTF measurement with handpicked A_{AWG} values for different frequency ranges. In this protocol, the in-file amplitudes are fixed to $\tilde{A}_1$ = 0.34 and $\tilde{A}_2$ = 0.66.

a

$\tilde{A}_1 + \tilde{A}_2$ (mV)	AWG channel output A_{AWG} (mV)	in-file waveform amplitude ω_1	in-file waveform amplitude ω_2
< 75	75	$\max\left(0.2, \frac{\tilde{A}_1}{A_{AWG}}\right)$	$\max\left(0.2, \frac{\tilde{A}_2}{A_{AWG}}\right)$
75 - 100	$\tilde{A}_1 + \tilde{A}_2$	$\max\left(0.2, \frac{\tilde{A}_1}{A_{AWG}}\right)$	$\max\left(0.2, \frac{\tilde{A}_2}{A_{AWG}}\right)$
> 1000	1000	$\frac{\tilde{A}_1}{\tilde{A}_1+\tilde{A}_2}$	$\frac{\tilde{A}_2}{\tilde{A}_1+\tilde{A}_2}$

b

ω_2 (Hz)	A_{AWG}(mV)
0-200M	75
200M-2.6G	100
2.6G-5.5G	250
5.5G-9.1G	150
9.1G-13.7G	250

This might be related to our imposed minimum amplitude in the AWG waveform file of 0.2 that is required to define the complex signal in the waveform without discretisation artifacts within the limited 8-bit voltage resolution. This can cause unintentionally high RF amplitude in the junction that could have moved the atom.

Without being able to quickly pinpoint the pairs with defective amplitudes, we fell back to hand-selected amplitudes for certain frequency ranges. These are listed in table 5.1b. We also found that these amplitude choices resulted in better signal-to-noise in some frequency regimes, likely due to the non-trivial bias and amplitude dependencies discussed in section 5.7. Although it performed worse for other sections, like 6.60 to 7.04 GHz, for which we again fell back to measurements with ATF-defined amplitudes. In most frequency sections, both amplitude approaches performed similarly.

5.9. BUILDING UP THE PTF

The process of combining consecutive doubling series to build up the PTF $\varphi(\omega)$ is illustrated in fig. 5.6a, b. The phase of the base frequency from each doubling series is obtained from an interpolation curve through all previously placed series, which adds more points to the PTF that can be used to interpolate for additionally measured doubling series from the lock-in phase measurements in fig. 5.5b. This results in the full phase transfer function $\varphi(\omega)$ plotted in fig. 5.6c.

5.9.1. DEFINING A ZERO PHASE POINT

The initial doubling series, starting at $\omega_2 = 2\omega_0$, does not have any previous series for interpolation to determine its base frequency phase at ω_0. Trivially, $\Delta\varphi(\omega_0, \omega_0) = 0$, so we could define $\varphi(\omega)$ relative to ω_0. However, as mentioned already, the measured lock-in phase also contains an offset in phase fixed for all frequencies due to the delay between tunneling signal and lock-in reference input, which is hard to calibrate, so the measured lock-in phase for at $\omega_2 = 2\omega_0$ is not equal to $\Delta\varphi(\omega_0, 2\omega_0)$. A practical solution is to also set $\Delta\varphi(\omega_0, 2\omega_0) = 0$ by subtracting the measured lock-in phase at $\omega_2 = 2\omega_0$ from the measured lock-in phases at all frequencies. This constitutes a change of definition in the zero point of the phase that does not change the relative phase relations, and thus can be applied freely. This phase subtraction can also be interpreted as an overall fixed time delay added to a signal by the PTF.

Rather than subtracting directly from $\Delta\varphi$, we applied the transformation to $\varphi(\omega)$ at the very end after the cumulative summing, where it corresponds to a slope subtraction. For the plots of the full PTF in fig. 5.6, the transformation was applied by first subtracting a linear fit and then adding an offset such that $\varphi(2\omega_0) = 0$. Without this transformation, the finite measured lock-in phase at $\omega_2 = 2\omega_0$ results in a large slope in the PTF plot that would be physically valid, but that obscures its features.

5.9.2. SPLINE INTERPOLATION FOR THE BUILD-UP

The cumulative build-up process of the PTF is particularly sensitive to lock-in phase noise in the low frequencies. The errors in the initial datapoints add up in their own series, but also all other doubling series because of the required interpolations. The

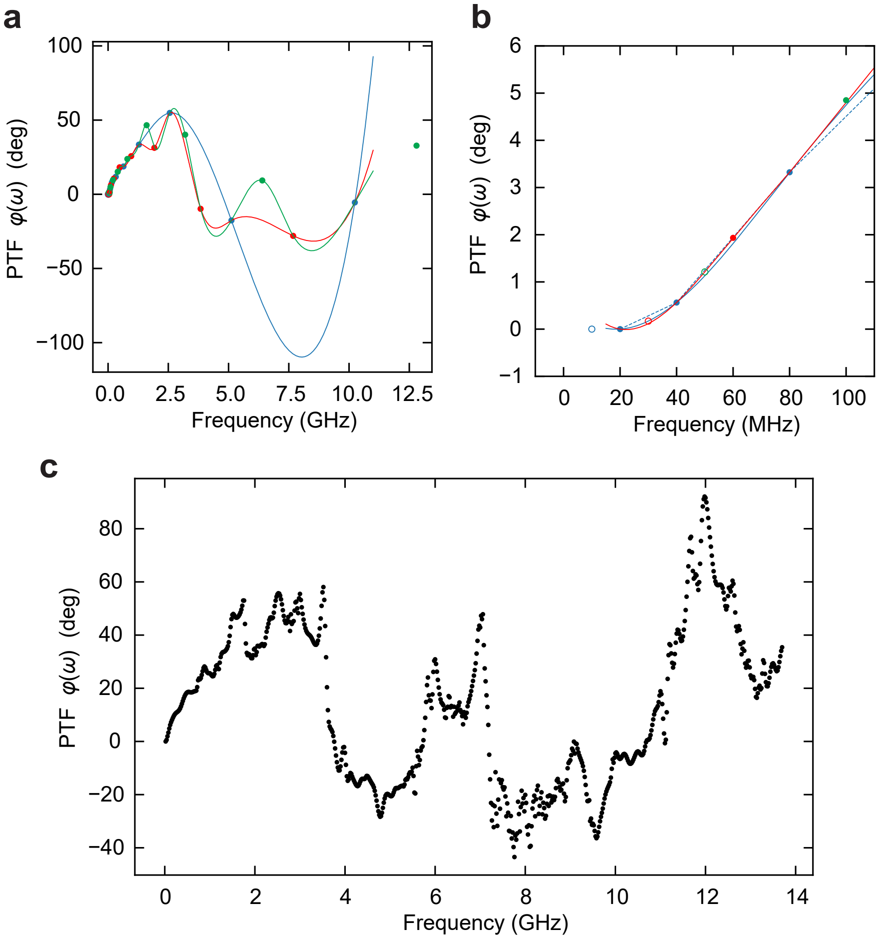

Fig. 5.6 | The phase transfer function. a Interpolation process to combine consecutive doubling series to build up the PTF. **b** is a zoom-in of the first 5 PTF points (filled markers) derived from measured lock-in phases. The phases at the series base frequencies (open markers) are obtained from a B-spline interpolation (solid lines) between PTF points from previously placed doubling series. The colours correspond to series in fig. 5.5a. Blue is measured first, then red, then green. Therefore, as can be seen in (**b**), the PTF of the red base frequency is determined by the spline interpolation between filled blue markers (blue solid line). The blue dashed line represents a linear interpolation that was not used. In turn, the green base frequency phase is obtained by the spline interpolation through all blue and red markers (red solid line). **c** Phase transfer function $\varphi(\omega)$ as a function of frequency, built from all doubling series present in the lock-in data from fig. 5.5b. A linear slope has been subtracted for all plots in this figure, and the phase at 20 MHz is defined as zero degrees.

interpolation method used to place the first handful of series thus plays an important role. We opted for interpolation of the PTF with (cubic) B-splines [11], rather than a linear interpolation used by Baumann *et al*.

A curve parameterizations with a B-spine produces a smooth curve, which is what we expect for the PTF. As can be seen in fig. 5.5b, a linear interpolation that does not factor in the curvature would have been less accurate in placing the base frequency of the red series, and this error would have propagated. This difference diminishes with smaller step size $2\omega_0$, but that increases the measurement time significantly. Furthermore, opposed to some other smooth curve parameterizations, like Taylor series, splines parameterize homogeneously over the full frequency range.

5.9.3. SPLINE SMOOTHENING OF LOCK-IN PHASES TO SUPPRESS NOISE EFFECTS

Due to the cumulative addition, we find that small, single datapoint features in the PTF at the low frequencies, that could either be signal or noise, get repeated as large structures in the higher frequencies. Small erratic spikes turn into periodic 'mountains'. The measured lock-in phase (fig. 5.5b) is a source of noise that is often responsible for producing such erroneous structures. We found that the periodic structures originating from lock-in phase noise overshadowed the PTF features already above ~1 GHz. This is seen most clearly in the upper plot of the PTF in fig. 5.7, where the measured lock-in phase is used to build the PTF without any additional data processing of the lock-in phase.

Our current solution, which is also an addition to the methods outlined by Baumann *et al.*, is to smoothen the measured lock-in phase as a function of frequency before sampling it to build the PTF. A smooth parameterization avoids the small spikes at the single datapoint level. We give up some of the frequency resolution for the smoothening to obtain only the broader features of the PTF, but avoid being overshadowed by the periodic structures for the majority of the frequency range.

We use a fit with a cubic spline for the parameterization of the lock-in phase, now with a finite smoothening factor s. (The previously mentioned splines for interpolation of the PTF during build-up do not use any spline smoothening). The spline used in our final PTF result is plotted together with the lock-in phase data in fig. 5.5b. The spline smoothening acts like a fit through noisy data, where s dictates how closely the spline must follow the position datapoints.

The smoothening factor s is a chosen input parameter in our analysis with a SciPy implementation [12]. Resulting PTFs for different choices of s are plotted infig. 5.7. The trade-off between avoiding the repeating patterns and the loss of detail in the PTF with increasing smoothness can clearly be observed. It is hard to quantify an optimal choice. An independent verification of the accuracy of the obtained PTF is required to properly distinguish between repeating structures originating from the real PTF and structures originating from noise. The save choice is to lean towards the smoother side. The spline fitting becomes less critical with better signal-to-noise ratio in the lock-in phase measurement.

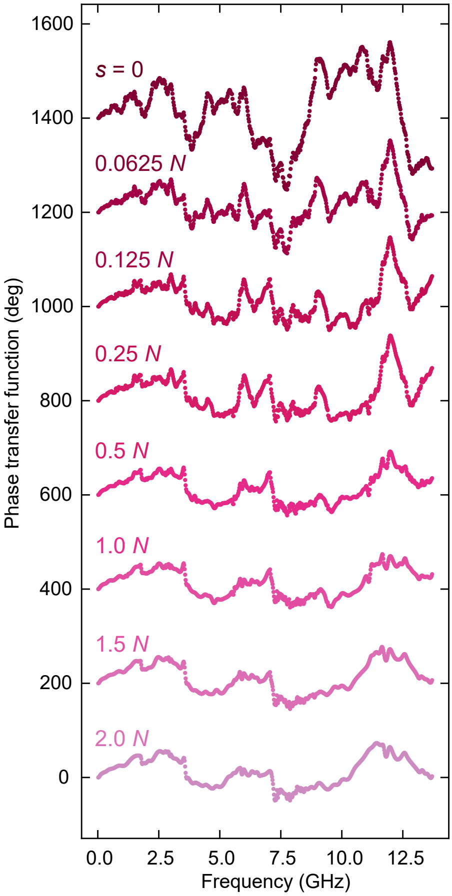

Fig. 5.7 | Spline smoothness dependence. Various PFT versions obtained using cubic spline parameterizations of the same lock-in phase measurements (Fig. 4b) with different smoothness factors *s*. The plots are offset vertically. The values of *s* are given as fractions of the number of frequency datapoints *N* = 685. We deemed *s* = 0.5*N* to be the best choice in this case. The broad features in the PTF that become present at 0.5*N* do not alter much more in even smoother options, while additional detail is still lost compared to 0.5*N*.

5.10. DC PULSE SHAPE CORRECTION

DC pump-probe delay time spectroscopy in STM setups [3], as describe in more detail in chapters 3 and 4, is the main application that drove the need for a PTF measurement method in addition to existing ATF methods. In DC pump-probe delay time spectroscopy, an initial DC voltage pulse pumps the system under study to a non-equilibrium state and, after a certain controlled delay time, a probe pulse reads out the change in conductance. This gives information about the time-evolution of the system after the delay time in a time-averaged current signal. This holds even if the delay time is much shorter compared to the time resolution in a direct current time trace, which is limited by the signal-to-noise ratio. The time resolution for pump-probe methods is, instead, limited by the pulse width. A shorter pulse can be used to distinguish smaller steps in delay time.

In turn, the minimum pulse width is limited by the voltage transfer function. A rectangular pulse consists of many frequency components, with the most significant frequency the inverse of the pulse width and other components at higher frequencies. As evidenced by the growing amount of ESR-STM setups operating at least up to 15

GHz, significant transmission through STM cabling of voltage amplitudes in the GHz range is not a bottleneck for pulse widths below 1 ns. Still, up until recently [2] no examples existed in the STM literature of DC pump-probe results using shorter pulse widths than the nanosecond range. These time scales were only be achieved with THz STM setups, which is have their own limitations [13, 14]. In these recent results with DC pulses, then, shorter pulses were only possible with knowledge of the PTF.

Without correcting for the PTF, the different frequency components in the rectangular pulse arrive at the junction with shifted timings. Consequently, the sinewaves do not add constructively when they need to and the pulse shape gets deformed. The deformed pulse is generally wider than the intended rectangular pulse shape, softening the sharp edges and sometimes creating side pulses. The non-uniform PTF has thus been the limiting factor for DC pulse widths in STM experiments.

The distortion of the pulse arriving at the junction can be corrected for by altering the pulse shape at the pulse generator to compensate for the effects of the voltage transfer function. Essentially, the corrected pulse at generation undergoes amplitude losses and phase shifts such that the pre-distortion cancels out and the pulse arrives at the junction exactly as the intended rectangular pulse. The corrected pulse shape can be quite complex. Therefore we use our AWG as the generator for corrected pulse waveforms. The AWG can in principle compensate for frequency components up to 25 GHz, although the transfer function has only been determined up to 13.7 GHz. In any case, a pulse width in the junction below 1 ns should be within reach with the AWG.

5.11. CORRECTED WAVEFORMS FOR DC PULSE AUTOCORRELATIONS

As is also outlined in section 4.1, we can use a DC pulse autocorrelation measurement to verify that the corrected pulse arriving at the junction is indeed rectangular. We sweep the delay time over a range where the pump and probe (partly) overlap. With a non-linear IV curve, in this case the earlier discussed conductance step in Ti on the oxygen binding site of MgO/Ag, sections with overlapping pulses with double the voltage do not necessarily contribute double the current, while you do get double the current with separated sections. The total time-averaged current in the pump-probe measurement then depends on the fraction of the pulse overlap. The pump-probe signal as a function of delay time is thus akin to an autocorrelation of the two pulses. For two identical rectangular pulses, the expected pump-probe signal is an isosceles triangle with a base width equal to twice the pulse width. If we experimentally observe a DC pulse autocorrelation shape that deviates from a triangle, the pulse correction must not have worked perfectly.

This pulse correction experiment also acts an independent verification of our transfer function measurement methods. In particular, the acquired PTF is untested outside of the very method we used to determine it, and some assumptions were made during the data analysis. A non-triangular shape of the resulting autocorrelation measurement indicates, most likely, a mistake in the determined phase or amplitude transfer function. The result of a DC pulse autocorrelation measurement is phase sensitive in this way, although it cannot in general be used to determine the PTF because the pulse autocorrelation is not uniquely determined by the pulse shape. One specific autocorrelation curve shape could be the result of multiple different DC pulse shapes in the junction.

5.11.1. Implementation of the pulse correction

Mathematically, the pulse correction consists of applying the inverse of the full transfer function on the discrete Fourier transform of the waveform $V(t)$ that contains the intended pulse shape in the junction, and then inversing the Fourier transform. The waveform $\tilde{V}(t)$ that needs to be generated by the AWG can then be expressed as

$$\tilde{V}(t) = \mathcal{F}^{-1}\left\{T^{-1}\left[\mathcal{F}\{\,V(t)\,\}\right](\omega)\,\right\}(t) \tag{5.15}$$

with

$$T^{-1}\left[\,\mathcal{F}\{V(\omega)\,\}\,\right] = \frac{e^{-i\,PTF(\omega)}}{|ATF(\omega)|}V(\omega) \tag{5.16}$$

Here, $\mathcal{F}\{\ \}(\omega)$ and $\mathcal{F}^{-1}\{\ \}(t)$ are the discrete and inverse discrete Fourier transform operators, respectively.

A few practical limitations give rise to some additions to this idealized protocol. First of all, we add the assumption that all frequencies below the smallest measured frequency in the transfer function have an ideal transmission without loss or a phase shift. Above the largest frequency, we assume loss equal to the largest measured loss and a phase shift equal to that of the maximum frequency in the measured range. Since the measured frequency data points in the transfer function might not be commensurate with the sampling rate of the AWG, we use a spline interpolation of the ATF and PTF to be able sample them at any convenient frequency.

5.11.2. Resulting waveforms

Examples of corrected autocorrelation waveforms are shown in fig. 5.8. The most striking features are the high amplitude peaks around the pulse edges. These sharp edge features correspond to the highest frequency components in our waveforms around the Nyquist limit of the 64 GSa/s AWG sampling rate, which is also the range with the largest losses. They are significant components to get sub 30 ps rise and fall times, but are not as essential for longer pulse widths like 1 ns. Unfortunately, the large in-file amplitude required for these edge components suppresses other frequency components within the dynamic range of the AWG. These other components get normalized to lower amplitudes, resulting in an overall lower amplitude of the pulse in the junction. Possibly, this is too low to observe signal from the pulses compared to the noise, even at maximum AWG output power. Furthermore, some significant pulse features even fall below the 8-bit voltage resolution of the AWG samples and are therefore not present in the corrected pulse when generated by the AWG.

A potential solution, which we did not use for our experiments here, is to assert a maximum waveform amplitude on the initially normalized waveform before 8-bit discretization by clipping down to a threshold amplitude, and then renormalize. In this

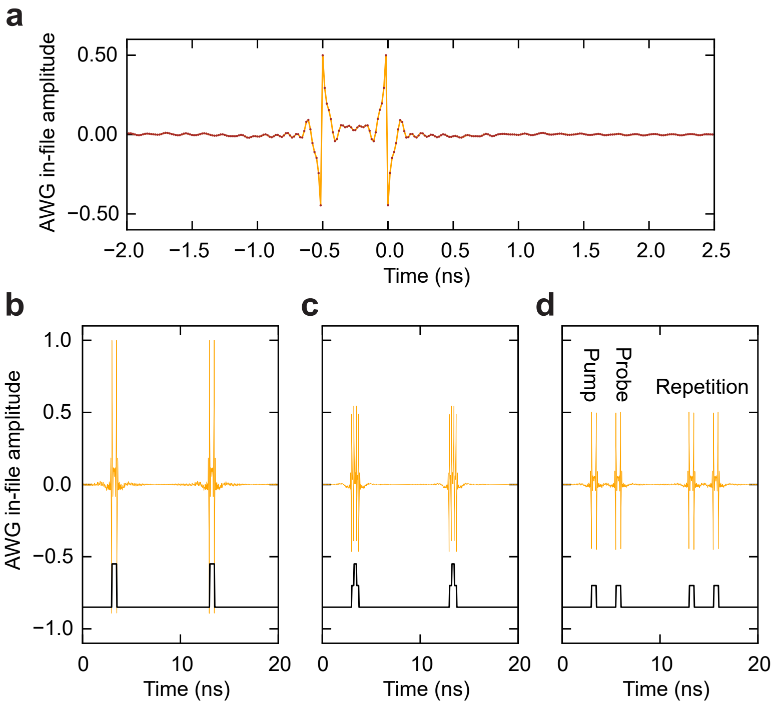

Fig. 5.8 | Corrected AWG waveform segments. **a** Section of an AWG waveform segment containing a single rectangular pulse after correction for the voltage transfer function. All sample voltages are represented in the AWG waveform file by an in-file amplitude between -1 and 1 that correspond to the fraction of the AWG maximum output voltage that can differ between experiments. The AWG sampling rate is 64 GSa/s. **b-d** Full AWG waveform segments with the minimal segment length of 1280 samples. These contain pulses for DC pulse autocorrelation measurements at different probe delay times, with correction for the transfer function applied. The black lines indicates the intended pulse shape in the junction (scaled and with an offset downwards). For (**b**), the pump and probe are overlapping entirely. For (**c**), there is still some overlap. In (**d**), the pump and probe are separated by the probe delay time. In all cases, the waveform segment contains a repetition of the pump and probe for additional signal strength in the time-averaged current.

way, the dynamic range of the AWG is better utilized for pulse shape details in most frequency components with larger pulse amplitudes in the junction, at the cost of undercompensating for the loss of these high frequencies. Since this might affect the rise times at the pulse edges, one could say that we reached the ATF limit in our pulse width, rather than the PTF.

The detection protocol in the DC pulse autocorrelation experiment will be a lock-in contrast scheme. The A cycle consists many repeats of a short waveform containing the pump and probe pulses, with different overlap for each datapoint. The B cycle will contain the same waveform with opposite polarity for optimal contrast of the pulse overlap current signal.

The length of this short waveform should be minimized for an improved signal-to-noise ratio: more cumulative pulse overlap current signal within the same averaging time of a lock-in cycle. The theoretical limit on the waveform width is the maximum delay time plus both effective pulse widths in the junction. However, the latter is an unknown initially, risking overlap between neighbouring waveform repeats if the pulse correction is not ideal. A more practical choice is at least twice the maximum delay time, acting as a range around the centred pump pulse.

This choice of waveform length is actually smaller than the minimum possible waveform length in the AWG of 20 ns (1280 samples at 64 GSa/s) for all of the measurements in this section. So for the smallest pulse widths we have multiple repeats of the pump-probe events within one AWG waveform. We apply the inverse transfer function to the entire 20 ns waveform. The full 20 ns autocorrelation waveforms for a pulse width of 500 ps, including a repeat, are shown in fig. 5.8b, c, and d for multiple probe delay times τ.

5.12. PULSE-CORRECTED AUTOCORRELATIONS

5.12.1. EXPERIMENTAL RESULTS

We start by establishing a baseline for the pulse shape quality with autocorrelation measurements using uncorrected pulses. The uncorrected pulses have a rectangular shape at the pulse's generation by the AWG, at varying pulse widths w = 2 ns, 1 ns, 500 ps, 203.125 ps, and 109.375 ps. All of these widths are integer number of AWG samples at 64 GSa/s. The number of samples in these pulse widths are 128, 64, 32, 13, and 7, respectively.

The uncorrected autocorrelation results are shown in fig. 5.9, where they can also be compared with the triangle shape that we expect for an ideal rectangular pulse in the junction. The triangle is a good match for w = 2 ns, but clear deviations are already visible for w = 1 ns. As the pulse width gets smaller, significant side peaks remain present with a spacing of approximately 1 ns away from the triangle centre. This indicates the effective width of the bulk of the pulse remains limited to ~1 ns no matter the generated pulse width, if the pulses are not corrected for the transfer function. The centre peak does become more narrow with decreasing w, with the centre peak in w = 500 ps still matching the upper part of the triangle. However, even the centre autocorrelation peak does not fit the triangle anymore for w = 109.375 ps.

Next, we repeat the autocorrelation measurements with waveform segments that are corrected for the voltage transfer function, where we use the same pulse widths as before as the intended pulse shapes in the junction. The results are also plotted in fig. 5.9 together with the uncorrected autocorrelation results.

As an initial observation, we see that the signal strength is significantly reduced for the corrected pulses compared to the uncorrected measurements. This was expected because, as mentioned in the previous section, asserting the proper ratios between the frequencies components with least and most loss, according to the ATF, pushes the amplitude of most components downwards relative to the maximum AWG output voltage, which produces the overall lower pulse heights in the junction. This is why implementations that improve the signal-to-noise ratio, like the repetitions within one waveform segment, are crucial for experiments with these short low-amplitude pulses. In future experiments, it might be useful to select pulse widths that correspond to low-loss frequency ranges in the ATF, which was not the case for *w* = 109.375 ps, to get higher pulse amplitudes in the junction.

5.12.2. DETAILED DISCUSSION

Comparing the autocorrelations to the ideal triangles, we can see that the corrected measurements better adhere to the triangle shapes than the uncorrected ones. Therefore we can conclude that the transfer function correction does produce more accurate rectangular pulses in the junction. For *w* = 500 ps, the correction is able to fully

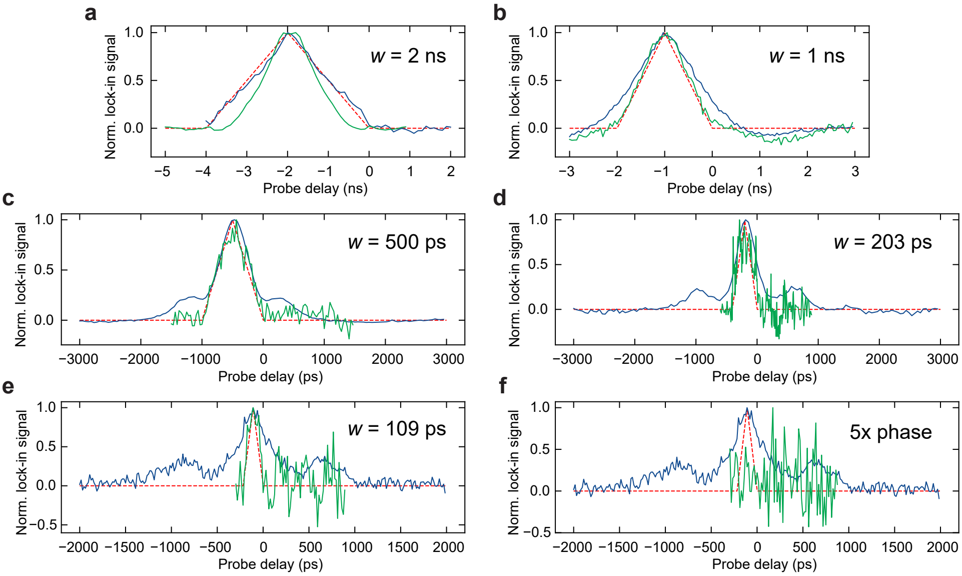

Fig. 5.9 | Autocorrelations of PTF-corrected DC pulses. a-e Autocorrelation measurements with different pulse widths *w*. Uncorrected pulses are in blue, corrected pulses in green, and the ideally expected autocorrelation triangles for DC pulses are plotted with red dashed lines. For better comparisons between measurements, all probe-delay spectroscopies have vertical offsets removed such that the edges corresponds to zero lock-in signal and they are subsequently normalized. Measurements were taken at constant tip height at a DC bias of 60 mV, with a setpoint current of 10 pA at 60 mV. **f** Autocorrelation measurements with *w* = 109 ps, but with a pulse shape correction with the phase TF function subtracted 5 times, instead of one time. The blue uncorrected comparison plot is the same as for (**e**). Plots in (**d**), (**e**), and (**f**) are averaged over multiple measurements. The effective total averaging times per datapoint are (**a**) 2 s, (**b**) 50 s, (**c**) 60 s, (**d**) 180 s, (**e**) 2640 s, (**f**)660 s.

compensate for side peaks, making these corrected pulses viable for future pump-probe experiments without any further complications. However, we were unable to completely removed side peaks for the shorter w = 203.125 ps and w = 109.375 ps. The correction in the former does improve significantly over the uncorrected side peak sizes, but the latter correction only resulted in similar-sized side peaks of a different shape. The declining quality of the pulse shape correction for shorter pulses could be linked to a worse accuracy of the determined phase transfer function for higher frequencies, which contain cumulative errors from lower frequencies.

At the same time, the pulse shaping did achieve a more narrow centre peak of the autocorrelations for both w = 203.125 ps and w = 109.375 ps. The presence of a narrow peak feature does imply a sensitivity to fast dynamics. So these pulses still hold potential for pump-probe applications at their respective intended time resolutions, especially for w = 203.125 ps with only a small side peak remaining. A more complex data analysis method must then be used for w = 109.375 ps to disentangle the pulse shape features from the time evolution of the physical system under study. This sort of analysis is, for example, commonplace for pump-probe (or time-domain) spectroscopy in THz-STM because single-cycle THz pulses can only be generated by optical rectification into shapes with zero time-averaged electrical field, and thus always involve some oscillatory features [14–16].

An exception to the improving pulse shapes is w = 2 ns, where we observed a too narrow autocorrelation shape with the correction applied. This could indicate that the phase transfer function might not be as accurately determined in the MHz range as we hoped, but it could also be a consequence of lost pulse shape details in the suppressed frequency components with high amplitude transmission due to 8-bit discretisation. Fortunately, the w = 2 ns pulses are shown to already be rectangular without corrections, so the inadequate pulse correction should not be a limitation for experiments using this pulse width.

5.12.3. EXPERIMENT WITH INTENTIONALLY ERRONEOUS CORRECTION

To confirm the consistency of our methodology, we also performed an autocorrelation measurement with an intentionally erroneous pulse correction for w = 109.375 ps. For this experiment, instead of shifting the phase of a frequency component by the determined PTF, we shift each phase 5 times as far in the same direction. The autocorrelation result is shown in fig. 5.9f.

As can be expected, the produced pulse shape in the junction is far from rectangular. We do not even observe a central peak in the autocorrelation. This result serves as an alternative check: making changes to the phase components really does affect the pulse shape significantly. This intentionally erroneous correction shows that, if we would have gotten an entirely incorrect PTF and applied the wrong phase shifts, as we have effectively done for fig. 5.9f, this would not have resulted in the more rectangular pulses we observed in the other measurements with corrections. Therefore, we can conclude that the observed improvement in the pulse shape by the corrections can truly be attributed to the particular PTF that we determined in section 5.9. In other words, we have verified that our measured PTF is at least mostly correct.

5.13. CONCLUSION

In this chapter, we have shown that existing *in-situ* methods in literature to measure both the voltage amplitude (ATF) and phase transfer function (PTF) of RF cabling in STMs can be successfully implemented with an AWG as the RF signal generation source. Moreover, we have explored modifications to the existing method. For the ATF, we have shown that a method based on feedback control can be an effective alternative for power sweep mapping that could require less effort for more accurate results. For the PTF, we introduced a lock-in detection method with a direct readout of the phase signal using the AWG, which speeds up measurement times. This also enabled a more thorough investigation of the bias dependence of the PTF rectification current signal that uncovered details that are relevant in setting up PTF measurements as a function of frequency.

Subsequently, we applied the newfound amplitude and phase transfer functions for pulse shaping to correct for the deformation of DC pulses at the STM tunnelling junction caused by the transfer function. The overarching goal was to lower the minimum pulse width available for future experiments. We showed experimentally that the pulse correction did significantly improve the rectangular pulse shape in the junction with DC pulse autocorrelation measurements using pump-probe delay time spectroscopy. This also independently verified our transfer function measurement methods were accurate. As such, we were able to reduce the minimum pulse width for DC pulses from 2 ns without correction to 500 ps, or even 203 ps with minor side peaks.

There are some evident improvements available for future transfer function measurements with the AWG. For the feedback in the ATF method, the error should be defined in dBm space for stable convergence in the entire dynamic range of the AWG. Furthermore, the lock-in phasing, crucial to prevent leakage of the out-of-phase signal into the rectification signal, should be optimized more carefully for this ATF method. The PTF could be measured again in the future with more averaging time to improve the signal-to-noise ratio in some frequency ranges. More investigations into interpolation methods to build up the PTF are also required to find a more stable and optimized data analysis process. These method improvements could lead to a better pulse shape correction of DC pulses, resulting in an even shorter minimum pulse width.

With sub-nanosecond DC pulses now established, we can start investigating faster spin dynamics at the atomic scale. The shorter pulses enable probing even shorter spin lifetimes, but also faster coherent spin dynamics [7]. Dynamics in engineered adatom systems with larger than GHz exchange couplings are now within reach, which, compared to more weakly couped spins, can be used to apply more quantum coherent operations within the same spin coherence time of the adatom. Furthermore, these coupling energy scales could also be larger than the thermal energy of the spin at the operating temperature of our STM (0.4 K), potentially leading in better initialization.

Shorter DC pulses could also be used to probe systems other than atomic spins. For example, it might be possible to locally manipulate and probe the coherent time-evolution of surface acoustic waves (SAWs) propagating with GHz frequencies, a range which has recently become technologically relevant for quantum devices [17]. Time-resolved DC pump-probe would complement existing continuous-wave STM methods to probe SAWs [18, 19]. Furthermore, DC pump-probe in STM has been applied in the past to study ionization in dopants in silicon, which happens at a wide range of time-scales up to the GHz regime and depends strongly on the atomic environment [20, 21]. Our improvements in the available time resolution can widen its applicability to understand dopant charge dynamics in more exotic systems, such as charge trapping in cuprate superconductors [22].

REFERENCES

[1] W. Paul, S. Baumann, C. P. Lutz and A. J. Heinrich. 'Generation of constant-amplitude radio-frequency sweeps at a tunnel junction for spin resonance STM'. In: *Review of Scientific Instruments* 87.7 (2016). ISSN: 10897623. DOI: `10.1063/1.4955446`.

[2] S. Baumann, G. McMurtrie, M. Hänze, N. Betz, L. Arnhold, L. Malavolti and S. Loth. 'An Atomic-Scale Vector Network Analyzer'. In: *Small Methods* 8.9 (2024), pp. 1–9. ISSN: 2366-9608. DOI: `10.1002/smtd.202301526`.

[3] S. Loth, M. Etzkorn, C. P. Lutz, D. M. Eigler and A. J. Heinrich. 'Measurement of Fast Electron Spin Relaxation Times with Atomic Resolution'. In: *Science* 329.5999 (2010), pp. 1628–1630. ISSN: 0036-8075. DOI: `10.1126/science.1191688`.

[4] Y. Chen, Y. Bae and A. J. Heinrich. 'Harnessing the Quantum Behavior of Spins on Surfaces'. In: *Advanced Materials* 35.27 (2023). ISSN: 0935-9648. DOI: `10.1002/adma.202107534`.

[5] L. Arnhold. 'Surface-governed dynamics of atomic-scale magnetic moments'. PhD thesis. University of Stuttgart, 2024. DOI: `10.18419/opus-15626`.

[6] D. Sostina, L. Arnhold, L. M. Veldman, N. Betz, W. Wernsdorfer, S. Baumann, F. Delgado, P. Willke and S. Loth. 'Tuning the orbital state of a single spin on a surface'. In: *Forthcoming* ().

[7] L. M. Veldman, L. Farinacci, R. Rejali, R. Broekhoven, J. Gobeil, D. Coffey, M. Ternes and A. F. Otte. 'Free coherent evolution of a coupled atomic spin system initialized by electron scattering'. In: *Science* 372.6545 (2021), pp. 964–968. ISSN: 0036-8075. DOI: `10.1126/science.abg8223`.

[8] L. Farinacci, L. M. Veldman, P. Willke and S. Otte. 'Experimental Determination of a Single Atom Ground State Orbital through Hyperfine Anisotropy'. In: *Nano Letters* 22.21 (2022), pp. 8470–8474. ISSN: 1530-6984. DOI: `10.1021/acs.nanolett.2c02783`.

[9] L. M. Veldman, E. W. Stolte, M. P. Canavan, R. Broekhoven, P. Willke, L. Farinacci and S. Otte. 'Coherent spin dynamics between electron and nucleus within a single atom'. In: *Nature Communications* 15.1 (2024), p. 7951. ISSN: 2041-1723. DOI: `10.1038/s41467-024-52270-0`.

[10] E. W. Stolte, J. Lee, H. G. Vennema, R. Broekhoven, E. Teng, A. J. Katan, L. M. Veldman, P. Willke and S. Otte. 'Single-shot readout of the nuclear spin of an on-surface atom'. In: *Nature Communications* 16.1 (2025), p. 7785. ISSN: 2041-1723. DOI: `10.1038/s41467-025-63232-5`.

[11] P. Dierckx. 'An algorithm for smoothing, differentiation and integration of experimental data using spline functions'. In: *Journal of Computational and Applied Mathematics* 1.3 (1975), pp. 165–184. ISSN: 03770427. DOI: `10.1016/0771-050X(75)90034-0`.

[12] P. Virtanen *et al.* 'SciPy 1.0: fundamental algorithms for scientific computing in Python'. In: *Nature Methods* 17.3 (2020), pp. 261–272. ISSN: 1548-7091. DOI: `10.1038/s41592-019-0686-2`.

[13] T. L. Cocker, V. Jelic, M. Gupta, S. J. Molesky, J. A. Burgess, G. D. L. Reyes, L. V. Titova, Y. Y. Tsui, M. R. Freeman and F. A. Hegmann. 'An ultrafast terahertz scanning tunnelling microscope'. In: *Nature Photonics* 7.8 (2013), pp. 620–625. ISSN: 17494885. DOI: `10.1038/nphoton.2013.151`.

[14] T. L. Cocker, V. Jelic, R. Hillenbrand and F. A. Hegmann. 'Nanoscale terahertz scanning probe microscopy'. In: *Nature Photonics* 15.8 (2021), pp. 558–569. ISSN: 17494893. DOI: `10.1038/s41566-021-00835-6`.

[15] S. E. Ammerman, V. Jelic, Y. Wei, V. N. Breslin, M. Hassan, N. Everett, S. Lee, Q. Sun, C. A. Pignedoli, P. Ruffieux, R. Fasel and T. L. Cocker. 'Lightwave-driven scanning tunnelling spectroscopy of atomically precise graphene nanoribbons'. In: *Nature Communications* 12.1 (2021), pp. 1–9. ISSN: 20411723. DOI: `10.1038/s41467-021-26656-3`.

[16] V. Jelic, S. Adams, M. Hassan, K. Cleland-Host, S. E. Ammerman and T. L. Cocker. 'Atomic-scale terahertz time-domain spectroscopy'. In: *Nature Photonics* 18.9 (2024), pp. 898–904. ISSN: 17494893. DOI: `10.1038/s41566-024-01467-2`.

[17] P. Delsing, A. N. Cleland, M. J. Schuetz, J. Knörzer, G. Giedke, J. I. Cirac, K. Srinivasan, M. Wu, K. C. Balram, C. Baüerle, T. Meunier, C. J. Ford, P. V. Santos, E. Cerda-Méndez, H. Wang, H. J. Krenner, E. D. Nysten, M. Weiß, G. R. Nash, L. Thevenard, C. Gourdon, P. Rovillain, M. Marangolo, J. Y. Duquesne, G. Fischerauer, W. Ruile, A. Reiner, B. Paschke, D. Denysenko, D. Volkmer, A. Wixforth, H. Bruus, M. Wiklund, J. Reboud, J. M. Cooper, Y. Q. Fu, M. S. Brugger, F. Rehfeldt and C. Westerhausen. 'The 2019 surface acoustic waves roadmap'. In: *Journal of Physics D: Applied Physics* 52.35 (2019). ISSN: 13616463. DOI: `10.1088/1361-6463/ab1b04`.

[18] J. Heil, J. Wesner and W. Grill. 'Determination of displacements in ultrasonic waves by scanning tunneling microscopy'. In: *Journal of Applied Physics* 64.4 (1988), pp. 1939–1944. ISSN: 00218979. DOI: `10.1063/1.341747`.

[19] W. Rohrbeck, E. Chilla, H.-J. Fröhlich and J. Riedel. 'Detection of surface acoustic waves by scanning tunneling microscopy'. In: *Applied Physics A Solids and Surfaces* 52.5 (1991), pp. 344–347. ISSN: 0721-7250. DOI: `10.1007/BF00324777`.

[20] M. Rashidi, J. A. Burgess, M. Taucer, R. Achal, J. L. Pitters, S. Loth and R. A. Wolkow. 'Time-resolved single dopant charge dynamics in silicon'. In: *Nature Communications* 7 (2016), pp. 1–7. ISSN: 20411723. DOI: `10.1038/ncomms13258`.

[21] V. Jelic, K. Iwaszczuk, P. H. Nguyen, C. Rathje, G. J. Hornig, H. M. Sharum, J. R. Hoffman, M. R. Freeman and F. A. Hegmann. 'Ultrafast terahertz control of extreme tunnel currents through single atoms on a silicon surface'. In: *Nature Physics* 13.6 (2017), pp. 591–597. ISSN: 17452481. DOI: `10.1038/nphys4047`.

[22] K. M. Bastiaans, D. Cho, T. Benschop, I. Battisti, Y. Huang, M. S. Golden, Q. Dong, Y. Jin, J. Zaanen and M. P. Allan. 'Charge trapping and super-Poissonian noise centres in a cuprate superconductor'. In: *Nature Physics* 14.12 (2018), pp. 1183–1187. ISSN: 17452481. DOI: `10.1038/s41567-018-0300-z`.

6

Single-shot readout of the nuclear spin of an on-surface atom

There was a time, it seemed, that time itself was free and would go on forever.
Wanted to cling to it, but now I see its fading is its greatest treasure.

Jacob Collier ('Time To Rest Your Weary Head')

Nuclear spins owe their long-lived magnetic states to their excellent isolation from the environment. At the same time, a finite degree of interaction with their surroundings is necessary for reading and writing the spin state. Therefore, detailed knowledge of and control over the atomic environment of a nuclear spin is key to optimizing conditions for quantum information applications. While various platforms enabled single-shot readout of nuclear spins, their direct environments were either unknown or impossible to controllably modify on the atomic scale. Scanning tunneling microscopy (STM), combined with electron spin resonance (ESR), provides atomic-scale information of individual nuclear spins via the hyperfine interaction. In this chapter, we demonstrate single-shot readout of an individual ^{49}*Ti nuclear spin with an STM. Employing a pulsed measurement scheme, we find its lifetime to be in the order of seconds. Furthermore, we shed light on the pumping and relaxation mechanisms of the nuclear spin by investigating its response to both ESR driving and tunneling current. These findings give an atomic-scale insight into the nature of nuclear spin relaxation and are relevant for the development of atomically assembled qubit platforms.*

The results of this chapter were conceived in close collaboration with Jinwon Lee, Hester Vennema, Rik Broekhoven, Esther Teng, Allard Katan, Lukas Veldman, Philip Willke, and Sander Otte. Parts of this chapter have been published in *Nature Communications* **16**, 7785 (2025). [1]

6.1. INTRODUCTION

Nuclear spins are unique in that they combine subatomic length scales with generally long coherence times. These properties make them appealing candidates for quantum technological applications, while at the same time posing challenges for their readout. Ideally, one would detect the time-dependent behavior of a spin via a single-shot readout, as opposed to a time-averaged measurement. This enables systematically linking specific changes in an open quantum system to observed or controlled changes in its environment, with the potential for real-time feedback. Single-shot readout of individual nuclear spins was achieved in a number of platforms: optically addressed color centers [2–4], molecular break junctions [5], dopants in semiconductors [6, 7], and gate-defined quantum dots [8]. While it was shown to be possible to trace the spins in these systems over time with excellent accuracy, their direct environments were either unknown or impossible to controllably modify on the atomic scale.

Spins in individual atoms on surfaces, probed through scanning tunneling microscopy (STM), can be positioned with atomic precision [9]. This allows for engineering the environment, including spin-spin [10] as well as spin-orbit interactions [11, 12], and for building desired atomic-scale spin structures for the purpose of atomic-scale quantum simulation experiments[13–15]. Moreover, combining STM with electron spin resonance (ESR) [16] has enhanced the energy resolution and enabled a wealth of detailed studies on composite spin systems [17–21], including their quantum coherent evolution over time [22–24]. Recently, access to the nuclear spin was provided through resolving the hyperfine interaction [25], potentially introducing spins with much longer coherence times to the quantum simulation efforts using atoms on surfaces. While it has been shown that ESR-STM allows for both reading [26, 27] and directly driving nuclear spins [28], STM has thus far only sparingly been used to investigate nuclear spins in the time domain [29]. As such, no nuclear spin lifetimes have yet been reported, and it remains unclear what the dominant relaxation processes are.

In this work, we demonstrate single-shot readout of the nuclear spin state of a single Ti atom, expanding on ESR-STM methodology. We apply a fixed radio frequency (RF), tuned to drive the electron spin if and only if the nuclear spin has magnetization $m_I = -7/2$. If this condition is met, spin-polarized transport through the electron orbital results in a measurable increase in the tunneling current I_{ESR}. We observe that the current switches between its base value I_0 and the increased value $I_0 + I_ESR$ on the timescale of seconds. From this, we determine the intrinsic lifetime of the nuclear spin to be 5.3 ± 0.5 s, seven orders of magnitude longer than the lifetime of the electron spin on the same atom [17, 23]. In addition, we investigate how the lifetime is affected by the presence of tunneling electrons or a continuous RF signal.

6.2. SINGLE-SHOT READOUT

We investigate individual Ti atoms on the oxygen binding site of an MgO/Ag(100) substrate (see section 6.5), which have been shown to carry an electron spin $S = 1/2$ that can be ESR driven by an RF voltage at the STM junction [17], in an external magnetic field oriented out-of-plane. Ti has different isotopes carrying nuclear spins 0, 5/2, or

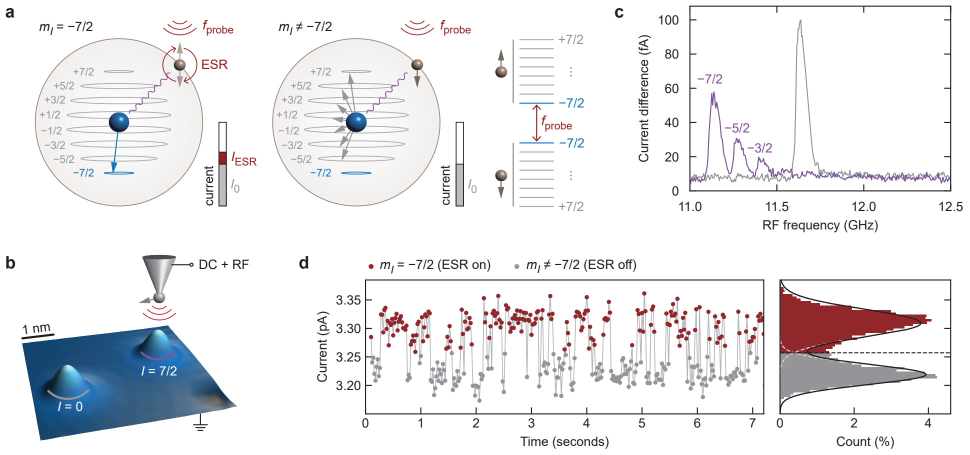

Fig. 6.1 | Time-resolved switching of the nuclear spin state. **a** Diagram of the measurement scheme: the $I = 7/2$ nuclear spin (blue) of a ^{49}Ti atom coupled to the $S = 1/2$ electron spin (brown) via the hyperfine interaction. Only when the nuclear spin is in the $m_I = -7/2$ state, does the applied RF signal at frequency fprobe lead to a tunneling current increase I_{ESR}. Right: spin energy diagram in the limit of a strong magnetic field, where the Zeeman splitting dominates and the eigenstates can be approximated by product states. **b** STM topography (10 pA, 60 mV) of two Ti isotopes on MgO/Ag(100). **c** ESR frequency sweeps (3.0 pA, 60 mV, $B_z = 1.35$ T, $V_{RF} = 17$ mV, averaging time 3 s, lock-in frequency 270 Hz) measured on the two Ti atoms in (b). V_{RF} refers to the zero-to-peak RF voltage amplitude at the tunnel junction. **d** Section of a time trace of the tunneling current at fixed tip height (60 mV, averaging time 20 ms) with f_{probe} corresponding to $m_I = -7/2$. The current histogram on the right is fitted with a two-Gaussian distribution (black line).

7/2. In particular, ^{49}Ti has nuclear spin $I = 7/2$ and couples to the electron spin with an out-of-plane hyperfine coupling component $A_\perp = 130$ MHz[29], resulting in a total of 16 energy levels (fig. 6.1a). The hyperfine coupling causes a shift in the ESR transition frequency that depends on the nuclear spin state, which is absent for Ti isotopes with $I = 0$ (fig. 6.1b, c). The observation of multiple ESR peaks in a single sweep indicates that the nuclear spin state changes much faster than the averaging time of 3 s for each datapoint under conventional ESR settings. The peak heights are a measure of the population distribution of the various nuclear spin states: the nuclear spin resides longer in the $m_I = -7/2$ state as a result of nuclear spin pumping by inelastic electron scattering [28, 29], where m_I refers to the magnetic quantum number of the nuclear spin along the external magnetic field B_z. Being a time-averaged measurement, however, the ESR frequency sweep does not provide information on nuclear spin transition timescales.

In order to resolve changes between the nuclear spin states, we measured the ESR signal in the time domain instead of in the frequency domain. We switched off the STM feedback loop and sent a continuous RF signal to the tunneling junction with a fixed frequency f_{probe}, resonant with a transition of the electron spin magnetic quantum number m_S between states $|m_S, m_I\rangle = |\downarrow, \text{-}7/2\rangle$ and $|\uparrow, \text{-}7/2\rangle$, resulting in an additional ESR current IESR only when $m_I = -7/2$, as illustrated in fig. 6.1a. Fig. 6.1d shows the current measured for several seconds, revealing stochastic switching between two discrete levels. The two levels become apparent in a histogram of the time trace as two Gaussian distributions separated by a current offset. In contrast, when we use an off-resonance frequency, the current is distributed as a single Gaussian (extended data fig. 6.6a). We also performed reference measurements on a Ti isotope with $I = 0$ (fig. 6.6b, c), each revealing a single Gaussian distribution as well. We thus attribute the observed switching to quantum jumps between the probed state ($m_I = -7/2$) and any of the other seven nuclear spin states ($m_I \neq -7/2$).

Since the observed switching time is considerably longer than the averaging time (20 ms), the majority of datapoints constitute a single-shot readout of the nuclear spin. Note that the nuclear spin state is projected at a singular event sometime during the averaging time by an electron passing the adatom. The state is then read out repeatedly during the remaining time to integrate the current to reach a measurable signal strength. This is possible because, in the product state limit, reading out the electron spin state mostly leaves the nuclear spin unchanged after projection. We achieve readout fidelities of up to 98% for both the probed state being occupied and it being unoccupied (see section 6.8).

We can probe different nuclear spin states without changing f_{probe} by adjusting the height of the magnetized probe tip, which exerts an additional magnetic field on the atom [30]. As we adjust the tip height (i.e., setpoint current), different values of m_I become resonant with f_{probe} (fig. 6.2a). We measured current time traces at different tip heights (i.e., different total fields), resulting in a set of current histograms plotted together in fig. 6.2b–f. Within the sweep range of the setpoint current, the histograms are found to feature a bimodal distribution in three windows around 3.2, 2.8, and 2.4 pA, matching the resonances of the nuclear spin states $m_I = -7/2$, $-5/2$, and $-3/2$, respectively. While for $m_I = -7/2$ the distribution is ~50–50 (fig. 6.2e, f), the other states are found to be occupied much less than half of the time (fig. 6.2c).

6.3. LIFETIME OF THE NUCLEAR SPIN

Analysis of the time traces enables us to extract the dwell times of the nuclear spin states. We label each point in the time trace as either in the probed state or not, using a threshold determined by the intersection point of the two Gaussian distributions (fig. 6.1d). We measure individual dwell times t_{dwell} for each occurrence of consecutive time spent in the probed state (fig. 6.3a,b). Using an exponential fit, we find a lifetime T_1^{CW} of about 100 ms for $m_I = -7/2$ (fig. 6.3a). We note that this is the nuclear spin lifetime under continuous-wave (CW) ESR driving and readout by the tunneling current. To compare T_1^{CW} between different nuclear spin states, we repeated the experiment for different f_{probe} values while leaving the tip height unchanged to avoid variations in current-induced nuclear spin pumping (fig. 6.3b, c, see also extended data fig. 6.7). We observe that for f_{probe} being resonant with any of the $m_I \neq -7/2$ transitions, T_1^{CW} is significantly shorter than for $m_I = -7/2$. This may be partly attributed to the fact that

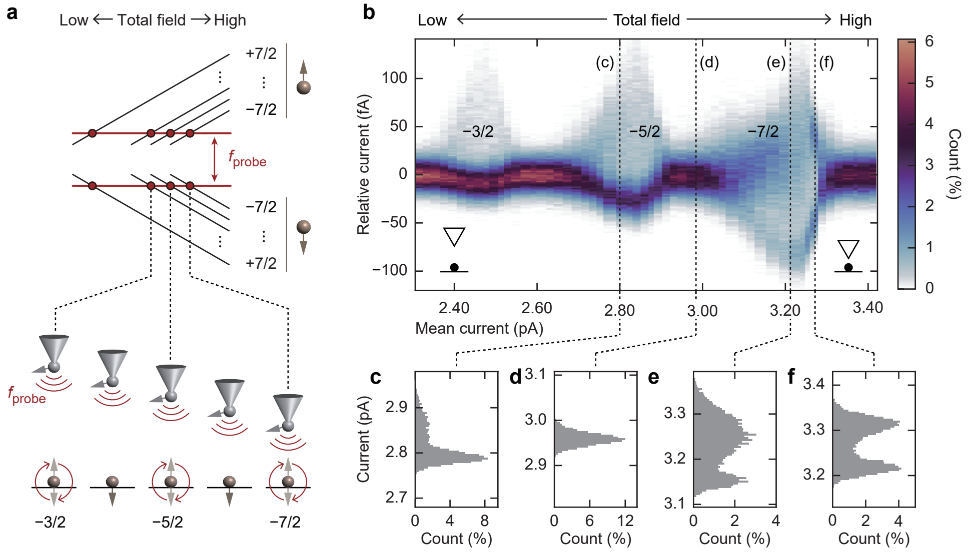

Fig. 6.2 | Readout of different nuclear spin states. **a** Energy diagram of the spin states as a function of magnetic field (top) and schematic of the experiment shown in (**b**), indicating that at certain tip heights f_{probe} matches the Zeeman splitting corresponding to one of m_I states (bottom). **b** Color map of current histograms similar to fig. 6.1d for different heights of the magnetic STM tip (bias voltage 60 mV). The horizontal axis represents the mean current for each time trace, which is a measure of the total magnetic field. **c-f** Current histograms, corresponding to the labeled vertical dashed lines in (**b**).

selection rules allow these states to transition in both directions ($\Delta m_I = \pm 1$), whereas the $m_I = -7/2$ state can only switch to $m_I = -5/2$ ($\Delta m_I = +1$). In addition, these experiments were performed in the presence of a spin-polarized current which constantly excites the system towards $m_I = -7/2$.

However, neither of the above arguments can explain the fact that T_1^{CW} keeps decreasing beyond $m_I = -5/2$, suggesting that the spin pumping efficiency depends on the nuclear spin state. We believe this may be because the hybridization between neighboring spin states depends on m_I directly, which derives from the Clebsch-Gordan coefficients (see extended data table 6.1 and section 7.3). In addition, fig. 6.3d shows how T_1^{CW} changes as we vary the tip height around the resonance point for $m_I = -7/2$. We find that T_1^{CW} is increasing further up to ~300 ms as the system is detuned from resonance. This implies that the continuous ESR driving of the electron spin may affect T_1^{CW} as well.

In order to find the intrinsic lifetime T_1 of the undisturbed nuclear spin and to identify its limiting relaxation mechanisms, we applied a pulsed readout scheme illustrated in fig. 6.4a (also see section 6.5). Here, we set the voltage (both DC and RF) to zero in between pulses. The probe pulses consisted of similar DC + RF conditions as in the

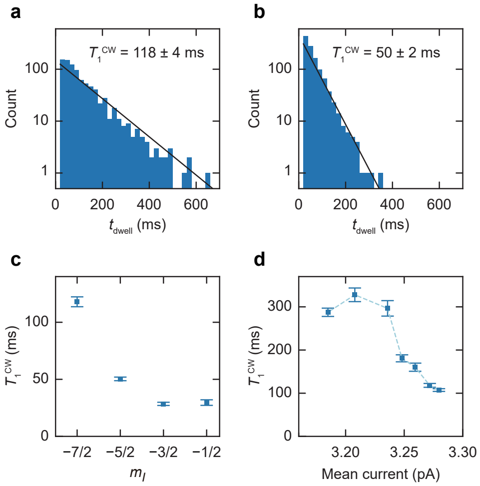

Fig. 6.3 | Dwell time of different nuclear spin states. a,b Histograms of the distribution of the individual dwell times t_{dwell} of m_I = - 7/2 and m_I = - 5/2, respectively. Fitting with an exponential function gives the characteristic dwell time T_1^{CW}. Error bars of T_1^{CW} are the standard deviations in the exponential fit parameter. **c** T_1^{CW} for $m_I = -7/2, -5/2, -3/2, -1/2$, applying corresponding f_{probe} at the same tip height. **d** T_1^{CW} for m_I = - 7/2 at different tip heights around the resonance point.

continuous-wave experiments mentioned above. We set the tip height such that f_{probe} matches the resonance frequency for $m_I = -7/2$. As shown in fig. 6.4b, the voltage pulses lead to sharp peaks in the current, each of which we can assign either the value 1 (for $m_I = -7/2$) or 0 ($m_I \neq -7/2$), using a threshold as introduced in fig. 6.1d. For each pair of probe pulses A and B, there are four possible event scenarios, resulting in conditional probabilities $P(B|A)$ (fig. 6.4c, d).

By changing the waiting time τ between the pulses, we find the conditional probabilities as a function of τ (fig. 6.4e). We take the unintentional pumping of the nuclear spin by the second probe pulse into account, correcting $P(1|1)$ to $P^*(1|1) = [P(1|1) - P(1|0)]/[1 - P(1|0)]$ (see section 6.7). $P^*(1|1)(\tau)$ is expected to decrease exponentially as a function of τ due to relaxation processes at a timescale of T_1. By fitting with an exponential function, we obtain T_1 = 5.3 ± 0.5 s for $m_I = -7/2$. Similar measurements on an identical ^{49}Ti atom yielded a value of T_1 = 4.3 ± 0.8 s (extended data fig. 6.8). This T_1 is seven orders of magnitude longer than the lifetime of the electron spin in the same atom (~100 ns) [17]. In addition, the extracted lifetime is an order of magnitude longer than T_1^{CW} measured in the continuous-wave experiment (fig. 6.3), confirming the hypothesis that the nuclear spin state is affected by continuous ESR driving and DC readout.

6.4. RELAXATION MECHANISM

To develop an understanding of how DC spin pumping and ESR driving affect the nuclear spin, we repeat the pulsed experiment introduced in fig. 6.4, but now with additional voltages in the waiting time to investigate perturbation of the nuclear spin (fig. 6.5a–c) (see section 6.5). In a first variant, we add a DC bias voltage during the waiting phase and fix the waiting time to 2 s. The figure of merit is $P(1|1)$, now left uncorrected by $P(1|0)$ as we intentionally disturb nuclear spins during the waiting time

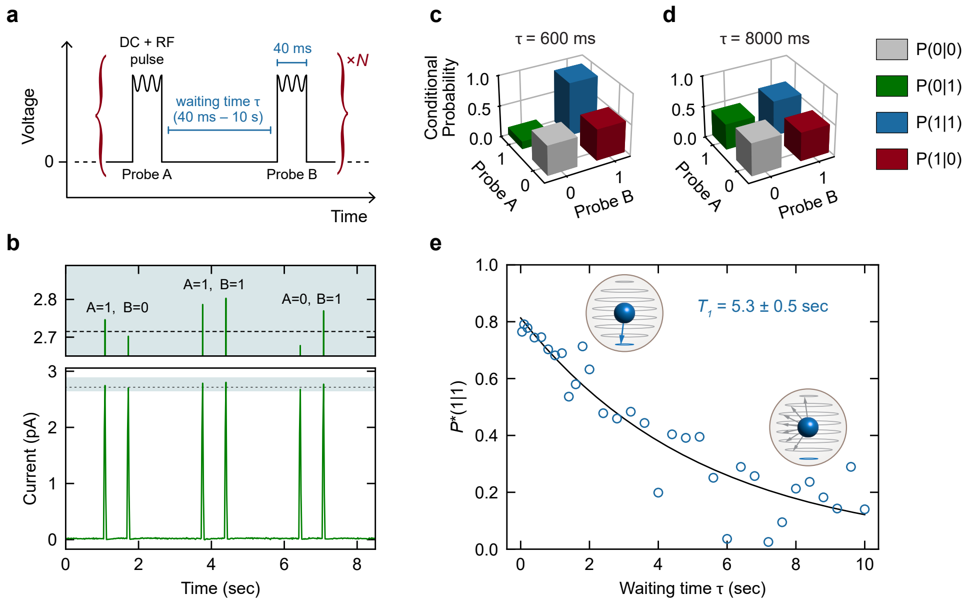

Fig. 6.4 | Intrinsic nuclear spin lifetime with pulsed detection scheme. a Schematic of the pulse measurement scheme. One detection event consists of two probe pulses, with a variable waiting time τ in between, with zero bias voltage. Each probe pulse consists of a DC voltage (70 mV) and an RF signal at $f_{\text{probe}} = 12.75$ GHz, corresponding to $m_I = -7/2$ ($B_z = 1.6$ T, $V_{RF} = 22.6$ mV). For each τ, we repeat between $N = 443$ and $N = 704$ detection events. **b** Bottom: section of a measured current time trace ($\tau = 600$ ms) showcasing three detection events. Top: zoom on the shaded area. For each event, the current of the probe pulses A and B indicates whether $m_I = -7/2$ (1) or not (0), based on the current threshold (dashed line) determined from a histogram of all probe pulses. **c,d** Conditional probabilities $P(B|A)$ for $\tau = 600$ ms and $\tau = 8000$ ms, respectively. **e** Corrected conditional probability $P^*(1|1)$ as a function of τ. $P^*(1|1)$ represents the intrinsic decay of the nuclear spin. An exponential fit ($Ae^{-\tau/T_1}$, black curve) gives the intrinsic lifetime T_1 of the $m_I = -7/2$ nuclear spin state ($T_1 = 5.3 \pm 0.5$ s, $A = 0.81 \pm 0.03$).

(see section 6.7). In fig. 6.5a, we plot $P(1|1)$ against the bias voltage in the waiting phase. $P(1|1)$ is found to increase with positive voltage, whereas it decreases with negative voltage. We attribute this to dynamic nuclear spin polarization resulting from electron spin pumping, which is a combination of two processes depicted in fig. 6.5d: flip-flop quantum jumps between a nuclear and electron spin due to hybridization as a result of the hyperfine coupling, and inelastic electron scattering. The former can happen both ways, while the latter is favored in one direction due to the spin polarization of the tip. As a result, the two processes together pump the system towards $m_I = -7/2$ or $m_I = +7/2$, depending on the voltage polarity [28, 29].

We note that, since Ti on the oxygen binding site displays a continuous-wave ESR signal only for positive voltages [31], it was previously not possible to observe nuclear spin pumping at negative bias voltage. With our pulsed readout scheme, however, we can now also confirm pumping in this bias regime. This points to an interesting aspect of our experiment compared to previous studies: we isolate the effect of the DC current from the ESR driving, the effect of which will be studied separately below.

In a second and third variant of the experiment, we send an RF signal during the waiting phase and fix the waiting time to 600 ms. In fig. 6.5c, d, we change the frequency and RF amplitude, respectively, to see the effect of detuning and ESR driving strength on the conditional probability. During the probe pulses, f_{probe} is kept at 12.75 GHz, corresponding to the $m_I = -7/2$ resonance. As we sweep the interim frequency, $P(1|1)$ dips down on resonance at around 12.75 GHz (fig. 6.5b). This is an indication that the nuclear spin relaxes significantly faster when the electron spin is driven most efficiently. As shown in fig. 6.5c, this effect increases with ESR driving amplitude but becomes weaker when the frequency is detuned.

This ESR-induced relaxation can be understood in terms of the availability of the relaxation pathway towards $m_I = -5/2$ via nuclear-electron spin flip-flops. Due to

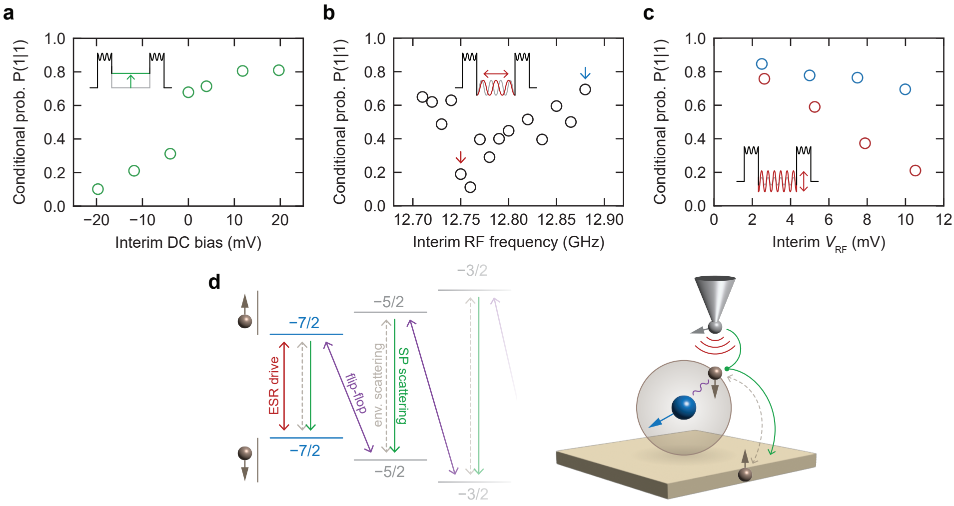

Fig. 6.5 | DC or RF in the waiting period. **a** Conditional probability $P(1|1)$ as a function of DC voltage during the waiting section between the two probe pulses (see inset schematic), with a fixed waiting time $\tau = 2$ s. **b** $P(1|1)$ as a function of RF frequency in the waiting section ($\tau = 600$ ms, $V_{RF} = 10.4\,\tau\,0.3$ mV). **c** $P(1|1)$ as a function of RF voltage amplitude in the waiting section (interim V_{RF}), for two different frequencies highlighted in (**b**) (red: on-resonance frequency, blue: off-resonance frequency). **d** Schematic of the possible transition dynamics between spin states: spin resonance drive of the electron spin (red), flip-flop quantum jump between nuclear and electronic spins mediated by hyperfine coupling (purple), environmental scattering of electronic spin (gray, dashed), electron spin scattering via spin-polarized STM tip (green).

conservation laws, this process can only happen when the electron spin is in the $m_S = \uparrow$ state, whereas $m_S = \downarrow$ is the ground state. The nuclear spin at $m_I = -7/2$ can relax to $m_I = -5/2$ by a hyperfine flip-flop interaction, transferring −1 angular momentum to the electron spin (see fig. 6.5d for a schematic). Thus, the relaxation rate is amplified when $mS = \uparrow$ state becomes more populated through ESR driving.

The pulsed experiments provide insight into the relaxation mechanisms limiting the intrinsic lifetime of the nuclear spin. We emphasize that we observed the relaxation by ESR driving to be strong in relation to any other relaxation source present. This indicates that the flip-flop interaction, which facilitates the relaxation by ESR, happens fast enough to be a dominating relaxation process whenever ESR continuously excites the electron spin. We note that the same flip-flop rate is present also when the electron spin is excited in ways other than ESR driving. In thermal equilibrium at 400 mK, electron scattering from the substrate significantly populates the $m_S = \uparrow$ state[32]. We therefore conclude that the nuclear-electron spin flip-flop relaxation channel is likely the main mechanism limiting the intrinsic lifetime.

As the flip-flop interaction results from a small in-plane component of the hyperfine coupling ($A_{||}$ = 10 MHz [26]), which in turn depends on the binding site [25, 33], the above implies that the atomic-scale position is a crucial parameter to extend the lifetime of on-surface nuclear spins. Furthermore, the flip-flop relaxation channel is expected to be reduced at higher magnetic fields, where the hybridization is minimized [2]. At that point, other relaxation sources may become relevant, such as spin-lattice coupling mediated by the nuclear quadrupole moment or magnetic Johnson noise from the bulk silver. Dipole-dipole flip-flops with the Mg and Ag nuclear spins can be considered negligible (see chapter 7).

In conclusion, we performed a single-shot readout of an individual nuclear spin using ESR-STM, which was found to have a lifetime in the order of seconds. Furthermore, we shed light on the pumping channel by a local DC bias and the relaxation channel by ESR driving. As the single-shot readout ESR-STM method presented here should work for any long-lived nuclear spin, the methodology may be transferable to different atomic or molecular spins in various platforms, such as semiconducting or insulating substrates [34, 35]. Crucially, the nuclear spin lifetime we observe is longer than the rise time of current amplifiers conventionally used for STM, which enables direct readout and high-fidelity state initialization by projective measurement [36]. Potentially, this could even combine spin operations with STM tip movements between different atoms and open up possibilities to perform simultaneous coherent operations on extended atomic structures comprising multiple spins.

6.5. GENERAL METHODS

The experiments were performed in a commercial Unisoku USM-1300 STM. MgO/Ag sample and surface atoms were prepared with the same method described in refs. [23], [29]. The tungsten STM tip was prepared for ESR-STM measurements by first indenting it into the Ag until we obtained scanning image quality, then picking up ~30 Fe atoms. All ESR measurements are taken at a sample temperature of 0.4 K. STM topography was obtained in constant current mode at 1.6 K. All DC bias values are reported with respect to the sample. The pre-amplifier for the tunneling current used for all measurements is the NF corp. SA608F2, with its internal analog 300 Hz low-pass filter active and the NF corp. LP5393 as a low-noise DC power supply for the pre-amplifier.

For CW-mode measurement (figs. 6.1 to 6.3), we used a Rhode & Schwarz SMA100B signal generator to deliver the RF signal to the STM junction. The DC voltage is generated by a Nanonis V4 Digital-to-Analog converter. During the ESR frequency sweeps, the RF signal was chopped at the frequency of 271 Hz. The ESR signal (difference between driven and non-driven) was detected at this frequency by a Stanford Instruments SR830m lock-in amplifier, resulting in an increased signal-to-noise ratio compared to direct averaging of the current. For the time-trace measurement that resolves nuclear spin state switching, the driving RF voltage is not chopped, and the current is instead recorded directly at a sampling time of 20 ms by a Nanonis V4 Analog-to-Digital converter (ADC). The RF wiring used for CW measurements corresponds to the schematic in fig. 3.2a, with the AWG output channel replaced by the CW RF generator. When recording a CW-mode time trace, we have the RF signal generator running before turning off the tip-height feedback. This provides time for the thermal drift in tip height due to heating to reach an equilibrium to prevent a time-varying drift during the recording.

6

For pulse-mode measurement (figs. 6.4 and 6.5), the voltage pulses were generated by a Keysight M8195a arbitrary waveform generator (AWG). A single channel was used to generate both the DC and RF voltages directly as one signal. A wiring schematic of the components used for pulse-mode measurement is shown in fig. 3.2b. In the pulse-mode, the feedback is turned off first before running the AWG, but we start recording after tens of seconds to wait out the drift from heating. The drift settles faster compared to CW-mode due to the short duty cycle of RF pulses. Each section of a signal (probe A, waiting period, probe B, and separation period) is generated by repeating a shorter waveform with a length of 10 μs. It is justified not to have a phase-coherent RF pulse during the probe pulses, because the coherence time of the ESR-driven electron spin is only 300 ns at best [24]. For all pulsed experiments presented with$\tau < 2$ s, the separation period has a length of 2 s. The separation period is equal to the waiting period for longer τ.

Pulsed experiments are recorded at the Nanonis ADC as full-time traces with a sampling rate of 20 ms. A marker signal is sent by the AWG simultaneously with each probe pulse and is recorded at each ADC sample alongside the tunneling current, in order to select the probe pulse samples from all other samples in the time trace for the data analysis. At least 40 ms probe pulse widths were chosen to always leave a full 20 ms sample in the center to avoid jitter artifacts at the edges of ADC samples. For details on probe sample selection and subsequent analysis, see section 6.7.

6.6. EXTENDED DATA FIGURES

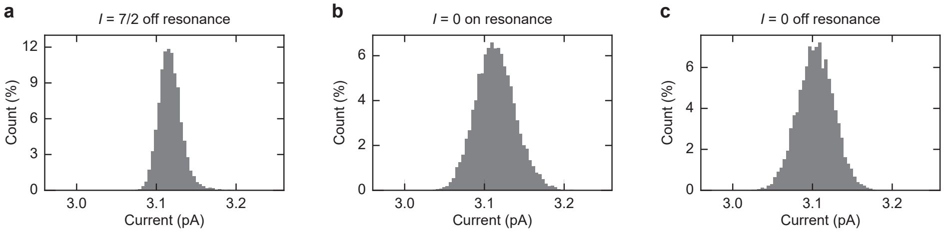

Fig. 6.6 | Current histograms of time traces. a Current histogram with off-resonance frequency on ^{49}Ti (I = 7/2). **b,c** Current histogram with on-resonance and off-resonance frequency on ^{48}Ti (I = 0), respectively. All histograms are unimodal, which indicates stochastic switching in current is absent.

m_s	+1/2 (|↑⟩)								−1/2 (|↓⟩)							
m_I / $\|n\rangle$	+7/2	+5/2	+3/2	+1/2	−1/2	−3/2	−5/2	−7/2	−7/2	−5/2	−3/2	−1/2	+1/2	+3/2	+5/2	+7/2
$\|0\rangle$	0.00588	-0.00098													-0.00104	0.99998
$\|1\rangle$	0.00001	0.00594	-0.00129											-0.00147	0.99998	0.00105
$\|2\rangle$		-0.00001	-0.00599	0.00146									0.00176	-0.99998	-0.00147	
$\|3\rangle$			0.00001	0.00605	-0.00153							-0.00197	0.99998	0.00177		
$\|4\rangle$				-0.00001	-0.00611	0.00149					0.00207	-0.99998	-0.00198			
$\|5\rangle$					0.00001	0.00617	-0.00135			-0.00203	0.99998	0.00208				
$\|6\rangle$						-0.00001	-0.00623	0.00104	0.00171	-0.99998	-0.00204					
$\|7\rangle$							0.00001	0.00630	0.99998	0.00171						
$\|8\rangle$							0.00102	0.99998	-0.00630	0.00103						
$\|9\rangle$						-0.00140	-0.99998	0.00101	-0.00001	0.00624	-0.00133					
$\|10\rangle$					0.00164	0.99998	-0.00139			0.00001	-0.00618	0.00147				
$\|11\rangle$				-0.00178	-0.99998	0.00163					-0.00001	0.00612	-0.00150			
$\|12\rangle$			-0.00183	-0.99998	0.00177							-0.00001	0.00606	-0.00144		
$\|13\rangle$		-0.00174	-0.99998	0.00182									-0.00001	0.00600	-0.00128	
$\|14\rangle$	-0.00142	-0.99998	0.00173											-0.00001	0.00594	-0.00096
$\|15\rangle$	0.99998	-0.00141													0.00001	-0.00588

Table 6.1 | The 16 eigenstates of the ^{49}Ti spin Hamiltonian. Based on eq. (2.10), with the experimental magnetic field strength filled in. We use B_ext = 1.35 T along z and a B_{tip} = 0.197 T with a 2° rotation angle with respect to the out-of-plane direction. The coefficients for each eigenstate are rounded to the fifth decimal place. A grey cell indicates the corresponding coefficient is smaller than 0.00001. Note that the hybridization between nuclear spin projections (the off-center shifted diagonals with opposite electron spin projection from the 0.9999(8) majority spin product) depends on m_I.

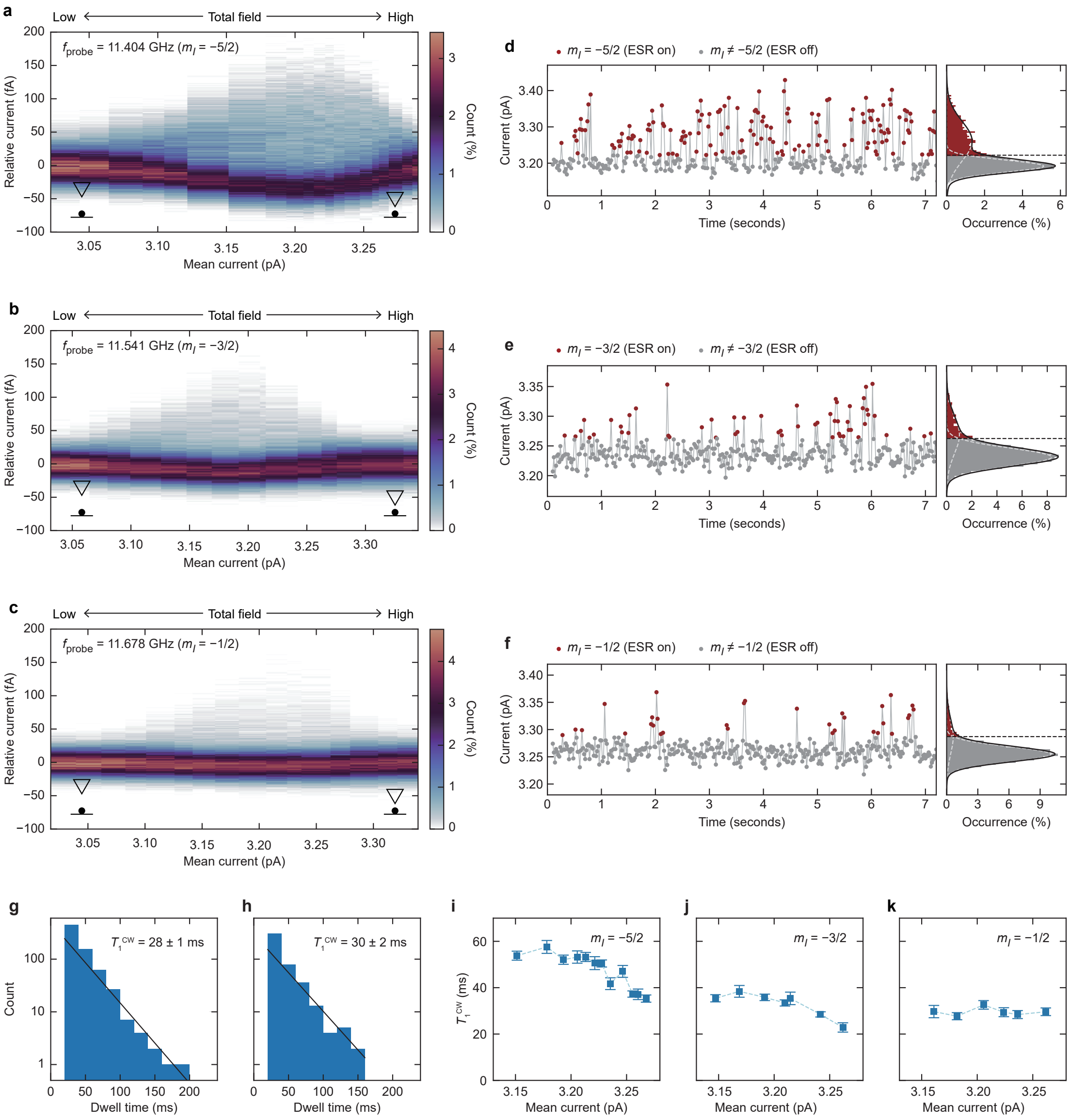

Fig. 6.7 | Readout of different nuclear spin states at the same tip height. a-c Colour maps of current histograms similar to fig. 6.4b with different f_{probe} of 11.404, 11.541, and 11.678 GHz, which corresponds to $m_I = -5/2$, $-3/2$, and $-1/2$, respectively. We used the same bias voltage of 60 mV. **d-f** Representative sections of time traces of the tunnelling current from (**a**)-(**c**), respectively. **g,h** Histograms of the distribution of the individual dwell times tdwell of $m_I = -3/2$ and $m_I = -1/2$, respectively. Fitting with an exponential function gives the characteristic dwell time T_1^{CW}. **i-k** T_1^{CW} of $m_I = -5/2$, $-3/2$, and $-1/2$ at different tip heights around the resonance point.

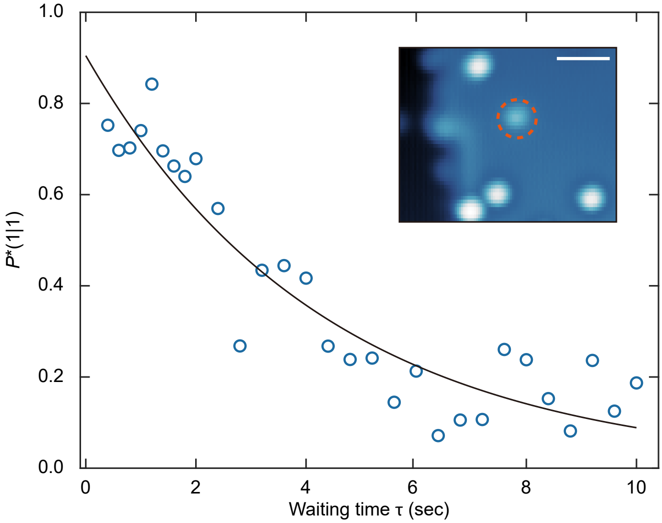

Fig. 6.8 | Intrinsic nuclear spin lifetime in another ^{49}Ti atom at the same oxygen binding site. Corrected conditional probability $P^*(1|1)$ as a function of the waiting time τ. These measurements were performed with a different microtip compared to the tip used for fig. 6.4e. With an exponential fit ($Ae^{-\tau/T_1}$, black curve), we measured the intrinsic lifetime T_1 of the $m_I = -7/2$ nuclear spin state ($T_1 = 4.3 \pm 0.8$ sec, A = 0.90 ± 0.10). Note that RF circuit configuration in fig. 3.3c was used here, with the DC pulses generated by the AWG marker channel, instead of the circuit in fig. 3.2b like the other results. Inset: STM topography. The ^{49}Ti atom is indicated with a dashed circle. Scale bar: 2 nm.

6.7. ANALYSIS OF PULSED EXPERIMENT MEASUREMENTS

For the probe pulse experiments, the current was measured as a continuous time trace, recording also the samples in between pulses as shown in fig. 6.5b. Already from this time trace it can be observed that there are two current levels in the current, corresponding to the spin being in the $m_I = -7/2$ state (1) for the higher current or $m_I \neq -7/2$ (0) for the lower current. Conditional probabilities were extracted from this data set by systematically selecting the probe pulses from the raw time trace and then categorizing them by their nuclear spin state.

The sampling time of our recording Nanonis V4 analogue-to-digital converter (ADC) was set to 20 ms. To guarantee at least one full sample period per probe pulse, we sent probe pulses at least 40 ms wide. Since the probe pulses were not synchronised with the sampling, typically on either side of the pulse there was one sample containing a partial pulse (edge signals). Thus we obtained more than one data point per pulse. For example, with 40 ms pulses, we have three data points per pulse: one with the full sampling (green circles in fig. 6.9a) and two edge signals with a partial sampling (grey circles in fig. 6.9a). To select the full-sample signal, we sent a DC marker pulse along with our probe pulse and recorded the marker signal and tunnelling current simultaneously with our multi-channel ADC.

To guarantee a statistical validity for both the state labelling of individual pulses and the conditional probabilities calculated from these pulses, we need a large enough

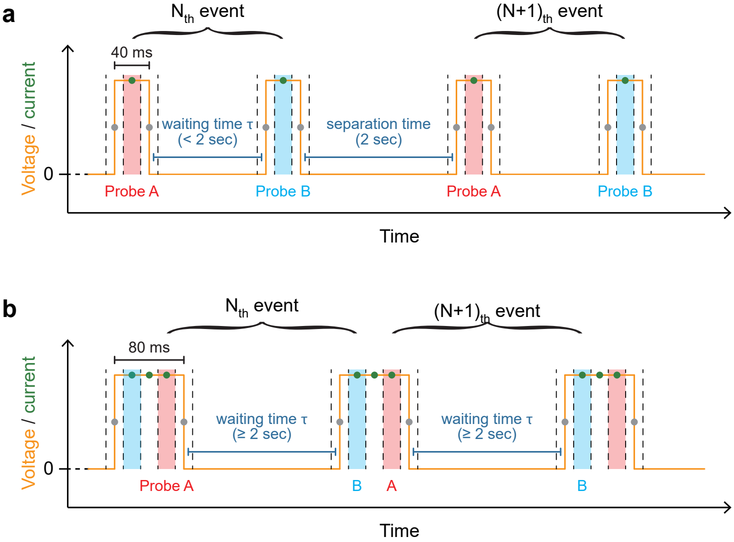

Fig. 6.9 | Selection of the full-sample probes. a Schematic of voltage pulses we send (orange line) and measured data points (dots) for short τ (pulse width = 40 ms). Green and grey circles indicate the full-sample signal and edge signal, respectively. **b** Similar schematic for long τ (pulse width = 80 ms).

number of (i) events of probe-waiting-probe and (ii) current values that correspond to either nuclear spin states. To have sufficient events, we measured for at least 24 minutes for the shortest τ values, reaching up to 80 minutes for τ = 10 sec. In practice, time traces at a constant tip height can be recorded only for a limited amount of time before the drift in tip height changes the tunnelling current. Thus, we measured multiple time traces, restoring the tip height feedback to correct the drift before starting a new time trace, and combined them in the analysis. The drift in tip height during an individual time trace (8 minutes) is less than 0.1 pm, equivalent to 10 fA in current, which is smaller than I_{ESR} that distinguishes the nuclear spin states in the probe pulses. For the measurements for $\tau \geq 2$ sec, we kept the separation time equal to the waiting time, where one probe pulse serves as the probe B for the former event and as the probe A for the latter event (fig. 6.9b). In this way, we could observe at least 443 events for each τ at a reasonable amount of measurement time. Note that for all experiments with a perturbing voltage in the waiting time (i.e. fig. 6.5), the probes A and B were again analysed as distinguishable with the separation time fixed to 2 seconds at zero bias.

In order to have enough current values, we sent proportionally longer pulses – more samples per pulse – for longer τ. In this case, we used all current values with the full sample of the probe signal to construct a histogram and determine a current threshold, while we used only the first (probe B) and the last (probe A) value of currents of each pulse to calculate the conditional probability fig. 6.9b). The current histogram of the full-sample signal (see fig. 6.10a as an example, for τ = 8 sec) consists of the two Gaussian-distributed current levels corresponding to the nuclear spin states that we have seen in our CW measurements.

As we did in the CW measurement, we can define a threshold by fitting a current histogram with the sum of two Gaussians and taking their intersection point and label either (1) or (0) for each current. We construct a current histogram and

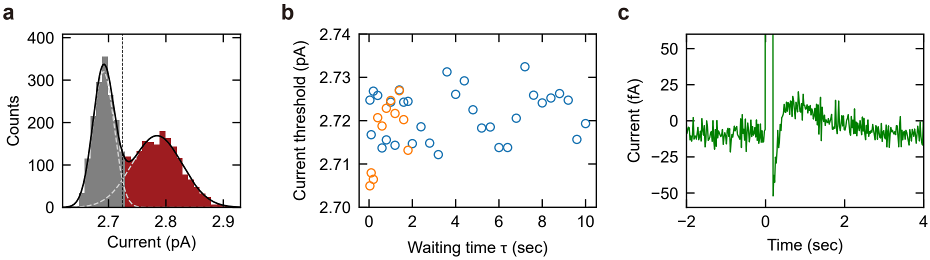

Fig. 6.10 | Thresholding of probe pulse samples. a Current histogram of probe pulse samples for τ = 8 sec fitted with the sum of two Gaussians (black). The intersection point sets the threshold (vertical dashed line) to label probes as either 0 (grey) or 1 (red). **b** Current threshold determined for different τ, in blue and orange for probe A and probe B samples respectively. Since time traces with $\tau \geq 2$ sec have pulses operating as both probe A and B, these τ have only one threshold. **c** Current time trace covering one probe pulse, with the pulse samples cut off vertically to highlight the signal settling after the pulse.

obtain a threshold for each type of probe (probe A or B) individually unless they are indistinguishable in measurements with $\tau \geq 2$ sec. As shown in fig. 6.10b, almost all thresholds are within a narrow band ~20 fA wide, except the first three data points for the probe B. This is because of a certain settling time (fig. 6.10c) before the voltage in the ADC reaches a flat DC value, potentially due to the current pre-amplifier acting as a low pass filter. When the probe B follows shortly within this settling time, its signal adds the same signal amplitude on top of a different background, resulting in different current levels representing the same nuclear spin states.

After labelling the current for every probe, we obtained four conditional probabilities $P(B|A)$ for each τ. As mentioned in the main text, we corrected for unintentional spin pumping in the probe B. Our figure of merit is the probability of the event that we observe the state (1) with both probe A and B. However, as illustrated in fig. 6.11, this inherently includes events where the state decays from (1) to (0) during the waiting time τ due to normal relaxation but is pumped back again to (1) with the probe B due to the DC voltage we need to readout the nuclear spin. To correct for this, we define P_{10X} as the probability that (1) decays to (0) at least once during τ,

$$P_{10X} = P_{100} + P_{101}, \tag{6.1}$$

where P_{100} and P_{101} denote the probability of the event that we observe (1) with the probe A and it decays to (0) during τ, followed by the observation of (0) and (1) with the probe B, respectively. The latter case (P101) corresponds to the nuclear spin pumping with the probe B. Only if we send zero voltage during τ, P_{101} is expressed as,

$$P_{101} = P_{10X} \cdot P(1|0). \tag{6.2}$$

In addition, by the definition, $P(1|1) = P^{*}(1|1) + P_{101}$, and $P(0|1) = P_{100}$. Using eqs. (6.1) and (6.2),

$$P(0|1) = P_{10X} - P_{101} = P_{10X} \cdot [1 - P(1|0)], \tag{6.3}$$

or

$$P_{10X} = \frac{P(0|1)}{1 - P(1|0)}. \tag{6.4}$$

By the definition,

$$P^{*}(1|1) = 1 - P_{10X} = \frac{P(1|1) - P(1|0)}{1 - P(1|0)}. \tag{6.5}$$

In a limit of $\tau \rightarrow \infty$, the event of observing (1) with the probe B is independent on the state measured with the probe A [$P(1|1) = P(1|0)$] (fig. 6.11c and d), yielding that $P^{*}(1|1)$ converges to zero.

This correction is valid only if we do not send any voltage during τ. If we intentionally interrupt the nuclear spin during τ, eq. (6.2) is not valid, which precludes the correction described above. This is why we use uncorrected $P(1|1)$ in fig. 6.5 in section 6.4.

Nevertheless, $P(1|1)$ still retains qualitative information about how likely the nuclear spin tends to remain in the (1) state.

There are also two assumptions made in the $P(1|1)$ correction described above, both of which we can justify experimentally. The first assumption is that (0) → (1) pumping events are mostly caused by the probe pulse and generally not by anything happening during the waiting time. If there would be a more 'intrinsic' mechanism of excitation to the $m_I = -7/2$ state during the waiting time, there must be a timescale associated with this process. This should then be reflected in our measured $P(1|0)$ as a function of waiting time τ. Instead, we find $P(1|0)(\tau)$ to be constant (see fig. 6.11d). So, we conclude that pumping events are generally caused by a factor that does not change with the waiting time: the probe pulse.

The second assumption is that the nuclear spin always finds itself in a state from where it can be pumped up to $m_I = -7/2$. This might not be the case in general, since

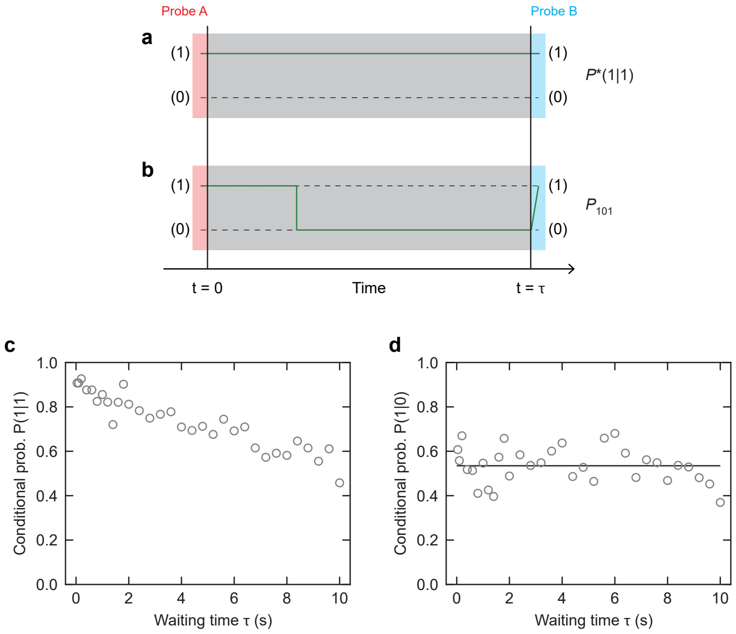

Fig. 6.11 | Nuclear spin pumping with the second probe. a The event for which we want to calculate probability $P^*(1|1)$. **b** Possible event that the state (1) observed with the probe A decays to the state (0) and is pumped back to the state (1), which corresponds to the P_{101}. The green line indicates the nuclear spin state over time. Because we are unaware of what is happening during the waiting time τ (grey box), uncorrected $P(1|1)$ includes the event of (b), that is, $P(1|1) = P^*(1|1) + P_{101}$. **c,d** Conditional probabilities $P(1|1)$ and $P(1|0)$, respectively, as a function of waiting time τ in the experiment described in fig. 6.4.

the –7/2 state can only be reached from the –5/2 state and there are 6 more nuclear spin projections. When measuring the probability $P(1|0)$, the initial state after the first probe pulse could be any of the states that fall under (0). When falling down from (1) during a $P(1|1)$ measurement, however, it is likely that the fallen state is m_I = –5/2 specifically and not any general state within (0). We want to correct $P(1|1)$ with $P(1|0)$ to account for pumping after falling, but $P(1|0)$ cannot be assumed to be representative of the probability to pump up soon after falling down from (1) due to this difference in initial state. So, $P(1|0)$ is a priori not the correct probability to use. However, we can take $P(1|0)$ as a good approximation if it can be shown that m_I = –5/2 is often occupied compared to other m_I in the general (0) state. This is what we will demonstrate below.

Since we only need to investigate the –5/2 occupation during the probe pulse with continuous readout when the (0) → (1) pumping events happen, we can analyse the CW current time traces that probe individual m_I states. From the magnitudes of the fitted T_1^{CW} for the different states (fig. 6.3c), we can see that the system is most likely to spend time in the –5/2 state if it is not in the –7/2 state. For m_I = –5/2 we find T_1^{CW} = 50 ± 2 ms, while we get 28 ± 1 ms and 30 ± 2 ms for m_I = –3/2 and –1/2, respectively.

Considering that our probe pulses are 40 ms wide, which is longer than the above characteristic T_1^{CW} in both the –3/2 and –1/2 states, we expect that the nuclear spin is often pumped up to at least the –5/2 state during a probe pulse. In other words, if the nuclear spin is neither occupying the –7/2 nor the –5/2 state during the second probe pulse, it will soon be occupying either of them within the 40 ms probe pulse width. In fact, the time needed to pump to –5/2 might be even shorter while probing –7/2 compared to time traces probing the –3/2 and –1/2 states directly, which we did to get the above T_1^{CW}, because ESR driving inhibits the spin pumping of the electron spin at the probed state.

Overall, this means that we can justify both our assumptions and our correction of $P(1|1)$ to $P^*(1|1)$ can be applied. This correction is important for a quantitative analysis, in particular to apply proper fitting to get the correct T_1. Using $P^*(1|1)$, we get a result for T_1 that is, in principle, independent of probe pulses properties like the DC voltage pulse height.

6.8. READOUT FIDELITY

Following Ref. [37], we calculate the readout fidelity (also referred to as measurement fidelity) using a model of the separate sample current distributions $N_1(I)$ and $N_0(I)$ for when the nuclear spin occupies the probed spin state (1: $m_I = -7/2$) and the other spin states (0: $m_I \neq -7/2$), respectively. Knowing these separate distributions, the readout fidelities F_0 and F_1 are then defined as the fractions of the distributions on the correct side of the chosen current threshold I_{thr}:

$$F_0 = \int_{-\infty}^{I_{thr}} N_0(I)dI, \tag{6.6}$$

$$F_0 = \int_{I_{thr}}^{\infty} N_1(I)dI. \tag{6.7}$$

Experimentally, we have access only to the total sample current distribution from both distributions combined. As such, before calculating the fidelity, we need to model the separate sample current distributions and fit this model to the experiment. For all data analysis presented in the main paper, we opted to model our measurements with an analytical model where $N_0(I)$ and $N_1(I)$ are both Gaussian distributions. The resulting fit with the experimental current distribution of one particular time trace is shown in fig. 6.1d. This model is justified because STM current noise is generally Gaussian-distributed.

We can find an optimal value for the threshold current where the maximum number of samples will be labelled correctly. Naturally, this value is the intersection point between the two Gaussians, resulting in readout fidelities F_0 = 98 % and F_1 = 98 % for the time trace showcased in fig. 6.1d, which was chosen with an optimal ESR drive. Other time traces generally show lower fidelities, in particular due to an increased current noise for the probed nuclear spin state when driven detuned (see, for example, fig. 6.2e), which is discussed in the next section. Across all analyzed CW and lifetime pulse-mode time traces reading out the $m_I = -7/2$ state, we find a mean fidelity of F_0 = 91 ± 5 % and F_1 = 90 ± 4 %.

6.9. SIMULATION OF ESR CURRENT NOISE IN TIME TRACES

The difference in noise between the two current levels, made visible in the bimodal current histrograms such as fig. 6.2d, is a striking feature of our measured current time traces. The current noise is generally higher with the probed nuclear spins state occupied (the higher current level) than when the nuclear spin is in another state and the ESR cannot be driven. Interestingly, the current noise of the occupied level also depends on detuning, with broader Gaussians at lower currents within one hyperfine resonance. This can be observed most clearly in the 2D colormap shown in fig. 6.2b.

Fortunately, this seemingly complex behavior can be understood with a simple model. The background tunnelling current I_0 is in general an exponential function of the tip height z. However, the ESR current I_{ESR} is also a function of tip height, because the magnetic field emanating from the tip apex changes the total field and detunes the ESR driving when using a constant frequency. This dependency of I_{ESR} on z can be approximated as a Lorentzian, equivalent to the symmetric resonance peak shape in our ESR frequency sweeps (fig. 6.1c). Thus, while the I-vs-z curve $I(z)$ is a smooth exponential with the probed nuclear spin projection m_I unoccupied, the ESR current introduces a strong non-linearity when the probed m_I is occupied and the total current becomes the sum of I_0 and I_{ESR}. Realistic I-vs-z models for both situations are presented in fig. 6.12a and b.

Crucially, the STM tip experiences the same tip height vibration noise with both nuclear spin occupations. This z noise translates to different current noise magnitudes depending on the slope of the $I(z)$ curve. When the probed nuclear spin state is occupied, setting the tip height on the side of the resonance closer to the sample (i.e. higher current) results in a smaller dI/dz compared to I_0 alone and therefore produces a lower current noise. Conversely, the low current side of the resonance has a steep slope and therefore the same z noise results in more current noise.

This effect is illustrated with a current simulation presented in fig. 6.12c. In the simulation, currents are sampled from the $I(z)$ curve many times for each of a range of center tip heights, with added Gaussian z noise around the center tip height for each sample. This generates a histogram of current for different tip heights, which can be represented on an x-axis by their mean current to form a 2D color plot, similarly to fig. 6.2b that was plotted with experimental data. In order to simulate probing the m_I = -7/2 state, 40% of all current samples are taken from the $I(z)$ in with the probed m_I occupied, and 40% from the unoccupied $I(z)$ (both are plotted in fig. 6.12a). This reflects the time-averaged populations of this spin state determined experimentally. The remaining 20% are distributed as a linear interpolation between both $I(z)$ curves, with a fraction from both currents at the sampled z adding to the total sample current. This simulates time trace samples where the nuclear spin state changed while the sample was measured.

The resulting simulated 2D color plot of histograms in fig. 6.12c strongly resembles the first (right-most) hyperfine resonance in fig. 6.2b. The simulation captures the broadening of the higher current level and the small range where this current level is narrow. The observed changes in the characteristic dwell time as a function of detuning via tip height are not taken into account in the model. This dependency links the nuclear spin state population distribution to the tip height. The simulated population distribution, which is kept constant, is therefore not accurate for the low current side of the resonance. Still, we can conclude that the non-linearity in the $I(z)$ curve due to the I_{ESR} is responsible for the broadening .

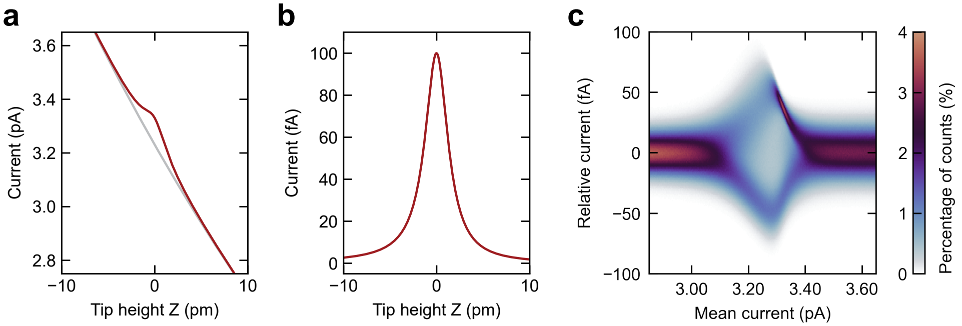

Fig. 6.12 | Simulation of ESR current noise. **a** Model for the tunneling current as a function of tip height z, both for the case with the probed nuclear spin projection m_I occupied (red) and unoccupied (grey). For the former, the total current is the sum of background current I_0 and ESR current I_{ESR}, while the later only consists of the exponential $I_0 = I_{res}e^{z/z_0}$. Here, I_{res} = 3.23 pA is the current corresponding to the tip height at which the ESR drive is resonant, and z_0 = 53 pm is the decay length of the tunnelling current, chosen to match experimental observations. **b** Plot of the ESR current I_{ESR}, which is modelled as a Lorentzian. **c** 2D colormap of current histograms, simulated for different STM tip heights (horizontal axis) displayed as the mean current for each vertical histogram. The simulation samples the current from the model in (**a**) at the corresponding z, with Gaussian z noise added on top with a standard deviation of 0.2 pm.

REFERENCES

[1] E. W. Stolte, J. Lee, H. G. Vennema, R. Broekhoven, E. Teng, A. J. Katan, L. M. Veldman, P. Willke and S. Otte. 'Single-shot readout of the nuclear spin of an on-surface atom'. In: *Nature Communications* 16.1 (2025), p. 7785. ISSN: 2041-1723. DOI: 10.1038/s41467-025-63232-5.

[2] P. Neumann, J. Beck, M. Steiner, F. Rempp, H. Fedder, P. R. Hemmer, J. Wrachtrup and F. Jelezko. 'Single-Shot Readout of a Single Nuclear Spin'. In: *Science* 329.5991 (2010), pp. 542–544. ISSN: 0036-8075. DOI: 10.1126/science.1189075.

[3] X. Y. Lai, R. Z. Fang, T. Li, R. Z. Su, J. Huang, H. Li, L. X. You, X. H. Bao and J. W. Pan. 'Single-Shot Readout of a Nuclear Spin in Silicon Carbide'. In: *Physical Review Letters* 132.18 (2024), p. 180803. ISSN: 10797114. DOI: 10.1103/PhysRevLett.132.180803.

[4] E. Hesselmeier, P. Kuna, W. Knolle, F. Kaiser, N. T. Son, M. Ghezellou, J. Ul-Hassan, V. Vorobyov and J. Wrachtrup. 'High-Fidelity Optical Readout of a Nuclear-Spin Qubit in Silicon Carbide'. In: *Physical Review Letters* 132.18 (2024), p. 180804. ISSN: 10797114. DOI: 10.1103/PhysRevLett.132.180804.

[5] R. Vincent, S. Klyatskaya, M. Ruben, W. Wernsdorfer and F. Balestro. 'Electronic read-out of a single nuclear spin using a molecular spin transistor'. In: *Nature* 488.7411 (2012), pp. 357–360. ISSN: 00280836. DOI: 10.1038/nature11341.

[6] J. J. Pla, K. Y. Tan, J. P. Dehollain, W. H. Lim, J. J. Morton, F. A. Zwanenburg, D. N. Jamieson, A. S. Dzurak and A. Morello. 'High-fidelity readout and control of a nuclear spin qubit in silicon'. In: *Nature* 496.7445 (2013), pp. 334–338. ISSN: 00280836. DOI: 10.1038/nature12011.

[7] S. Asaad, V. Mourik, B. Joecker, M. A. Johnson, A. D. Baczewski, H. R. Firgau, M. T. Mądzik, V. Schmitt, J. J. Pla, F. E. Hudson, K. M. Itoh, J. C. McCallum, A. S. Dzurak, A. Laucht and A. Morello. 'Coherent electrical control of a single high-spin nucleus in silicon'. In: *Nature* 579.7798 (2020), pp. 205–209. ISSN: 14764687. DOI: 10.1038/s41586-020-2057-7.

[8] B. Hensen, W. Wei Huang, C. H. Yang, K. Wai Chan, J. Yoneda, T. Tanttu, F. E. Hudson, A. Laucht, K. M. Itoh, T. D. Ladd, A. Morello and A. S. Dzurak. 'A silicon quantum-dot-coupled nuclear spin qubit'. In: *Nature Nanotechnology* 15.1 (2020), pp. 13–17. ISSN: 17483395. DOI: 10.1038/s41565-019-0587-7.

[9] C. F. Hirjibehedin, C. P. Lutz and A. J. Heinrich. 'Spin coupling in engineered atomic structures'. In: *Science* 312.5776 (2006), pp. 1021–1024. ISSN: 00368075. DOI: 10.1126/science.1125398.

[10] L. Zhou, J. Wiebe, S. Lounis, E. Vedmedenko, F. Meier, S. Blügel, P. H. Dederichs and R. Wiesendanger. 'Strength and directionality of surface Ruderman-Kittel-Kasuya-Yosida interactionmapped on the atomic scale'. In: *Nature Physics* 6.3 (2010), pp. 187–191. ISSN: 17452481. DOI: 10.1038/nphys1514.

[11] B. Bryant, A. Spinelli, J. J. Wagenaar, M. Gerrits and A. F. Otte. ‘Local control of single atom magnetocrystalline anisotropy’. In: *Physical Review Letters* 111.12 (2013), pp. 1–5. ISSN: 00319007. DOI: `10.1103/PhysRevLett.111.127203`.

[12] Y. L. Hsueh, D. Keith, Y. Chung, S. K. Gorman, L. Kranz, S. Monir, Z. Kembrey, J. G. Keizer, R. Rahman and M. Y. Simmons. ‘Engineering Spin-Orbit Interactions in Silicon Qubits at the Atomic-Scale’. In: *Advanced Materials* 36.26 (2024). ISSN: 15214095. DOI: `10.1002/adma.202312736`.

[13] A. A. Khajetoorians, J. Wiebe, B. Chilian, S. Lounis, S. Blügel and R. Wiesendanger. ‘Atom-by-atom engineering and magnetometry of tailored nanomagnets’. In: *Nature Physics* 8.6 (2012), pp. 497–503. ISSN: 17452481. DOI: `10.1038/nphys2299`.

[14] A. Spinelli, B. Bryant, F. Delgado, J. Fernández-Rossier and A. F. Otte. ‘Imaging of spin waves in atomically designed nanomagnets’. In: *Nature Materials* 13.8 (2014), pp. 782–785. ISSN: 14764660. DOI: `10.1038/nmat4018`.

[15] R. Toskovic, R. Van Den Berg, A. Spinelli, I. S. Eliens, B. Van Den Toorn, B. Bryant, J. S. Caux and A. F. Otte. ‘Atomic spin-chain realization of a model for quantum criticality’. In: *Nature Physics* 12.7 (2016), pp. 656–660. ISSN: 17452481. DOI: `10.1038/nphys3722`.

[16] S. Baumann, W. Paul, T. Choi, C. P. Lutz, A. Ardavan and A. J. Heinrich. ‘Electron paramagnetic resonance of individual atoms on a surface’. In: *Science* 350.6259 (2015), pp. 417–420. ISSN: 10959203. DOI: `10.1126/science.aac8703`.

[17] K. Yang, Y. Bae, W. Paul, F. D. Natterer, P. Willke, J. L. Lado, A. Ferrón, T. Choi, J. Fernández-Rossier, A. J. Heinrich and C. P. Lutz. ‘Engineering the Eigenstates of Coupled Spin-1/2 Atoms on a Surface’. In: *Physical Review Letters* 119.22 (2017), p. 227206. ISSN: 0031-9007. DOI: `10.1103/PhysRevLett.119.227206`.

[18] T. Choi, W. Paul, S. Rolf-Pissarczyk, A. J. MacDonald, F. D. Natterer, K. Yang, P. Willke, C. P. Lutz and A. J. Heinrich. ‘Atomic-scale sensing of the magnetic dipolar field from single atoms’. In: *Nature Nanotechnology* 12.5 (2017), pp. 420–424. ISSN: 17483395. DOI: `10.1038/nnano.2017.18`.

[19] Y. Bae, K. Yang, P. Willke, T. Choi, A. J. Heinrich and C. P. Lutz. ‘Enhanced quantum coherence in exchange coupled spins via singlet-triplet transitions - SuppMat’. In: *Science Advances* 4.11 (2018). ISSN: 23752548. DOI: `10.1126/sciadv.aau4159`.

[20] K. Yang, S. H. Phark, Y. Bae, T. Esat, P. Willke, A. Ardavan, A. J. Heinrich and C. P. Lutz. ‘Probing resonating valence bond states in artificial quantum magnets - SuppMat’. In: *Nature Communications* 12.1 (2021), pp. 1–18. ISSN: 20411723. DOI: `10.1038/s41467-021-21274-5`.

[21] H. Wang, P. Fan, J. Chen, L. Jiang, H. J. Gao, J. L. Lado and K. Yang. ‘Construction of topological quantum magnets from atomic spins on surfaces’. In: *Nature Nanotechnology* 19.12 (2024), pp. 1782–1788. ISSN: 17483395. DOI: `10.1038/s41565-024-01775-2`.

[22] K. Yang, W. Paul, S.-H. Phark, P. Willke, Y. Bae, T. Choi, T. Esat, A. Ardavan, A. J. Heinrich and C. P. Lutz. 'Coherent spin manipulation of individual atoms on a surface'. In: *Science* 366.6464 (2019), pp. 509–512. ISSN: 0036-8075. DOI: 10.1126/science.aay6779.

[23] L. M. Veldman, L. Farinacci, R. Rejali, R. Broekhoven, J. Gobeil, D. Coffey, M. Ternes and A. F. Otte. 'Free coherent evolution of a coupled atomic spin system initialized by electron scattering'. In: *Science* 372.6545 (2021), pp. 964–968. ISSN: 0036-8075. DOI: 10.1126/science.abg8223.

[24] Y. Wang, Y. Chen, H. T. Bui, C. Wolf, M. Haze, C. Mier, J. Kim, D.-J. Choi, C. P. Lutz, Y. Bae, S.-h. Phark and A. J. Heinrich. 'An atomic-scale multi-qubit platform'. In: *Science* 382.6666 (2023), pp. 87–92. ISSN: 0036-8075. DOI: 10.1126/science.ade5050.

[25] P. Willke, K. Yang, Y. Bae, A. J. Heinrich and C. P. Lutz. 'Magnetic resonance imaging of single atoms on a surface'. In: *Nature Physics* 15.10 (2019), pp. 1005–1010. ISSN: 17452481. DOI: 10.1038/s41567-019-0573-x.

[26] L. Farinacci, L. M. Veldman, P. Willke and S. Otte. 'Experimental Determination of a Single Atom Ground State Orbital through Hyperfine Anisotropy'. In: *Nano Letters* 22.21 (2022), pp. 8470–8474. ISSN: 1530-6984. DOI: 10.1021/acs.nanolett.2c02783.

[27] J. Kim, K. Noh, Y. Chen, F. Donati, A. J. Heinrich, C. Wolf and Y. Bae. 'Anisotropic Hyperfine Interaction of Surface-Adsorbed Single Atoms'. In: *Nano Letters* 22.23 (2022), pp. 9766–9772. ISSN: 1530-6984. DOI: 10.1021/acs.nanolett.2c02782.

[28] K. Yang, P. Willke, Y. Bae, A. Ferrón, J. L. Lado, A. Ardavan, J. Fernández-Rossier, A. J. Heinrich and C. P. Lutz. 'Electrically controlled nuclear polarization of individual atoms'. In: *Nature Nanotechnology* 13.12 (2018), pp. 1120–1125. ISSN: 17483395. DOI: 10.1038/s41565-018-0296-7.

[29] L. M. Veldman, E. W. Stolte, M. P. Canavan, R. Broekhoven, P. Willke, L. Farinacci and S. Otte. 'Coherent spin dynamics between electron and nucleus within a single atom'. In: *Nature Communications* 15.1 (2024), p. 7951. ISSN: 2041-1723. DOI: 10.1038/s41467-024-52270-0.

[30] K. Yang, W. Paul, F. D. Natterer, J. L. Lado, Y. Bae, P. Willke, T. Choi, A. Ferrón, J. Fernández-Rossier, A. J. Heinrich and C. P. Lutz. 'Tuning the Exchange Bias on a Single Atom from 1 mT to 10 T'. In: *Physical Review Letters* 122.22 (2019), p. 227203. ISSN: 10797114. DOI: 10.1103/PhysRevLett.122.227203.

[31] P. Kot, M. Ismail, R. Drost, J. Siebrecht, H. Huang and C. R. Ast. 'Electric control of spin transitions at the atomic scale'. In: *Nature Communications* 14.1 (2023), p. 6612. ISSN: 2041-1723. DOI: 10.1038/s41467-023-42287-2.

[32] M. Ternes. 'Spin excitations and correlations in scanning tunneling spectroscopy'. In: *New Journal of Physics* 17.6 (2015). ISSN: 13672630. DOI: 10.1088/1367-2630/17/6/063016.

[33] S. Shehada, M. dos Santos Dias, F. S. M. Guimarães, M. Abusaa and S. Lounis. 'Trends in the hyperfine interactions of magnetic adatoms on thin insulating layers'. In: *npj Computational Materials* 7.1 (2021), pp. 1–10. ISSN: 20573960. DOI: `10.1038/s41524-021-00556-y`.

[34] L. Sellies, R. Spachtholz, S. Bleher, J. Eckrich, P. Scheuerer and J. Repp. 'Single-molecule electron spin resonance by means of atomic force microscopy'. In: *Nature* 624.7990 (2023), pp. 64–68. ISSN: 0028-0836. DOI: `10.1038/s41586-023-06754-6`.

[35] T. Esat, D. Borodin, J. Oh, A. J. Heinrich, F. S. Tautz, Y. Bae and R. Temirov. 'A quantum sensor for atomic-scale electric and magnetic fields'. In: *Nature Nanotechnology* 19.10 (2024), pp. 1466–1471. ISSN: 1748-3387. DOI: `10.1038/s41565-024-01724-z`.

[36] D. Ristè, J. G. Van Leeuwen, H. S. Ku, K. W. Lehnert and L. Dicarlo. 'Initialization by measurement of a superconducting quantum bit circuit'. In: *Physical Review Letters* 109.5 (2012), pp. 1–5. ISSN: 00319007. DOI: `10.1103/PhysRevLett.109.050507`.

[37] A. Morello, J. J. Pla, F. A. Zwanenburg, K. W. Chan, K. Y. Tan, H. Huebl, M. Möttönen, C. D. Nugroho, C. Yang, J. A. Van Donkelaar, A. D. Alves, D. N. Jamieson, C. C. Escott, L. C. Hollenberg, R. G. Clark and A. S. Dzurak. 'Single-shot readout of an electron spin in silicon'. In: *Nature* 467.7316 (2010), pp. 687–691. ISSN: 00280836. DOI: `10.1038/nature09392`.

7

Theoretical investigation of the nuclear spin lifetime

That's the trouble with science.
Always upending itself, ruining perfect systems for the little inconvenience of them being wrong.

Zahel ('Rhythm of War')

We argue in the previous chapter, based on experimental results, that the nuclear spin lifetime of a ^{49}Ti adatom of MgO/Ag on the oxygen binding site is most likely limited by the degree of hybridization of the nuclear spin with the accompanying electron spin in the same atom. This hybridization, mediated by the hyperfine coupling, induces flip-flops upon projection of the electronic spin, which are interpreted as quantum jumps that relax the nuclear spin state. In this chapter, we will support and expand on this notion by showing, with an analytical solution to a model spin Hamiltonian, that the nuclear spin lifetime should increase quadratically with the external magnetic field strength and scales inversely with the in-plane hyperfine coupling cubed. Furthermore, we show that the lifetime should theoretically depend on the nuclear spin projection m_I *and we compare the dependency with experiment. Our model does confirm the experimentally observed trends, but there are significant numerical discrepancies that could originate either from incorrect hyperfine coupling parameters in the literature or from electronic orbital excitations. Lastly, we discuss the contributions of other nuclear spin relaxation mechanisms, and conclude that they are not significant for the experimental conditions in chapter 6.*

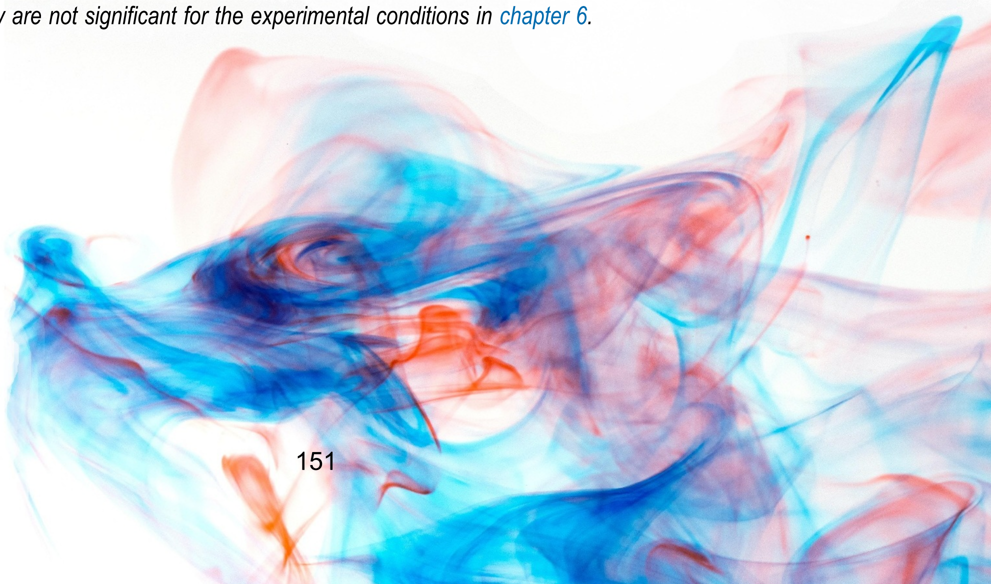

7.1. INCOHERENT FLIP-FLOP QUANTUM JUMPS

The lifetime of a quantum system describes the timescale at which energy is lost to the environment. Our system under study is a single ^{49}Ti atom adsorbed solidly on the oxygen binding site of thin-film MgO with a silver substrate. The atom has an electron spin and a nuclear spin. The electronic spin is known to have a fairly short lifetime because of Kondo scattering with the metallic substrate, which can move energy to and from the thermal bath that is the substrate [1]. However, since the nucleus does not exchange particles with its environment for an exchange interaction like Kondo, the nuclear spin is not directly affected by scattering events. We must look at non-exchange magnetic interactions to theoretically understand the lifetime of the nuclear spin we measured in chapter 6.

The strongest interaction present for the nuclear spin is the hyperfine coupling with the electron spin in the same atom. The hyperfine coupling hybridizes the electron and nuclear spin states, such that the eigenstates of the combined system are not strictly tensor product states of the two individual spins. This means that you cannot projectively measure one spin without potentially affecting the other. Projective measurements of the electron spin happen often, on account of the Kondo scattering, which could thus also flip the nuclear spin indirectly. The energy of the nuclear spin is thus indirectly lost to the bath, resulting in nuclear spin relaxation.

Due to the vector-like nature of the hyperfine interaction in our on-surface atom (see section 2.10), hybridization only occurs between spin product states with the same total angular momentum. So a flip of the nuclear spin is always accompanied by a flop of the electronic spin in the other spin direction, such that the total angular momentum is conserved. This is illustrated in fig. 7.1: different nuclear spin projections are only

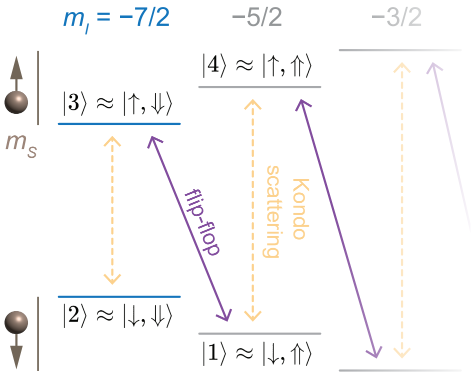

Fig. 7.1 | Spin energy level schematic of the combined nuclear and electron spin system Only a subspace of the full spin system with $I = 7/2$ and $S = 1/2$ is shown. In the regime of large Zeeman splitting, the four eigenstates with the two nuclear spin projections m_I = -7/2 and -5/2 can be mapped to the numbered eigenstates in eqs. (7.6) to (7.9) from model Hamiltonian eq. (7.1). Possible transitions are indicated with arrows: flip-flop quantum jumps between nuclear and electronic spins mediated by the hyperfine coupling (purple), and Kondo scattering of electronic spin with the environment (yellow, dashed).

connected with so-called ’flip-flops’ along the diagonals. Note that these are not strictly coherent flip-flop oscillations. These are incoherent flip-flop quantum jumps, caused by projections to the quantization axis of the electronic spin during decoherence or relaxation events due to interactions with the environment [2].

Of course, other nuclear spin relaxation pathways could exist in our system under study, but we found experimental indications that the flip-flop channel is dominating over others. Thus the nuclear spin lifetime is likely limited by the incoherent flip-flop rate with the accompanying electron spin in the same atom due to hybridization mediated by the hyperfine coupling. In this chapter, therefore, we want to investigate the flip-flop rate theoretically to develop an understanding of the dependencies of the nuclear spin lifetime.

7.2. ANALYTICAL MODEL FOR A HYBRIDIZATION-LIMITED NUCLEAR SPIN LIFETIME

The flip-flop rate, and thus the nuclear spin lifetime, depends on the degree of hybridization. The closer the eigenstates are to the spin product states, the more likely a projective event on the electron spin quantization axis, like Kondo scattering, will collapse to a state close to the same eigenstate. The subsequent time evolution with dephasing from the environment will bring the system to this closest eigenstate.[1] Most electron spin scattering events will thus leave the nuclear spin direction unchanged. In this regime of low hybridization, only an unlikely collapse to the product state with the small state vector amplitude will flip the nuclear spin.

The hybridization strongly depends on the external field we apply to our system, with higher fields resulting in lower hybridization and larger nuclear spin lifetimes. This was investigated in a theoretical model by Neumann *et al.* [3] for a nuclear spin in an individual NV center, which turns out to be a very similar system to ours. They also show that their model successfully fits experimental observation on the NV center, validating their approach. Here, we will follow this approach in our derivation for an expression of the hybridization-limited nuclear spin lifetime.

The full effective spin Hamiltonian of the combined $S = 1/2$ electron spin and $I = 7/2$ nuclear spin quantum system of the ^{49}Ti adatom was introduced in section 2.10 and given as eq. (2.10). For the sake of simplicity, we will initially work with a less complex model. We set the nuclear spin to $I = 1/2$, which will also leave out the quadrupole moment. Furthermore, we neglect the Zeeman energy of the nuclear spin, which is much smaller than the contribution of the hyperfine splitting in experiments. The electron spin is taken $S = 1/2$, as in the experiment. We assume an entirely out-of-plane total magnetic field B_z with a corresponding g-factor g_z in the same direction for the electron spin [4], but we include an anisotropic hyperfine coupling with an out-of-plane

---

[1] That is at least the interpretation of scattering events maintained for this chapter. It would also be a valid interpretation to say the system never gets to an eigenstate and keeps coherently precessing close to the eigenstate after projection, starting from the product state. During this precession, the probability of a flipped nuclear spin oscillates (zero when in the product state, finite otherwise). Because the next electron spin projection happens after a random time interval, the chance to flip the nuclear spin is ultimately equivilant, and both interpretations give the same result in this case.

component $A_\perp = A_z = 130$ MHz and in-plane component $A_\parallel = A_x/2 = A_y/2 = 5$ MHz [5]. The resulting model spin Hamiltonian is then

$$\hat{H} = B\hat{S}_z + A_\perp \hat{S}_z \hat{I}_z + A_\parallel(\hat{S}_+\hat{I}_- + \hat{S}_-\hat{I}_+), \tag{7.1}$$

where $B = \mu_B g_z B_z$ (μ_B is the Bohr magneton), $\hat{S}_z$ and $\hat{I}_z$ are the spin projection operators in the out-of-plane direction, and $\hat{S}_+$, $\hat{S}_-$, $\hat{I}_+$, and $\hat{I}_-$ are the spin ladder operators. These ladder operators are responsible for a flip-flop interaction. A matrix representation of the model Hamiltonian is given by

$$\begin{pmatrix} \frac{1}{2}B + \frac{1}{4}A_\perp & 0 & 0 & 0 \\ 0 & \frac{1}{2}B - \frac{1}{4}A_\perp & A_\parallel & 0 \\ 0 & A_\parallel & -\frac{1}{2}B - \frac{1}{4}A_\perp & 0 \\ 0 & 0 & 0 & -\frac{1}{2}B + \frac{1}{4}A_\perp \end{pmatrix} \tag{7.2}$$

with the spin product states $|m_S, m_I\rangle$ representing the unit vectors

$$|\uparrow,\Uparrow\rangle = \begin{pmatrix}1\\0\\0\\0\end{pmatrix}, |\uparrow,\Downarrow\rangle = \begin{pmatrix}0\\1\\0\\0\end{pmatrix}, |\downarrow,\Uparrow\rangle = \begin{pmatrix}0\\0\\1\\0\end{pmatrix}, |\downarrow,\Downarrow\rangle = \begin{pmatrix}0\\0\\0\\1\end{pmatrix}. \tag{7.3}$$

The m_S and m_I are the eigenvalues of S_z and I_z, respectively, and are also referred to as the spin projections. In this spin-1/2 system, they take the values up or down ($m_S = \uparrow, \downarrow$; $m_I = \Uparrow, \Downarrow$). In the convention of our model Hamiltonian, $m_S = \downarrow$ has the lower energy in the magnetic field B, and it is energetically favourable for the nuclear and electron spin to be anti-aligned due to the $A_\perp$ hyperfine coupling.

Before solving for the eigenstates of this Hamiltonian for arbitrary B, note that the eigenstates are the Bell states when the magnetic field approaches zero, with the singlet state as the ground state, and the nuclear spin and electron are maximally hybridized. When using a more complete model, this avoided level crossing is located at a finite magnetic field on the order of $A_\perp$, which has also been observed experimentally [5]. The nuclear spin lifetime at the avoided crossing $T_{1,n}(B = 0)$ can be estimated by considering that the flip-flop starting from a product state will be a coherent time evolution at a rate set by the energy difference $2A_\parallel$ between the two eigenstates in the avoided crossing. The period of a full flip-flop precession back to the starting product state is then $1/2A_\parallel$, so the estimated characteristic time to just flip the nuclear spin is half of this:

$$T_{\text{flip}}(B = 0) = 1/4A_\parallel = 50\ \text{ns}. \tag{7.4}$$

Note that this should be considered an upper limit: a faster electron spin projection rate might flip the nuclear spin before a coherent oscillation is completed. However, analytical expressions for the spin projection rates are more complicated [6] and are based on less tangible parameters compared to the directly experimentally observable in-plane hyperfine coupling [7, 8].

In the zero-field coherent flip-flop, the nuclear spin energy only completely relaxes to the environment if the electron spin scatters right after the nuclear spin flip. Otherwise the nuclear spin will flop back coherently without any energy lost. We can model this notion for the total nuclear spin lifetime $T_{1,n}$ by adding the electron spin lifetime $T_{1,e}$ of 190 ns [1] to T_{flip}. Unlike T_{flip}, $T_{1,e}$ is set mostly by the coupling to the metallic bath and does not significantly depend on the hybridization with the nuclear spin, so we shall see that this addition becomes negligible compared to T_{flip} in the limit of large magnetic field.

A flip-flop can only happen with the electron spin anti-aligned with the nuclear spin. We can expect scattering from the metallic bath to bring the electron spin to a certain mixed state distribution, which makes sure the appropriate electron spin state is available to initiate flip-flops some of the time. With the singlet state as the groundstate, and at zero temperature, the fraction in the correct electron spin direction for flip-flops P_e equals 1, because projection on either product state components in the singlet ($|\uparrow,\Downarrow\rangle$ and $|\downarrow,\Uparrow\rangle$) initiate flip-flops. However, at finite temperature some time-averaged population in, for example, the $|\downarrow,\Downarrow\rangle$ eigenstate could extend $T_{1,n}$ due to the partial unavailability of the electron spin to participate in the flip-flop. In this case we roughly estimate:

$$T_{1,n}(B=0) \approx \frac{1}{P_e} \cdot T_{\text{flip}}(B=0) + T_{1,e} = 1 \cdot 50\text{ ns} + 190\text{ ns} = 240\text{ ns}. \tag{7.5}$$

For a finite B field, the eigenstates will transition from the bell states to spin product states $|m_S, m_I\rangle$ with lower hybridization as the field increases. Using an exact solution, the Hamiltonian results in the following eigenstates [2], in order of increasing eigen energy for $B > A_{\|}$:

$$|1\rangle = \frac{1}{A_{\|}C_-}\left(\frac{1}{2}B - \sqrt{\frac{1}{4}B^2 + A_{\|}^2}\right)|\uparrow,\Downarrow\rangle + \frac{1}{C_-}|\downarrow,\Uparrow\rangle \approx |\downarrow,\Uparrow\rangle, \tag{7.6}$$

$$|2\rangle = |\downarrow,\Downarrow\rangle, \tag{7.7}$$

$$|3\rangle = \frac{1}{A_{\|}C_+}\left(\frac{1}{2}B + \sqrt{\frac{1}{4}B^2 + A_{\|}^2}\right)|\uparrow,\Downarrow\rangle + \frac{1}{C_+}|\downarrow,\Uparrow\rangle \approx |\uparrow,\Downarrow\rangle, \tag{7.8}$$

$$|4\rangle = |\uparrow,\Uparrow\rangle, \tag{7.9}$$

with

$$C_\pm^2 = 2 + \frac{B^2}{2A_{\|}^2} \pm \sqrt{\frac{B^4}{4A_{\|}^4} + \frac{B^2}{A_{\|}^2}}\,. \tag{7.10}$$

Note that the hybridization between the electron and nuclear spin states only depends on B and $A_{\|}$. The hybridization is totally independent of $A_\perp$. This means the in-plane hyperfine coupling is solely responsible for the flip-flop rate and hybridization is weaker for smaller $A_{\|}$, regardless of $A_\perp$. Experimentally for ESR-STM, a strong hyperfine

---

[2] Note that the Supplementary Material of [9], to which this derivation is a direct analogy to, has an (inconsequential) typo in the normalization of the eigenstates. The expressions on this page, with a factor $1/(A_{\|}C_\pm)$ in front of $|\uparrow,\Downarrow\rangle$, are the correct ones.

out-of-plane anisotropy is thus favourable to achieve long nuclear spin lifetimes (small $A_{\parallel}$) with sufficient frequency splitting between hyperfine resonances (large $A_{\perp}$).

In the analogy with the decay of the excited nuclear spin state in the full ^{49}Ti system, as depicted in the energy diagram in fig. 7.1, $|2\rangle$ and $|3\rangle$ correspond to the excited nuclear spin subspace m_I = -7/2 with either m_S, while $|1\rangle$ and $|4\rangle$ correspond to the next lower energy nuclear spin state m_I = -5/2. These subspaces are connected by a spin flip-flop quantum jump from $|3\rangle$ to $|1\rangle$, which relaxes the nuclear spin. Using a Fermi golden rule argument [2], the rate of this quantum jump – the inverse of the flipping time $T_{\text{flip}}(B)$ – scales with the probability P_{flip} of finding $|3\rangle$ in the spin product predominantly associated with $|1\rangle$ ($|\downarrow,\Uparrow\rangle$) upon projective measurement of $|3\rangle$ by the environment. This probability is non-zero because of the hybridization and can be calculated from our eigenstate exactly as

$$P_{\text{flip}} = |\langle\downarrow,\Uparrow|3\rangle|^2 = \frac{1}{|C_+|^2} \sim \frac{1}{T_{\text{flip}}} . \tag{7.11}$$

The found proportional scaling can be combined with $T_{\text{flip}}(B=0)$ to get $T_{1,n}$ at any magnetic field.

$$T_{1,n}(B) = \frac{1}{P_e} \cdot T_{\text{flip}}(B=0)\frac{T_{\text{flip}}(B)}{T_{\text{flip}}(B=0)} + T_{1,e} \tag{7.12}$$

$$= \frac{1}{P_e} \cdot T_{\text{flip}}(B=0)\frac{P_{\text{flip}}(B=0)}{P_{\text{flip}}(B)} + T_{1,e} \tag{7.13}$$

$$= \frac{1}{P_e} \cdot \frac{1}{4A_{\parallel}} \cdot \frac{1}{2}|C_+|^2 + T_{1,e}. \tag{7.14}$$

Here we used that $P_{\text{flip}}(B=0) = 1/2$. In the regime of large Zeeman splitting compared to the in-plane hyperfine coupling ($B >> A_{\parallel}$), we can approximate $|C_+|^2$ by only keeping the terms quadratic in $(B/A_{\parallel})$. The electron spin lifetime $T_{1,e}$ can also be neglected in this limit.

$$T_{1,n} \approx \frac{1}{P_e} \cdot \frac{1}{4A_{\parallel}} \cdot \frac{1}{2} \cdot \frac{B^2}{A_{\parallel}^2} = \frac{1}{P_e} \cdot \frac{B^2}{8A_{\parallel}^3} \tag{7.15}$$

P_e is determined by the distribution of the electron spin within the subspace of the excited nuclear spin $m_I = \Downarrow$. The lifetime of the electron spin (190 ns [1]) will be much shorter than the flip-flop time, so we can assume this distribution will be a Boltzmann distribution at temperature T. The flip-flop can happen from $|3\rangle \approx |\uparrow,\Downarrow\rangle$, but not from $|2\rangle = |\downarrow,\Downarrow\rangle$, so P_e is the probability to have the electron spin in the excited $m_s = \uparrow$ state. Since we are working in the product state regime by approximation, the energy difference for the thermal distribution is essentially the electron spin Zeeman splitting B. Therefore $P_e = e^{-B/k_bT}/Z$, with the partition function $Z = 1 + e^{-B/k_bT}$. This leads to the final analytical result:

$$T_{1,n} \approx (1 + e^{B/k_bT}) \cdot \frac{B^2}{8A_{\parallel}^3}. \tag{7.16}$$

In our probe-probe experiment where we measure the lifetime of the nuclear spin in section 6.3, we have an electron spin Zeeman splitting of 13.205 GHz. [3] The experiment was performed at a temperature of 0.4 K, which corresponds to a thermal energy of $k_b T = 8.33$ GHz, resulting in $e^{-B/k_b T} = 0.205$. This corresponds to $P_e = 0.170$ in the excited electron state.

Filling in all the parameters gives a numeric estimate $T_{1,n} = 1.03$ sec, which can be directly compared with our experimental value of 5.3 ± 0.5 sec. Even though the calculated nuclear spin lifetime lies outside the experimental errorbar, the result from our model does fall within the correct order of magnitude despite the significant simplifications made. Note that the model is sensitive to our rough estimate of $T_{\text{flip}}(B = 0)$. A zero-field flipping time of 257 ns instead of our estimated 50 ns would already match the model's $T_{1,n}$ to the experimental value.

Outside of just the numerical estimate of $T_{1,n}$, we analytically find in our model that the nuclear spin lifetime should grow quadratically with the magnetic field strength, if no other relaxation processes are limiting the lifetime beside the flip-flop channel. The fact that we experimentally observe a lifetime on the same order of magnitude as our theoretical result above suggests, among other (experimental) evidence, that our experiments were indeed performed in the flip-flop-limited regime. As such, we can expect the nuclear spin lifetime is also flip-flop limited for smaller magnetic fields, where the hybridization is even larger. More interestingly, on the condition that the flip-flop rate remains limiting, the lifetime could potentially be increased 16-fold to over 1 minute when using higher magnetic fields and RF frequencies that lay within state-of-the-art technical ability of existing ESR-STM setups (e.g. Drost *et al.* [10], with an out-of-plane field up to 6 T and operating at up to 100 GHz). An experimental observation of a quadratic dependence of the nuclear spin lifetime on the magnetic field strength, as was done for NV centers [3], could serve as a strong confirmation of flip-flop limited nuclear spin relaxation in nuclear spins in adatoms probed with ESR-STM.

7.3. LARGER NUCLEAR SPIN

With the basic model in place, we can reintroduce a total nuclear spin I larger than 1/2 back into the model. This would allow us to theoretically compare the nuclear spin lifetime in the different titanium isotopes that exist, and also explore the lifetime for different nuclear spin projections within the same atom. Experimentally, we can either do lifetime measurements on the isotopes ^{47}Ti with $I = 5/2$ or on ^{49}Ti with $I = 7/2$. However, including the $S = 1/2$ electronic spin, spin systems with these I have fairly large Hilbert spaces with 12 and 16 eigenstates, respectively. For illustrative purposes, we will instead begin with $I = 3/2$, which has only 8 eigenstates. It turns out this will reveal a pattern to derive $T_{1,n}$ for all I, so only the model with $I = 3/2$ needs to be worked out explicitly.

We take the same approach as before; (1) Solve for eigenstates of the Hamiltonian in eq. (7.1). (2) Identify for each eigenstate the corresponding approximate spin product states in large magnetic fields and the other product state that it is hybridized with. (3)

---

[3] The ESR frequency we used is 12.75 GHz, which includes Zeeman splitting and also the $A_\perp$ contribution of $-3.5 \cdot 130$ MHz for the $m_I = -7/2$ probed state.

Project on this hybridized product state to get the flip probability. (4) Finally, take the limit to large magnetic fields.

For I = 3/2, the matrix representation of the Hamiltonian in eq. (7.1) is:

$$\begin{pmatrix}
\frac{1}{2}B+\frac{3}{4}A_\perp & 0 & 0 & 0 & 0 & 0 & 0 & 0 \\
0 & \frac{1}{2}B+\frac{1}{4}A_\perp & 0 & 0 & \sqrt{3}A_\parallel & 0 & 0 & 0 \\
0 & 0 & \frac{1}{2}B-\frac{1}{4}A_\perp & 0 & 0 & 2A_\parallel & 0 & 0 \\
0 & 0 & 0 & \frac{1}{2}B-\frac{3}{4}A_\perp & 0 & 0 & \sqrt{3}A_\parallel & 0 \\
0 & \sqrt{3}A_\parallel & 0 & 0 & -\frac{1}{2}B-\frac{3}{4}A_\perp & 0 & 0 & 0 \\
0 & 0 & 2A_\parallel & 0 & 0 & -\frac{1}{2}B-\frac{1}{4}A_\perp & 0 & 0 \\
0 & 0 & 0 & \sqrt{3}A_\parallel & 0 & 0 & -\frac{1}{2}B+\frac{1}{4}A_\perp & 0 \\
0 & 0 & 0 & 0 & 0 & 0 & 0 & -\frac{1}{2}B+\frac{3}{4}A_\perp
\end{pmatrix} \tag{7.17}$$

using the spin product states $|m_S, m_I\rangle$ as the basis vectors, with an allocation described by

$$\left(|\uparrow,+\tfrac{3}{2}\rangle \quad |\uparrow,+\tfrac{1}{2}\rangle \quad |\uparrow,-\tfrac{1}{2}\rangle \quad |\uparrow,-\tfrac{3}{2}\rangle \quad |\downarrow,+\tfrac{3}{2}\rangle \quad |\downarrow,+\tfrac{1}{2}\rangle \quad |\downarrow,-\tfrac{1}{2}\rangle \quad |\downarrow,-\tfrac{3}{2}\rangle\right). \tag{7.18}$$

The Hamiltonian can be interpreted in the same way as with eq. (7.2), where the off-diagonals with $A_\parallel$ denote which product states are hybridized. In this case, there are multiple hybridizations, always with neighbouring nuclear spin projections. Note in particular the prefactors of $A_\parallel$, which depend on $|m_I|$. For the hybridization between $|\uparrow,-\frac{1}{2}\rangle$ and $|\downarrow,+\frac{1}{2}\rangle$, this coefficient equals 2. However, between product states with m_I = 3/2 and 1/2 (and m_I = -3/2 and -1/2), the coefficient is $\sqrt{3}$. This dependence on m_I is built into the definition of the spin ladder operators in the Hamiltonian:

$$\hat{I}_\pm|m_I\rangle = \sqrt{I(I+1) - m_I(m_I \pm 1)}\,|m_I \pm 1\rangle \tag{7.19}$$

The matrix elements $k(I, m_I)$ of $\hat{I}_\pm$ (the square root factor) ultimately reflect the fact that $|m_I\rangle$ and $|m_I + 1\rangle$ are eigenstates of both the $\hat{I}_z$ and $\hat{I}^2$ operators, and its values are derived from the accompanying normalization requirements of those eigenstates [11].

We can solve for all eight eigenstates of eq. (7.17) exactly, and identify the corresponding approximate spin product states in the limit of large B.

$$|1\rangle = |{\downarrow}, -\tfrac{3}{2}\rangle \,, \tag{7.20}$$

$$|2\rangle = |{\uparrow}, +\tfrac{3}{2}\rangle \,, \tag{7.21}$$

$$|3\rangle = \frac{1}{\sqrt{3}A_{\parallel}X_{-}}\left(\frac{B}{2} - \frac{A_{\perp}}{2} - \sqrt{\frac{B^2}{4} + 3A_{\parallel}^2 - \frac{BA_{\perp}}{2} + \frac{A_{\perp}^2}{4}}\right)|{\uparrow}, -\tfrac{3}{2}\rangle + \frac{1}{X_{-}}|{\downarrow}, -\tfrac{1}{2}\rangle \tag{7.22}$$

$$\approx |{\downarrow}, -\tfrac{1}{2}\rangle \,, \tag{7.23}$$

$$|4\rangle = \frac{1}{\sqrt{3}A_{\parallel}X_{+}}\left(\frac{B}{2} - \frac{A_{\perp}}{2} + \sqrt{\frac{B^2}{4} + 3A_{\parallel}^2 - \frac{BA_{\perp}}{2} + \frac{A_{\perp}^2}{4}}\right)|{\uparrow}, -\tfrac{3}{2}\rangle + \frac{1}{X_{+}}|{\downarrow}, -\tfrac{1}{2}\rangle \tag{7.24}$$

$$\approx |{\uparrow}, -\tfrac{3}{2}\rangle \,, \tag{7.25}$$

$$|5\rangle = \frac{1}{\sqrt{3}A_{\parallel}Y_{-}}\left(\frac{B}{2} + \frac{A_{\perp}}{2} - \sqrt{\frac{B^2}{4} + 3A_{\parallel}^2 + \frac{BA_{\perp}}{2} + \frac{A_{\perp}^2}{4}}\right)|{\uparrow}, +\tfrac{1}{2}\rangle + \frac{1}{Y_{-}}|{\downarrow}, +\tfrac{3}{2}\rangle \tag{7.26}$$

$$\approx |{\downarrow}, +\tfrac{3}{2}\rangle \,, \tag{7.27}$$

$$|6\rangle = \frac{1}{\sqrt{3}A_{\parallel}Y_{+}}\left(\frac{B}{2} + \frac{A_{\perp}}{2} + \sqrt{\frac{B^2}{4} + 3A_{\parallel}^2 + \frac{BA_{\perp}}{2} + \frac{A_{\perp}^2}{4}}\right)|{\uparrow}, +\tfrac{1}{2}\rangle + \frac{1}{Y_{+}}|{\downarrow}, +\tfrac{3}{2}\rangle \tag{7.28}$$

$$\approx |{\uparrow}, +\tfrac{1}{2}\rangle \,, \tag{7.29}$$

$$|7\rangle = \frac{1}{A_{\parallel}Z_{-}}\left(\frac{1}{4}B - \sqrt{\frac{1}{16}B^2 + A_{\parallel}^2}\right)|{\uparrow}, -\tfrac{1}{2}\rangle + \frac{1}{Z_{-}}|{\downarrow}, +\tfrac{1}{2}\rangle \approx |{\downarrow}, +\tfrac{1}{2}\rangle \,, \tag{7.30}$$

$$|8\rangle = \frac{1}{A_{\parallel}Z_{+}}\left(\frac{1}{4}B + \sqrt{\frac{1}{16}B^2 + A_{\parallel}^2}\right)|{\uparrow}, -\tfrac{1}{2}\rangle + \frac{1}{Z_{+}}|{\downarrow}, +\tfrac{1}{2}\rangle \approx |{\uparrow}, -\tfrac{1}{2}\rangle \,. \tag{7.31}$$

with state normalisation factors $X_{\pm}$, $Y_{\pm}$ and $Z_{\pm}$ given as

$$X_{\pm}^2 = 2 + \frac{1}{6A_{\parallel}^2}\left(B^2 - 2BA_{\perp} + A_{\perp}^2 \pm (B - A_{\perp})\sqrt{B^2 - 2BA_{\perp} + A_{\perp}^2 + 12A_{\parallel}^2}\right), \tag{7.32}$$

$$Y_{\pm}^2 = 2 + \frac{1}{6A_{\parallel}^2}\left(B^2 + 2BA_{\perp} + A_{\perp}^2 \pm (B + A_{\perp})\sqrt{B^2 + 2BA_{\perp} + A_{\perp}^2 + 12A_{\parallel}^2}\right), \tag{7.33}$$

$$Z_{\pm}^2 = 2 + \frac{B^2}{8A_{\parallel}^2} \pm \sqrt{\frac{B^4}{64A_{\parallel}^4} + \frac{B^2}{4A_{\parallel}^2}} \,. \tag{7.34}$$

To give an overview of the relationships: $|1\rangle$ and $|2\rangle$ are extremal states that do not hybridize. $|3\rangle$ flip-flops with $|4\rangle$ on the negative m_I = -3/2 side. Similarly, $|5\rangle$ flip-flops with $|6\rangle$ on the positive m_I = +3/2 side. The state $|7\rangle$ flip-flops with $|8\rangle$ between m_I = ±1/2 and these are essentially the same states as with I = 1/2 in eqs. (7.6) and (7.8), but with a substitution $A_{||} \rightarrow 2A_{||}$.

We can find the flip-flop probabilities for the different nuclear spin transitions $T_{m_I \leftrightarrow m_I \pm 1}$ by projecting the various hybridized eigenstates on different product states. As before, we make the approximation $B >> A$ for the high field regime, keeping only the terms quadratic in B:

$$T_{\text{flip}}^{-\frac{3}{2}\leftrightarrow -\frac{1}{2}}(B) \sim 1/P_{\text{flip}} = \frac{1}{|\langle \downarrow, -\frac{1}{2}|4\rangle|^2} = X_+^2 \approx \frac{1}{3}\frac{B^2}{A_{||}^2} \, , \tag{7.35}$$

$$T_{\text{flip}}^{+\frac{1}{2}\leftrightarrow +\frac{3}{2}}(B) \sim 1/P_{\text{flip}} = \frac{1}{|\langle \downarrow, +\frac{3}{2}|6\rangle|^2} = Y_+^2 \approx \frac{1}{3}\frac{B^2}{A_{||}^2} \, , \tag{7.36}$$

$$T_{\text{flip}}^{-\frac{1}{2}\leftrightarrow +\frac{1}{2}}(B) \sim 1/P_{\text{flip}} = \frac{1}{|\langle \downarrow, +\frac{1}{2}|8\rangle|^2} = Z_+^2 \approx \frac{1}{4}\frac{B^2}{A_{||}^2} \, . \tag{7.37}$$

It is no coincidence that the numeric prefactors to $B^2/A_{||}62$ are the inverse of the fourth power of the corresponding $\hat{I}_{\pm}$ matrix elements $k_{\pm}(I, m_I)$ (eq. (7.19)). This is a systematic result that holds up for any I and any m_I, because the high field approximation neglects the contributions of $A_{\perp}$ (which will never scale with B^2). Besides the inconsequential $A_{\perp}$ contribution, the form of the hybridization is the consequence of isolated 2x2 sub-matrices between m_I states due to the in-plane hyperfine coupling. The ladder operators in the Hamiltonian in *eq.* (7.1) do not produce sub-Hilbert spaces that are connected beyond than 2x2. What remains are the prefactors of the off-diagonal matrix elements, which depend solely on I and m_I and are given systematically by eq. (7.19). It is essentially a scaling of $A_{||}$ in eq. (7.16).

Working towards a complete expression for the nuclear spin lifetimes of the different m_I analogous to eq. (7.16), we still need to introduce the flop-flop time $T_{\text{flip}}(B = 0)$ at the avoided crossing, and the electron spin population P_e for the time-averaged availability of the flipping state. The flip-flop times at the avoided crossing are set by the energy difference between eigenstates at the avoided crossing. Note that the avoided crossing is not necessarily positioned at $B = 0$. For flip-flop transitions $|3\rangle \leftrightarrow |4\rangle$ and $|5\rangle \leftrightarrow |6\rangle$ the avoid crossings are at $B = A_{\perp}$ and $-A_{\perp}$, respectively. $|7\rangle \leftrightarrow |8\rangle$ still has the avoided crossing at $B = 0$. We will need to get the energy difference for $T_{\text{flip}}(B = 0)$ at these points instead of $B = 0$, although we will keep the $B = 0$ in $T_{\text{flip}}(B = 0)$ to refer to its value at the avoided crossing. Furthermore, we will add a shift in the quadratic B term in the $T_{1,n}(B)$ expressions $B \rightarrow B + (m_I \pm 1/2)A_{\perp}$, to redefine it as the magnetic field difference to the avoided crossing. The sign depends on whether m_I increases (+) or decreases (-). Optionally, this shift could also be neglected. This would be justified if $B >> A_{\perp}$, and it keeps the results general for all m_I at any I without needing eigenstate calculations. At the magnetic fields in our experiment, the difference between calculated lifetimes with or without the shift is about 5%, so we include the shift in our extended model for now.

This time, we do still need to calculate the eigenenergies E_i to support the general solution. They are given by:

$$E_1 = \frac{1}{4}(3A_\perp - 2B),\ E_2 = \frac{1}{4}(3A_\perp + 2B), \tag{7.38}$$

$$\begin{aligned} &E_3 = -\frac{1}{2}\sqrt{(B - A_\perp)^2 + 12A_\parallel^2} - \frac{A_\perp}{4}, \quad E_4 = +\frac{1}{2}\sqrt{(B - A_\perp)^2 + 12A_\parallel^2} - \frac{A_\perp}{4}, \\ &\Delta E_{3,4}(+A_\perp) = 2\sqrt{3}A_\parallel, \end{aligned} \tag{7.39}$$

$$\begin{aligned} &E_5 = -\frac{1}{2}\sqrt{(B + A_\perp)^2 + 12A_\parallel^2} - \frac{A_\perp}{4}, \quad E_6 = +\frac{1}{2}\sqrt{(B + A_\perp)^2 + 12A_\parallel^2} - \frac{A_\perp}{4}, \\ &\Delta E_{5,6}(-A_\perp) = 2\sqrt{3}A_\parallel, \end{aligned} \tag{7.40}$$

$$\begin{aligned} &E_7 = -\frac{1}{2}\sqrt{B^2 + 16A_\parallel^2} - \frac{A_\perp}{4}, \quad E_8 = +\frac{1}{2}\sqrt{B^2 + 16A_\parallel^2} - \frac{A_\perp}{4}, \\ &\Delta E_{7,8}(-A_\perp) = 4A_\parallel. \end{aligned} \tag{7.41}$$

Since we take half of the periods of the free-evolution flip-flop precession, the flip times at the avoided crossings are:

$$T_{\text{flip}}^{-\frac{3}{2}\leftrightarrow-\frac{1}{2}}(B=0) = \frac{1}{4\sqrt{3}\cdot A_\parallel}, \quad T_{\text{flip}}^{+\frac{1}{2}\leftrightarrow+\frac{3}{2}}(B=0) = \frac{1}{4\sqrt{3}\cdot A_\parallel}, \quad T_{\text{flip}}^{-\frac{1}{2}\leftrightarrow+\frac{1}{2}}(B=0) = \frac{1}{4\cdot 2\cdot A_\parallel}. \tag{7.42}$$

These can be compared to the zero field flip time of $1/4A_\parallel$ in the $I = 1/2$ model (eq. (7.4)). Again, we see the $\hat{I}_\pm$ matrix element $k_\pm(I, m_I)$ entering here. It should be clear that the general expression for the flip time at the avoided crossing, for any I and m_I equals

$$T_{\text{flip}}(B = 0) = \frac{1}{4k_\pm(I, m_I)}\frac{1}{A_\parallel} \tag{7.43}$$

Continuing with the electron spin availability, we have to consider that flip-flops with increasing nuclear spin projection ($m_I + 1$) require occupation of the $m_S = \uparrow$ eigenstate, opposed to the $m_S = \downarrow$ eigenstate at the same m_I. The P_e is therefore equal to the thermal population in this excited electron state, $e^{-B/k_bT}/(1 + e^{-B/k_bT})$, as before. However, for nuclear spin transitions with decreasing m_I, the relevant electron spin population is the population of the groundstate in this subsystem, with $m_S = \downarrow$. So the $P_e = 1/(1 + e^{-B/k_bT})$ is larger, and the T_{flip} is actually shorter. Furthermore, the electron spin energy difference within a given m_I subspace is actually the hyperfine resonance transition energy $B + m_I A_\perp$. We also implement this shift.

Note that we will also need the probability to project on the other product state at the avoided crossing $P(B = 0)$. These are simply equal to 1/2, as in the original $I = 1/2$ model, since either of the two product state involved in any avoided crossing is equally likely during time-averaged precession. This enters as an extra factor. Putting it all together, according to eq. (7.13), for the total time $T_{1,n}(B)$ for a particular transition from one m_I state to another, we get our final result:

$$\text{For increasing } m_I: \quad T_{1,n}^{m_I \to m_I+1} \approx \left(1 + e^{+\frac{B + m_I A_\perp}{k_b T}}\right) \cdot \frac{(B + (m_I + \frac{1}{2})A_\perp)^2}{8A_\parallel^3 \cdot k_+(I, m_I)^3}, \tag{7.44}$$

$$\text{For decreasing } m_I: \quad T_{1,n}^{m_I \to m_I-1} \approx \left(1 + e^{-\frac{B + m_I A_\perp}{k_b T}}\right) \cdot \frac{(B + (m_I - \frac{1}{2})A_\perp)^2}{8A_\parallel^3 \cdot k_-(I, m_I)^3}, \tag{7.45}$$

$$\text{with}: \quad k_\pm(I, m_I) = \sqrt{I(I+1) - m_I(m_I \pm 1)} \tag{7.46}$$

This more general result is consistent with result from our basic model in eq. (7.16), with $k_+ = 1$ for $I = 1/2$ and $m_I = -1/2$. In the experiment from chapter 6 on an ^{49}Ti isotope, which has $I = 7/2$, we measured the nuclear spin lifetime of the $m_I = -7/2$ state as it increases to -5/2.. Filling in all the other parameters for this spin systems ($B = 13.205$ GHz, $A_\parallel = 5$ MHz, $A_\perp = 130$ MHz, $k_B T = 0.4$ K $= 8.33$ GHz), we get $T_{1,n}^{-\frac{7}{2} \to -\frac{5}{2}} = 50$ ms.

As mentioned, the experimental value was 5.3 ± 0.5 sec. In our simpler $I = 1/2$ model, we had a lifetime of 1.03 sec. This means that our estimate has actually gotten two orders of magnitude worse with this more complete model. This large difference can be attributed to the parameter $k_\pm$ that increases with I.

7.4. DISCUSSION ON THE DISCREPANCY BETWEEN THEORY AND EXPERIMENT

The large mismatch between numeric result of the theory and experimental value prompts a discussion on the origin of this discrepancy. Inaccuracies in the analytical model as a whole might enter due to the elementary treatment of electron scattering. For instance, the rate of electron scattering events that could project to a spin product state is hidden in the proportionality between P_{flip} and $1/T_{\text{flip}}$.

A proper treatment that adds the presence of the electron tunneling barrier might show a more realistic number of projections over time, potentially resulting in a different estimate of the nuclear spin lifetime and a stronger temperature dependence due to the Fermi-Dirac distributions in the metallic baths. The inclusion of the sizable quadrupole energy could also change the calculated nuclear spin lifetime. Interestingly, however, a rate equation approach to this problem with quadrupole included and rates based on Kondo scattering with the substrate and the tip has also yielded nuclear spin lifetimes around 50 ms [9]. Although it is disappointing that neither match the experimental lifetime, it is encouraging that the analytical model agrees with numerical methods.

7.4.1. HYPOTHESIS: INACCURATE IN-PLANE HYPERFINE COUPLING VALUE

Both the rate equation model and the analytical approach in this chapter are based on literature values of the in-plane hyperfine coupling and Zeeman splitting. These have been measured in two published ESR-STM experiments on titanium isotopes [5, 12]. On one hand, the in-plane hyperfine splitting of 10 MHz ($A_x = A_y = 2A_{||}$) rivals the achieved ESR linewidths in these experiments. Furthermore, a true in-plane magnetic field, without any out-of plane field component that introduces a fraction of $A_\perp$ to the peak splitting, might not have been achieved due to misalignments of the sample or an angle in the tip magnetic field.

On the other hand, spectra from the two different labs clearly show a splitting of resonance peaks, or at least a single broadened resonance peak, that would not be compatible with the in-plane hyperfine splitting of only $2A_{||} = 2.1$ MHz required to match the theory to the experimental $T_{1,n}$. Getting the additional 7.9 MHz splitting from an unintended out-of-plane magnetic field component would correspond to a sample plane missalignment of 3.5° (130 MHz · sin(3.5°) = 7.9 MHz). This angle is large, but could be reasonable. Still, it would be surprising if both setups had the exact same vertical misalignment angle. The same is true for the ~ 30 mT out-of-plane tip field components [13] required to apply the equivalent magnetic field angle with the 0.5 T in-plane external field used in the experiment in [5].

The experiments in [12] were performed with an external field $B_x = 0.9$ T and $B_x = 0.1$ T. This corresponds to an out-of-plane angle of 6.3°. With the hindsight of the indisputable out-of-plane hyperfine coupling splitting of $A_z = 130$ MHz measured years later by [5], the ~11 MHz hyperfine splitting observed in [12] can actually be entirely attributed to the out-of-plane hyperfine coupling, despite the majority in-plane field: 130 MHz·sin(6.3°) = 14 MHz. This suggests the actual A_x was likely considerably smaller than the claimed 9.1 MHz.

We have to consider that a comparible sample misalignment could be present in our experiment to measure the nuclear spin lifetime, too. After all, one of our two sources [5] used the same STM setup. This means we would have a similarly increased effectively in-plane hyperfine coupling $A_{||}$, regardless of what the true value of the in-plane hyperfine is. Or alternatively, we could have an inherent $A_{||}$ that is so small, that the effective $A_{||}$ originates entirely from magnetic field angle. In the case of an hypothestical intrinsic $A_{||} = 0$ MHz, only a 1° rotation of an otherwise out-of-plane magnetic field would result in an effective $A_{||} = 1.1$ MHz required to match the lifetime theory to experiment. That 1° corresponds to an in-plane magnetic tip field of 28 mT in the 1.6 T out-of-plane field used. Although again somewhat large, this is a reasonable value.

A tip-field-dependent in-plane hyperfine coupling would imply that the hybridization, and thus the nuclear spin lifetime, depends very strongly on the microtip. Moreover, it would explain reports that the DC bias nuclear spin pumping in CW ESR-STM experiments is microtip-dependent and can be tuned with tip height [5, 14]. Arguably, we have already found a microtip dependence in our repeat experiment of the nuclear spin lifetime in fig. 6.8 that yielded $T_{1,n} = 4.3 \pm 0.8$ sec with a different tip, compared to the original 5.3 ± 0.5 sec.

7.4.2. HYPOTHESIS: ORBITAL EXCITATIONS AND IONIZATION

While an inaccurate input parameter value would thus be a reasonable explanation, we should investigate alternative explanations for the lifetime value discrepancy between theory and experiment. Assuming then that $A_{||}$ really is 5 MHz, we could question our theoretical approaches. Rate equation models, however, have been very successful in capturing the behaviour of electron spins on surfaces, also when nuclear spins are involved [6, 15]. Furthermore, the analytical approach used for the chapter has been verified experimentally for individual nuclear spins hyperfine-coupled to an NV center, which is in many ways analogous to our spin system [3].

If we, hypothetically, trust both the models' approaches and the input parameter values, we have to assume the calculated degree of hybridization and the accompanying flip-flop rate are accurate. The discrepancy with the experimentally acquired lifetime then suggests that our theory, a nuclear spin lifetime limited by incoherent flip-flops due to hybridization mediated by the hyperfine coupling, might not be the whole story. Since the lifetimes were calculated with models that are as realistic as possible, it raises the question: how could the experimental lifetime even be longer than the theoretical prediction of the hybridization-limited lifetime? We have to find an argument why a theoretically predicted flip-flop rate would be suppressed.

Such arguments are, unfortunately, hard to find. One possiblity would be that the electronic spin state for the flip-flop is, for some reason, much less populated over time than the effective spin Hamiltonian $\hat{H}$ in eq. (7.1) suggests in thermal equilibrium. For example, the Ti atom could be ionized some of the time. Without an electron present in the outer shell that could facilitate a flip-flop, the lifetime would increase. At the same time, the observed hyperfine coupling in CW-ESR experiments would remain the same if the non-ionized state is still often occupied time-averaged. The ESR current signal would just be lower. It should be noted, however, that the flip-flop state must only be available for 1% of the time to scale the $T_{1,n}$ = 50 ms flip-flop limit to the observed 5.3 sec. Instead, ionizing the Ti adatom requires energies in the range of volts, which is larger even than the adsorption energy that binds it to the surface. Thermal occupation of the ionized state is therefore negligible.

A similar idea might still be realized if there is an entirely different electron orbital configuration with its own effective spin Hamiltonian $\hat{H}'$ that is often thermally occupied. This hypothetical orbital state could have much smaller hyperfine coupling, and thus a reduced flip-flop rate. If the electron thermally spends significant time in that orbital excitation, the nuclear spin lifetime would be longer. Ti on the oxygen binding site does, in fact, have an orbital (momentum) excitation at ± 80 mV [16, 17] and the role of this orbital for the nuclear spin lifetime for this system has been discussed before [18]. This orbital excitation energy is much higher than the thermal energy, however, so its effect on the lifetime should also be minimal at the zero bias we used in our experiment. Furthermore, the experimentally-observed increase of the nuclear spin polarization around the orbital excitation bias in CW-ESR experiments [5] suggests that the flip-flop rate is actually larger in this orbital excitation, rather then the lower rate required for a lifetime improvement.

Based on this, one interesting hypothesis would be that all observed ESR spectra on Ti on the oxygen binding site are actually a reflection of the spin Hamiltonian in this orbital excitation, instead of the groundstate orbital. This would rationalize a low thermal occupation of the state that can initiate an incoherent flip-flop: it is a state with a high excitation energy. In this hypothesis, the groundstate orbital would then have a different electron g-factor and hyperfine coupling with a low flip-flop rate. This assumption could also tie into another open question for Ti on the oxygen binding site: ESR-STM signal can only be observed with positive bias [19], which would then be explained by only the positive bias orbital having a g-factor in the ESR range.

The above discussion should be considered as hypothetical. We will need more experimental data of nuclear spin lifetimes, with different microtips and also from other types of adatoms, to understand the spin system. Yet, the hypothesis of the unavailability of the flip-flop state discussed in this section does make the prediction that the nuclear spin lifetime is still limited by some flip-flop rate due to hybridization. Hence, the funtional form of our analytical model should still apply, albeit with a much different scaling factor (50 ms / 5.3 sec) that does not depend on the nuclear spin state. The same, of course, applies for the situation where the hyperfine coupling is simply a smaller value than previously measured. In the next section, therefore, we will investigate the ratios between lifetimes of different nuclear spin states to test our analytical model on a relative basis.

7.5. RATIOS OF NUCLEAR SPIN DWELL TIMES

Even though the theoretical model in eq. (7.44) does not yield numerical nuclear lifetime values that match the experimental results, we can try to verify the functional relationships between the lifetimes of different nuclear spin projections m_I that derives from our analytical model by looking at the ratios of lifetimes. Since experimental values of the unperturbed nuclear spin lifetimes for multiple m_I states are not available, we have to resort to measurements of the characteristic dwell time T_1^{CW} instead (see figs. 6.3 and 6.7). The experimental T_1^{CW} is available for m_I = -7/2, -5/2, -3/2, and -1/2 in the ^{49}Ti adatom with I = 7/2.

These dwell times were measured with the disturbance of a continuous ESR drive and DC bias that, as we have shown experimentally, reduce the nuclear spin lifetime and dynamically pump the nuclear spin projection, respectively. Importantly, however, these processes are driven by the hybridization between spin product states and should also be limited by the same flip-flop rate. The DC bias and ESR driving only perturb the nuclear spin by changing the electron spin populations. This we can account for in our model by choosing a P_e (flip-flop state availability within a m_I subspace) that is different from the thermal Boltzmann distribution of the electron spin that we had implemented before. In this case we will assume that the ESR driving is dominant, which will populate both electron spin projections equally, resulting in P_e = 0.5 for the flip-flop time of both increasing and decreasing m_I (this is equivalent to the limit of large temperature T in eq. (7.44)).

We will make another approximation by taking the $B >> A_\perp$ limit. This removes a shift in B due to the avoided crossing at non-zero field from eq. (7.44) for the nuclear spin lifetime. After that, the only remaining dependence on m_I is contained in factor with the ladder operator matrix elements $k_\pm$. Hence, the ratio between $T_1^{CW}(m_I)$ is solely a function of $k_\pm(m_I)$.

The total lifetime of a particular m_I is determined by the sum of all outgoing flip-flop rates. These are the rate of an increasing $m_I + 1$ and a decreasing $m_I - 1$ flip-flop. According to eqs. (7.44) and (7.45) these rates, which are the inverse of $T_{1,n}^{m_I \to m_I \pm 1}$, scale as ~ $k_\pm^3$. So the total outgoing rate $r(m_I)$ scales as ~ $k_+^3 + k_-^3$. Using this, we get the derived expression for the ratio of characteristic dwell times:

$$\frac{T_1^{CW}(m_I)}{T_1^{CW}(m_I+1)} = \frac{r(m_I+1)}{r(m_I)} = \frac{k_+(m_I+1)^3 + k_-(m_I+1)^3}{k_+(m_I)^3 + k_-(m_I)^3} \tag{7.47}$$

Both the ratios obtained from the experiments and from theory are plotted together in fig. 7.2. Comparing the two, our flip-flop model does reproduce the trends in the experimental data. Thus the observed increase in the dwell time ratio with larger $|m_I|$ can be attributed to the decrease in $k_\pm(|m_I|)$. Furthermore, the model also matches numerically for two of the three points.

Note that $k_+ = 0$ for $m_I = +7/2$ and $k_- = 0$ for $m_I = -7/2$, which can be interpreted as these edge states having only a relaxation path to one neighbour, rather the possibility of flipping to either side. This enhances the lifetime of these edge states on top of the fact that $k_\pm(m_I)$ is smaller for larger $|m_I|$. However, $T_1^{CW}(-7/2)$ turns out to be even longer than the model predicts. This could be attributed to the spin pumping of the DC bias, which we did not properly take into account in this version of the model.

Overall, we can conclude that the incoherent flip-flop limit on the nuclear spin lifetime does likely apply to the ^{49}Ti adatom spin system. The flip-flop rate is just a different numerical value than the value calculated using the models in this chapter. This means that our hypotheses brought forward in section 7.4 might apply. As discussed, the discrepancy could be explained by a potential small off-axis angle away from the intended in-plane magnetic field in the CW-ESR experiments from literature that determined the $A_\parallel$ value we used [5, 12], which might thus not reflect the effective hyperfine coupling in our lifetime experiments. Alternatively, the discrepancy could be explained by the presence of an orbital excitation with distinct hyperfine couplings.

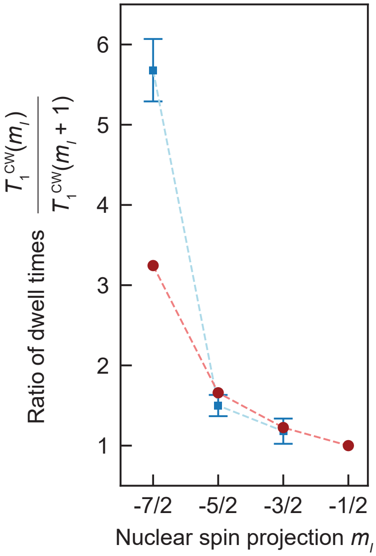

Fig. 7.2 | Ratios of characteristic dwell times $T_1^{CW}(m_I)$ between neighbouring nuclear spin projections m_I. Blue: ratios obtained from experimental data on ^{49}Ti in fig. 6.3d and fig. 6.7i-k. Note that the current setpoint datapoints with the longest T_1^{CW} were selected for this plot, because the analysis of these points is less affected by the 20 ms sampling resolution. Red: ratios based on theoretical calculations with the hyridization-limited flip-flop relaxation channel (eq. (7.47)).

7.6. INVESTIGATION OF OTHER NUCLEAR SPIN RELAXATION CHANNELS

We have argued, based on experimental results and the theoretical model discussed in the previous sections, that the nuclear spin lifetime of our ^{49}Ti adatom is most likely limited by the degree of hybridization between the nuclear spin and the accompanying electron spin in the same atom. In this section, we will further support our reasoning with a theoretical investigation of other potential contributions to nuclear spin relaxation. We will discuss the following relaxation sources: (A) dipole-dipole coupling to other nuclear spins, (B) hyperfine coupling with bulk electron spins in silver, (C) magnetic Johnson noise, and (D) phonon-mediated relaxation.

(A) DIPOLE-DIPOLE COUPLING TO OTHER NUCLEAR SPINS

One potential relaxation channel for the ^{49}Ti nuclear spin might be via magnetic dipole-dipole coupling to nuclear spins in the MgO layer and the bulk silver underneath. Silver consists solely of isotopes with nuclear spin $I_{\mathrm{Ag}} = 1/2$. The isotope ^{25}Mg has nuclear spin $I_{\mathrm{Mg}} = 5/2$ with a natural abundance of 10%, meaning there is a 34% chance of the ^{49}Ti atom neighbouring at least one ^{25}Mg. Oxygen also has a stable isotope with finite nuclear spin, but this isotope has a natural abundance of only 0.04%.

Relaxation via a direct flip-flop between two nuclear spins, a similar channel to the dominating hyperfine-mediated flip-flop with the electron spin discussed in section 7.2, is highly suppressed because of the large energy detuning between the spins compared to the weak dipole coupling. This can be illustrated with a simplified spin Hamiltonian analogous to eq. (7.1) with two nuclear spins A and B, both I_{A}, $I_{\mathrm{B}} = 1/2$, with an energy detuning Δ and an off-diagonal term D from the dipole-dipole coupling:

$$\hat{H} = \Delta \hat{I}_z^A + D(\hat{I}_+^A \hat{I}_-^B + \hat{I}_-^A \hat{I}_+^B) \tag{7.48}$$

where $\hat{I}_z^A$ is a spin projection operator on the quantization axis for spin A, and $\hat{I}_+^A$, $\hat{I}_-^A$, $\hat{I}_+^B$, and $\hat{I}_-^B$ are the spin ladder operators for the two spins. Spin A corresponds to the ^{49} nuclear spin and spin B to a nuclear spin in the bulk.

We find the characteristic flip-flop time T_{flip} in the same way as in section 7.2. For simplicity, we take the limit of large temperature, because the Zeeman energy splitting are much smaller for nuclear spins. Substituting variables $B = \Delta$ and $A_{||} = D$ in eq. (7.16) results in the following expression:

$$T_{\mathrm{flip}} \approx \frac{\Delta^2}{4D^3} \tag{7.49}$$

The ^{25}Mg nuclear spin will often be closest to the ^{49}Ti nuclear spin, resulting in the largest dipole-dipole coupling. The dipole-dipole flip-flop matrix element is given by

$$D = \frac{\mu_0 \gamma_{\mathrm{Ti}} \gamma_{\mathrm{Mg}} \hbar^2}{8\pi d^3} \cdot (3\cos^2\theta - 1) \tag{7.50}$$

with μ_0 the vacuum magnetic permeability, γ_{Ti} and γ_{Mg} the gyromagnetic ratios for ^{49}Ti and ^{25}Mg nuclear spins respectively and Planck's constant $\hbar = h/2\pi$. We estimate the distance d from the Ti nucleus to the closest Mg nucleus in the MgO layer to be 0.2 nm[20], with $\theta = 45°$ the angle with the quantization axis. Filling in these parameters, we find a dipole-dipole flip-flop coupling $D = 26$ Hz. The detuning is mainly set by the hyperfine coupling, which is present only for ^{49}Ti. For $m_I = -7/2$ we estimate a transition energy of ~49 MHz, which also includes nuclear Zeeman splitting at 1.6 T and the quadrupole moment. ^{25}Mg has a Zeeman splitting of only ~4 MHz, thus $\Delta \approx 45$ MHz. The resulting estimated decay time from nuclear spin flip-flops T_{flip} is then 3×10^{10} seconds. Therefore, we deem this relaxation channel negligible.

We also considered flip-flops with other ^{49}Ti on oxygen binding sites of MgO. Note that none were present on the same approx. 50 nm wide MgO island in our experiment, but a 20 nm separation distance would result in a reasonable non-detuned flip-flop time of $1/4D = 3$ hours. These nuclear spins of the same species are still detuned, however, because the magnetic field from the STM tip adds Zeeman splitting only for the spin under study [13]. A typical tip field strength of 20 mT corresponds to $\Delta = 302$ kHz, which is enough to suppress this relaxation channel, too.

(B) Hyperfine coupling with bulk electron spins in silver

Another less likely candidates for limiting the relaxation time is direct hyperfine coupling to electronic spins in the silver metallic bath [21] (Fermi-contact). There is too little wavefunction overlap between the nucleus and the silver electrons. With a mean free path of silver electrons larger than microns below 1 K [22], we estimate a Fermi-contact interaction that is at least 12 orders of magnitude smaller than the Ti electron hyperfine coupling (ratio of wavefunction volumes), resulting in a coupling of less than 0.1 mHz.

(C) Magnetic Johnson noise

A more significant contribution comes from magnetic Johnson noise originating from thermal ballistic electron transport in the silver bulk [23, 24]. This magnetic noise can drive nuclear spin transitions, leading to spin relaxation. Extrapolating from experimental results on NV centers in close proximity to silver [24] — accounting for the different g-factor, temperature, and distance between the spin and the bulk — results in an estimated nuclear spin lifetime on the order of hours, if this relaxation channel would be limiting.

(D) Phonon-mediated relaxation

Another potentially large contribution could be spin-lattice relaxation via inelastic Raman-like processes [25]. Phonons can couple to the nuclear spin in different ways. (i) Vibrations in the lattice move the nucleus through the gradient magnetic dipole field from Mg and Ag nuclear spins in the bulk or other nearby magnetic adatom on the surface, which can drive spin transitions. (ii) Moving point charges around the Ti nucleus modulate the electric field gradient at the position of the nucleus, which couples to its quadrupole moment. (iii) Moving point charges modulate the hyperfine coupling. This could also change the hyperfine-mediated flip flop rate.

In these spin-lattice relaxation mechanisms, one phonon from a THz band scatters on the nuclear spin and returns to the same band with a slightly different energy. This is limited, however, by the thermal occupation of the phonon modes. Spin-phonon scattering rates fall off quickly with temperature far below the Debye temperature [25], which we estimate to be 1×10^3 K in our MgO thin film [26]. Therefore, spin-lattice relaxation is likely not a factor relative to the hyperfine-mediated flip-flop with the Ti electron spin at our operating the magnetic field. For reference, the nuclear spin of ^{25}Mg in MgO, which has a similar quadrupole moment as ^{49}Ti and is also positioned next to oxygen in the lattice, has a T_1 of 49 seconds at room temperature [27].

Since the spin-lattice relaxation does not depend on magnetic field strength, we hypothesize that spin-lattice relaxation could be more relevant than the hyperfine-mediated flip flop relaxation channel at high magnetic fields. Of the three coupling mechanisms, quadrupole-mediated coupling is often the strongest [28] and can thus be expected to be the largest contribution in this regime.

(E) CONCLUSION

We find that all sources of nuclear spin relaxation discussed above have a characteristic lifetime that is orders of magnitude longer than the lifetime of 5.3 seconds we found experimentally. Supported further by the theory in this chapter and the observed enhancement of relaxation due to ESR driving, which is discussed in chapter 6 ,we conclude that the nuclear spin lifetime of ^{49}Ti in our experiment is limited by the hyperfine-mediated flip-flop between the nuclear spin and the Ti electron spin. In the absence of this relaxation channel, the next-biggest contributions to relaxation might be magnetic Johnson noise or spin-lattice coupling.

REFERENCES

[1] K. Yang, Y. Bae, W. Paul, F. D. Natterer, P. Willke, J. L. Lado, A. Ferrón, T. Choi, J. Fernández-Rossier, A. J. Heinrich and C. P. Lutz. 'Engineering the Eigenstates of Coupled Spin-1/2 Atoms on a Surface'. In: *Physical Review Letters* 119.22 (2017), p. 227206. ISSN: 0031-9007. DOI: `10.1103/PhysRevLett.119.227206`.

[2] B. Joecker, H. G. Stemp, I. F. D. Fuentes, M. A. Johnson and A. Morello. 'Error channels in quantum nondemolition measurements on spin systems'. In: *Physical Review B* 109 (8 Feb. 2024). ISSN: 24699969. DOI: `10.1103/PhysRevB.109.085302`.

[3] P. Neumann, J. Beck, M. Steiner, F. Rempp, H. Fedder, P. R. Hemmer, J. Wrachtrup and F. Jelezko. 'Single-Shot Readout of a Single Nuclear Spin'. In: *Science* 329.5991 (2010), pp. 542–544. ISSN: 0036-8075. DOI: `10.1126/science.1189075`.

[4] M. Steinbrecher, W. M. J. van Weerdenburg, E. F. Walraven, N. P. E. van Mullekom, J. W. Gerritsen, F. D. Natterer, D. I. Badrtdinov, A. N. Rudenko, V. V. Mazurenko, M. I. Katsnelson, A. van der Avoird, G. C. Groenenboom and A. A. Khajetoorians. 'Quantifying the interplay between fine structure and geometry of an individual molecule on a surface'. In: *Physical Review B* 103.15 (2021), p. 155405. ISSN: 2469-9950. DOI: `10.1103/PhysRevB.103.155405`.

[5] L. M. Veldman, E. W. Stolte, M. P. Canavan, R. Broekhoven, P. Willke, L. Farinacci and S. Otte. 'Coherent spin dynamics between electron and nucleus within a single atom'. In: *Nature Communications* 15.1 (2024), p. 7951. ISSN: 2041-1723. DOI: 10.1038/s41467-024-52270-0.

[6] M. Ternes. 'Spin excitations and correlations in scanning tunneling spectroscopy'. In: *New Journal of Physics* 17.6 (2015). ISSN: 13672630. DOI: 10.1088/1367-2630/17/6/063016.

[7] L. Farinacci, L. M. Veldman, P. Willke and S. Otte. 'Experimental Determination of a Single Atom Ground State Orbital through Hyperfine Anisotropy'. In: *Nano Letters* 22.21 (2022), pp. 8470–8474. ISSN: 1530-6984. DOI: 10.1021/acs.nanolett.2c02783.

[8] J. Kim, K. Noh, Y. Chen, F. Donati, A. J. Heinrich, C. Wolf and Y. Bae. 'Anisotropic Hyperfine Interaction of Surface-Adsorbed Single Atoms'. In: *Nano Letters* 22.23 (2022), pp. 9766–9772. ISSN: 1530-6984. DOI: 10.1021/acs.nanolett.2c02782.

[9] E. W. Stolte, J. Lee, H. G. Vennema, R. Broekhoven, E. Teng, A. J. Katan, L. M. Veldman, P. Willke and S. Otte. 'Single-shot readout of the nuclear spin of an on-surface atom'. In: *Nature Communications* 16.1 (2025), p. 7785. ISSN: 2041-1723. DOI: 10.1038/s41467-025-63232-5.

[10] R. Drost, M. Uhl, P. Kot, J. Siebrecht, A. Schmid, J. Merkt, S. Wünsch, M. Siegel, O. Kieler, R. Kleiner and C. R. Ast. 'Combining electron spin resonance spectroscopy with scanning tunneling microscopy at high magnetic fields'. In: *Review of Scientific Instruments* 93.4 (2022). ISSN: 10897623. DOI: 10.1063/5.0078137.

[11] J. J. Sakurai and J. Napolitano. *Modern Quantum Mechanics*. Cambridge University Press, 2017. ISBN: 9781108499996. DOI: 10.1017/9781108499996.

[12] P. Willke, Y. Bae, K. Yang, J. L. Lado, A. Ferrón, T. Choi, A. Ardavan, J. Fernández-Rossier, A. J. Heinrich and C. P. Lutz. 'Hyperfine interaction of individual atoms on a surface'. In: *Science* 362.6412 (2018), pp. 336–339. ISSN: 0036-8075. DOI: 10.1126/science.aat7047.

[13] K. Yang, W. Paul, F. D. Natterer, J. L. Lado, Y. Bae, P. Willke, T. Choi, A. Ferrón, J. Fernández-Rossier, A. J. Heinrich and C. P. Lutz. 'Tuning the Exchange Bias on a Single Atom from 1 mT to 10 T'. In: *Physical Review Letters* 122.22 (2019), p. 227203. ISSN: 10797114. DOI: 10.1103/PhysRevLett.122.227203.

[14] H. G. Vennema, C. Mier, E. W. Stolte, L. Edens, J. Lee and S. Otte. 'Nuclear magnetic resonance on a single atom with a local probe'. In: *arXiv* (2025). DOI: 10.48550/arXiv.2512.11652.

[15] K. Yang, P. Willke, Y. Bae, A. Ferrón, J. L. Lado, A. Ardavan, J. Fernández-Rossier, A. J. Heinrich and C. P. Lutz. 'Electrically controlled nuclear polarization of individual atoms'. In: *Nature Nanotechnology* 13.12 (2018), pp. 1120–1125. ISSN: 17483395. DOI: 10.1038/s41565-018-0296-7.

[16] Y. Chen, Y. Bae and A. J. Heinrich. 'Harnessing the Quantum Behavior of Spins on Surfaces'. In: *Advanced Materials* 35.27 (2023). ISSN: 0935-9648. DOI: 10.1002/adma.202107534.

[17] D. Sostina, L. Arnhold, L. M. Veldman, N. Betz, W. Wernsdorfer, S. Baumann, F. Delgado, P. Willke and S. Loth. 'Tuning the orbital state of a single spin on a surface'. In: *Forthcoming* ().

[18] L. Arnhold. 'Surface-governed dynamics of atomic-scale magnetic moments'. PhD thesis. University of Stuttgart, 2024. DOI: 10.18419/opus-15626.

[19] P. Kot, M. Ismail, R. Drost, J. Siebrecht, H. Huang and C. R. Ast. 'Electric control of spin transitions at the atomic scale'. In: *Nature Communications* 14.1 (2023), p. 6612. ISSN: 2041-1723. DOI: 10.1038/s41467-023-42287-2.

[20] S. Baumann, I. G. Rau, S. Loth, C. P. Lutz and A. J. Heinrich. 'Measuring the Three-Dimensional Structure of Ultrathin Insulating Films at the Atomic Scale'. In: *ACS Nano* 8.2 (2014), pp. 1739–1744. ISSN: 1936-0851. DOI: 10.1021/nn4061034.

[21] E. Fermi. 'Über die magnetischen Momente der Atomkerne'. In: *Zeitschrift für Physik* 60.5-6 (1930), pp. 320–333. ISSN: 1434-6001. DOI: 10.1007/BF01339933.

[22] B. R. Barnard, A. D. Caplin and M. N. B. Dalimin. 'The electrical resistivity of Ag and Ag-based alloys below 9K'. In: *Journal of Physics F: Metal Physics* 12.4 (1982), pp. 719–744. ISSN: 0305-4608. DOI: 10.1088/0305-4608/12/4/014.

[23] F. Delgado and J. Fernández-Rossier. 'Spin decoherence of magnetic atoms on surfaces'. In: *Progress in Surface Science* 92.1 (2017), pp. 40–82. ISSN: 00796816. DOI: 10.1016/j.progsurf.2016.12.001.

[24] S. Kolkowitz, A. Safira, A. A. High, R. C. Devlin, S. Choi, Q. P. Unterreithmeier, D. Patterson, A. S. Zibrov, V. E. Manucharyan, H. Park and M. D. Lukin. 'Probing Johnson noise and ballistic transport in normal metals with a single-spin qubit'. In: *Science* 347.6226 (2015), pp. 1129–1132. ISSN: 0036-8075. DOI: 10.1126/science.aaa4298.

[25] J. Van Kranendonk. 'Theory of Quadrupolar Nuclear Spin-Lattice Relaxation'. In: *Physica* 20.7-12 (1954), pp. 781–800. DOI: https://doi.org/10.1016/S0031-8914(54)80191-1.

[26] H. Garai-Marin, J. Ibañez-Azpiroz, P. Garcia-Goiricelaya, I. G. Gurtubay and A. Eiguren. 'Electron-phonon coupling of Fe-adatom electron states on MgO/Ag(100)'. In: *Physical Review B* 104.19 (2021), p. 195422. ISSN: 2469-9950. DOI: 10.1103/PhysRevB.104.195422.

[27] P. S. Fiske, J. F. Stebbins and I. Farnan. 'Bonding and dynamical phenomena in MgO: A high temperature 17O and 25Mg NMR study'. In: *Physics and Chemistry of Minerals* 20.8 (1994), pp. 587–593. ISSN: 0342-1791. DOI: 10.1007/BF00211854.

[28] R. V. Pound. 'Nuclear Electric Quadrupole Interactions in Crystals'. In: *Physical Review* 79.4 (1950), pp. 685–702. ISSN: 0031-899X. DOI: 10.1103/PhysRev.79.685.

8

Conclusion & Outlook

It’s easy to feel like this is the end of history... But of course, it’s not the end.
This is the middle of the story, and it falls to us to write a better end.

John Green

8.1. CONCLUSION

In this thesis, we have explored two directions to improve the degree and complexity of coherent control of individual spins in on-surface atoms using an STM equipped with ESR capabilities. Firstly, we generated voltage signals with an AWG for faster spin control within the same given coherence time and in more complex experiments. Secondly, we explored the use of individual nuclear spins in adatoms as quantum systems with potentially longer coherence times. We focused on time-resolved readout of the nuclear spin state with the STM via the hyperfine-coupled electron spin, which had not been done before in any extensive manner.

We have shown in chapters 3 and 4 that a 65 GSa/s AWG interfaced with an STM can be used, as a singular signal generator, to accomplish previously reported techniques for coherent single-atom spin control that have required multiple instruments in the past, including Rabi oscillations and initialization of coherent flip-flop dynamics with electron scattering. Furthermore, with the AWG we were able to combine these separate techniques in one experiment by generating nanosecond DC and RF pulses together, and in general go beyond previous experimental capabilities in terms of the complexity in experiment design.

We also used the AWG to measure both the amplitude and phase voltage transfer functions of the RF cabling in the STM (see chapter 5). This allowed us to compensate for the distortions to pulse shapes caused by the phase transfer function when generating the pulses with the AWG. The compensation was sufficient to achieve sub-nanosecond DC pulse widths in the STM junction, with the shortest accomplished rectangular pulse width of 203 ps better than any reported in literature.

Parts of chapter 4 are dedicated to initial experiments to probe the time-evolution of on-surface nuclear spins. In section 4.3 we observed coherent nuclear spin dynamics with the STM for the first time. This experiment used DC pulses to initialize a singlet-triple electron and nuclear spin system into a non-eigenstate by projecting on a spin product state, and we readout the ensuing coherent flip-flop oscillations. We find that the coherence time of the total system is limited by the short lifetime of the electron spin, because we operate in the low-field regime with large hybridization between the nuclear spin and electron spin. In section 4.7, we performed an initial experiment to measure the nuclear spin lifetime in the high-field regime that resulted in a tentative lower bound of 50 μs.

We extended the search for the nuclear spin lifetime in Ti adatoms to longer time scales in chapter 6 and found a T_1 in the order of seconds, which is orders of magnitude longer than any other on-surface spin that has been shown to be controllable by ESR-STM. Furthermore, this lifetime is long enough to perform single-shot readout of the nuclear spin state, which allowed us to investigate various relaxation mechanisms of the nuclear spin experimentally.

In chapter 7 we investigated the nuclear spin lifetime theoretically. From the combination of experimental and theoretical results, we conclude that the incoherent flip-flop rate between the electron and nuclear spin in the same adatom is the limiting factor for the lifetime. This relaxation rate is strongly suppressed with a larger external magnetic field strength or a smaller in-plane hyperfine coupling. Both are experimental parameters that can be manipulated to a certain degree, with the field strength limited in practice by the maximum RF frequency available for ESR driving in STM setups and the in-plane hyperfine coupling depending on the atomic binding site of the adatom.

8.2. OUTLOOK

8.2.1. APPLICATIONS OF STM ELECTRON SPIN CONTROL WITH AN AWG

Since we demonstrated the width of voltages pulse is limited to 2 ns by the phase transfer function, and not RF power losses, breaking that limit for future experiments requires pulse shape correction and thus an AWG. The ability to send sub-nanosecond pulses could enable faster coherent control of individual on-surface spins. Faster control might be a necessity to execute more complex quantum coherent experiments within the given coherence time, if no coupled spin platforms with significantly longer coherence times are found for ESR-STM in the foreseeable future. Furthermore, shorter pulses lead to better time resolution in pump-probe experiments. For experiments on free coherent spin time evolution [1], this corresponds to probing systems with larger spin-spin coupling that undergo faster dynamics. This includes artificially spin system, that could thus be engineered for faster two-qubit SWAP gates within the same coherence time.

In our view, the adoption of AWGs for coherent control in ESR-STM experiments is inevitable in the long term, because of the increasing amount of synchronized RF sources with different frequencies required for universal control over the entire Hibert space of coupled qubits. There are already 12 separate ESR transitions in an existing three-qubit platform [2], where indeed an AWG (max 480 MHz) was used in an IQ mixing configuration with two CW RF generators to access all these transitions. For future experiments with even more transitions covering yet larger frequency spans, it is impractical to synchronize the phases of all pulsed signals coming from separate RF signal generators without an AWG, not to mention the monetary costs of this number of instruments.

One downside of the AWG used in this thesis is the limited frequency range of 25 GHz analog bandwidth, reduced to 12.5 GHz for dual channel operation. This is solvable in principle because even faster models up to 80 GHz are now available on the market [3]. A remaining downside of AWGs is the significantly larger software overhead. Here we could learn from more mature qubit platforms and iterate on their existing solutions. Furthermore, if the ESR-STM community manages to grow significantly, commercial players might be interested in developing specialized RF modules for STM setups with user-friendly front-ends.

8.2.2. COHERENT CONTROL OF A NUCLEAR SPIN

Many on-surface electron spin platforms investigated with ESR-STM have reached a coherence time that is fundamentally limited by their spin relaxation time of < 1 μs to the metallic bath, with the exception of erbium atoms and remote Ti atoms on 3 mono-layer MgO (both yet unpublished) that were probably limited by magnetic tip field fluctuations or the lifetime of the strongly-coupled readout electron spins. The seconds-long nuclear spin lifetime that we found in chapter 6 and the lower susceptibility for magnetic noise due to the smaller g-factor, make nuclear spins promising candidates for longer coherence times for future ESR-STM experiments. While NMR-type driving of these spins has been demonstrated in CW experiments [4–6] and coherent time-evolution has been observed in this thesis, no true coherent control with pulsed NMR has yet been performed that can lead to universal qubit control.

The next experimental step in exploring the potential of nuclear spins is to show coherent Rabi oscillations of the nuclear spin are possible. If successful, such an experiment will also yield the coherence time T_2^* and the achievable Rabi times directly, which cannot be extracted unambiguously from CW frequency sweeps. The ratio of these parameters is an important figure of merit to compare the performance of nuclear spins to other on-surface atoms: how many coherent operations ('gates') can you do before the spin decoheres.

There are multiple processes that can be expected to limit the T_2^* before the 5 second relaxation time. For instance, bulk nuclear spins in the Ag and MgO constitute a fluctuating magnetic field that likely already cause dephasing faster than 5 seconds. For reference, Ag nuclear spins in bulk Ag at a 1 K temperature have a spin-echo T_2 around 10 ms [7]. A slightly longer T_2^* can be expected from this decoherence source for an individual Ti nuclear spin on MgO/Ag because of the separation from the Ag surface.

Nevertheless, the fluctuations of the nucleus moving through the field gradient from the vibrating magnetic tip will probably be a more significant dephasing source. An elementary estimation of the corresponding coherence time can be obtained by scaling the Ti electron spin coherence time we found in section 4.5 (~100 ns), which was likely limited by tip field fluctuations, by the three order of magnitude smaller g-factor of the nuclear spin. Hence we get a tip vibration limit of $T_2^* \approx 100\ \mu$s.

The decoherence channel that most-likely dominates is flipping of the electron spin in the same adatom. The Zeeman and the quadrupole energy of the nuclear spin, in presence of the hyperfine coupling, split the NMR transitions depending on the electron spin state. This means the NMR driving during a Rabi pulse suddenly becomes off-resonant whenever the electron spin changes to the excited state. At this point, the Larmor precession frequencies does not match the NMR drive anymore, which leaves the spin with an essentially random phase when the electron spin switches back and the drive is resonant again. The coherence timescale corresponding to this dephasing process is given by the lifetime of the electron spin groundstate excited by thermal processes. For Ti on the oxygen binding site of MgO, this groundstate lifetime has not been measured directly, but we can estimate it based on the measured excited state lifetime of 190 ns [8] and the thermal occupation of the groundstate of ≈ 80% with a Zeeman splitting of 12.75 GHz: the T_1 of the ground state = 190 ns · (0.8 / 0.2) = 760 ns, which would also be the estimated T_2^* for the nuclear spin according to the above reasoning.

This 760 ns is unfortunately not a great improvement on the coherence times achieved with ESR-STM using electron spins, but there might be ways to mitigate this decoherence channel. It is essentially a type of inhomogeneous broadening. Therefore it can be compensated with a spin echo pulse scheme if the achieved Rabi rates are faster than the timescale of thermal electron spin excitations. If the Rabi rate turns out to be too slow, another approach could be to use electron scattering to minimize the excited electron spin state lifetime, such that the random phase accumulation during this interval with another Larmor precession frequency is small. Using adatoms with overall longer electron spin lifetimes would also help, but that brings us back to the original motivation of using nuclear spins: the availability of ESR-STM-drivable electron spins with long spin lifetimes is limited. Note however that a longer electron spin coherence time is not necessarily required for this, as long as separate hyperfine peaks can be resolved with ESR-STM for nuclear spin readout, so more adatom systems might qualify.

It would be ideal if the electron spin could be removed from the atom and only brought back for the ESR-based readout. This is how the longest coherence times are achieved for nuclear spins in dopant quantum dot devices in semiconductors [9]. Implementing such a protocol for ESR-STM requires a zero-electron-spin adatom with a spin-carrying ionized state that can be ESR-driven, or the other way around. The readout charge state must have an ESR line width sufficient to resolve the hyperfine coupling. Adatom charge states excited with the tip-sample voltage can be stable [10] or short-lived [11]. For the former scenario, Au or Ag adatoms on NaCl/Cu or MgO/Ag(100) substrates are promising candidates [10, 12]. In the latter case, a back-gate voltage could be considered for stable ionization with electron spin coherence times sufficient for nuclear spin state readout. Alternatively, using any adatom or magnetic molecule with switchable meta-stable (orbital) states [13] where one of the states has a much reduced hyperfine coupling to the target nuclear spin, could improve the nuclear spin coherence time in a similar way. This would be akin to the scenario discussed in section 7.4.

Whichever decoherence channel mentioned above will dominate for the nuclear spin, the Keysight M8195A AWG can be used to perform pulsed experiments for all hypothesized timescales. Using the perfectly periodic waveform method outlined in section 3.4.7, the AWG can send coherent signals for indefinite Rabi pulse lengths with a frequency resolution of 100 Hz in the MHz range suitable for NMR. When using the AWG, NMR pulses can also be readily integrated with ESR and DC pulses for time-resolved nuclear spin readout.

The single-shot readout method of the nuclear spin developed in this thesis is an important asset for any future experiments on the coherent control, too. Not only does it boast a high readout fidelity (up to 98%), but this readout can also be used for initialization by projective measurement (possibly implemented as a post-selection) [14]. This initialization method is likely to outperform nuclear spin pumping via a DC spin-polarized current [4], which has been used in some time-averaged experiments [5, 6], in the high-field regime of low electron-nuclear spin hybridization.

8.2.3. PROSPECTS OF IMAGING NUCLEAR SPINS WITH STM

The research in this thesis has focused on the time-domain readout and control of nuclear spins with STM, which was a previously unexplored niche in the limited ESR-STM research done on nuclear spins. However, just the ability of ESR-STM to image the positions of individual nuclear spins with atomic resolution is unique and warrants more attention. No other atomic-resolution microscopy platform, except possibly ESR-AFM [15], has the potential to image nuclear spins in a multitude of solid state materials. Other sensing platforms that have achieved atomic-resolution spin imaging - such as NV centers [16] and gate-defined quantum dots [17] - are limited to only imaging the nuclear spins in their host material and do not retain sufficient magnetic field sensitivity when implemented as a scanning probe [18]. There are also other scanning probe platforms that could potentially reach single nuclear spin sensitivity, such as MRFM [19, 20] and scanning SQUIDs [21, 22], but are not able to image them with atomic resolution.

It would be essential for many application in nuclear spin imaging that ESR-STM capabilities are extended to other substrate types besides the proven thin-film insulators on metals like MgO/Ag. For instance, many quantum devices are fabricated on semiconductor or superconductor substrates. Furthermore, nuclear spins of bulk atoms that are not accompanied by a net electron spin for ESR driving are particularly challenging to image due to a lack of native hypefine coupling, while exactly these nuclear spins are the most technologically relevant in quantum applications due to their isolation. ESR-drivable adatoms could potentially be used to image those bulk spin-carrying nuclei by manipulating an adatom around on the surface to probe for an induced hyperfine coupling or magnetic dipole-dipole coupling, which would be visible as a ESR peak splitting if the ESR line width is sharp enough. To illustrate, the dipole-dipole coupling for a oxygen-site Ti electron spin to an ^{25}Mg in the bulk MgO/Ag can be estimated to be on the order of 80 kHz.

A more efficient approach might be to functionalize the STM tip by attaching an ESR probe at the apex, such as the PTCDA molecule in Ref. [23] that was shown to retain its ESR-STM signal above a bare metal surface. For this approach to succeed, other molecules with smaller ESR line widths than PTCDA will need to be found to resolve the small hyperfine coupling induced by proximity to the surface, which will likely also be less than 1 MHz. Yet another method, suitable only for semiconductors surfaces, could be to use an electron trapped in a tip-induced quantum dot [24] as a scanning ESR probe. The wavefunction of this dot extents deeper into the surface, which would increase the Fermi contact potential with bulk nuclear spins for a larger hyperfine splitting. However, the effective size of this scanning probe might be larger than atomic.

8.2.4. IMAGING NUCLEAR SPINS FOR SPIN QUBIT NANOFABRICATION

The technological potential for imaging nuclear spins with an STM is limited, but there are some use cases that could make a more application-focussed research direction worthwhile in the long-term. One key application niche is a need to interface with an individual nuclear spin for a nano-fabricated device, or a need to actively avoid interfacing with them in an environment with a semi-sparse nuclear spin distribution. Nuclear spins are always going to be atomically sized, so you'll need an atomic-resolution probe to either select or avoid them.

One concrete example are quantum dot spin qubits fabricated in silicon. These devices use isotopically pure ^{28}Si substrates to avoid the decoherence of fluctuating magnetic fields of nuclear spins from the isotope ^{29}Si in the bulk, but state-of-the-art substrates still contain ~0.07% ^{29}Si [25]. For a scalable quantum computer with at least thousands of qubits, adverse coupling to these remaining bulk nuclear spins is likely, especially for the nanometer surface area of gate-defined dots. This can be avoided in the nanofabrication of the device with the knowledge of the position of the nuclear spins.

Another approach is to intentionally couple quantum dots to individual ^{29}Si nuclear spins in the bulk to employ them as the primary qubits, with the electrons in the quantum dots serving as the means to couple nuclear spins indirectly. The original proposal for a spin qubit platform in silicon [26] outlined only the use of nuclear spins of individual dopants, but it was realized that individual ^{29}Si nuclear spins can also be employed as qubits [27] and multiple nuclear spins hyperfine-coupled to a quantum dot could serve as a quantum register [28, 29]. This approach has ultimately not been pursued very actively in silicon spin qubit platforms due to the historical lack of options for imaging the locations of the nuclear spins.

Instances of silicon quantum dots hyperfine-coupled to individual bulk nuclear spins, fabricated with trial and error, have been reported in Refs. [29] and [17]. These devices showed promising results in terms of coherence times of the ^{29}Si spins and compatibility with electron spin shuttling [30, 31] for scaling up to multiple coupled sites. Imaging nuclear spins could make scaling up possibly in practice by providing the means to systematically engineer the hyperfine coupling between an electron in the dot and a ^{29}Si nucleus.

STMs are not a common nanofabrication instrument, and the implementation of cryogenic ESR-STM into a spin qubit device production pipeline should be considered a long-term application ambition. On the other hand, STM has recently been employed successfully as a lithography patterning technique with atomic resolution to construct phosphorus dopant quantum dot spin qubits in Si [32–34]. Moreover, this nanofabrication approach is getting more widespread attention, with efforts to also use STM lithography to build NV center arrays in diamond [35], which could similarly benefit from engineered couplings to nuclear spins for a qubit register [36]. Both undertakings have thus already passed the significant hurdle of bringing an STM into the nanofabrication process.

8.2.5. TRACING ON-SURFACE CHEMICAL REACTANTS WITH ISOTOPIC LABELING

Labelled molecular compounds in which a specific atom has been replaced by an isotope that is otherwise chemically identical, have played a major role in elucidating the mechanisms of many chemical reactions [37]. Isotopic labeling traces the initial and final position of a specific reactant in a compound, which is can be crucial information to understand the complex process in between. In bulk experiments, the analysis of the labeled compounds is often performed with mass spectrometry, NMR spectroscopy, or the detection of radioactive decay.

One of the current frontiers of chemical synthesis is the use of a surface to stabilize certain extremely reactive (organic) molecules that can otherwise not be studied or even synthesized at all [38]. The chemical reactions involved in on-surface synthesis can be complex due to the catalytic function of the surface, so isotopic labeling would be a helpful method to understand the mechanisms. However, bulk detection methods for isotopic labeling can often not be applied because of the low volume yields of the used on-surface synthesis processes. For instance, many chemical reactions used to synthesize the most interesting and reactive molecules are made possibly by actuation with a surface scanning probe [39–42]. While such methods are systematic, the yield consists of only a handful of constructed molecules.

Recently, it has been proposed to use a surface scanning probe with nuclear spin imaging at atomic resolution, such as ESR-STM, to trace isotopically labeled reactants in products of on-surface synthesis [43]. This single molecule targeting overcomes the spatial averaging of bulk methods and could thus enable isotopic labeling for a field filled with complex chemistry questions. At the same time, the common usage of a scanning probe microscope in these on-surface synthesis studies also makes it relatively straightforward to integrate of scanning probe nuclear spin imaging techniques into the process.

8.2.6. OUTLOOK ON THE ESR-STM FIELD

From a zoomed out perspective, the contribution of this thesis to the field of ESR-STM has been, at the core, to develop new ESR-STM methods. The same is true for most works in the field since its inception a decade ago. We add more hardware capabilities (like with the AWG in this thesis), we explore what type of things can be probed by applying ESR-STM to model systems (now also nuclear spins in time), and we find novel ways to use the tools at hand (probe long-lived spins with time-resolved millisecond ESR pulses).

ESR-STM is a relatively recent addition to the long scanning probe tradition, but it is not a young field anymore either. It has grown into a triving community that, together, had to discover step-by-step all the complex processes that happen when you send RF voltages to a tunneling junction with a spin-polarized tip. And yet, with every new spin systems we bring under our tip we are reminded that our understanding of ESR-STM is still not complete.

We must realize that, despite this, our understanding has slowly crystalized and that our methods are solid. We are, in my opinion, at a point where we can harness our coherent control on-surface spins as a tool beyond only investigating the tool itself. A scientific microscope should be used to look outwardly at the world filled with questions to answer. Our community must look for open problems that the broader scientific condensed matter community cares about and that ESR-STM could solve, be it probing nuclear spins, artificial atomic spin structures or, most likely, magnetic quantum materials.

The opportunities to use ESR-STM as a genuine microscopy tool for a broad range of problems are already present. Over the past 4 years during my PhD, the scope of potential substrates that can be probed with the ESR-STM energy resolution has been extended tremendously. New classes of on-surface adatoms and molecules have been succesfully added to the list of ESR-STM compatibility. Most significantly, the recent approach to functionalize the STM tip with an ESR-active molecule resulted in a quantum sensor that could, in principle, bring ESR magnetic field sensitivity at atomic resolution to any surface accessible to STM [23]. Hopefully, the bigger and smaller insights cataloged in this thesis can also help propel the field of ESR-STM towards serving the wider scientific community.

There is a certain risk that we keep our heads turned inwards and we get stuck in our research ways. We might keep improving our methods in small steps, never gaining the confidence to apply our tool in the ’real world’, because we perceive ESR-STM as not yet ready and our understanding as still too incomplete to extract insights from more complex systems. However, this approach is not likely to contribute to useful scientific knowledge anymore. I want to encourage the ESR-STM community to attempt bigger steps, possibly even a jump. Adapting from the famous quote in Marcus Aurelius's Meditations: "Put an end to this research exploring what physics problems ESR-STM could solve, and solve one."

8.3. THESIS DATA AVAILABILITY

The data and analysis scripts used for this thesis can be found in a repository hosted by Zenodo.
DOI: 10.5281/zenodo.17504801

REFERENCES

[1] L. M. Veldman, L. Farinacci, R. Rejali, R. Broekhoven, J. Gobeil, D. Coffey, M. Ternes and A. F. Otte. 'Free coherent evolution of a coupled atomic spin system initialized by electron scattering'. In: *Science* 372.6545 (2021), pp. 964–968. ISSN: 0036-8075. DOI: `10.1126/science.abg8223`.

[2] Y. Wang, Y. Chen, H. T. Bui, C. Wolf, M. Haze, C. Mier, J. Kim, D.-J. Choi, C. P. Lutz, Y. Bae, S.-h. Phark and A. J. Heinrich. 'An atomic-scale multi-qubit platform'. In: *Science* 382.6666 (2023), pp. 87–92. ISSN: 0036-8075. DOI: `10.1126/science.ade5050`.

[3] Keysight Technologies inc. *M8100 series Arbitrary Waveform Generators*. URL: `https://www.keysight.com/nl/en/products/arbitrary-waveform-generators/m8100-series-arbitrary-waveform-generators.html` (visited on 26/10/2025).

[4] K. Yang, P. Willke, Y. Bae, A. Ferrón, J. L. Lado, A. Ardavan, J. Fernández-Rossier, A. J. Heinrich and C. P. Lutz. 'Electrically controlled nuclear polarization of individual atoms'. In: *Nature Nanotechnology* 13.12 (2018), pp. 1120–1125. ISSN: 17483395. DOI: `10.1038/s41565-018-0296-7`.

[5] L. M. Veldman, E. W. Stolte, M. P. Canavan, R. Broekhoven, P. Willke, L. Farinacci and S. Otte. 'Coherent spin dynamics between electron and nucleus within a single atom'. In: *Nature Communications* 15.1 (2024), p. 7951. ISSN: 2041-1723. DOI: `10.1038/s41467-024-52270-0`.

[6] H. G. Vennema, C. Mier, E. W. Stolte, L. Edens, J. Lee and S. Otte. 'Nuclear magnetic resonance on a single atom with a local probe'. In: *arXiv* (2025). DOI: `10.48550/arXiv.2512.11652`.

[7] A. Narath, A. T. Fromhold and E. D. Jones. 'Nuclear Spin Relaxation in Metals: Rhodium, Palladium, and Silver'. In: *Physical Review* 144.2 (1966), pp. 428–435. ISSN: 0031-899X. DOI: `10.1103/PhysRev.144.428`.

[8] K. Yang, Y. Bae, W. Paul, F. D. Natterer, P. Willke, J. L. Lado, A. Ferrón, T. Choi, J. Fernández-Rossier, A. J. Heinrich and C. P. Lutz. 'Engineering the Eigenstates of Coupled Spin-1/2 Atoms on a Surface'. In: *Physical Review Letters* 119.22 (2017), p. 227206. ISSN: 0031-9007. DOI: 10.1103/PhysRevLett.119.227206.

[9] J. J. Pla, K. Y. Tan, J. P. Dehollain, W. H. Lim, J. J. Morton, F. A. Zwanenburg, D. N. Jamieson, A. S. Dzurak and A. Morello. 'High-fidelity readout and control of a nuclear spin qubit in silicon'. In: *Nature* 496.7445 (2013), pp. 334–338. ISSN: 00280836. DOI: 10.1038/nature12011.

[10] J. Repp, G. Meyer, F. E. Olsson and M. Persson. 'Controlling the charge state of individual gold adatoms'. In: *Science* 305.5683 (2004), pp. 493–495. ISSN: 00368075. DOI: 10.1126/science.1099557.

[11] M. Rashidi, J. A. Burgess, M. Taucer, R. Achal, J. L. Pitters, S. Loth and R. A. Wolkow. 'Time-resolved single dopant charge dynamics in silicon'. In: *Nature Communications* 7 (2016), pp. 1–7. ISSN: 20411723. DOI: 10.1038/ncomms13258.

[12] E. Fernandes, F. Donati, F. Patthey, S. Stavrić, Ž. Šljivančanin and H. Brune. 'Adsorption sites of individual metal atoms on ultrathin MgO(100) films'. In: *Physical Review B* 96.4 (2017), pp. 1–7. ISSN: 24699969. DOI: 10.1103/PhysRevB.96.045419.

[13] F. Paschke, M. Briganti, V. Enenkel, T. Birk, J. Dreiser, P. Schmitt, R. F. Winter, F. Totti and M. Fonin. 'Cooperative and selective redox doping switches single-molecule magnetism'. In: *Science Advances* 11.21 (2025), pp. 1–10. ISSN: 2375-2548. DOI: 10.1126/sciadv.adu0916.

[14] D. Ristè, J. G. Van Leeuwen, H. S. Ku, K. W. Lehnert and L. Dicarlo. 'Initialization by measurement of a superconducting quantum bit circuit'. In: *Physical Review Letters* 109.5 (2012), pp. 1–5. ISSN: 00319007. DOI: 10.1103/PhysRevLett.109.050507.

[15] L. Sellies, R. Spachtholz, S. Bleher, J. Eckrich, P. Scheuerer and J. Repp. 'Single-molecule electron spin resonance by means of atomic force microscopy'. In: *Nature* 624.7990 (2023), pp. 64–68. ISSN: 0028-0836. DOI: 10.1038/s41586-023-06754-6.

[16] M. H. Abobeih, J. Randall, C. E. Bradley, H. P. Bartling, M. A. Bakker, M. J. Degen, M. Markham, D. J. Twitchen and T. H. Taminiau. 'Atomic-scale imaging of a 27-nuclear-spin cluster using a quantum sensor'. In: *Nature* 576.7787 (2019), pp. 411–415. ISSN: 14764687. DOI: 10.1038/s41586-019-1834-7.

[17] B. Hensen, W. Wei Huang, C. H. Yang, K. Wai Chan, J. Yoneda, T. Tanttu, F. E. Hudson, A. Laucht, K. M. Itoh, T. D. Ladd, A. Morello and A. S. Dzurak. 'A silicon quantum-dot-coupled nuclear spin qubit'. In: *Nature Nanotechnology* 15.1 (2020), pp. 13–17. ISSN: 17483395. DOI: 10.1038/s41565-019-0587-7.

[18] R. Schirhagl, K. Chang, M. Loretz and C. L. Degen. 'Nitrogen-vacancy centers in diamond: Nanoscale sensors for physics and biology'. In: *Annual Review of Physical Chemistry* 65 (2014), pp. 83–105. ISSN: 0066426X. DOI: 10.1146/annurev-physchem-040513-103659.

[19] C. L. Degen, M. Poggio, H. J. Mamin, C. T. Rettner and D. Rugar. 'Nanoscale magnetic resonance imaging'. In: *Proceedings of the National Academy of Sciences of the United States of America* 106.5 (2009), pp. 1313–1317. ISSN: 00278424. DOI: 10.1073/pnas.0812068106.

[20] J. Plugge. 'Probing the Limits of Quantum Mechanics using a Cold Mechanical Force Sensor'. PhD thesis. Leiden University, 2025.

[21] D. Vasyukov, Y. Anahory, L. Embon, D. Halbertal, J. Cuppens, L. Neeman, A. Finkler, Y. Segev, Y. Myasoedov, M. L. Rappaport, M. E. Huber and E. Zeldov. 'A scanning superconducting quantum interference device with single electron spin sensitivity'. In: *Nature Nanotechnology* 8.9 (2013), pp. 639–644. ISSN: 17483395. DOI: 10.1038/nnano.2013.169.

[22] M. Rog, T. J. Blom, D. B. Boltje, J. D. de Haan, R. Fermin, J. Niu, Y. C. Doedes, M. P. Allan and K. Lahabi. 'Tapping-mode SQUID-on-tip Microscopy with Proximity Josephson Junctions'. In: (2025), pp. 1–16. arXiv: 2508.21575.

[23] T. Esat, D. Borodin, J. Oh, A. J. Heinrich, F. S. Tautz, Y. Bae and R. Temirov. 'A quantum sensor for atomic-scale electric and magnetic fields'. In: *Nature Nanotechnology* 19.10 (2024), pp. 1466–1471. ISSN: 1748-3387. DOI: 10.1038/s41565-024-01724-z.

[24] R. Dombrowski, C. Steinebach, C. Wittneven, M. Morgenstern and R. Wiesendanger. 'Tip-induced band bending by scanning tunneling spectroscopy of the states of the tip-induced quantum dot on InAs(110)'. In: *Physical Review B - Condensed Matter and Materials Physics* 59.12 (1999), pp. 8043–8048. ISSN: 1550235X. DOI: 10.1103/PhysRevB.59.8043.

[25] H. G. Stemp, M. R. van Blankenstein, S. Asaad, M. T. Mądzik, B. Joecker, H. R. Firgau, A. Laucht, F. E. Hudson, A. S. Dzurak, K. M. Itoh, A. M. Jakob, B. C. Johnson, D. N. Jamieson and A. Morello. 'Scalable entanglement of nuclear spins mediated by electron exchange'. In: *Science* 389.6766 (2025), pp. 1234–1238. ISSN: 10959203. DOI: 10.1126/science.ady3799.

[26] B. E. Kane. 'A silicon-based nuclear spin quantum computer'. In: *Nature* 393.6681 (1998), pp. 133–137. ISSN: 00280836. DOI: 10.1038/30156.

[27] T. D. Ladd, J. R. Goldman, F. Yamaguchi, Y. Yamamoto, E. Abe and K. M. Itoh. 'All-silicon quantum computer'. In: *Physical Review Letters* 89.1 (2002), pp. 179011–179014. ISSN: 00319007. DOI: 10.1103/PhysRevLett.89.017901.

[28] M. V. G. Dutt, L. Childress, L. Jiang, E. Togan, J. Maze, F. Jelezko, A. S. Zibrov, P. R. Hemmer and M. D. Lukin. 'Quantum Register Based on Individual Electronic and Nuclear Spin Qubits in Diamond'. In: *Science* 316.5829 (2007), pp. 1312–1316. ISSN: 0036-8075. DOI: 10.1126/science.1139831.

[29] J. J. Pla, F. A. Mohiyaddin, K. Y. Tan, J. P. Dehollain, R. Rahman, G. Klimeck, D. N. Jamieson, A. S. Dzurak and A. Morello. 'Coherent control of a single Si 29 nuclear spin qubit'. In: *Physical Review Letters* 113.24 (2014), pp. 1–5. ISSN: 10797114. DOI: 10.1103/PhysRevLett.113.246801.

[30] A. J. Skinner, M. E. Davenport and B. E. Kane. 'Hydrogenic Spin Quantum Computing in Silicon: A Digital Approach'. In: *Physical Review Letters* 90.8 (2003), p. 4. ISSN: 10797114. DOI: 10.1103/PhysRevLett.90.087901.

[31] M. De Smet, Y. Matsumoto, A.-M. J. Zwerver, L. Tryputen, S. L. de Snoo, S. V. Amitonov, A. Sammak, N. Samkharadze, Ö. Gül, R. N. M. Wasserman, M. Rimbach-Russ, G. Scappucci and L. M. K. Vandersypen. 'High-fidelity single-spin shuttling in silicon'. In: *Nature Nanotechnology* July 2024 (2024). DOI: 10.1038/s41565-025-01920-5.

[32] S. R. Schofield, N. J. Curson, M. Y. Simmons, F. J. Rueß, T. Hallam, L. Oberbeck and R. G. Clark. 'Atomically precise placement of single dopants in si'. In: *Physical Review Letters* 91.13 (2003), pp. 2–5. ISSN: 10797114. DOI: 10.1103/PhysRevLett.91.136104.

[33] Y. He, S. K. Gorman, D. Keith, L. Kranz, J. G. Keizer and M. Y. Simmons. 'A two-qubit gate between phosphorus donor electrons in silicon'. In: *Nature* 571.7765 (2019), pp. 371–375. ISSN: 14764687. DOI: 10.1038/s41586-019-1381-2.

[34] J. Reiner, Y. Chung, S. H. Misha, C. Lehner, C. Moehle, D. Poulos, S. Monir, K. J. Charde, P. Macha, L. Kranz, I. Thorvaldson, B. Thorgrimsson, D. Keith, Y. L. Hsueh, R. Rahman, S. K. Gorman, J. G. Keizer and M. Y. Simmons. 'High-fidelity initialization and control of electron and nuclear spins in a four-qubit register'. In: *Nature Nanotechnology* 19.5 (2024), pp. 605–611. ISSN: 17483395. DOI: 10.1038/s41565-023-01596-9.

[35] L. Oberg, C. Weber, H. H. Yang, W. M. Klesse, P. Reinke, S. Corujeira Gallo, A. Stacey, C. I. Pakes and M. W. Doherty. 'Bottom-up fabrication of scalable room-temperature diamond quantum computing and sensing technologies'. In: *Materials for Quantum Technology* 5.3 (2025). ISSN: 26334356. DOI: 10.1088/2633-4356/ade359.

[36] T. H. Taminiau, J. Cramer, T. Van Der Sar, V. V. Dobrovitski and R. Hanson. 'Universal control and error correction in multi-qubit spin registers in diamond'. In: *Nature Nanotechnology* 9.3 (2014), pp. 171–176. ISSN: 17483395. DOI: 10.1038/nnano.2014.2.

[37] J. R. Hanson. *The Organic Chemistry of Isotopic Labelling*. The Royal Society of Chemistry, 2011. ISBN: 978-1-84973-188-1. DOI: 10.1039/9781839169076.

[38] S. Clair and D. G. De Oteyza. 'Controlling a Chemical Coupling Reaction on a Surface: Tools and Strategies for On-Surface Synthesis'. In: *Chemical Reviews* 119.7 (2019), pp. 4717–4776. ISSN: 15206890. DOI: 10.1021/acs.chemrev.8b00601.

[39] N. Pavliček, A. Mistry, Z. Majzik, N. Moll, G. Meyer, D. J. Fox and L. Gross. 'Synthesis and characterization of triangulene'. In: *Nature Nanotechnology* 12.4 (2017), pp. 308–311. ISSN: 17483395. DOI: 10.1038/nnano.2016.305.

[40] K. Kaiser, L. M. Scriven, F. Schulz, P. Gawel, L. Gross and H. L. Anderson. 'An sp-hybridized molecular carbon allotrope, cyclo[18]carbon'. In: *Science* 365.6459 (2019), pp. 1299–1301. ISSN: 10959203. DOI: 10.1126/science.aay1914.

[41] L. Sun, W. Zheng, W. Gao, F. Kang, M. Zhao and W. Xu. ‘On-surface synthesis of aromatic cyclo[10]carbon and cyclo[14]carbon’. In: *Nature* 623.7989 (2023), pp. 972–976. ISSN: 14764687. DOI: `10.1038/s41586-023-06741-x`.

[42] Y. Gao, F. Albrecht, I. Rončević, I. Ettedgui, P. Kumar, L. M. Scriven, K. E. Christensen, S. Mishra, L. Righetti, M. Rossmannek, I. Tavernelli, H. L. Anderson and L. Gross. ‘On-surface synthesis of a doubly anti-aromatic carbon allotrope’. In: *Nature* 623.7989 (2023), pp. 977–981. ISSN: 14764687. DOI: `10.1038/s41586-023-06566-8`.

[43] L. Sellies and J. Repp. ‘Electron Spin Resonance at the Single-Molecule Scale’. In: *Angewandte Chemie International Edition* 202506539 (2025). ISSN: 1433-7851. DOI: `10.1002/anie.202506539`.

Acknowledgements

I have found myself, somehow, writing this very last chapter in Sydney, Australia. When I started my PhD in 2021, I could never have imagined the places my scientific journey would bring me: from the brutalist campus of Regensburg to the snowy forests of Maryland, the cityscapes of Seoul, or just the conference hotel in Veldhoven. In short, my PhD has felt like an adventure, also on the research side of things.

On the other hand, there were many mundane working days, too. I have spent a lot of time trying out ideas that were not very successful, or performing experiments that were essentially reproductions of results achieved earlier by others. It does not help that a cryogenic STM is a machine with an extensive learning curve. I will freely admit that I still don't know how to execute everything our setup should be able to do.

But the ideas kept coming and I'm glad that I did get the opportunity to try out most of them in the lab. In the end, one idea was quite successful: observing the nuclear spin switching states live on the computer screen might have been one of the most exciting moments in my life. It's a mix of the happiness of discovery, combined with healthy skepticism whether anything else could be the cause. Possibly, there was even a hint of pride. While many other milestone achievements in my life were arguably forgone conclusions, any sort of scientific discovery was definitely not one of them.

There was also a subdued relief that this idea finally did work. I have to say that getting that experimental result did take a load off my mind. Even though the progress of science might be perpetuated by all the little failures, it's hard to envision my PhD as entirely successful without also achieving some (slightly) larger step forward. It is, maybe, a duality of the modern scientific world. Most certainly it is, in my mind, the story of my PhD.

Great places and stories to tell are nice and all, but time and time again it was the people that joined me on my adventures that have taken center stage. I have found great social communities everywhere I went. Often, I've happily felt that I was in the middle of them. It fueled my motivation over the last few years and for that I'm grateful.

My list of people to thank and acknowledge is long, so bear with me. As many of you know, I've never been good at limiting the length of my speeches, explanations, or anything I wrote down, ever.

First of all, I want to thank my promotor, **Sander Otte**. Right from the start, you granted me your trust in my experimental adventures, but you were also able to give the right amount of pushback on my overenthusiasm and my, at times, opinionating person. Your excellent ability to provide feedback on physics ideas underpins many of the results that I have achieved during my PhD.

While the memories of working together for over four years boils down to an overall good feeling about the whole thing, it is the specific moments together that will always stick with me. For example: piano at the QN Christmas lunch; free parking 100 m from the Capital building in Washington DC; getting the surprise news of the ERC advanced grant while we were in a brainstorm session for, of all things, a long-term research strategy; the dance floor at NWO Physics; a certain Valk sailing boat missing the dock by a mile on a very windy afternoon.

I also want to thank my other promotor, **Herre van der Zant**, for his support from down the hallway. Even if, by design, you were a bit further removed from my day-to-day activities, you have made a crucial contribution to my PhD progression by prompting me to come up with a rock-solid motivation for my research topic.

My gratitude extends to the entire promotion committee for their efforts in evaluating my thesis. **Yujeong Bae** and **Taner Esat**, research from both of you has inspired many of the experiment ideas I've had. Thanks for taking the time to look at my contributions to our field and carefully read my words.

Gary Steele, I've come to know you as an eternal rebel. Even now that you are essentially the establishment yourself, you can't help fighting the system. Driven by strong opinions and an urge to do something about it, the social openness that you exude reflects on the entire QN department, including me and the rest of the C&C!

Miriam Blaauboer, it has been an honor to have worked in the office next to the best higher education teacher in the Netherlands. This was the case during all of my time at the TU Delft, I presume, but they somehow only decided to give you the award last year. Your sincere and enthusiastic voice rising up from your office always brought a smile to my face. However, it often also brought out the headphones from my bag. It is what it is…

During my Master studies, I developed a fascination with the magic of scanning probe microscopy, and I had an interest in quantum magnetism and spin resonance as well. Imagine my surprise when it turned out there was a research group combining all of these topics just around the corner in Delft! Looking back, there might be no other group in the world that would have fit me better than the Otte Lab. This is in no small part, probably most of the parts, due to the people that made up the group whilst I was there.

Where else to start than **Rik Broekhoven**, our in-house theorist and my great friend (quite tall, you are). Having you as a like-minded companion in the group has meant a lot to me. Brainstorming about experiments with you is the best thing ever! On the personal side, I could also count on you. We've experienced many great small adventures together: hiking the cliffs of San Sebastian with limited supplies, karaoke in the canteen, puzzling with a pint, and exploring food culture in Berlin. Now we both are heading into new adventures after our PhDs, but I'm very excited to have you by my side once more as my paranymph.

Jinwon Lee, you joined us as a postdoc at the halfway mark of my PhD during a changing of the guard. Looking back, you had great timing: it turned out I had a pretty good idea for an experiment and I was in need for a sparring partner. I already knew we could work well together due to our collaborative kagome project when you were still in Leiden, so, unsurprisingly, you soon became my trusted lab partner. I really like that we can be frank with each other in discussions. We just operate on the same wavelengths. I think the most important thing is that I could simply trust you, in the lab and outside. My PhD wouldn't have been the same without your efforts and your friendship. On a different note, you are also the central embodiment of how South Korea has somehow played a surprisingly significant role in my adult life. I don't know how that happened…

Lukas Veldman, almost everything I know about operating an ESR-STM setup, at least the one in the He3 lab, I learned from you. Moreover, it was also really fun to learn from you. Thanks for your patience with me. I'm happy that I was able to provide a functional AWG in return. You brought both serious science and a chill atmosphere to the lab. I remember moments of laughter and moments of dead silence focus. We didn't even dare to cheer when we saw the flip-flop oscillations return after a horizontal offset, lest the signal would be gone again. It is probably that moment together with you (and Mark) that I'll remember the most. Even though I'm doing something slightly different now, I hope to see you around again in the overlapping region of single-atom spin business.

Hester Vennema, you are my PhD senior by two weeks. Still, we followed quite different paths to our final goal. Fortunately, we are both gonna get there. It's been fun with you around again, especially when your silly side comes out. And, of course, you have had great experimental success! The NMR project results were so exciting. I also appreciate that you were a person I could talk to and share my thoughts. You have been a person I can rely on.

Cristina Mier, San Sebastian is yet another specific place that became common thread in my PhD adventures. That connection was deepened with your arrival in Delft. Thanks for bringing your heartwarming charm to the lab, the many daily lunches, and all the many other mundane moments. Despite all the opportunities, however, we have never been present in San Sebastian at the same time. Hopefully we can change that sometime in the future, now that you'll head back there again.

Laëtitia Farinacci, there is a certain French-German bluntness to you in scientific discussions that I really appreciate, which is distinctly different from the infamous 'rude Dutch bluntness' that one might find on my side. However, I think it is fair to say I did need some time to get used to it. I've learned a lot from you during our overlap in Delft and I wish you all the best as a new group leader. It was meant to be.

Robbie Elbertse, in my first months I learned some medium-advanced LabVIEW methods from you, the magical maker of silly games. This emboldened me at the time to build on the existing LabVIEW codebase for my AWG project, rather than start from scratch entirely in Python. I'm still not sure whether I should thank you or curse you for that… In any case, thanks for hosting us at NIST and good luck as a young father.

Rasa Rejali, the sound of your roaring laugh is the happiest and loudest laugh I have witnessed in my life yet. And we got to hear it almost every day when you were around! You brought an upbeat atmosphere to the group that was sorely missed after your defense. However, you also had no issue making your opinion heard if you disagreed with someone. Best wishes in Norway!

Koen Bastiaans, you might not remember this, but my interest in STM started in earnest the moment I had to interview you during my Masters program. Great that we got to work together later on! I'm grateful for your help during the Kagome project, even if it didn't lead to any meaningful discovery.

Fenghuan Zhang, the life of an experimentalist can be a hard one. Sometimes the STM is just broken and you have to wait for one specific German guy to finally have time to visit our lab for repairs. But, if I understand correctly, it finally happened! Cheers to a bright results-filled future and many more festive hotpot evenings in BalPol.

Alexandra Meerovici, you moved in the opposite direction from me: while I'm leaving to spin qubits in silicon, you came from there to the ESR-STM field. I wish you good luck as the destined inheritor of the He3 lab. May the spin chains flip ever in your favor and may 10V pulses be a horror of the past.

Michael Schelchshorn, you joined as I was on my way out. Enjoy your time in Delft and Den Haag!

It's not the Otte Lab anymore, but it still counts for sure: **Alex Artaud**, you have your own group now! The value of your perspectives on the setup and experimental data over my years has been immeasurable. Your strong political rhetoric was more than welcome, too. Can you call it a debate if we actually mostly agree with each other? I'm also very curious about what will come of your (everyone's?) surprise STM. I wish you all the best with both the experiments and the teaching!

Mohamed Abouelela, the first generation of the Artaud lab. It is not easy to start such a new project, but you're rising up to the challenge despite the logistical setbacks. You're a hard worker and I'm certain you will succeed.

Talking about Otte Lab members in a broader category: **Allard Katan**, I fear we cannot entirely claim you as our own. You are a treasure trove of technical knowledge about scanning probes (and more) and I have consulted you many times. The Otte Lab, the entire QN department, and also the bio-nanoscience department are lucky to have you. I also fondly remember occasional Friday afternoon drinks in the TPKV and watching the World Cup from your backyard garden.

While I was in the group, multiple people have taken on the responsibility to steer the Otte Lab from the administrative side. **Maria Roodenburg-van Dijk** was there for me to provide a good start, but it is **Karin Wilhelm** that supported us for most of my time. Thanks for the help and warm company during all these years! Shootouts to **Anne Wellin**, who took over the direct support role at the end, and **Lidewij Hickey** and **Lizzy Groote**, who inevitably also answered my questions about the many diverse and specific non-physics things that tend to happen in a physics department.

I've also had the privilege to supervise multiple brilliant bachelor and master students over the years. Successively, **Bart Segers**, **William Holster**, and **Mart Jochems** have worked together with me on measuring the phase transfer function of the RF line, each building on work of their predecessor. What began as a side project, ended up as an entire chapter in my thesis! It was a blast with all three of you, and I hope you feel the same.

Esther Teng joined me as a master student on a different project. In the whirlwind of discoveries following the first nuclear spin time trace measurements, you contributed significantly to our data analysis and even came up with a detailed algebraic model (unfortunately, I had no time to include that model in my thesis). You can be proud of your results!

I'm very fortunate that I've been a part of many social communities over the last few years. It has made everything I did more enjoyable. More than anything, I've felt myself at home in the TU Delft Quantum Nanoscience department.

When I arrived in Autumn 2021, the milder covid restrictions in the later stages of the pandemic were in the process of getting phased out. After these years of relative inward isolation, the different research groups at QN started to grow towards each other again.

Social barriers were lifted thanks to some of the senior PhD students at QN (**Iacopo**, **Luigi**, **Sonakshi**, **Thierry**, and others!). Quite soon, as the covid restrictions were withdrawn entirely, I found myself getting dragged along by them to the TPKV and other Friday evening cafes. I got a taste of the social side of QN. Still, many pre-covid traditions that brought everyone in QN together were lost over that time. No problem: we just built new ones!

One of the initiatives to bring back a QN-wide social community was the Culture & Community Committee, or simply the C&C. After helping to organize the first spring QN Party in many years (and personally hosting a somewhat infamous team battle scavenger hunt game), I decided to join officially. Not that the C&C was very officially organized or anything. I believe that, with Gary Steele at the helm, the C&C will always operate a bit on the rogue side.

Due to our efforts with the C&C, QN now finally has a central coffee/chill room of appropriate size, that feels homely for everyone to meet each other. (If you have some time: ask Gary how we got the couches and how much effort it was to hang up the TV. Do not ask about dishwashers.) We started organizing monthly events and we brought back the Christmas potluck lunch. We have even hosted gatherings on more weighty topics like social safety. While all of these are relatively small things, QN feels more one whole than ever. I have to say that I'm a bit proud of that.

This would not have been possible without the vocal members of the C&C over the years: **Sonakshi Arora**, you were there from the beginning, at least for me. Organising that game was hard work, and I wouldn't do it again, but it was worth it. Hope everything is going well out there in the world! **Talieh Ghiasi**, I remember the first QN bytes event: picking up the sushi was a real adventure. It was great to welcome you back in Delft.

Furthermore, **Àlvaro Bermejillo**, the social engine; **Maurits Houmes**, the secret mathematician; **Michiel Dubbelman**, the normal Dutch student guy; **Yasmin Doedes**, the good witch; **Massi Rossi**, part of PhysicsWorld.com's 2025 highlights list, right above a picture of cats (yes, really); **Sarah Meihof**, a voice of reason; and finally, **Cosimo Tommasi**, Mr. Cable Bacteria himself: thanks for all the smaller and bigger contributions to the events we organized together.

Moreover, the C&C is an organic entity, where membership could be considered a fluid identity. I want to thank all the other people that have helped us over the years!

I shared office D113 with some great people who, somehow, stuck around in that same office about as long as me. **Michael Borst**, I've enjoyed your warm presence from the desk next to me for the entirety of my four years. Thanks for the many small chats. Also, your plants provided the must-needed ambiance in the room. Unfortunately, mine didn't fare as well… **Jin Chang**, I've definitely spent too much time with you discussing the details of the world's goings-on and our opinions about it. Still, I have no regrets. Have fun in Singapore! **Yong Yu**, your expertise as a postdoc was underlined every time a G-Lab PhD student entered the office. It made our office a lively place, for sure. **Dylan Litchfield**, the new guy. Your utter Australianness, I now realize, must have prevented some of the culture shock when I finally did arrive there. Good luck with the new-born and hit me up when you happen to be in Sydney in the coming years.

A shootout to our lunch buddies from a certain disappearing lab upstairs, deconstructed bit by bit. **Ulderico Filippozzi**, I don't know if it felt this way for you, but it always seemed you made the best of it. I find your determinism very admirable. Of course, you're also just a great guy, with a great sense of dry humor. **Mattias Matthiessen**, if Ulderico is a great guy, then you're a sweet guy. At the same time, you're also a sharp debater: somehow that goes together quite well. **Patrick Blah**, to complete the guy characterization, I would say that you're a no-nonsense kind of guy, and also definitely Irish.

Many people in QN during my years contributed to the great atmosphere I experienced and the great science being done. I know something like that is not a given, not even within QN itself. It is a long list, where I inevitably cannot include everyone:

Rául Luna Mena, the enthusiasm for teaching radiates from you. From the very start I knew our PhD-run bachelor Research Practical would be in good hand with you and Cosimo! **Nico Alberts**, thanks for the fabrications the new design for the Research Practical and many other small things needed throughout the years. **Siebe Visser** & **Vinod Narain**, thanks for the liquid helium support over the years. **Gesa Welker**, we have a history going way back! Your gentle care for people is something I admire. It was a beautiful thing to combine our goodbye events. I wish you the best in Eindhoven and everything that follows. **Clinton Potts**, it's amazing how quickly someone can feel like a friend after a few songs of karaoke together. Never stop with your enthusiasm for research! **Sercan Deve**, our connection to the TU Delft-wide PhD council. In some ways, a thankless task, but quite important for our representation. **Samer Kurdi**, the two most important things I will remember about you are: 1) you are secretly not a physicist at all, although now an honorary one after your 'defense'. 2) Man… you can eat! **Trent Kyrk**, you have demonstrated the uncanny ability to show up at the unexpected places. Naturally, it was always a pleasure. **Maz Ali** & **Yaojia Wang**, thanks for collaborating on the kagome STM project, right at the very beginning of my PhD. It was a great idea that unfortunately didn't work out. **Yaroslav Blanter**, **Toeno van der Sar** & **Eliška Greplovà**: Thanks for organizing the weekly QN 'werkbespreking' talks. Now that I'm working elsewhere, I appreciate even more what a broad view these talks from all QN groups have given me on the current topics in quantum research. **Roald van der Kolk** & **Artem Bondarenko**, I leave the responsibility and duty to ask questions during the QN talks to you (and Àlvaro). **Sonia Conesa Boj**, every day is brighter after a short little chat with you. **Abel Brokkelkamp**, I was happy to learn I was not going to be the sole representative of QN at the 2024 APS March Meeting. In the end, I think we can conclude that Minneapolis was a fine city, but maybe not the most interesting after all.

My gratitude for all the fun moments also extends to: **Sabrya van Heijst**, **Chris Soukaras**, **Onima Bisht**, **Jeroen Sangers**, **Riccardo Conte**, **Robin Dekker**, **Matteo Arfini**, **Liu Chen**, **Gaia Da Prato**, **Xiong Yao**, **Harmen Smedes**, **Riccardo Bellese**, **Pim Vree**, **Yufan Li**, **Roland Mulder**, **Fabian Gerritsen**, **Vinicius Fonseca Hernandes**, **Thom Spriggs**, **Sebastian Miles**. It would have been a lot less enjoyable without you all.

The world of physics research is quite a bit larger than just our QN faculty. Outside the confines of the TU Delft campus, I have found community and friendship in the physicists I've met all over the world. With only a handful of STM research groups in the Netherlands, I've felt a certain kinship between us. Unsurprisingly, I even studied together with some of the PhD students in the Dutch section of the field (**Maialen Ortego**, **Amber Mozes**!). We've met each other at various events quite regularly over the years and often happen to take the same trains back. Thanks for the companionship, Utrecht's **Swart Lab**, Leiden's **Allan Lab**, and Nijmegen's **Radboud SPM department**!

In general, though, most academic research fields in physics are distinctly international endeavors. The same is true for my little patch of scanning probe enthusiasts in atomic magnetism. While collaboration is the goal in science, some competition is common and you naturally cannot choose or select your 'competitors'. I've felt very fortunate, therefore, that the international Spins on Surfaces research field is one of the most welcoming communities you can find for a PhD student like me. Here, open discussion and scientific collaboration are the norm, which is not a given! I've met many amazing and friendly international scientists during my years in the field. Thanks to everyone in the community for shaping it into what it is today. I want to list some of them below:

Philip Willke, aside from the fact that you are a great person to drink a beer with, you have also been absolutely instrumental in my physics research during my PhD. It was on your suggestion, during lunch at SoS3 in the beautiful San Sebastian, that I considered how I might measure seconds-long nuclear spin lifetimes. It triggered the epiphany that, in fact, I had already accidentally observed live nuclear spin switching a few months prior! I've also learned a thing or two from you about writing papers. One of those lessons, as you said yourself during one of the many zoom calls: "This is the burger and the patty, and now we need to add the sauce." Although there are, apparently, downsides to working with you, too. Here I quote, verbatim, from your esteemed student **Paul Greule** while hiking to a high-up castle in Bad Honnef: "Philip said it was going to be fun. Don't trust Philip again."

The title of friendliest 'competitor' goes to the **Sebastian Loth** group in Stuttgart. It was always great fun to meet you all again all over the world, and even once in Stuttgart itself on your invitation. **Susanne Baumann**, thanks for the open communication about the phase TF methods. As you might have noticed, it turned into an entire chapter! **Nicolaj Betz**, we've had so many great discussions over the years. It helped me see many things in a different light. This includes stochastic resonance, of course, but also some aspects of life outside physics. **Lukas Arnhold**, thanks for initiating the DPG STM dinners. You are a crazy nice guy with crazy postcards. Keep them coming! **Johannes Schust** & **Henrik Lichtl**, let me say, honestly, that I didn't really know what to expect: joining two German guys I barely knew on a trip to South Korea's holiday island. And I was driving. Looking back, I can only say that I had a great time.

Moving on to non-Stuttgart people: **Lisanne Sellies**, you were the one who made our trip to Jeju happen, of course. In fact, ever since I've met you (the day before your faithful talk in Regensburg), you've made a lot of great things happen around you. Thanks for all the scientific fun, the late-night discussions, and the friendship. **Stepan Kovarik**, you are inquisitive and ready to point out a flaw in reasoning, but you would always do so exceptionally calm and clear in all discussions. It is truly admirable. Although

I would never dare to join you on a mountainous hike, since I will simply not keep up. **Mark Cavanan**, you were an awesome master student in the Otte Lab. I hope your chill personality is also serving you well in Zürich. **Fabian Paschke**, purely with your enormous social aura, you dragged me into a bar in Regensburg on a Monday evening, while I really should have gone to bed. In the following years, we have since achieved great things together, like winning the shared 3rd-place poster prize in Bad Honnef. But how to divide one 50-euro bill in three? **Johannes Schwenk**, you were a cheerful constant at conferences and a great source of fun conversations. All the best at KIT! **Leo Edens**, it was great to have you over in Delft, even in only for a short while. The result is there: we'll have our names on the same published paper (soon-ish, hopefully)! **Joe Stroscio**, thanks for hosting us at NIST and for the home-made pasta at your house. **Andreas Heinrich**, thanks for curating a collaborative ESR-STM community, by openly sharing experimental methods early on and bringing together the community in organized focus sessions on conferences. **Stefano Reale**, it turned out we have somewhat similar views on our futures in spins on surfaces: I hope to see you again soon in the silicon spin qubit community. **Shinjae Nam**, your great social energy hit me directly the first time we met outside of the canteen in Regensburg. Thanks for the guided tours and great conversations, in Germany and later in Seoul. **Lukas Spree**, chemist outsider and the last of the three Lukas's in my list, but definitely not the least. I'm looking forward to your progress with the bucky balls, now that I've heard so much about them. **Chris Wolf**, **Jose Reina-Gálvez**, **Nicolas Lorente**, thanks for the open discussions on the ESR and NMR driving mechanisms. Together, you really moved the field forward, although most of us need(ed) a little convincing.

There is a group of physicists closer to home who are also closer to my heart: the friends I made during the very beginning of my physics journey, during my bachelor studies in Leiden. It's a testament to our collective interest in natural science that three of us decided to pursue a PhD and the other one somehow knows as much about physics as if he had done one. Maybe that's what subconsciously pulled us towards each other in the first place, while working together on our Optics homework or something (aka 'harmonic oscillator #1'). More likely, it was the fact that mentor groups were divided based on last name in alphabetical order and a little bit of SSR sprinkled in.

Jean-Paul van Soest, it has been amazing to have a close friend present in the same department. We've come a long way in our physics journeys since we were dripping sugar water droplets down slopes. Your humor and your honest interest in others are both great qualities that I've admired and enjoyed over the years. Cheers to **Inês** and **Emily**!

Steven Riedijk, you're one of the sharpest minds I've ever met. Our two months of overlap in Sydney are still fresh in the back of my mind. Going on small trips together must have been the most fun way to integrate into my new home city and overcome the initial weeks of social nothingness. Good luck in the new office back in the Netherlands!

Thomas Steenbergen, a PhD student after all. Back in the Leiden Optics group no less. During the bachelors, you have often said I was the better physicist, while you got the better grades. I believe that relation has slowly inversed over the years. It's been great to keep up with you, even as we left behind the communities where we originally met. Now that I'm all the way on the other side of the world, I won't randomly meet you on the bicycle paths in Leiden or see you in Veldhoven. Let's stay in touch regardless!

My connection with the Leiden physics department LION has remained strong over the years. It is, after all, not that far away. Thanks everyone: **Martijn Janse**, **Jaimy Plugge**, **Dennis Uitenbroek**, **Koen van Deelen**, **Guido Stam**, **Matthijs Rog**, **Tycho Blom**, **Kaveh Lahabi**.

I also want to thank **Sam Arend** and **Camiel Efferen** from TNO. I've had a lot of fun with our little side project. Sometimes you must bend to rules a bit to make science happen, logistically that is. Thanks for approaching and including me.

Een PhD student leven is een stuk dragelijker met vrienden om je heen. Gelukkig is Delft niet ver van Leiden, waar ik ooit in 2015 lid werd bij een zeker dispuut genaamd BLOQ. Met de lichting die dat jaar lid werd, is de band alleen maar hechter geworden over de jaren. Toen ik in Delft begon werden we als 'Bierleden' officieel ouwelullen. Ondertussen hebben we zelfs het volgende niveau bereikt: tien jaar BLOQ-lidmaatschap, tien jaar kennen we elkaar nu al! Bedankt voor alle leuke avonden, weekenden, reizen de afgelopen jaren, en voor de steun die ik vanuit de lichting heb gevoeld.

Jeffrey van Raasdorp, als we het over steun hebben, ben jij de meest robuuste pilaar die er bestaat. Ik ben zo blij dat jij als paranimf naast mij komt te staan. **Iris Haex**, het is geweldig dat ik bevriend ben geraakt met iemand die zo capabel is. 'Lichting Incapabel' onwaardig, zou ik bijna zeggen. Ik heb wel het gevoel dat je milder geworden bent de afgelopen jaren. Wat is de laatste keer dat je Nathan echt goed uit balans hebt gebracht? Of misschien zijn het nu jouw collega's die het moeten moet vergelden? **Charlotte Groenendijk**, het is niet makkelijk om onderlinge sociale contacten onderhouden over de jaren. In de context van het dispuut ontmoetten we elkaar automatisch tijdens onze studietijd zonder moeite te doen, maar nu is dat natuurlijk anders. Ik denk dat we allemaal hebben overwogen hoe we dat zouden moeten aanpakken, maar jouw inzet om de lichtingsbanden vast te houden was belangrijk. Zo was een lichtingsvakantie naar Athene een geweldig voorstel. Ik heb goede herinneren aan een zekere fietstocht over een zeker bergachtig eilandje. **Wouter van Berkel**, waar ik besloot om slechts 30 km verderop te wonen na Leiden, ging jij 'helemaal' naar Breda! Ondertussen ben je onofficieel geïntegreerd Brabander en vierden we Carnaval met je mee. Het zat waarschijnlijk altijd al diep in je hart, als echt Bourgondiër. **David Groenendijk**, Huize Mors is niet meer, maar de samenhorigheid leeft voort. Al is die niet per se te vinden in Alphen, maar wel in de spare-ribs. Een van mijn beste mini-beslissingen van de afgelopen jaren was om samen met jou door te wandelen naar het uitzichtpunt over de vallei van Barbarano Vicentino. Terugkijkend voelde dat als een soort moment buiten de tijd, die hele vakantie in Noord-Italië eigenlijk ook. **Nathan Looije**, een echte Man van de Vrede. En een man van de historie. En van buitenlandse voetbalclubs. Die laatste twee zijn toch niet zó vredig, hebben we ook zelf ervaren. Na een valse start in Amersfoort: een nieuw appartement en een nieuw begin. De passie voor geschiedenis is gebleven, misschien wel sterker dan ooit!

Naast mijn BLOQ-lichting zijn er nog veel meer BLOQqers die mijn leven een blauw-en-oranje kleur hebben gegeven tijdens mijn PhD jaren. Een onvolledige lijst: **Ineke Huitema**, ik wil het toch even zeggen: Medium BLOQ was zo'n goed idee van jou, mij en Sanne! Jammer dat Jeffrey er niet bij was toen we dat bedachten… Medium BLOQ is de reden dat ik de afgelopen jaren nog zoveel leuke dingen heb gedaan met jou en met zoveel andere BLOQqers. En toch is er in deze jaren ook zoveel veranderd. Had jij vijf jaar geleden gedacht dat je op de semi-Zuidas zou werken, met zulke andere persoonlijke zorgen dan daarvoor? **Sem Kluiver**, man, man, man, wat is het werkende leven taai zeg. Waar is al onze vrije tijd ineens naartoe om, bijvoorbeeld, een thuisbezorgd kerstdiner te koken met 2 uur vertraging??? Enorm verliezen dit. Gelukkig bestaan er tegenwoordig brainrot memes als troost. Een eigen rijtjeshuis samen met Iris is natuurlijk ook niet verkeerd, of een reis naar Japan. Dat dan weer wel, met een inkomen. **Fleur Meulenmeester**, ik moet het uiteraard níet over PhD werk hebben met jou. Het hele punt van vrienden is dat je werk even achter je kan laten, aldus jijzelf. Daar ben jij beter in dan ik, en toch (of misschien daarom) heb jij de sterkere PhD work ethic. Ondertussen ik heb eindelijk durven doen waar jij al ervaringsdeskundige in bent: onderzoek in het buitenland. **Lars van der Burg**, de volgende keer dat ik jouw appartement bezoek, verwacht ik dat het ondertussen uitgegroeid is naar een echte jungle. **Qiong-Yi Wu**, de volgende keer dat ik jouw appartement bezoek, is het jouw beurt om Aziatisch te koken. **Sanne Zweekhorst**, de volgende keer dat ik … wacht, ik ben nog niet eens één keer bij jou langs geweest in Deventer! Gelukkig kwam je sporadisch naar Leiden de afgelopen jaren, zoals met Koningsdag. **Maud Straatsma**, ik heb goede herinneringen aan de bordspelavonden samen, bij jullie in het keukentje en elders. Het wordt nog een uitdaging om even fijne medespelers te vinden in Sydney. **Sascha Donath**, we hebben samen zoveel kleine leuke dingen meegemaakt over de jaren. Een soort side quests. De meest memorabele tijdens mijn PhD: het ThuisBezorgd BLOQ kerstdiner. Wat een geweldige vermoeiende chaos was dat, tijdens èn na het koken. **Jeanette Sadiq**, ook jij hoort bij de 2015/16 lichting, maar dan net op een andere manier. De volgende ronde social deduction spellen bij jou thuis zal wel een andere sfeer hebben met de tweeling in de kamer. Veel geluk samen! **Naomi Schutte**, als je om een of andere reden smacht naar nog meer natuurkunde in je leven, kun je altijd* even bellen voor een mono/dialoog. (*time zone restrictions may apply: ik ben niet altijd wakker).

Dan is er natuurlijk ook het Parabellum DnD party dat Jeffrey bij elkaar heeft weten te brengen. Hopelijk krijgen jullie het, in de afwezigheid van Emmett, voor elkaar om de 'Big Bad' te verslaan, of er tenminste achter te komen wie ze zijn. Op ons eerdere tempo ging dat in ieder geval niet lukken. **Thomas Griep**, niet alleen de drijvende kracht achter onze zeldzame daadwerkelijke plot-progressions, maar ook groot fan van bordspellen. Joinen gaat helaas de komende tijd moeilijk zijn voor mij vanuit Sydney. **Cornelie Schitker**, niet alleen een bron van gespeelde (?) sociale awkwardness, maar ook groot fan van musicals als de portemonnee het toelaat. Zo blij dat ik met jou naar Hadestown ben geweest. **Jasper Mulder**, niet alleen de drijvende kracht achter zo'n beetje alle plot-diversions, maar ook groot fan van bier, energy, en chocomel (of moet ik zeggen: cécémel). **Janna Linder** niet alleen een grote verrassing, maar ook medium fan van almanakken designen. Ik ben nog steeds trots op ons resultaat!

De vriendengroep die ik nog veel langer aan mijn zijde heb gehad, ken ik al sinds het begin van de middelbare school. Misschien hebben we elkaar te weinig gezien de afgelopen tijd, en verhuizen naar Australië gaat dat niet de juiste kant op brengen, maar elke keer als we samen zijn, voelt het weer vertrouwd. De jaarlijkse vakanties samen waren elke keer een hoogtepunt van mijn zomer.

Kyrian Maat, ondertussen heb ook jij de knoop doorgehakt om een PhD te beginnen. Welcome to the dark side. Wie had dat gedacht: van smashen op de bank met tosti in de hand, naar wonen in Amstelveen en presentaties in het buitenland. **Gido Limperg**, sorry nog dat ik Leiden verliet net toen jij er kwam wonen. Gelukkig was het dichtbij genoeg om af en toe samen eens naar de film te gaan. Toen ik dit jaar de aankondigingen van het IFFR zag, voelde ik wel teleurstelling dat ik het dit jaar niet mee kan maken. **Matthieu Rood**, aeiou aeiou aeiou. Uuuuuuuuuuuuuu. Aeiou aeiou aaaeiiiooou, aeiouaeiou. sjaak, Sjaak, Sjààààààkkie. Aeiou aeiou aeiou. ebrbrbrbrbrbrbr. (dit kun je vast ook wel vertalen, toch?) **Sjaak Wester**, succes met het opknaphuis. Een echte plek van en voor jezelf, en al jouw apparatuur. Als het eenmaal af is dan, natuurlijk. **Jeffrey Ng**, dan doe jij het toch slimmer: gewoon een nieuw huis kopen. Kan gewoon. Zoiets duurt vast niet jaren totdat je er kan wonen. Vast niet. Ik kijk er naar uit om bij jullie beiden op bezoek te komen.

Tenslotte wil ik mijn familie bedanken.

Oom Wim, **tante Jantina**, **oom Harko**, en **tante Randi**: zo heeft de stad Delft, net als bij jullie, ook bij mij een verrassend belangrijke rol gekregen in mijn leven. Het heeft ons nog weer een beetje dichter bij elkaar gebracht.

Pelle, nu ben jij ook zelfstandig gaan wonen in Delft! Hopelijk biedt het je een frisse blik op de stad waarin je bent opgegroeid en vele nieuwe avonturen.

Janne, zo leuk om samen naar Fontainebleau te gaan om te boulderen. En ook een goede mini-vakantie tijdens mijn PhD. Ondertussen ben jij een stuk betere klimmer geworden dan ik. Dat was natuurlijk onvermijdelijk. Blijf zo doorgaan!

Mijn oma en stiefoma hebben beide hun eigen indruk achtergelaten op mijn leven. Helaas, na mooie levens te hebben geleefd, zijn we ze allebei verloren de afgelopen jaren. **Oma Dicky**, bedankt. **Oma Clara**, bedankt.

Opa Wim, jouw oprechte interesse en openheid in een dialoog heeft mij altijd geïnspireerd. Voor jou waren dit zware, bewogen maanden. Weet dat we altijd voor je klaar staan.

Dagmar, ik vind het mooi dat we beide ons eigen pad hebben weten te bewandelen, in Enkhuizen, in Leiden, en nu ook de wijde wereld in.

Pap & **Mam**, na al die jaren weg van thuis ben ik uiteindelijk zelfs helemaal uitgevlogen naar het verst mogelijke. Maar waar ik ook ben, en waar onze gesprekken ook over gaan, ik voel altijd jullie steun. Jullie hebben me het vertrouwen gegeven dat het goed komt.

"He finds he often struggles for things to tell people at home, because the small things are too mundane and the rest is too astounding and there seems to be nothing in between."[1]

---

[1] Samantha Harvey, Orbital

Curriculum Vitæ

Evert Willem Stolte

03-08-1997	Born in Hoorn, The Netherlands.

EDUCATION

2009–2015	VWO (Secondary Education) RSG Enkhuizen
2015–2018	BSc. Natuurkunde Universiteit Leiden
2019–2021	MSc. Physics Specialization: Quantum Matter & Optics Universiteit Leiden
2020–2021	Research internships Allan Lab, LION, Leiden Oosterkamp Group, LION, Leiden
2021–2025	PhD. in Physics Technische Universiteit Delft Department of Quantum Nanoscience *Thesis:* Faster control or longer lifetimes: Expanding the toolbox for electron and nuclear spin dynamics in on-surface atoms *Promotor:* Prof. dr. A.F. Otte

List of Publications

3. H. G. Vennema, C. Mier, E. W. Stolte, L. Edens, J. Lee and S. Otte. ‘Nuclear magnetic resonance on a single atom with a local probe’. In: *arXiv* (2025). DOI: `10.48550/arXiv.2512.11652`

2. E. W. Stolte, J. Lee, H. G. Vennema, R. Broekhoven, E. Teng, A. J. Katan, L. M. Veldman, P. Willke and S. Otte. ‘Single-shot readout of the nuclear spin of an on-surface atom’. In: *Nature Communications* 16.1 (2025), p. 7785. ISSN: 2041-1723. DOI: `10.1038/s41467-025-63232-5`

1. L. M. Veldman, E. W. Stolte, M. P. Canavan, R. Broekhoven, P. Willke, L. Farinacci and S. Otte. ‘Coherent spin dynamics between electron and nucleus within a single atom’. In: *Nature Communications* 15.1 (2024), p. 7951. ISSN: 2041-1723. DOI: `10.1038/s41467-024-52270-0`

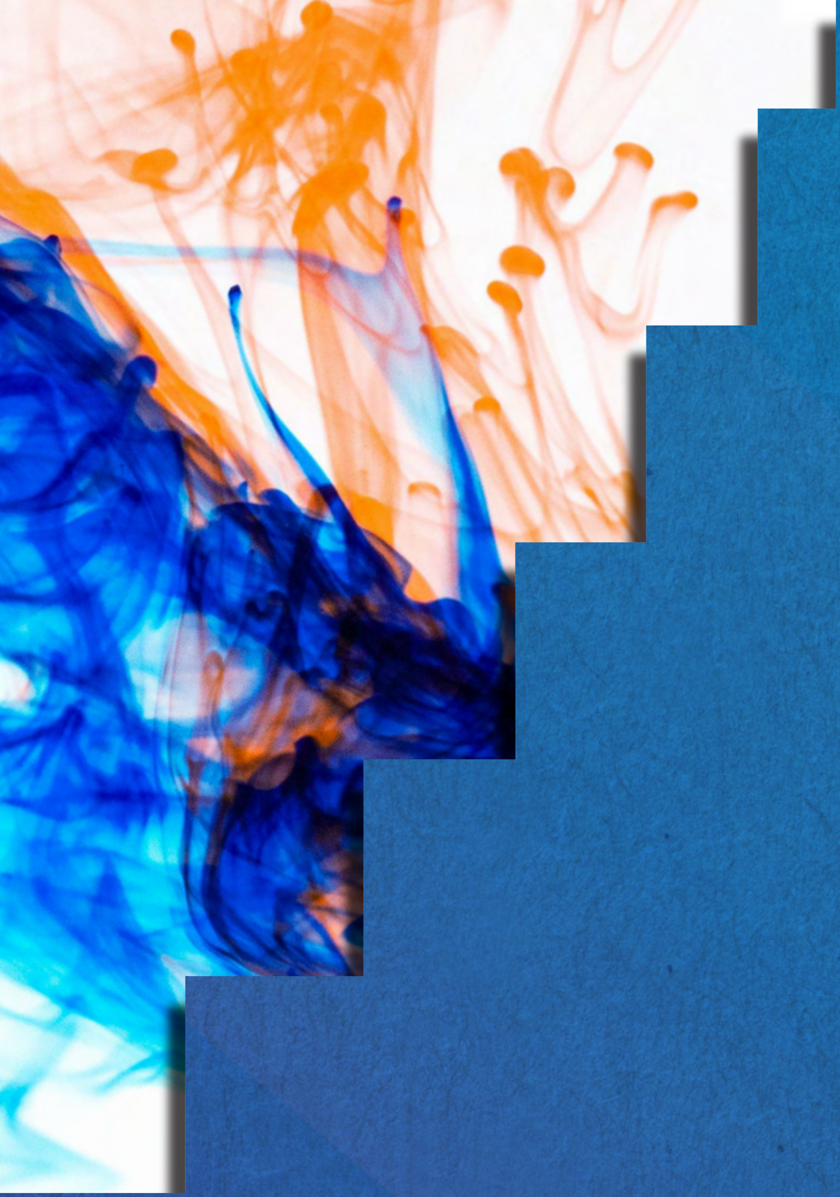

PhD thesis of Evert Stolte
Researched at Delft University of Technology
Supervised by Sander Otte

ISBN: 9789463849227